Dissertations

Summer 8-2017

Cellulose Reinforced Thermoplastic Composites By In-Situ Ring-Opening Polymerization

Shahab Kashani Rahimi
University of Southern Mississippi

CELLULOSE REINFORCED THERMOPLASTIC COMPOSITES

BY *IN-SITU* RING-OPENING POLYMERIZATION

by

Shahab Kashani Rahimi

A Dissertation
Submitted to the Graduate School,
the College of Science and Technology,
and the School of Polymers and High Performance Materials
at The University of Southern Mississippi
in Partial Fulfillment of the Requirements
for the Degree of Doctor of Philosophy

August 2017

CELLULOSE REINFORCED THERMOPLASTIC COMPOSITES

BY IN-SITU RING-OPENING POLYMERIZATION

by Shahab Kashani Rahimi

August 2017

Approved by:

_____
Dr. Joshua U. Otaigbe, Committee Chair
Professor, Polymers and High Performance Materials

_____
Dr. Robson F. Storey, Committee Member
Professor, Polymers and High Performance Materials

_____
Dr. Sarah E. Morgan, Committee Member
Professor, Polymers and High Performance Materials

_____
Dr. Jeffrey S. Wiggins, Committee Member
Associate Professor, Polymers and High Performance Materials

_____
Dr. Sergei I. Nazarenko, Committee Member
Professor, Polymers and High Performance Materials

_____
Dr. Jeffrey S. Wiggins
Director, School of Polymers and High Performance Materials

_____
Dr. Karen S. Coats
Dean of the Graduate School

Published by the Graduate School

THE UNIVERSITY OF
SOUTHERN
MISSISSIPPI.

ABSTRACT

CELLULOSE REINFORCED THERMOPLASTIC COMPOSITES

BY IN-SITU RING-OPENING POLYMERIZATION

by Shahab Kashani Rahimi

August 2017

Over the past two decades, the increasing concern about the negative

environmental impacts of synthetic materials has led to rising interests in utilizing

renewable natural resources to develop polymer materials with comparable properties and

performance to their synthetic counterparts. One of the major fields of interest is polymer

composites where the replacement of synthetic fibers with bio renewable natural fibers is

of great potential. However, the processing difficulties, in terms of fiber dispersion and

thermal stability have limited the application of cellulosic fibers to polymers with low

processing temperatures which are mostly hydrophobic polymers. As a result, the true

reinforcing ability of the fiber could not be fully exploited due to polymer-fiber

incompatibility.

This dissertation discusses a novel approach to develop nanocomposite and

composite materials based on high melting point polyamide 6 engineering thermoplastic

matrix utilizing the in-situ ring-opening polymerization. Both nanoscale cellulose

nanocrystals as well as macroscale natural fibers were used as reinforcement. The initial

study consisted of a detailed analysis of physical, viscoelastic and rheological properties

polyamide 6 nanocomposites reinforced with cellulose nanocrystals in correlation with

the morphology and microstructure of the nanocomposites. These nanocomposites were

then used a masterbatch for further processing via melt extrusion technique. The effect of

surface modification of cellulose nanocrystals with silane coupling agents on isothermal and non-isothermal crystallization of the obtained nanocomposites were fully investigated using a number of different theoretical models to gain a better understanding of the interrelation of surface functionality, microstructure and crystallization behavior. In addition, the effect of polymer-particle interfacial modification on shear and extensional rheological behavior as well as the mechanical properties of the nanocomposites were investigated. The results were correlated with the development of "interphase" in modified systems as confirmed by quantitative nanomechanical analysis.

In addition, a series of polyamide 6 composites reinforced with flax fabric and kraft pulp cellulose fibers were successfully developed using vacuum assisted resin infusion process and a through processing-structure-property relationship study was conducted. The findings of this research effort provide a better understanding of the complex processing-structure-property relations of engineering thermoplastics reinforced with cellulosic fibers.

.

ACKNOWLEDGMENTS

DEDICATION

First and foremost, I would like to thank my parents. Without their continuous support, help and encouragement, none of this would have been possible.

I would like to thank my dear wife, Mahtab, for her patience, understanding, help and support during my entire graduate career. I would like to dedicate this document to my wife and parents.

.

TABLE OF CONTENTS

LIST OF TABLES

LIST OF ILLUSTRATIONS

CHAPTER I - INTRODUCTION

1.1 Thesis Organization

This thesis includes seven chapters. Chapter 1 is a summary of the literature on nanocomposite materials containing cellulose nanocrystals (CNCs) focusing on preparation techniques of CNC, processing methods, surface modification and polymer-cellulose interfaces, and properties of CNC-based nanocomposites such as mechanical, thermal and rheological properties. Chapter 1 a part of an invited book chapter titled "Green Hybrid Composite from Cellulose Nanocrystal" in "Hybrid Polymer Composite Materials", Elsevier, currently in press. Chapter 2 is a published manuscript in Polymer Engineering and Science journal that examines the morphology, viscoelastic, creep, and dynamic mechanical and rheological behavior of polyamide 6 (PA6) /CNC nanocomposites prepared by *in-situ* ring-opening polymerization (ROP) technique. Chapter 3 is a published manuscript in Polymer journal that investigates the effect of the surface functionality of the CNCs in PA6 matrix on isothermal and non-isothermal crystallization behavior of the PA6/CNC nanocomposites. Chapter 4 discusses the effects of the interfacial modification of PA6/CNC nanocomposites with organosilane coupling agent on microstructure, mechanical and rheological properties of PA6/CNC nanocomposites prepared by *in-situ* ROP and subsequent melt extrusion process. Chapter 5 discusses processing-structure-property relationship of PA6 composites reinforced with flax fabric and kraft cellulose pulp mat via vacuum assisted resin infusion technique. Chapter 6 is an extension of the project to a fully biodegradable and biocompatible nanocomposite system of poly (butylene adipate-co-terephthalate) (PBAT) reinforced with CNCs prepared via reactive extrusion method and is focused on investigation of the

structure-property relations and biocompatibility of the nanocomposites. Chapter 7 provides a summary of relevant conclusions of the thesis and provides a view on potential future directions.

1.2 Literature Review

1.2.1 Overview

Over the past decade, tremendous research and development efforts have been focused on cellulose nanomaterials both as reinforcing and functional additives for polymer composite application as well as building block for development of novel functional materials. These efforts are motivated by a number of enhanced benefits of cellulosic fibers such as natural abundance and availability, inherent bio-renewability and sustainability, exceptional structural and mechanical properties, low cost, low density and biodegradability. One of the main challenges in using natural fibers as reinforcing components of polymer composites is the variation of properties based on their original climatic conditions, species, age and spatial distribution of properties within the lingocellulosic fibers. One approach to avoiding the negative impact of this variation of properties is to eliminate the hierarchical structure inherent to cellulosic fibers by removing the fiber constituents to extract the highly rigid and crystalline core of the fibrillar assembly known as cellulose nanocrystals (CNC) or cellulose whiskers. These nano-scale cellulosic moieties have attracted a great level of academic and industrial attention not only because of their superior structural and mechanical properties (as will be discussed in this review) but also due to their nanoscale dimensions, high surface area and natural abundance of their source cellulosic material which makes them superior alternatives to conventional nano-additives and fibers such as silicates, glass and

inorganic nanomaterials traditionally used in composites applications. As an example, taking the density of CNCs to be at approximately 1.5 g/cm^3 (*cf.* 2.6-3 g/cm^3 for inorganic clays), a significant weight reduction of the final nanocomposite material is expected to be obtained simply by replacing clays with CNCs in the nanocomposite [1].

In fact, cellulose nanocrystals (CNCs) or cellulose whiskers are the highly crystalline core fraction of cellulosic fibers where other components such as lignin, hemicellulose, proteins, extractives and para-crystalline inter-fibrillar regions are removed in the extraction process, leaving behind the tightly packed rod-shape defect free cellulose fraction that are held together by strong hydrogen bonding of cellulose macromolecules. The hierarchical structure of cellulose fiber is shown in Figure 1.1 [2]. These nanocrystals possess exceptional mechanical properties with axial Young's modulus reported to be as high as 160 GPa, a value surpassing that of Kevlar and steel [3].

Cellulose macromolecule is comprised of rigid linear chain of ringed glucose units that are formed by a covalent link of β 1-4 glucosidic bond between the anhydroglucose rings ($C_6H_{10}O_5$) [4]. Strong intermolecular hydrogen bonding via hydroxyl units of the glucose and oxygen of neighboring ring unit stabilizes the links, resulting in linear chain configuration with chair conformation [5]. This strong hydrogen bonding is the basis of formation of this elementary fibrillar structure which further aggregates into microfibrillar arrangement. Depending on the nature of the natural cellulose fiber, the arrangement of the fibrils and the degree of polymerization of the cellulose (or its length) varies among different species and sources. The microfibrils are the basic building-blocks of the wood/plant cell wall. These fibrils are composed of cellulose crystallites that are connected via amorphous regions which are further wrapped in a polyglucosan material

and hemicellulose. These microfibrils are held together via a matrix of lignin, proteins and extractives. Therefore, certain processes have been developed in order to isolate the highly crystalline cellulose in the core of the fibrils. In this chapter, a survey is provided that covers previous research efforts together with some recent developments in the area of polymer/CNC nanocomposites and properties of CNCs, processing and properties of CNC-based nanocomposite materials.

1.2.2 Preparation of Cellulose Nanocrystals

Cellulose nanocrystals are usually prepared using a number of different methods such as acid hydrolysis, mechanical process, enzymatic synthesis and a recent approach using ionic liquids [5]. Normally, in a typical process, a two stage procedure is followed which depends on the cellulose source material. The first step involves the removal of polyglucosan components (except the cellulose fibrils) and the second stage involves extraction of the nanocrystalline regions. Specifically, lingocellulosic fibers are first chemically treated to remove the lignin, hemicellulose and extractives. A more recent approach that has been used in a number of studies is based on steam explosion technology [6-7] to remove the lignin and hemicellulosic portions of the biomass where typically the lingocellulosic fibers are subjected to high pressure steam at a pressure of around 15 bars for a certain amount of time (usually less than 20 minutes) at temperature range of 220-270°C. The fibers are then immediately exposed to atmospheric pressure by opening the chamber which causes the lignin/hemicellulose fractions to explode. These fractions can then be removed by extraction leaving the highly crystalline cellulose fibrils for further processing of CNC extraction.

In the case of CNCs derived from the tunicate [8], the mantle is isolated from the animal followed by removal of the encapsulating protein components surrounding the microfibrills. In the case of bacterial and enzymatic cellulose production, after the cellulose micrfibrills are cultivated, the walls and other components are removed by washing with alkaline solutions [9-10]. After the removal of the matrix material in the cellulose source, the second stage of the production of CNCs usually involves a number of treatments that include acid hydrolysis, mechanical process and a bacterial/enzymatic treatment that will be described later in detail in this section.

One of the major factors that dictates the final morphology and structure of the cellulose nanocrystals, is the source material used to isolate the CNCs. Various cellulosic materials have been used to prepare the CNCs including wood fibers such as bleached softwood [11] and sugar beet pulp [12], cotton fibers [13], plant fibers such as flax [14], sisal [15], ramie [16] and hemp fibers [17]. In addition, the major non-plant/wood based sources are various types of bacteria [10] as well as tunicate [8]. Typical cellulose nanocrystals are rod-like whiskers with lengths of 25-1000nm and diameters of 4-50 nm. It has been shown that the CNCs obtained from tunicate and bacterial growth method have typically larger lengths due to the higher amount of crystalline fraction in the cellulosic part of these materials [18]. For example, Lima et al [19] reported a length value of 1160nm and a diameter of 16nm for whiskers obtained from tunicate giving an aspect ratio of 72.5 while the whiskers obtained from cotton had a length of 255nm and diameter of 15nm with an aspect ratio of 17. Figure 1.2 depicts a TEM image of typical morphology of the CNCs obtained from various sources.

Sulfuric acid hydrolysis is the most common method for fabrication of cellulose nanocrystals [5-6]. In a typical process, the cellulose starting material (i.e., after first stage of removal of the matrix containing the crystalline regions in the fiber) is suspended in DI water followed by addition of sulfuric acid at prescribed composition. Then the reaction continues for a set amount of time at a fixed temperature. The final mixture is quenched using ice cubes, filtered or centrifuged and dialyzed against water until a neutral pH is achieved [20]. The purpose of the acid hydrolysis process is to remove the amorphous or para-crystalline regions surrounding the highly crystalline cores of the cellulose fibrils to leave the cellulose nanocrystals that are more resistant towards acidic medium in the final mixture. Sulfuric acid hydrolysis results in surface negative charges (sulfonate groups) that are responsible for colloidal stability of CNCs in aqueous solution at the price of reducing the thermal stability. A number of extensive studies have been carried out to investigate the effect of acid hydrolysis parameters such as time, temperature and concentration of acid. For example, Dong and coworkers [21] found that a concentration of 64% (w/v) with a liquor ratio of 1:8.75 with the reaction conditions of 1 hour at 45°C and ultrasonic treatment time of 5 minutes result in a suspension with anisotropic behavior above 4.5 % (w/v).

In a comprehensive study by Bondenson and co-workers [22], the yield of the hydrolysis process as well as the particle polydispersity was examined and the obtained results correlated to hydrolysis conditions. Their results indicated that particles with an average length between 200 and 400 nm and diameter of less than 10 nm with a yield of 30% could be achieved with a reaction time of 2 hours while longer reaction times decreased the CNC length (via depolymerization of cellulose) and increased surface

negative charge. In a systematic study by Hamdu *et al* [23], it was found that a temperature of 65°C with shorter reaction times of about 5 minutes resulted in the highest CNC yield of 38%. In another study [24], the effect of hydrolysis temperature on preparation of cellulose nanocrystals obtained from cotton fibers was investigated. Using a fixed reaction time of 30min and sulfuric acid concertation of 65%, the authors showed that by incremental increase in temperature from 45 to 72°C, the length of the crystals reduced from 141 to 105 nm while the polydispersity of crystal size increased from 1.15 to 1.21 indicating a more non-homogenous hydrolysis process at elevated temperatures. Interestingly, Beck-candanedo *et al* [11] in a study of the effect of sulfuric acid hydrolysis time and acid-to-pulp ratio on dimensions of cellulose nanocrystals obtained from black spruce wood pulp showed that acid hydrolysis at longer reaction times produced shorter nanocrystals with lower size distribution (or polydispersity). The effect of acid-to-pulp ratio was found to be inversely related to the nanocrystal dimension, implying that higher acid-to-pulp weight ratio results in formation of smaller crystals. The effect of acid-to-pulp ratio was found to be dependent on the retain time in such a way that the effect of acid-to-pulp ratio is more pronounced at shorter reaction time.

In an effort to reduce the polydispersity of the nanocrystals obtained by acid hydrolysis, differential centrifugation [25] and ultracentrifugation [26] methods have been adopted. Bai et al [25] used a multi-step centrifugation process with step-wise incremental increase in the centrifugal speed to separate various fractions of CNC from the suspension at different velocities. It was found that smaller nanocrystal fractions could be separated at higher centrifugal speeds while each fraction at each speed showed a narrow size distribution.

In addition to sulfuric acid, a number of other mineral acids have also been used to prepare cellulose nanocrystals by the hydrolysis process. Yu *et al* [27] studied the effect of hydrochloric acid hydrolysis parameters in preparation of cellulose nanocrystals. The optimized conditions to achieve highest yield and smallest diameter were reported to be a reaction time of 3 hours at 110°C with acid-to-pulp ratio of 60ml.g^{-1}. Under these conditions, the CNC production yield from cotton and wood pulp material were 85% and 81% respectively. In addition, it was found in the same study that the HCl-extracted nanocrystals improved thermal stability compared with that of the samples prepared by sulfuric acid hydrolysis, as well as, produced relatively narrower size distribution of the cellulose nanocrystals. However, one of the major disadvantages of extraction of CNC with hydrochloric acid, is the lack of surface charge after the treatment process that results in significant flocculation and aggregation of whiskers and poor dispensability [28]. This characteristic is opposite to that of the treatment with sulfuric acid hydrolysis as the sulfate anions on the surface of CNC provide colloidal stability in aqueous medium. A shown in AFM images of Figure 1.3, it is clearly seen that a cast film of the dispersion of CNC prepared from sulfuric acid hydrolysis shows a much better dispersion of whiskers compared to an aggregated structure obtained from hydrochloric acid hydrolysis method. In a series of studies by Wang and coworkers [29-30] a mixture of sulfuric and hydrochloric acid was used under ultrasonic treatment which resulted in development of spherical cellulose nanocrystals where the high polydispersity of the spheres resulted in formation of a liquid crystalline phase.

A number of other researchers have reported the use of phosphoric acid in the hydrolysis process [31-32]. Espinosa *et al* [31] optimized the hydrolysis process with

phosphoric acid at 100°C with an acid concentration of 10.7M for 90 minutes. The whiskers obtained under these conditions had an average length of 316nm and dimeter of 31 nm. A conductometric titration study showed a 10 times less surface phosphate groups compared to the sulfate groups after hydrolysis with sulfuric acid, indicating of very low charge density on the CNC surface. The thermal stability of the CNCs were studied with thermogravimetric analysis (TGA) and compared with the CNCs obtained from sulfuric and hydrochloric acid hydrolysis. The results revealed that the phosphoric acid hydrolyzed CNCs had higher thermal stability compared to those bearing sulfate groups, but with less thermal stability compared to those obtained by hydrochloric acid process.

In another study [33], hydrobromic acid was used to prepare cellulose nanocrystals from cotton fibers. The optimization of the hydrolysis process was carried out by varying the reaction time, temperature and acid concentration. It was found that the hydrolysis temperature of 100°C for 3 hours of reaction with acid concentration of 2.5 M of HBr. Increasing the acid concentration from 1.5 to 2.5M increased the yield. However, higher concentration of HBr was found to result in side reactions and produced darker nanocrystals. In addition, it was found that the application of ultrasonic energy especially at the intervals during the hydrolysis process enhanced the final yield of CNC extraction especially at lower reaction temperatures. This was attributed to the fact that the ultrasonic waves can break apart the micro-aggregates and provide higher surfaces for acid hydrolysis. In addition, at lower temperatures, the input from the ultrasound treatment can compensate for the lower thermal energy and significantly increase the overall yield.

1.2.3 Surface Modification of Cellulose Nanocrystals

Cellulose whiskers possess hydroxyl rich surfaces with the potential of developing interconnected percolated network structure of hydrogen bonded whiskers in polymer matrix with significant improvement of structural properties [34-35]. Note that this network structure may pose a challenge regarding both interfacial adhesion and efficient dispersion in relatively more hydrophobic polymer matrices [36-37]. This special surface property of the cellulose at nanoscale just mentioned, if controlled properly, can provide significant opportunities that can be exploited to engineer the surface in order to enhance the polymer/CNC interfacial adhesion and to improve CNC dispersion in the polymer to achieve optimal interfacial area with the host polymer. However, care should be taken to ensure that the morphology and structural properties of the CNCs are preserved during the surface modification reaction. The approaches that have been adopted so far to tailor the surface chemical functionality of CNCs can be categorized into three major routes: (1) generation of various chemical functionalities depending on the application using surface synthetic methods, (2) physical adsorption of surfactants/compatibilizers via physical forces such as electrostatic or hydrogen bonding, and (3) grafting of polymeric chains using both "graft onto" and "graft from" approaches. Some of the recent advances using these techniques are now described briefly.

Silylation and acetylation of nanocellulose surface

The idea of silylation of cellulose nanocrystals originated from the modification of cellulosic fibers with organosilane coupling agents that is a widely used method of surface functionalization of cellulose and wood fibers with prescribed functionality especially in polymer composite applications [38-40]. In this method, the surfaces of the

CNCs are covered with crosslinked polysiloxane layers with desired functionality on the surface of the silane layer chosen to be compatible with the polymer matrix to enhance the interfacial adhesion. Typically, alkyl- dimethylchlorosilanes are used and the surface chemistry involves evolution of HCl and formation of Si-O-C bond between the siloxane layer and CNC surface. Gousse *et al* [41] studied the role of the alkyl chain length on the structure of partially silylated CNCs ranging from isopropyl to n-butyl, n-octyl and n-dodecyl moieties. The surface of the CNCs was characterized based on degree of substitution (or DS) of the silane. It was found that a DS value of 0.6-1 preserved the whisker morphology of the CNCs. However, DS values higher than 1, resulted in deformation and loss of the original whisker morphology. In addition, the partially silylated whiskers were found to be readily dispersible in organic solvents such as THF. In order to reduce the surface hydrophilicity and make the CNCs compatible with cellulose butyrate acetate matrix, Grunert *et al* [42] carried out trimehtylsilylation of the CNC surface in formamide. Yu *et al* [43] used 3-isocyanatepropyltriethoxysilane via the reaction of isocyanate groups of the silane coupling agents with CNC surface hydroxyls catalyzed by $Sn(Oct)_2$ in anhydrous DMF and incorporated the modified CNCs in silicon elastomer. These surface modifications gave better dispersion of CNCs in the respective polymer matrices and significant improvement of mechanical properties of the final nanocomposite elastomers. In an alternative method, Raquez *et al* [44] used an aqueous solution of methacryloxypropyltrimethoxysilane in a suspension of cellulose whiskers followed by the hydrolysis of the silane. The observed modified CNCs were recovered through centrifugation and vacuum drying or freeze-drying after the adsorption step. The condensation of silane on CNC surface was achieved by curing the silane-adsorbed-CNC

particles in a vacuum oven at 110°C. In addition, the authors showed that application of an excessive amount of silane (more than 200mM) was not attainable due to the formation of a biphasic solution. This method was called a "green and sustainable" approach because it eliminates the evolution of HCl as in the case of chlorosilane agents.

Surface acetylation of CNCs has mostly been achieved through utilization of various anhydride- based compounds. Yu *et al* [45] prepared acetylated CNCs by reacting succinic anhydride with CNCs under pyridine reflux and the unreacted anhydride was removed by successive washing with water, acetone and ethanol. These carboxylated CNCs were used for metal ion adsorption applications. In another simple approach [46], alkenyl succinic anhydride aqueous emulsion was mixed with CNC suspension and freeze-dried followed by heating at 105°C to produce highly hydrophobic CNC particles that were dispersible in low polarity solvents such as 1,4-dioxane. Sassi *et al* [47] studied the role of the reaction medium on structure of CNCs during acetylation reaction. Using a non-swelling reaction mechanism where only surface cellulose chains are considered, they found that when acetylation is carried out under homogenous reaction conditions, the acetylated layers of the whisker are immediately released in the reaction medium after obtaining sufficient solubility. However, under heterogeneous reaction conditions, only surface cellulose chains are acetylated, resulting in formation of a layer of non-soluble cellulose acetate that surrounds the highly crystalline core of unreacted cellulose.

Polymer Grafting via Surface-Initiated Polymerization

Ring-opening polymerization (ROP) has been one of the major routes to grafting polymer chains from the surface of cellulose substrates due to the presence of surface hydroxyl groups that can act as polymerization initiation points [48]. In an early study,

12

Hafren *et al* [49] used surface-initiated ROP to graft poly (ε-caprolactone) (PCL) onto cotton and filter paper surface where the reaction was catalyzed by organic and amino acids. Habibi *et al* [50] used the same concept to graft PCL through surface-initiated ROP catalyzed by $Sn(Oct)_2$ from the cellulose nanocrystal surface. Their results suggested that the structure and morphology of the cellulose nanocrystals remained intact after the grafting reaction. The obtained modified CNC particles showed significantly improved dispersion and compatibility with a PCL matrix in a nanocomposite material. Carlsson *et al* [51] studied the effect ROP reaction time on surface properties and grafting density of the PCL on the CNC surface characteristics. Their results showed that the surface graft density was constant at 3-7% and independent on the ROP reaction time. In order to enhance the efficiency of the reaction, Lin *et al* [52] used microwave assisted surface-initiated ROP to graft PCL on CNC surface. The obtained modified CNC was melt mixed with PLA matrix to give a nanocomposite that and showed enhanced interfacial compatibility with the hydrophobic matrix. In another approach to prepare hydrophobically modified CNCs, Morandi and co-workers [53] grafted polystyrene chains onto CNC surface via surface-initiated atom transfer radical polymerization (ATRP). This approach used a 2-bromoisobutyryl bromide as the ATRP initiating site on the CNC surface followed by polymerization. The brush chain length and grafting density was easily controlled by adjusting the reaction conditions. Using a similar approach, Zeinali and co-workers [54] prepared thermo-responsive CNC whiskers by grafting poly (N-isopropyl acrylamide) and pol (acrylic acid) through surface initiated RAFT (Reversible-Addition Fragmentation Transfer) polymerization by attaching 2-

(dodecylthiocarbonothioylthio)-2-methylpropionic acid as chain transfer agent followed by polymerization of acrylic monomers.

Surface Modification by Physical Adsorption

This approach towards modification of CNC surface is based on utilization of physical forces such as electrostatic attraction or hydrogen bonding to adsorb various functional molecules or polymers on the CNC surface especially when the CNC is prepared by sulfuric acid hydrolysis that leaves the surface negatively charged. Application of surfactants has been shown to be a promising method of interfacial compatibilization of cellulosic fibers with polymer matrix [55-56] where the hydrophilic head of the surfactant interact with the hydrophilic surface of cellulose, and the hydrophobic tail interacts with the matrix. For example, Hu *et al* [57] used surfactants such as didecyldimethylammonium bromide (DMAB) and cetyltrimethylammonium bromide (CTAB) to modify the surface of CNC through electrostatic attraction of positively charged surfactant and negatively charged CNC surface. They found that the morphology of the surface layer on CNC surface was concentration dependent where low concentrations resulted in brush-like morphology with hydrophobic tails of the surfactant pointing outward thereby rendering the CNC surface highly hydrophobic. On the other hand, higher concentrations resulted in aggregation of surfactant on the CNC surface with a decrease in hydrophobic character. Salajkova *et al* [58] modified the surface of the TEMPO-oxidized nanocellulose with various functional groups such as epoxide, benzyl and acrylate groups through the use of the corresponding ammonium salt adsorbed on the surface through electrostatic force. This was demonstrated to be a promising method for composite applications because various chemical functionalities can be introduced on the

14

CNC surface that, in turn, could potentially interact/react with the host matrix polymer. The use of non-ionic surfactants such as sorbitan menstruate has also been used to disperse CNCs in hydrophobic matrix [59-60].

1.2.4 Processing of CNC-based Polymer Nanocomposites

In this section a brief overview is given of the most commonly used approaches in preparation of thermoplastic and thermoset polymer nanocomposites based on cellulose nanocrystals.

Solvent Casting

Solvent casting is the most widely used technique for preparing CNC based nanocomposites [61]. In a typical process, the CNCs are dispersed in the dispersing medium which is mostly aqueous dispersions although other solvents have been used. Once fully dispersed, the polymer is added to the dispersion and the final nanocomposite hybrid material is developed by removing the solvent. Aqueous dispersion is a highly favorable dispersion medium because the CNCs can be readily dispersed in water at nanoscale without aggregation. However, one limitation of this technique is the fact that only water soluble/dispersible polymers or latex materials can be formulated. Paralikar *et al* [62] prepared nanocomposite membranes of CNC incorporated into polyvinyl alcohol (PVOH) through solvent casting in water. The membranes had CNC concentration of 0-20 wt% . The process involved mixing of two separate master batches of a solution of PVOH and dispersion of CNC in water followed by a sonication of 25 minutes for breaking up any agglomerates formed during mixing. Because of the high solubility of PVOH and dispersability of CNC in water, a synergistic effect of the CNC/PVOH interaction was observed as evidenced by highly dispersed CNCs in the PVOH

membrane that resulted in enhanced physical and mechanical properties. Samir and coworkers [63] used water based casting technique to prepare poly(oxyethylene) (POE) nanocomposite reinforced with CNCs. In their method, CNCs were dispersed in the POE solution and mixed for 24 hours followed by drying at 40°C for a week and at 100°C for 72 hours.

In addition to water, a number of polar organic solvents have also been successfully used as dispersing medium for preparation of CNC based nanocomposites such as Dimehtylformamide (DMF) [64], dimethyl sulfoxide (DMSO) and N-methyl Pyrrolidine (NMP) [65]. In a recent study by Van den Berg *et al* [65] the dispersibility of the cellulose whiskers in various organic solvents based on the surface charge of the whiskers was studied. It was found that the presence of negative surface charges (sulfate groups) obtained from sulfuric acid hydrolysis as already described is necessary for successful dispersion of whiskers in polar solvents such as DMSO, DMF and NMP as shown in Figure 1.4. However, protic solvents such as the formic acid and m-cresol are able to disperse even the CNC whiskers with neutral surfaces due to their ability to disrupt the intra-particle hydrogen bonded network structure.

Marcovich *et al* [66] used DMF as suspending agent to obtain a stable suspension of CNCs using ultrasonic treatment. This stable suspension was then added to a mixture of polyol-isocyanate to obtain CNC reinforced polyurethane films. Using a similar approach, Liu *et al* [67] fabricated PMMA nanocomposite reinforced with up to 10 wt% CNCs. This facile preparation method involves mixing of a stable suspension of CNCs in DMF with a solution of hydrophobic PMMA in DMF and drying the resulting mixture to give cast solid composite films with enhanced benefits.

Solvent exchange process is another method of transferring cellulose whisker dispersions to organic solvents from aqueous dispersion. The advantage of this technique is the fact that a percolating network structure of CNC whiskers that can be obtained in the aqueous solutions that can be directly transferred to organic solvent in the form of "organo-gels". This method is known as the template approach developed by Capadona et al [68-69]. In this method, a dispersion of CNC in water is solvent exchanged with acetone over a period of a week through formation of aqueous-organic bilayer mixture. The solvent exchange results in development of an organo-gel of CNCs in acetone. Nanocomposites of ethylene-oxide/epichlorohydrin copolymer were prepared by the template approach by placing the CNC-in-acetone organo-gel in the copolymer solution followed by compression molding and drying. The obtained nanocomposites developed by this novel approach had mechanical properties comparable with that of samples that were directly solution-cast in DMF. Wang et al [70] used the same organo-gel template approach to prepare poly(propylene-carbonate) green nanocomposites reinforced with cellulose nanocrystals. The reported morphological observations showed a sub-micron scale dispersion of the CNCs within the matrix polymer which was further confirmed by enhancement of mechanical properties. The solvent exchange process has also been used to transfer CNCs from aqueous solutions to highly water-immiscible solvents such as toluene [71] in order to prepare atactic PP/CNC nanocomposites. By contrast, severe aggregation of CNCs was observed in toluene.

Other approaches such as surface modification of CNCs with more hydrophobic functionalities [72] or long chain hydrophobic moieties [73] have also been used in order to disperse the CNCs in water-immiscible solvents. Note, however, that although a good

dispersion of particles may be achieved, the interaction of particles through hydrogen

bonding and formation of interconnected network structure would be severely limited.

Melt Processing

Although solvent casting process is effective in achieving fine dispersion of

cellulose nanocrystals in polymer matrices that is a necessary requirement of effective

property enhancement of the host polymer matrix, it is both lengthy and non-economical

approach from the practical application point of view because the plastic industry is more

interested in solvent-free "green" processing methods with significantly shorter cycle

times. In this context, melt extrusion is the most widely used polymer processing

technique in industry for fabrication of composites and nanocomposites [74]. However,

there is a challenge of obtaining a well dispersed morphology of CNC in the polymer

matrix during extrusion because CNC tends to severely aggregate when blended with

hydrophobic thermoplastics. A significant number of studies have been reported in the

literature for the preparation of polymer/CNC nanocomposites using extrusion process

such as polyethylene [75-76], polypropylene [77-78], polystyrene [79], polylactic acid [80-81],

polyvinyl chloride [82] and poly(3-hydroxybutyrate-co-3-hydroxyvalerate) (PHBV) [83]

,poly(ε-caprolactone) [84] and thermoplastic starch [85]. Typically, a surface modifier such as

a graft polymer layer or surfactant or simply a compatibilizer is used in order to enhance

the CNC dispersion and compatibility with the matrix. For example, Bondeson *et al* [86]

prepared a suspension of the cellulose whiskers with polyvinyl alcohol and introduced the

mixture in the PLA matrix with extrusion process using dry and liquid feeding

techniques. It was found that although liquid feeding produced a better dispersed

morphology of the CNCs in the PLA, the majority of the particles were located inside a

discontinuous phase of PVOH within the continuous PLA matrix phase. Direct pumping of an aqueous solution of cellulose nanocrystals into the PLA matrix in the extrusion process did not show any improvement in the structural properties of the nanocomposites due to poor dispersion of CNCs in the matrix [87].

Application of 5wt% anionic surfactant [80] was found to improve the dispersion of CNCs in the PLA matrix during extrusion with improved mechanical properties. However, higher surfactant content was found to degrade the PLA matrix. In another approach, Goffin *et al* [88] grafted PLA chains on the CNC surface via surface-initiated ring opening polymerization and melt extruded the modified CNC particles with PLA matrix. The results showed enhanced compatibility between the obtained PLA-*g*-CNC and PLA matrix indicated by improvement of mechanical properties and promotion of crystallization nucleation in the matrix. A similar strategy [89] was used to graft poly(ε-caprolactone) (PCL) on the CNC surface by ring-opening polymerization and reported that gave significantly improved dispersion as a consequence of the PCL graft layer due to enhanced interfacial compatibility.

In the case of polyethylene matrix, de Menezes *et al* [75] grafted fatty acid chains on the CNC surface and melt extruded the modified particles with low density polyethylene matrix. The results showed that increasing the fatty acid chain length enhanced the dispersion of the CNCs in the LDPE matrix. Ben Azouz and coworkers [76] prepared a dispersion of CNCs in high molecular weight polyethylene oxide (PEO) solution to wrap the CNC surface with PEO layers. Subsequently, they freeze-dried the mixture and used in the desired product in an extrusion process to incorporate the modified CNCs in the PE matrix. The extrusion of PEO-modified CNC with PE resulted in no significant

degradation of particles while direct melt mixing of CNC with PE resulted in severe

discoloration. This is thought to be a promising approach in order to effectively disperse

the CNCs in the hydrophobic matrix while preserving their thermal stability during melt

processing. Interestingly, similar approach[83] used polyethylene glycol (PEG) instead as

the surface wrapping agent for CNCs in poly(3-hydroxybutyrate-co-3-hydroxyvalerate)

(PHBV) matrix during the high shear extrusion process, and the obtained results showed

that the PEG layer was completely removed from the CNC surface and mixed with the

PHBV matrix, leaving the cellulose whiskers aggregated in the matrix. Consequently,

therefore, the molecular weight of the wrapping agent was found to be the determining

success factor in this method.

1.2.5 Properties of CNC-based Polymer Nanocomposites

Mechanical Properties

Cellulose nanocrystals are attractive potential reinforcing additives for polymer

matrices due to their exceptionally high mechanical properties and relatively lower

density compared to most conventional nano-reinforcing agents that translates into

nanocomposites with relatively lighter weight [90]. This is evidenced by considering the

longitudinal modulus of CNCs to be in the range of 100-170 GPa with an average value

of 130 GPa which is almost equivalent to that of aramid fibers [3]. Depending on the source

of CNC extraction, various longitudinal modulus values have been reported (e.g., 105

GPa for the CNCs from cotton and 143 GPA for CNCs from tunicate) [91-92]. Transverse

elastic moduli of cellulose whiskers were investigated by Lahiji *et al* [93] at 30% and 0.1%

relative humidity by Atomic Force Microscopy (AFM). They measured a transverse

elastic modulus (E_T) value of 18-50 GPa for wood-derived CNC whiskers and the

effective stiffness in higher relative humidity condition was found to be slightly higher. Wagner and co-workers [94] used AFM force-displacement measurements to estimate the transverse modulus of CNC whiskers derived from tunicate and found to range from 2 to 37 GPa. This large variation in measurement of ET by AFM was attributed to the uncertainties related with the sensitivity of AFM tip rather than the property variation.

Cao et al [95] reported a significant mechanical property enhancement by cellulose nanocrystals in thermoplastic starch with tensile strength increasing from 3.9 to 11.5 MPa and elastic modulus increasing from 31.9 to 823.9 MPa, respectively, with increasing CNC content up to 30wt%. In a study [96] on electro-spun PLA mats, addition of up to 5wt% of CNCs resulted in 5- and 22-fold increase in tensile strength and modulus compared to that of neat PLA fiber mats, respectively. Biodegradable poly(butylene succinate) (PBS) foams reinforced by cellulose nanocrystals was developed by Lin et al [97] and incorporation of 5wt% of CNC in the foam resulted in 50 and 62.9 % improvement in flexural strength and modulus, respectively, compared to neat PBS foams. The reinforcing capability of the cellulose nanocrystals has been demonstrated in a number of other studies on thermoplastic polymers such as PVA [98], PLA [99], PMMA [100], Poly (vinylidene-fluoride) [101], Poly (3-hydroxybutyrate) [102]. Engineering thermoplastics such as polyamide 6 has also been reinforced with cellulose nanocrystals [103-104].

In addition, CNCs have been used to mechanically reinforce elastomeric polymers as well. Bio-compatible waterborne polyurethane matrix was reinforced with small volume fraction of cellulose nanocrystals (1wt%) that increased the tensile strength and Young's modulus from 5.43 to 12.22 MPa and from 1.16 to 4.83 MPa, respectively [105]. The reinforcing efficiency of CNCs has also been demonstrated in natural rubber

nanocomposites [106]. However, the addition of CNCs has been shown to decrease the elongation at break in the nanocomposite material compared to the host polymer matrix due to the stiffening effect of CNCs in the polymer [71, 89]. Furthermore, the mechanical property enhancement has also been studied in thermoset polymers. Pan *et al* [107] studied the reinforcing ability of cellulose nanocrystals in an epoxy-acrylate UV-curable transparent film. The DMA results indicated a significant enhancement of modulus above the glass transition temperature (i.e., rubbery state) with increasing CNC loading. The reinforcing effect of CNCs in a phenolic thermoset resin [108] was adequately described by Halpin-Kardos model suggesting the domination of matrix-filler interaction over filler-filler interaction. The studies of the effects of CNC on mechanical properties of unsaturated polyester resin was studied [109] where it was found that surface modification of CNC with organosilane coupling agents resulted in improvement of strength and stiffness of the of the polyester resin whereas no significant changes were observed on the impact energy of the polyester nanocomposites after the surface treatment.

There are a number of important characteristics of the cellulose whiskers that play a critical role in its mechanical reinforcement efficiency in polymer composites. Cellulose whiskers, owing to their nano-scale dimensions, have significantly large specific surface area which has been reported to be in the range of 100 m^2/g to several hundred m^2/g [110-111]. This large available surface could in fact be exploited to enhance the interfacial interaction in CNC/polymer nanocomposites through favorable interfacial interactions such as hydrogen bonding [112]. Moreover, the available surface interfacial area between the CNC whiskers and the host polymer is governed by the state of dispersion of CNCs in the matrix as well as the effect aspect ratio of the whiskers. Good

CNC dispersion in the polymer at the molecular level and its relatively large aspect ratio (i.e., ratio of length to diameter) will increase the interfacial area between the particles and the polymer. The increased interfacial area will facilitate the stress transfer under mechanical load from the neighboring polymer chains to relatively very stiff and strong whiskers [113-114]. On the other hand, the highly hydrophilic nature of CNCs may lead to severe aggregation of whiskers in the polymer matrix which, in turn, reduces the available surface area, the effective aspect ratio and the reinforcing potential of the whiskers. Rusli and co-workers [115] studied the role of CNC surface charge and aspect ratio and the corresponding micro-structural properties on stress transfer efficiency from matrix to whiskers in an epoxy matrix by Raman spectroscopy. Their results demonstrated that the tunicate-derived cellulose whiskers had significantly higher stress transfer capability due to their exceptionally large aspect ratios compared to that of the cotton-derived whiskers. In addition, the sulfuric acid hydrolyzed samples had better dispersion throughout the matrix while the hydrochloric acid hydrolyzed whiskers showed negligible stress transfer capacity due to their excessive aggregation as a result of surface neutrality that, in turn, reduced their effective aspect ratio in aggregated state. In addition, the effect of interfacial compatibility between the matrix and CNC particles on mechanical properties was demonstrated by Goffin *et al* [84] who used un-modified and PLA-grafted-CNC particles (by surface initiated ROP of lactide) to reinforce PLA matrix. The reinforcing efficiency of the interfacial compatibility was shown by enhanced stiffness of the matrix above the *Tg* in the case of grafted CNCs.

The strong mechanical reinforcing ability of cellulose whiskers has spurred a number of researchers to use micro-mechanical models to theoretically describe the

23

mechanical properties of polymer/CNC nanocomposites. However, it was found that the use of conventional short fiber composites models such as Halpin-Tsai equations failed in a number of polymer/CNC nanocomposites systems reported in the literature by underestimating the reinforcing ability of CNCs [116]. This was attributed to the formation of a percolating rigid network structure of CNC whiskers that are strongly bonded together through hydrogen bonding that is not accounted for in the theoretical equations. To better understand the mechanical reinforcing property of the CNC/polymer nanocomposites with a percolated structure, the series-parallel model of Takayanagi *et al.* [117] (as modified by Ouali *et al.* [118]) can be applied to predict the elastic shear modulus of the composite according to the following equation:

$$G_c' = \frac{(1 - 2\psi + \psi\chi_r)G'_r G'_s + (1 - \chi_r)\psi G'^2_r}{(\chi_r - \psi)G'_s + (1 - \chi_r)G'_r} \tag{1.1}$$

Where the subscripts r and s refer to rigid (whisker) and soft (polymer) phases and ψ is related with the volume fraction of the percolating phase (in this case the whiskers). The ψ parameter can be obtained using the following equations:

$$\psi = 0 \qquad for\ \chi_r < \chi_c \tag{1.2}$$

$$\psi = \chi_r\left(\frac{\chi_r - \chi_c}{1 - \chi_c}\right)^b \quad for\ \chi_r > \chi_c \tag{1.3}$$

In these equations $b=0.4$ for a three dimensional percolating network, X_c is the critical volume fraction at which the percolation begins. According to Favier *et al* [34], this parameter can be estimated using the equation $Xc = 0.7d/l$ where d and l are the diameter and length of the whiskers. X_r is the volume fraction of the rigid whiskers phase. At sufficiently high temperatures, the stiffness of the matrix can be assumed to be zero and the equation is then simplified to $G'_c = \psi G'_r$.

24

It has also been explained that the good agreement between the experimental data and the values predicted by the model just described that takes the percolating phase structure into account is ascribed to the formation of infinite agglomerations of cellulose whiskers. It is also worth noting that the percolation threshold and structure formation of CNC network structure in the matrix can be controlled by the interfacial interaction, compatibility with the matrix the dispersion quality, and the original aspect ratio of the fibers. The larger the effective *in-situ* aspect ratio of the CNCs in the matrix, the lower the volume fraction at which a percolating network structure of the CNCs is formed.

Thermal Properties

The thermal properties of CNC/polymer nanocomposites such as the thermal stability, glass transition temperature, melting and crystallization behavior are important variables in development of the novel functional nanocomposites. Roman *et al* [119] studied the effect of sulfate groups on the CNC surface on the thermal stability of sulfuric acid hydrolyzed bacterial cellulose whiskers through controlling the sulfuric acid hydrolysis conditions. They reported a significant decrease in thermal stability of the CNC as the sulfate groups increased on the surface. It was also reported that the sulfate groups increase the char fraction after thermal degradation, implying the additional role of the CNCs as flame retardants. Note that the presence of sulfate groups catalyzed the degradation processes as indicated by relatively lower thermal degradation activation energy in CNCs with high sulfate group's concentrations. Similar observations were made with thermal stability of the CNCs prepared by enzymatic process was found to be higher than those of sulfuric acid hydrolyzed [120]. Incorporation of bacterial grown CNCs into PVA matrix resulted in significant thermal stability improvement from the onset

25

temperature of thermal degradation of 184°C in the case of sulfuric acid hydrolyzed CNC in PVA to 378°C in the case of the bacterial grown CNC in PVA matrix. The presence of CNCs in a PMMA matrix [67], however, showed only slight reduction in the onset temperature of thermal degradation with the addition of CNCs. It is clear that a strong interfacial interaction or chemical bond facilitates enhancement of thermal stability in CNC based nanocomposite. In such cases, the presence of CNC in the matrix is advantageous for thermal stability of the host polymer matrix by increasing the energy required for the onset of polymer decomposition and associated reduction in thermal expansion [121-122].

Considering the effect of CNCs on the glass transition temperature of host polymers, a great number of studies have reported no obvious change in systems including but not limited to poly (styrene-co-butyl acrylate) [123], Polyvinyl chloride (PVC) [124], PP [71], poly (oxyethylene) [63], and natural rubber [125] Nanocomposites. On other hand, polymers that form strong interfacial interaction with the CNC surface through hydrogen bonding have typically increased Tg with incorporation of CNCs. For example, in our previously reported study [126], we demonstrated that the Tg of the amorphous portion of polyamide 6 increased slightly with a small volume fraction of cellulose nanocrystals. In addition, a similar effect has been observed in strong hydrogen bond-forming matrices such as polyvinyl alcohol [120] and glycerol plasticized starch [127] where the strong interfacial interaction severely inhibits the molecular motion and viscous flow of the polymer chains, resulting in an increasing trend of glass transition temperature with addition of CNCs.

The melting temperature of semi-crystalline polymers has also been affected by CNCs in various ways to an extent that depends on the surface chemistry and interfacial interaction of polymer with CNC surface. For example, in a number of systems such as poly (ethylene oxide) [63], cellulose acetate butyrate [42], plasticized starch [128] and polycaprolactone [129] based nanocomposite, no significant change in melting behavior of the polymer was observed. However, surface modified CNCs have been shown to promote the crystallization of some particular polymer systems. For example, in the cellulose acetate butyrate system, trimethylsilylation of CNC surface resulted in enhanced crystallization and increased melting temperature of the matrix that was attributed to the promotion of polymer-CNC interfacial interaction by surface modification. In another study [130], a completely amorphous polyurethane elastomer was found to transform into a thermoplastic-like material with partial crystallinity when CNCs with a surface layer of grafted polyurethane pre-polymer were incorporated in the matrix.

Crystallization behavior of the CNC nanocomposites is also affected by the presence of the CNCs depending on their surface chemistry, dispersion quality and micro-structure development within the host polymer matrix. Pei *et al* [131] studied the role of surface modification of CNCs with silane agent on crystallization behavior of PLA and found that the modified CNC particles were very well dispersed in the PLA matrix and enhanced the crystallization kinetics by acting as effective nucleating agents. However, no such effect was found for non-modified CNCs because they formed highly aggregated structures in the matrix. Gray *et al* [132] reported strong nucleating effect of CNC in PP matrix as evidenced by the development of a transcrystalline layer on the cellulose

surface. Han and co-workers [133] studied the role of cellulose whiskers in polyurethane matrix during isothermal crystallization by using Avrami model and found that the CNCs act as nucleating agents during isothermal crystallization.

Melt Rheological Properties

Rheology is a powerful tool to study the effect of nanoparticle additives and their interaction with matrix on viscoelastic and microstructural properties of the nanocomposites. In addition, rheological data provide helpful insights into the behavior of the nanocomposite and hybrid materials during the melt processing stage. As in the case of nano-particulate filled polymer composites, rheological properties can provide fundamental understanding of the structure-property relationships in CNC based nanocomposite materials. Typically, this is accomplished through observation of changes in viscoelastic variables such as the storage and loss modulus (G' and G''), complex viscosity (η^*) and *tan δ*. In a series of studies on rheological behavior of CNC suspensions [134-136], it was observed that the suspension develop strong elasticity at high concentrations where the behavior resembles that of an elastic gel. Temperature sweep experiments indicated a structural rearrangement between 30°-40°C where G' initially increases and then decreases at higher temperatures. The structure formation was also confirmed in a sonicated CNC suspension by observation of the failure of Cox-Merz rule [137]. Rheological analysis of nanocomposites of poly (3-hydroxybutyrate-co-3-hydroxyvalerate) (PHBV) reinforced with cellulose nanocrystals [138] revealed that the most rapid changes in the G' and G'' occurred in the concentration range of 0.5-2 wt% of CNC while the viscoelastic transition crossover point occurred at 1.2wt% of CNC above which the nanocomposite melt behaved like an elastic gel. In our previously reported

28

study [126] on polyamide 6 nanocomposites we demonstrated the formation of CNC network structure within the PA6 matrix. It was shown that the formed structure could be broken apart by application of $10 s^{-1}$ shear rate and reformed upon removal of shear. In fact, the failure of the Cox-Merz rule for the samples with the highest concentration of CNC studied (i.e., 2wt%) confirmed the structure formation. Increasing the CNC concentration from 0.6 to 2wt% was also associated with a decrease in the slope of the terminal zone of the plot of G' and G'' versus frequency that was attributed to enhanced elasticity of the melt upon increasing the CNC concentration. In a study on polyurethane nanocomposites reinforced with CNCs [66], the onset of percolation was found to be 1wt% of the CNC. Above this concentration, a network of H-bonded whiskers formed throughout the matrix. This network was easily destructible by shear in the non-linear viscoelastic zone. Mahi and coworkers [139] studied the linear and non-linear rheological properties of ethylene vinyl acetate (EVA) copolymer nanocomposite reinforced with cellulose nanocrystals. Small amplitude oscillatory shear experiments showed a significant enhancement of melt elasticity by development of a non-terminal behavior in storage and loss modulus versus frequency which is indicative of transition to pseudo-solid like behavior. The onset of percolation and network formation significantly affects the long-range motion of polymer chains in the low frequency region and prevents the polymer relaxation as in the case of the neat polymer melt. The transient shear experiments did not show an overshoot in low shear region while an overshoot developed at high shear rates. This observation was attributed to the nano-network break-up and orientation in the flow direction.

A similar increase of storage and loss modulus was also observed in various CNC based nanocomposite systems such as polyurethane [140], poly (ethylene-glycol) [141], nitrile rubber [142], poly (oxyethylene) [76], and poly (vinyl acetate) [143].

The complex viscosity (η^*) of the nanocomposites is also affected by the presence of nanocrystals in the polymer melt. Normally, addition of stiff rigid nanoparticles with high surface area results in increase of the complex viscosity as a result of molecular motion restriction imposed by the nanoparticles [144]. This effect is dependent on the state of dispersion of particles in the matrix. The complex viscosity CNC/polymer nanocomposites show strong dependence on frequency and the nanocomposites exhibit shear-thinning behavior. While the neat polymer matrix shows no dependence of complex viscosity on angular frequency at low frequency values as evidenced by and a plateau in the complex viscosity versus frequency plot, addition of CNC was shown to significantly promote non-Newtonian behavior and increase of viscosity at low frequency ranges which is related with the nanostructure signature [145].

In addition, surface chemistry and interfacial compatibility with the matrix, play a major role in rheological behavior of CNC nanocomposites. Application of polyaniline-grafted-CNC was found to develop non-Newtonian shear thinning behavior in PU matrix [146] at low concentrations unlike the non-modified CNC. It was suggested that the liquid-solid transition is significantly promoted through the compatibility of the surface PANI layer with the PU matrix.

Goffin et al [84] studied the role of PCL-grafted-CNC in a PCL matrix through rheological characterization. It was seen that above 8% of the modified CNC, a network-like structure formed within the matrix that enhanced the elasticity and solid-like

behavior of the matrix. This finding is ascribed to the co-entanglement of the surface

grafted PCL layer with the PCL matrix which promoted the stress transfer to particles and

imposed significant molecular motion restriction on the matrix. In fact, the length of the

grafted surface layer was found to significantly affect the interfacial network formation.

As shown in Figure 1.5, the non-terminal behavior of rheological properties observed

only if sufficient chain length of grafted layer was obtained during the polymerization.

1.3 References

1.   Hubbe, M. A.; Rojas, O. J.; Lucia, L. A.; Sain, M., Cellulosic
nanocomposites: a review. *BioResources* **2008,** *3* (3), 929-980.

2.   John Rojas; Mauricio Bedoya; Yhors Ciro, Current Trends in the
Production of Cellulose Nanoparticles and Nanocomposites for Biomedical Applications.
In *Cellulose - Fundamental Aspects and Current Trends*, Matheus Poletto; Heitor Luiz
Ornaghi, Eds. InTech: 2015.

3.   Spence, K.; Habibi, Y.; Dufresne, A., Nanocellulose-based composites. In
Cellulose fibers: bio-and nano-polymer composites, Springer: 2011; pp 179-213.

4.   Atalla, R. H.; Brady, J. W.; Matthews, J. F.; Ding, S. Y.; Himmel, M. E.,
Structures of plant cell wall celluloses. *Biomass recalcitrance: deconstructing the plant
cell wall for bioenergy* **2008**, 188-212.

5.   Habibi, Y.; Lucia, L. A.; Rojas, O. J., Cellulose nanocrystals: chemistry,
self-assembly, and applications. *Chemical reviews* **2010,** *110* (6), 3479-3500.

6.   Moon, R. J.; Martini, A.; Nairn, J.; Simonsen, J.; Youngblood, J.,
Cellulose nanomaterials review: structure, properties and nanocomposites. *Chemical
Society Reviews* **2011,** *40* (7), 3941-3994.

7.   Kaushik, A.; Singh, M.; Verma, G., Green nanocomposites based on thermoplastic starch and steam exploded cellulose nanofibrils from wheat straw. *Carbohydrate Polymers* **2010,** *82* (2), 337-345.

8.   Sacui, I. A.; Nieuwendaal, R. C.; Burnett, D. J.; Stranick, S. J.; Jorfi, M.; Weder, C.; Foster, E. J.; Olsson, R. T.; Gilman, J. W., Comparison of the properties of cellulose nanocrystals and cellulose nanofibrils isolated from bacteria, tunicate, and wood processed using acid, enzymatic, mechanical, and oxidative methods. *ACS applied materials & interfaces* **2014,** *6* (9), 6127-6138.

9.   Jonas, R.; Farah, L. F., Production and application of microbial cellulose. *Polymer Degradation and Stability* **1998,** *59* (1), 101-106.

10.   George, J.; Ramana, K.; Bawa, A., Bacterial cellulose nanocrystals exhibiting high thermal stability and their polymer nanocomposites. *International journal of biological macromolecules* **2011,** *48* (1), 50-57.

11.   Beck-Candanedo, S.; Roman, M.; Gray, D. G., Effect of Reaction Conditions on the Properties and Behavior of Wood Cellulose Nanocrystal Suspensions. *Biomacromolecules* **2005,** *6* (2), 1048-1054.

12.   Saïd Azizi Samir, M. A.; Alloin, F.; Paillet, M.; Dufresne, A., Tangling effect in fibrillated cellulose reinforced nanocomposites. *Macromolecules* **2004,** *37* (11), 4313-4316.

13.   Yue, Y.; Zhou, C.; French, A. D.; Xia, G.; Han, G.; Wang, Q.; Wu, Q., Comparative properties of cellulose nano-crystals from native and mercerized cotton fibers. *Cellulose* **2012,** *19* (4), 1173-1187.

14.   Cao, X.; Dong, H.; Li, C. M., New Nanocomposite Materials Reinforced with Flax Cellulose Nanocrystals in Waterborne Polyurethane. *Biomacromolecules* **2007,** *8* (3), 899-904.

15.   Garcia de Rodriguez, L. N.; Thielemans, W.; Dufresne, A., Sisal cellulose whiskers reinforced polyvinyl acetate nanocomposites. *Cellulose* **2006,** *13* (3), 261-270.

16.   Habibi, Y.; Foulon, L.; Aguié-Béghin, V.; Molinari, M.; Douillard, R., Langmuir–Blodgett films of cellulose nanocrystals: Preparation and characterization. *Journal of Colloid and Interface Science* **2007,** *316* (2), 388-397.

17.   Wang, B.; Sain, M.; Oksman, K., Study of structural morphology of hemp fiber from the micro to the nanoscale. *Applied Composite Materials* **2007,** *14* (2), 89-103.

18.   Brinchi, L.; Cotana, F.; Fortunati, E.; Kenny, J., Production of nanocrystalline cellulose from lignocellulosic biomass: technology and applications. *Carbohydrate Polymers* **2013,** *94* (1), 154-169.

19.   De Souza Lima, M.; Wong, J.; Paillet, M.; Borsali, R.; Pecora, R., Translational and rotational dynamics of rodlike cellulose whiskers. *Langmuir* **2003,** *19* (1), 24-29.

20.   Kargarzadeh, H.; Ahmad, I.; Abdullah, I.; Dufresne, A.; Zainudin, S. Y.; Sheltami, R. M., Effects of hydrolysis conditions on the morphology, crystallinity, and thermal stability of cellulose nanocrystals extracted from kenaf bast fibers. *Cellulose* **2012,** *19* (3), 855-866.

21.   Dong, X. M.; Revol, J.-F.; Gray, D. G., Effect of microcrystallite preparation conditions on the formation of colloid crystals of cellulose. *Cellulose* **1998,** *5* (1), 19-32.

22.   Bondeson, D.; Mathew, A.; Oksman, K., Optimization of the isolation of nanocrystals from microcrystalline cellulose by acid hydrolysis. *Cellulose* **2006,** *13* (2), 171-180.

23.   Hamad, W. Y.; Hu, T. Q., Structure–process–yield interrelations in nanocrystalline cellulose extraction. *The Canadian Journal of Chemical Engineering* **2010,** *88* (3), 392-402.

24.   Elazzouzi-Hafraoui, S.; Nishiyama, Y.; Putaux, J.-L.; Heux, L.; Dubreuil, F.; Rochas, C., The shape and size distribution of crystalline nanoparticles prepared by acid hydrolysis of native cellulose. *Biomacromolecules* **2007,** *9* (1), 57-65.

25.   Bai, W.; Holbery, J.; Li, K., A technique for production of nanocrystalline cellulose with a narrow size distribution. *Cellulose* **2009,** *16* (3), 455-465.

26.   de Souza Lima, M. M.; Borsali, R., Static and dynamic light scattering from polyelectrolyte microcrystal cellulose. *Langmuir* **2002,** *18* (4), 992-996.

27.   Yu, H.; Qin, Z.; Liang, B.; Liu, N.; Zhou, Z.; Chen, L., Facile extraction of thermally stable cellulose nanocrystals with a high yield of 93% through hydrochloric acid hydrolysis under hydrothermal conditions. *Journal of Materials Chemistry A* **2013,** *1* (12), 3938-3944.

28.   Araki, J.; Wada, M.; Kuga, S.; Okano, T., Flow properties of microcrystalline cellulose suspension prepared by acid treatment of native cellulose. *Colloids and Surfaces A: Physicochemical and Engineering Aspects* **1998,** *142* (1), 75-82.

29.   Wang, N.; Ding, E.; Cheng, R., Preparation and liquid crystalline properties of spherical cellulose nanocrystals. *Langmuir* **2008,** *24* (1), 5-8.

30.   Wang, N.; Ding, E.; Cheng, R., Thermal degradation behaviors of spherical cellulose nanocrystals with sulfate groups. *Polymer* **2007,** *48* (12), 3486-3493.

31.   Camarero Espinosa, S.; Kuhnt, T.; Foster, E. J.; Weder, C., Isolation of thermally stable cellulose nanocrystals by phosphoric acid hydrolysis. *Biomacromolecules* **2013,** *14* (4), 1223-1230.

32.   Tang, Y.; Shen, X.; Zhang, J.; Guo, D.; Kong, F.; Zhang, N., Extraction of cellulose nano-crystals from old corrugated container fiber using phosphoric acid and enzymatic hydrolysis followed by sonication. *Carbohydrate polymers* **2015,** *125*, 360-366.

33.   Sadeghifar, H.; Filpponen, I.; Clarke, S. P.; Brougham, D. F.; Argyropoulos, D. S., Production of cellulose nanocrystals using hydrobromic acid and click reactions on their surface. *Journal of materials science* **2011,** *46* (22), 7344-7355.

34.   Favier, V.; Canova, G.; Cavaillé, J.; Chanzy, H.; Dufresne, A.; Gauthier, C., Nanocomposite materials from latex and cellulose whiskers. *Polymers for Advanced Technologies* **1995,** *6* (5), 351-355.

35.   Gindl, W.; Keckes, J., All-cellulose nanocomposite. *Polymer* **2005,** *46* (23), 10221-10225.

36.   Gardner, D. J.; Oporto, G. S.; Mills, R.; Samir, M. A. S. A., Adhesion and surface issues in cellulose and nanocellulose. *Journal of Adhesion Science and Technology* **2008,** *22* (5-6), 545-567.

37.   Salas, C.; Nypelö, T.; Rodriguez-Abreu, C.; Carrillo, C.; Rojas, O. J., Nanocellulose properties and applications in colloids and interfaces. *Current Opinion in Colloid & Interface Science* **2014,** *19* (5), 383-396.

38.   Salon, M.-C. B.; Abdelmouleh, M.; Boufi, S.; Belgacem, M. N.; Gandini, A., Silane adsorption onto cellulose fibers: Hydrolysis and condensation reactions. *Journal of colloid and interface science* **2005,** *289* (1), 249-261.

39.   Huda, M. S.; Drzal, L. T.; Mohanty, A. K.; Misra, M., Effect of fiber surface-treatments on the properties of laminated biocomposites from poly (lactic acid)(PLA) and kenaf fibers. *Composites Science and Technology* **2008,** *68* (2), 424-432.

40.   Xie, Y.; Hill, C. A.; Xiao, Z.; Militz, H.; Mai, C., Silane coupling agents used for natural fiber/polymer composites: A review. *Composites Part A: Applied Science and Manufacturing* **2010,** *41* (7), 806-819.

41.   Goussé, C.; Chanzy, H.; Excoffier, G.; Soubeyrand, L.; Fleury, E., Stable suspensions of partially silylated cellulose whiskers dispersed in organic solvents. *Polymer* **2002,** *43* (9), 2645-2651.

42.   Grunert, M.; Winter, W. T., Nanocomposites of Cellulose Acetate Butyrate Reinforced with Cellulose Nanocrystals. *Journal of Polymers and the Environment* **2002,** *10* (1), 27-30.

43.   Yu, H.-Y.; Chen, R.; Chen, G.-Y.; Liu, L.; Yang, X.-G.; Yao, J.-M., Silylation of cellulose nanocrystals and their reinforcement of commercial silicone rubber. *Journal of Nanoparticle Research* **2015,** *17* (9), 1-13.

44.   Raquez, J. M.; Murena, Y.; Goffin, A. L.; Habibi, Y.; Ruelle, B.; DeBuyl, F.; Dubois, P., Surface-modification of cellulose nanowhiskers and their use as nanoreinforcers into polylactide: A sustainably-integrated approach. *Composites Science and Technology* **2012,** *72* (5), 544-549.

45.   Yu, X.; Tong, S.; Ge, M.; Wu, L.; Zuo, J.; Cao, C.; Song, W., Adsorption of heavy metal ions from aqueous solution by carboxylated cellulose nanocrystals. *Journal of Environmental Sciences* **2013,** *25* (5), 933-943.

46.   Yuan, H.; Nishiyama, Y.; Wada, M.; Kuga, S., Surface acylation of cellulose whiskers by drying aqueous emulsion. *Biomacromolecules* **2006,** *7* (3), 696-700.

47.   Sassi, J.-F.; Chanzy, H., Ultrastructural aspects of the acetylation of cellulose. *Cellulose* **1995,** *2* (2), 111-127.

48.   Carlmark, A.; Larsson, E.; Malmström, E., Grafting of cellulose by ring-opening polymerisation – A review. *European Polymer Journal* **2012,** *48* (10), 1646-1659.

49.   Hafrén, J.; Córdova, A., Direct Organocatalytic Polymerization from Cellulose Fibers. *Macromolecular Rapid Communications* **2005,** *26* (2), 82-86.

50.   Habibi, Y.; Goffin, A.-L.; Schiltz, N.; Duquesne, E.; Dubois, P.; Dufresne, A., Bionanocomposites based on poly(?-caprolactone)-grafted cellulose nanocrystals by ring-opening polymerization. *Journal of Materials Chemistry* **2008,** *18* (41), 5002-5010.

51.   Carlsson, L.; Ingverud, T.; Blomberg, H.; Carlmark, A.; Larsson, P. T.; Malmström, E., Surface characteristics of cellulose nanoparticles grafted by surface-initiated ring-opening polymerization of ε-caprolactone. *Cellulose* **2015,** *22* (2), 1063-1074.

52.   Lin, N.; Chen, G.; Huang, J.; Dufresne, A.; Chang, P. R., Effects of polymer-grafted natural nanocrystals on the structure and mechanical properties of poly

(lactic acid): A case of cellulose whisker-graft-polycaprolactone. *Journal of Applied Polymer Science* **2009,** *113* (5), 3417-3425.

53.   Morandi, G.; Heath, L.; Thielemans, W., Cellulose Nanocrystals Grafted with Polystyrene Chains through Surface-Initiated Atom Transfer Radical Polymerization (SI-ATRP). *Langmuir* **2009,** *25* (14), 8280-8286.

54.   Zeinali, E.; Haddadi-Asl, V.; Roghani-Mamaqani, H., Nanocrystalline cellulose grafted random copolymers of N-isopropylacrylamide and acrylic acid synthesized by RAFT polymerization: effect of different acrylic acid contents on LCST behavior. *RSC Advances* **2014,** *4* (59), 31428-31442.

55.   de Souza Lima, M. M.; Borsali, R., Rodlike Cellulose Microcrystals: Structure, Properties, and Applications. *Macromolecular Rapid Communications* **2004,** *25* (7), 771-787.

56.   Gradwell, S. E.; Renneckar, S.; Esker, A. R.; Heinze, T.; Gatenholm, P.; Vaca-Garcia, C.; Glasser, W., Surface modification of cellulose fibers: towards wood composites by biomimetics. *Comptes Rendus Biologies* **2004,** *327* (9–10), 945-953.

57.   Hu, Z.; Ballinger, S.; Pelton, R.; Cranston, E. D., Surfactant-enhanced cellulose nanocrystal Pickering emulsions. *Journal of Colloid and Interface Science* **2015,** *439*, 139-148.

58.   Salajková, M.; Berglund, L. A.; Zhou, Q., Hydrophobic cellulose nanocrystals modified with quaternary ammonium salts. *Journal of Materials Chemistry* **2012,** *22* (37), 19798-19805.

59.   Rojas, O. J.; Montero, G. A.; Habibi, Y., Electrospun nanocomposites from polystyrene loaded with cellulose nanowhiskers. *Journal of Applied Polymer Science* **2009,** *113* (2), 927-935.

60.   Kim, J.; Montero, G.; Habibi, Y.; Hinestroza, J. P.; Genzer, J.; Argyropoulos, D. S.; Rojas, O. J., Dispersion of cellulose crystallites by nonionic surfactants in a hydrophobic polymer matrix. *Polymer Engineering & Science* **2009,** *49* (10), 2054-2061.

61.   Dufresne, A., Processing of polymer nanocomposites reinforced with polysaccharide nanocrystals. *Molecules* **2010,** *15* (6), 4111-4128.

62.   Paralikar, S. A.; Simonsen, J.; Lombardi, J., Poly(vinyl alcohol)/cellulose nanocrystal barrier membranes. *Journal of Membrane Science* **2008,** *320* (1–2), 248-258.

63.   Azizi Samir, M. A. S.; Alloin, F.; Gorecki, W.; Sanchez, J.-Y.; Dufresne, A., Nanocomposite Polymer Electrolytes Based on Poly(oxyethylene) and Cellulose Nanocrystals. *The Journal of Physical Chemistry B* **2004,** *108* (30), 10845-10852.

64.   Azizi Samir, M. A. S.; Alloin, F.; Sanchez, J.-Y.; El Kissi, N.; Dufresne, A., Preparation of cellulose whiskers reinforced nanocomposites from an organic medium suspension. *Macromolecules* **2004,** *37* (4), 1386-1393.

65.   Van den Berg, O.; Capadona, J. R.; Weder, C., Preparation of Homogeneous Dispersions of Tunicate Cellulose Whiskers in Organic Solvents. *Biomacromolecules* **2007,** *8* (4), 1353-1357.

66.   Marcovich, N.; Auad, M.; Bellesi, N.; Nutt, S.; Aranguren, M., Cellulose micro/nanocrystals reinforced polyurethane. *Journal of materials research* **2006,** *21* (04), 870-881.

67.   Liu, H.; Liu, D.; Yao, F.; Wu, Q., Fabrication and properties of transparent polymethylmethacrylate/cellulose nanocrystals composites. *Bioresource Technology* **2010,** *101* (14), 5685-5692.

68.   Capadona, J. R.; Van Den Berg, O.; Capadona, L. A.; Schroeter, M.; Rowan, S. J.; Tyler, D. J.; Weder, C., A versatile approach for the processing of polymer nanocomposites with self-assembled nanofibre templates. *Nature Nanotechnology* **2007,** *2* (12), 765-769.

69.   Capadona, J. R.; Shanmuganathan, K.; Trittschuh, S.; Seidel, S.; Rowan, S. J.; Weder, C., Polymer nanocomposites with nanowhiskers isolated from microcrystalline cellulose. *Biomacromolecules* **2009,** *10* (4), 712-716.

70.   Wang, D.; Yu, J.; Zhang, J.; He, J.; Zhang, J., Transparent bionanocomposites with improved properties from poly (propylene carbonate)(PPC) and cellulose nanowhiskers (CNWs). *Composites Science and Technology* **2013,** *85*, 83-89.

71.   Ljungberg, N.; Bonini, C.; Bortolussi, F.; Boisson, C.; Heux, L.; Cavaillé, New Nanocomposite Materials Reinforced with Cellulose Whiskers in Atactic Polypropylene: Effect of Surface and Dispersion Characteristics. *Biomacromolecules* **2005,** *6* (5), 2732-2739.

72.   Cetin, N. S.; Tingaut, P.; Özmen, N.; Henry, N.; Harper, D.; Dadmun, M.; Sèbe, G., Acetylation of cellulose nanowhiskers with vinyl acetate under moderate conditions. *Macromolecular bioscience* **2009,** *9* (10), 997-1003.

73.   Berlioz, S.; Molina-Boisseau, S.; Nishiyama, Y.; Heux, L., Gas-phase surface esterification of cellulose microfibrils and whiskers. *Biomacromolecules* **2009,** *10* (8), 2144-2151.

74.   Ray, S. S.; Okamoto, M., Polymer/layered silicate nanocomposites: a review from preparation to processing. *Progress in polymer science* **2003,** *28* (11), 1539-1641.

75.   Junior de Menezes, A.; Siqueira, G.; Curvelo, A. A. S.; Dufresne, A., Extrusion and characterization of functionalized cellulose whiskers reinforced polyethylene nanocomposites. *Polymer* **2009,** *50* (19), 4552-4563.

76.   Ben Azouz, K.; Ramires, E. C.; Van den Fonteyne, W.; El Kissi, N.; Dufresne, A., Simple method for the melt extrusion of a cellulose nanocrystal reinforced hydrophobic polymer. *ACS Macro Letters* **2011,** *1* (1), 236-240.

77.   Lee, K.-Y.; Aitomäki, Y.; Berglund, L. A.; Oksman, K.; Bismarck, A., On the use of nanocellulose as reinforcement in polymer matrix composites. *Composites Science and Technology* **2014,** *105*, 15-27.

78.   Pandey, J. K.; Lee, H. T.; Takagi, H.; Ahn, S. H.; Saini, D. R.; Misra, M., Dispersion of Nanocellulose (NC) in Polypropylene (PP) and Polyethylene (PE) Matrix. In *Handbook of Polymer Nanocomposites. Processing, Performance and Application: Volume C: Polymer Nanocomposites of Cellulose Nanoparticles*, Pandey, K. J.; Takagi, H.; Nakagaito, N. A.; Kim, H.-J., Eds. Springer Berlin Heidelberg: Berlin, Heidelberg, 2015; pp 179-189.

79.   Lin, N.; Dufresne, A., Physical and/or chemical compatibilization of extruded cellulose nanocrystal reinforced polystyrene nanocomposites. *Macromolecules* **2013,** *46* (14), 5570-5583.

80.   Bondeson, D.; Oksman, K., Dispersion and characteristics of surfactant modified cellulose whiskers nanocomposites. *Composite Interfaces* **2007,** *14* (7-9), 617-630.

81.   Oksman, K.; Mathew, A. P.; Bondeson, D.; Kvien, I., Manufacturing process of cellulose whiskers/polylactic acid nanocomposites. *Composites Science and Technology* **2006,** *66* (15), 2776-2784.

82.   Chazeau, L.; Cavaillé, J. Y.; Terech, P., Mechanical behaviour above Tg of a plasticised PVC reinforced with cellulose whiskers; a SANS structural study. *Polymer* **1999,** *40* (19), 5333-5344.

83.   Jiang, L.; Morelius, E.; Zhang, J.; Wolcott, M.; Holbery, J., Study of the poly (3-hydroxybutyrate-co-3-hydroxyvalerate)/cellulose nanowhisker composites prepared by solution casting and melt processing. *Journal of Composite Materials* **2008,** *42* (24), 2629-2645.

84.   Goffin, A. L.; Raquez, J. M.; Duquesne, E.; Siqueira, G.; Habibi, Y.; Dufresne, A.; Dubois, P., Poly(ε-caprolactone) based nanocomposites reinforced by surface-grafted cellulose nanowhiskers via extrusion processing: Morphology, rheology, and thermo-mechanical properties. *Polymer* **2011,** *52* (7), 1532-1538.

85.   Karimi, S.; Tahir, P. M.; Dufresne, A.; Karimi, A.; Abdulkhani, A., A comparative study on characteristics of nanocellulose reinforced thermoplastic starch biofilms prepared with different techniques. *Nordic Pulp & Paper Research Journal* **2014,** *29* (1).

86.   Bondeson, D.; Oksman, K., Polylactic acid/cellulose whisker nanocomposites modified by polyvinyl alcohol. *Composites Part A: Applied Science and Manufacturing* **2007,** *38* (12), 2486-2492.

87.   Mathew, A. P.; Chakraborty, A.; Oksman, K.; Sain, M. In *The structure and mechanical properties of cellulose nanocomposites prepared by twin screw extrusion*, ACS symposium series, Oxford University Press: 2006; pp 114-131.

88.   Goffin, A.-L.; Raquez, J.-M.; Duquesne, E.; Siqueira, G.; Habibi, Y.; Dufresne, A.; Dubois, P., From Interfacial Ring-Opening Polymerization to Melt Processing of Cellulose Nanowhisker-Filled Polylactide-Based Nanocomposites. *Biomacromolecules* **2011,** *12* (7), 2456-2465.

89.   Habibi, Y.; Goffin, A.-L.; Schiltz, N.; Duquesne, E.; Dubois, P.; Dufresne, A., Bionanocomposites based on poly (ε-caprolactone)-grafted cellulose nanocrystals by ring-opening polymerization. *Journal of Materials Chemistry* **2008,** *18* (41), 5002-5010.

90.   Siqueira, G.; Bras, J.; Dufresne, A., Cellulosic bionanocomposites: a review of preparation, properties and applications. *Polymers* **2010,** *2* (4), 728-765.

91.   Šturcová, A.; Davies, G. R.; Eichhorn, S. J., Elastic Modulus and Stress-Transfer Properties of Tunicate Cellulose Whiskers. *Biomacromolecules* **2005,** *6* (2), 1055-1061.

92.   Rusli, R.; Eichhorn, S. J., Determination of the stiffness of cellulose nanowhiskers and the fiber-matrix interface in a nanocomposite using Raman spectroscopy. *Applied Physics Letters* **2008,** *93* (3), 033111.

93. Lahiji, R. R.; Xu, X.; Reifenberger, R.; Raman, A.; Rudie, A.; Moon, R. J., Atomic Force Microscopy Characterization of Cellulose Nanocrystals. *Langmuir* **2010,** *26* (6), 4480-4488.

94. Wagner, R.; Raman, A.; Moon, R., Transverse elasticity of cellulose nanocrystals via atomic force microscopy. *Cellulose* **2010,** *7*, 27.

95. Cao, X.; Chen, Y.; Chang, P. R.; Stumborg, M.; Huneault, M. A., Green composites reinforced with hemp nanocrystals in plasticized starch. *Journal of Applied Polymer Science* **2008,** *109* (6), 3804-3810.

96. Shi, Q.; Zhou, C.; Yue, Y.; Guo, W.; Wu, Y.; Wu, Q., Mechanical properties and in vitro degradation of electrospun bio-nanocomposite mats from PLA and cellulose nanocrystals. *Carbohydrate Polymers* **2012,** *90* (1), 301-308.

97. Lin, N.; Yu, J.; Chang, P. R.; Li, J.; Huang, J., Poly (butylene succinate)-based biocomposites filled with polysaccharide nanocrystals: Structure and properties. *Polymer Composites* **2011,** *32* (3), 472-482.

98. Ibrahim, M. M.; El-Zawawy, W. K., Poly (vinyl Alcohol)-Cellulose and Nanocellulose Composites. In *Handbook of Polymer Nanocomposites. Processing, Performance and Application*, Springer: 2015; pp 297-322.

99. Fortunati, E.; Luzi, F.; Puglia, D.; Petrucci, R.; Kenny, J. M.; Torre, L., Processing of PLA nanocomposites with cellulose nanocrystals extracted from Posidonia oceanica waste: Innovative reuse of coastal plant. *Industrial Crops and Products* **2015,** *67*, 439-447.

100.   Anžlovar, A.; Huskić, M.; Žagar, E., Modification of nanocrystalline cellulose for application as a reinforcing nanofiller in PMMA composites. *Cellulose* **2016,** *23* (1), 505-518.

101.   Zhang, Z.; Wu, Q.; Song, K.; Lei, T.; Wu, Y., Poly (vinylidene fluoride)/cellulose nanocrystals composites: rheological, hydrophilicity, thermal and mechanical properties. *Cellulose* **2015,** *22* (4), 2431-2441.

102.   Seoane, I. T.; Fortunati, E.; Puglia, D.; Cyras, V. P.; Manfredi, L. B., Development and characterization of bionanocomposites based on poly(3-hydroxybutyrate) and cellulose nanocrystals for packaging applications. *Polymer International* **2016**, n/a-n/a.

103.   Corrêa, A. C.; de Morais Teixeira, E.; Carmona, V. B.; Teodoro, K. B. R.; Ribeiro, C.; Mattoso, L. H. C.; Marconcini, J. M., Obtaining nanocomposites of polyamide 6 and cellulose whiskers via extrusion and injection molding. *Cellulose* **2014,** *21* (1), 311-322.

104.   Peng, J.; Walsh, P. J.; Sabo, R. C.; Turng, L.-S.; Clemons, C. M., Water-assisted compounding of cellulose nanocrystals into polyamide 6 for use as a nucleating agent for microcellular foaming. *Polymer* **2016,** *84*, 158-166.

105.   Gao, Z.; Peng, J.; Zhong, T.; Sun, J.; Wang, X.; Yue, C., Biocompatible elastomer of waterborne polyurethane based on castor oil and polyethylene glycol with cellulose nanocrystals. *Carbohydrate Polymers* **2012,** *87* (3), 2068-2075.

106.   Bras, J.; Hassan, M. L.; Bruzesse, C.; Hassan, E. A.; El-Wakil, N. A.; Dufresne, A., Mechanical, barrier, and biodegradability properties of bagasse cellulose

whiskers reinforced natural rubber nanocomposites. *Industrial Crops and Products* **2010,** *32* (3), 627-633.

107.   Pan, H.; Song, L.; Ma, L.; Hu, Y., Transparent Epoxy Acrylate Resin Nanocomposites Reinforced with Cellulose Nanocrystals. *Industrial & Engineering Chemistry Research* **2012,** *51* (50), 16326-16332.

108.   Liu, H.; Laborie, M.-P. G., Bio-based nanocomposites by in situ cure of phenolic prepolymers with cellulose whiskers. *Cellulose* **2011,** *18* (3), 619-630.

109.   Kargarzadeh, H.; M. Sheltami, R.; Ahmad, I.; Abdullah, I.; Dufresne, A., Cellulose nanocrystal: A promising toughening agent for unsaturated polyester nanocomposite. *Polymer* **2015,** *56*, 346-357.

110.   Islam, M. T.; Alam, M. M.; Zoccola, M., Review on modification of nanocellulose for application in composites. *Int J Innov Res Sci Eng Technol* **2013,** *2* (10), 5444-5451.

111.   Silvério, H. A.; Flauzino Neto, W. P.; Dantas, N. O.; Pasquini, D., Extraction and characterization of cellulose nanocrystals from corncob for application as reinforcing agent in nanocomposites. *Industrial Crops and Products* **2013,** *44*, 427-436.

112.   Littunen, K.; Hippi, U.; Saarinen, T.; Seppälä, J., Network formation of nanofibrillated cellulose in solution blended poly(methyl methacrylate) composites. *Carbohydrate Polymers* **2013,** *91* (1), 183-190.

113.   Rebouillat, S.; Pla, F., State of the art manufacturing and engineering of nanocellulose: a review of available data and industrial applications. *Journal of Biomaterials and Nanobiotechnology* **2013,** *4* (2), 165.

114.   Minelli, M.; Baschetti, M. G.; Doghieri, F.; Ankerfors, M.; Lindström, T.; Siró, I.; Plackett, D., Investigation of mass transport properties of microfibrillated cellulose (MFC) films. *Journal of Membrane Science* **2010,** *358* (1–2), 67-75.

115.   Rusli, R.; Shanmuganathan, K.; Rowan, S. J.; Weder, C.; Eichhorn, S. J., Stress Transfer in Cellulose Nanowhisker Composites—Influence of Whisker Aspect Ratio and Surface Charge. *Biomacromolecules* **2011,** *12* (4), 1363-1369.

116.   Halpin, J. C.; Kardos, J. L., Moduli of Crystalline Polymers Employing Composite Theory. *Journal of Applied Physics* **1972,** *43* (5), 2235-2241.

117.   Takayanagi, M.; Uemura, S.; Minami, S., Application of equivalent model method to dynamic rheo-optical properties of crystalline polymer. *Journal of Polymer Science Part C: Polymer Symposia* **1964,** *5* (1), 113-122.

118.   Ouali, N.; Cavaillé, J.; Perez, J., Elastic, viscoelastic and plastic behavior of multiphase polymer blends. *Plastics, Rubber and Composites Processing and Applications(UK)* **1991,** *16* (1), 55-60.

119.   Roman, M.; Winter, W. T., Effect of Sulfate Groups from Sulfuric Acid Hydrolysis on the Thermal Degradation Behavior of Bacterial Cellulose. *Biomacromolecules* **2004,** *5* (5), 1671-1677.

120.   George, J.; Ramana, K. V.; Bawa, A. S.; Siddaramaiah, Bacterial cellulose nanocrystals exhibiting high thermal stability and their polymer nanocomposites. *International Journal of Biological Macromolecules* **2011,** *48* (1), 50-57.

121.   Liu, H.; Cui, S.; Shang, S.; Wang, D.; Song, J., Properties of rosin-based waterborne polyurethanes/cellulose nanocrystals composites. *Carbohydrate Polymers* **2013,** *96* (2), 510-515.

122.   Huq, T.; Salmieri, S.; Khan, A.; Khan, R. A.; Le Tien, C.; Riedl, B.; Fraschini, C.; Bouchard, J.; Uribe-Calderon, J.; Kamal, M. R.; Lacroix, M., Nanocrystalline cellulose (NCC) reinforced alginate based biodegradable nanocomposite film. *Carbohydrate Polymers* **2012,** *90* (4), 1757-1763.

123.   Hajji, P.; Cavaillé, J. Y.; Favier, V.; Gauthier, C.; Vigier, G., Tensile behavior of nanocomposites from latex and cellulose whiskers. *Polymer Composites* **1996,** *17* (4), 612-619.

124.   Chazeau, L.; Cavaillé, J. Y.; Canova, G.; Dendievel, R.; Boutherin, B., Viscoelastic properties of plasticized PVC reinforced with cellulose whiskers. *Journal of Applied Polymer Science* **1999,** *71* (11), 1797-1808.

125.   Bendahou, A.; Kaddami, H.; Dufresne, A., Investigation on the effect of cellulosic nanoparticles' morphology on the properties of natural rubber based nanocomposites. *European Polymer Journal* **2010,** *46* (4), 609-620.

126.   Kashani Rahimi, S.; Otaigbe, J. U., Polyamide 6 nanocomposites incorporating cellulose nanocrystals prepared by In-situ ring opening polymerization: Viscoelasticity, creep behavior, and melt rheological properties. *Polymer Engineering & Science* **2016**.

127.   Lu, Y.; Weng, L.; Cao, X., Biocomposites of Plasticized Starch Reinforced with Cellulose Crystallites from Cottonseed Linter. *Macromolecular Bioscience* **2005,** *5* (11), 1101-1107.

128.   Mathew, A. P.; Dufresne, A., Morphological Investigation of Nanocomposites from Sorbitol Plasticized Starch and Tunicin Whiskers. *Biomacromolecules* **2002,** *3* (3), 609-617.

129.   Habibi, Y.; Dufresne, A., Highly Filled Bionanocomposites from Functionalized Polysaccharide Nanocrystals. *Biomacromolecules* **2008,** *9* (7), 1974-1980.

130.   Cao, X.; Habibi, Y.; Lucia, L. A., One-pot polymerization, surface grafting, and processing of waterborne polyurethane-cellulose nanocrystal nanocomposites. *Journal of Materials Chemistry* **2009,** *19* (38), 7137-7145.

131.   Pei, A.; Zhou, Q.; Berglund, L. A., Functionalized cellulose nanocrystals as biobased nucleation agents in poly (l-lactide)(PLLA)–crystallization and mechanical property effects. *Composites Science and Technology* **2010,** *70* (5), 815-821.

132.   Gray, D. G., Transcrystallization of polypropylene at cellulose nanocrystal surfaces. *Cellulose* **2008,** *15* (2), 297-301.

133.   Han, J.; Zhu, Y.; Hu, J.; Luo, H.; Yeung, L. Y.; Li, W.; Meng, Q.; Ye, G.; Zhang, S.; Fan, Y., Morphology, reversible phase crystallization, and thermal sensitive shape memory effect of cellulose whisker/SMPU nano-composites. *Journal of Applied Polymer Science* **2012,** *123* (2), 749-762.

134.   Liu, D.; Chen, X.; Yue, Y.; Chen, M.; Wu, Q., Structure and rheology of nanocrystalline cellulose. *Carbohydrate Polymers* **2011,** *84* (1), 316-322.

135.   Hasani, M.; Cranston, E. D.; Westman, G.; Gray, D. G., Cationic surface functionalization of cellulose nanocrystals. *Soft Matter* **2008,** *4* (11), 2238-2244.

136.   Shafiei-Sabet, S.; Hamad, W. Y.; Hatzikiriakos, S. G., Rheology of Nanocrystalline Cellulose Aqueous Suspensions. *Langmuir* **2012,** *28* (49), 17124-17133.

137.   Cox, W.; Merz, E., Correlation of dynamic and steady flow viscosities. *Journal of Polymer Science* **1958,** *28* (118), 619-622.

138.   Ten, E.; Bahr, D. F.; Li, B.; Jiang, L.; Wolcott, M. P., Effects of Cellulose Nanowhiskers on Mechanical, Dielectric, and Rheological Properties of Poly(3-hydroxybutyrate-co-3-hydroxyvalerate)/Cellulose Nanowhisker Composites. *Industrial & Engineering Chemistry Research* **2012,** *51* (7), 2941-2951.

139.   Mahi, H.; Rodrigue, D., Linear and non-linear viscoelastic properties of ethylene vinyl acetate/nano-crystalline cellulose composites. *Rheologica Acta* **2012,** *51* (2), 127-142.

140.   Mendez, J.; Annamalai, P. K.; Eichhorn, S. J.; Rusli, R.; Rowan, S. J.; Foster, E. J.; Weder, C., Bioinspired Mechanically Adaptive Polymer Nanocomposites with Water-Activated Shape-Memory Effect. *Macromolecules* **2011,** *44* (17), 6827-6835.

141.   Yang, J.; Han, C.-R.; Duan, J.-F.; Xu, F.; Sun, R.-C., Mechanical and Viscoelastic Properties of Cellulose Nanocrystals Reinforced Poly(ethylene glycol) Nanocomposite Hydrogels. *ACS Applied Materials & Interfaces* **2013,** *5* (8), 3199-3207.

142.   Cao, X.; Xu, C.; Wang, Y.; Liu, Y.; Liu, Y.; Chen, Y., New nanocomposite materials reinforced with cellulose nanocrystals in nitrile rubber. *Polymer Testing* **2013,** *32* (5), 819-826.

143.   Dagnon, K. L.; Way, A. E.; Carson, S. O.; Silva, J.; Maia, J.; Rowan, S. J., Controlling the Rate of Water-Induced Switching in Mechanically Dynamic Cellulose Nanocrystal Composites. *Macromolecules* **2013,** *46* (20), 8203-8212.

144.   Krishnamoorti, R.; Yurekli, K., Rheology of polymer layered silicate nanocomposites. *Current Opinion in Colloid & Interface Science* **2001,** *6* (5), 464-470.

145.   Kamal, M. R.; Khoshkava, V., Effect of cellulose nanocrystals (CNC) on rheological and mechanical properties and crystallization behavior of PLA/CNC nanocomposites. *Carbohydrate Polymers* **2015,** *123*, 105-114.

146.   Auad, M. L.; Richardson, T.; Orts, W. J.; Medeiros, E. S.; Mattoso, L. H. C.; Mosiewicki, M. A.; Marcovich, N. E.; Aranguren, M. I., Polyaniline-modified cellulose nanofibrils as reinforcement of a smart polyurethane. *Polymer International* **2011,** *60* (5), 743-750.

Figure 1.1 Hierarchal structure of cellulose derived from wood/plants
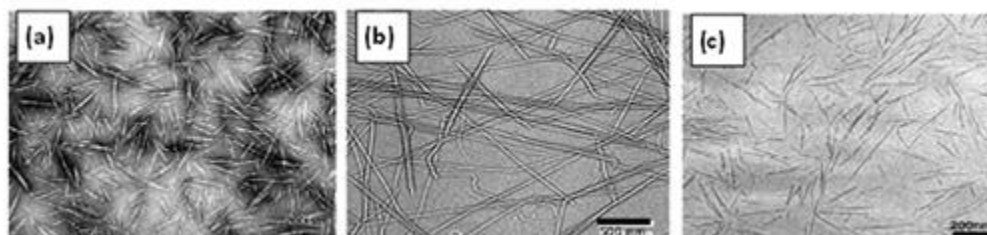
Figure 1.2 TEM images of cellulose nanocrystals extracted from (a)ramie fiber, (b)tunicate, and (c)sugar beet

Figure 1.3 AFM images of cellulose nanocrystals obtained from (a)sulfuric acid hydrolysis and (b) hydrochloric acid hydrolysis of cotton

Figure 1.4 Dispersion of CNC through cross-polarizers from left to right: as preared in water, freeze-dried and re-dispersed in water, DMF, DMSO, NMP, formic acid and m-cresol
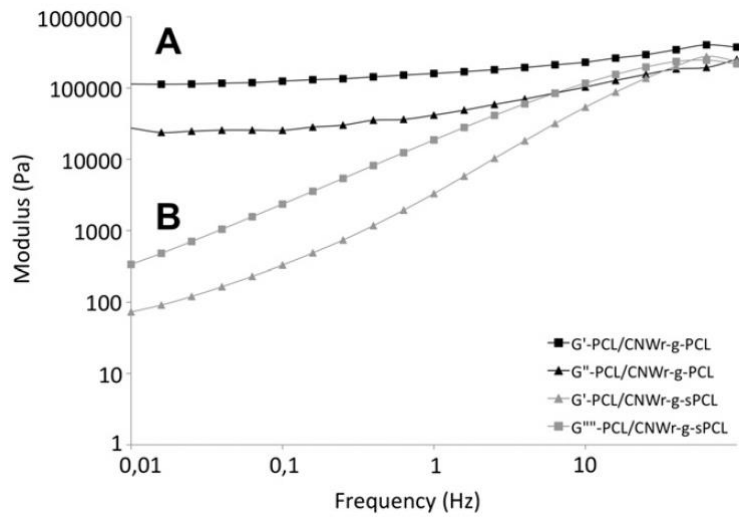
Figure 1.5 The effect of chain length of the surface grafted PCL layer on rheological properties of the PCL/8% PCL-g-cellulose nanowhisker nanocomposites: (A) long chain surface grafted layer and (B) short chain surface grafted PCL layer

CHAPTER II - POLYAMIDE 6 INCORPORATING CELLULOSE NANOCRYSTALS

BY IN-SITU RING-OPENING POLYMERIZATION: VISCOELASTICITY, CREEP

BEHAVIOR AND MELT RHEOLOGICAL PROPERTIES

Published Manuscript

Abstract

The creep behavior and solid and melt linear viscoelasticity of novel polyamide 6 (PA6) nanocomposites reinforced with cellulose nanocrystals (CNCs) prepared via in situ anionic ring-opening polymerization (ROP) were investigated to accelerate research efforts to develop new polymeric materials with improved properties for lightweight, load-bearing applications. The obtained results showed that incorporation of relatively small amounts of ≤ 2wt% CNCs into the PA6 thermoplastic matrix gave nanocomposite samples with significantly enhanced creep and viscoelastic materials functions of the PA6 as indicated by lower creep strain, lower creep compliance, improved elastic recovery after removal of load, and reduced Arrhenius activation energies for time-dependent viscoplastic flow. The obtained results were analyzed and interpreted by theoretical equations for predicting the viscoelasticity and creep behavior of polymeric systems. The melt rheological properties showed enhanced melt strength and elasticity. The formation of a percolated network structure of CNC was revealed by morphological observations that were consistent with the dynamic structure break-up and reformation

rheological experiments. The stiffness, rigidity of the CNCs along with their special

ROP-facilitated intrinsic strong chemical interactions with the PA6 matrix is believed to

be responsible for the observed superior creep and viscoelastic materials functions even

with very little CNC concentration.

2.1 Introduction

Polymer nanocomposites are an important class of polymer based materials that

have found numerous applications in science, engineering and advanced technologies due

to their unique properties that are attainable through the combination specific

characteristics of the polymer matrix and the relatively small concentration of nano-filler

reinforcements. In this context, engineering thermoplastics like polyamide 6 are currently

of academic and industrial research interest due to their superior mechanical properties,

wear and chemical resistance, and good thermal stability [1-2]. However, in a similar way to

other thermoplastic polymers, they undergo viscoelastic deformation and creep under

load when used in load bearing applications.

Recently, addition of various kinds of nanoparticles into polymer matrices has

been shown to effectively improve the creep resistance of the polymer matrix to an extent

that depends on the type, shape and concentration of the nanoparticles. For example,

Yang and co-workers [3-4] reported that low content (i.e., 1 wt%) of spherical (TiO_2) and

platelet-like (organoclay) particles in polyamide 6,6 improved the creep resistance of the

polymer matrix even at elevated temperatures and different stress levels.

A number of research studies that aim to improve the physical properties of

polyamide 6 (PA6) matrix through the addition of various nanoparticles such as silica [5],

organoclays [6], graphene [7] and carbon nanotubes [8] have been reported. For example,

56

nanoclay has been found to improve the viscoelastic and rheological properties of PA6 matrix [9], where it was found that addition of a small volume fraction of clay to PA6 reduced the creep strain of both water saturated and dry PA6 samples through molecular level viscous slippage inhibition effect.

More recently, there has been a great interest in both the scientific and industrial communities in application of natural fibers from renewable agricultural resources as the reinforcing additive in polymer composites. This interest is primarily due to the low cost and abundance of plant-based cellulose fiber resources, low density of the final composite part, low wear of processing equipment, and biodegradability [10-11]. Therefore, this cost effectiveness, lightweight, renewability and environmental sustainability compared to traditional glass or carbon fiber composites have made these natural fibers very attractive for polymer composite applications. Gong and co-workers [12] developed composites of polyvinyl acetate reinforced with cellulose nanofibers (CNFs). Their results showed that the final creep deformation of the matrix can be reduced by using 1-10% of CNFs. They also showed that the activation energy of the molecular motion through analysis of *α*-transition *tan δ* peak measured at different frequencies could be increased by increasing the CNF content. Spoljaric et al [13] used microcrystalline cellulose (MCC) as reinforcing filler in polypropylene matrix. They found that MCC can effectively reduce the creep strain of polypropylene at various loading levels as well as increase the storage modulus and glass transition temperature. The MCC was also found to increase the elastic recovery of strain in recovery process and reduce the permanent deformation which is an important factor in dimensional stability of polymer materials

57

when the load is removed. Their results showed that upon application of a reactive interfacial modifier, the reinforcing effect can be significantly improved.

Cellulose nanocrystals (CNCs) have gained particular interest among bio-derived nano-fillers due to their exceptional mechanical properties having a longitudinal modulus in the range of 100-150 GPa with an average value of 130 GPa that is almost equivalent to that of aramid fibers [14-15]. CNCs have been used as an effective reinforcing agent in a number of polymer systems including polyurethanes [16], poly lactic acid (PLA) [17], epoxy thermosets [18], and polyvinyl acetate adhesives [19]. In a study on shape memory polyurethane reinforced with CNCs [20], a significant enhancement in creep resistance was observed by a reduction of around 40% of the total creep strain with only 1% of CNC in the composite. Iyer and co-workers [2121] developed low-density polyethylene (LDPE)/CNC composites using solid state pulverization technique. The excellent dispersion of CNCs in this hydrophobic LDPE matrix obtained by this mixing strategy resulted in effective property enhancement of mechanical properties and creep resistance.

Despite this reported successes in the application potential of cellulosic fibers as reinforcement for polymers, their use in engineering thermoplastic composites have remained a challenge due to the high melting point (and thus processing temperature) of these thermoplastics such as polyamide 6 ($T_m \sim 220°C$) which overlaps with the thermal degradation temperature of CNCs [22]. Consequently, most nanocomposites containing these nanocrystals have been made by either using hydrophobic polymers with low melting points, or by solvent casting techniques with less than optimal impact [23-24]. Recently, in a series of studies, Kiziltas and co-workers [25-26] reported a melt processing strategy that has been used to blend microcrystalline cellulose with polyamide 6 matrix in

a Barbender® mixer. The rheological characterization of the composite showed an increase in melt elasticity and viscosity at high MCC content; and the crystallization studies showed some molecular motion inhibition in crystal formation in presence of MCC particles. Carolina-Correra et al [27] used a combination of solvent casting and melt processing method to fabricate nano-cellulose reinforced PA6 composites and their obtained results showed promising reinforcing capability even at very low CNC content of 1 wt%. This observed reinforcement efficiency is primarily due to the good dispersion of CNC particle and good protection of CNCs by the cast nylon chains in the melt processing step against thermal degradation.

In addition to the melt processing techniques already described, anionic ring-opening polymerization (ROP) of ε-caprolactam has been used in resin infusion type processes [28] to fabricate PA6 based macro- and nano-composite. In a series of relatively recent studies by Rijswijk et al [29-32] on glass fiber-reinforced PA6 composites and other studies by other researchers on clay [33], zinc [34] and carbon nanotube [35] reinforced PA6 composite, the authors showed that by using the ROP reaction, an effective dispersion of particles (or excellent fiber wet out in the case of macro-fibers [28]) could be achieved by the selection of optimized ROP and processing conditions. An example of the efficiency of this ROP technique was reported by Tung et al [36] where rheological experiments were used to compare clay-reinforced polyamide 6 nanocomposites prepared by both melt blending and *in situ* ROP technique. Their results indicated that ROP facilitated the fabrication of composites with improved properties due to better dispersion of clay.

The work described in the current paper is part of a long-range research effort to develop novel composite materials based on polyamide 6 matrix reinforced by cellulosic

fibers using the ROP technique because the relatively low polymerization temperature ($\sim$ 150°C) minimizes the thermal degradation of the cellulosic fibers that is observed in conventional polymer processing methods like extrusion and injection molding as already described. In addition, the low viscosity of the starting reactive monomeric system allows for better dispersion of nanoparticles. The aim of the current paper is to report on the preparation, viscoelastic and creep behavior of PA6/CNC nanocomposite prepared by *in situ* ROP reaction using optimal prescribed conditions with improved results. The obtained results are analyzed and interpreted within the context of a number of extant theoretical equations that pervade the literature for predicting the viscoelasticity and creep behavior of polymeric systems. It is hoped that the interesting results of this study will provide a basis for further exploitation and better understanding of the facile strategy of developing new engineered thermoplastic nanocomposites reinforced with cellulosic fibers with improved properties for a number of load-bearing applications with enhanced benefits.

In addition to their superior mechanical properties like high stiffness and high surface area available for interaction with matrix, CNC particles have a low density compared to conventional reinforcements such as silicates, glass fiber and carbon fiber. Therefore, the PA6/CNC nanocomposite material of this study is lighter and has superior performance properties for targeted metal replacement component spare parts in vehicular applications where light weighting while meeting CO_2 reduction standards is crucially important.

2.2 Experimental

2.2.1 Materials and Preparation of Nanocomposite

The caprolactam monomer used was an AP-Nylon® caprolactam grade (purchased from Brueggemann Chemical, Pennsylvania) with low moisture content (< 100 ppm) suitable for anionic ring-opening polymerization. The phenyl isocyanate and sodium hydride used were purchased from Aldrich and used as-received. Bleached kraft pulp paper (from southern yellow pine) with 99-100 wt% cellulose (lignin-free pulp) was obtained from Weyerhaeuser and used as the starting material for the preparation of cellulose nanocrystals (CNCs).

In this study cellulose nanocrystals were prepared by sulfuric acid hydrolysis of bleached cellulose paper (kraft pulp) following the method reported by Capadona *et al* [37] with some modifications. The paper was cut into small pieces and blended at high speed with de-ionized water (20 g/L) to achieve a lumpy cellulose pulp followed by placement in a glass reactor in an ice bath. Acid sulfuric (98%) was slowly added to the cold suspension to reach a concentration of 35 v/v% of acid in total suspension. The mixture was then heated to 50°C and stirred for 3.5 hr. The obtained suspension was subsequently quenched with 10 fold excess of de-ionized (DI) water and filtered over fine gritted glass filter and washed slowly with DI water until the running water showed pH ∼ 6. The resulting mixture was decanted to remove the unhydrolyzed fibers and then centrifuged (5 cycles) at 3000 rpm for 10 minutes to concentrate the CNCs. The nanocrystals were recovered by freeze-drying of the suspension and were neutralized with 2nM NaOH solution to convert the surface sulfonic acid groups to sodium salt (indicated by pH

neutrality of the CNC dispersions). The obtained neutralized CNCs were dried overnight in a vacuum oven at 100°C prior to preparation of the nanocomposite samples.

Nanocomposites were prepared by *in situ* ring-opening polymerization of caprolactam monomer in the presence of CNCs. For this purpose, the CNCs were dispersed in the monomer at 0.6, 1 and 2 wt% CNC concentrations by high-speed agitation (700 rpm) for 30 minutes and sonicated for 25 minutes at 85-95°C. The ROP activator was synthesized separately by reaction of the phenyl isocyanate with caprolactam under inert atmosphere for 1 hour at 95°C. The ROP initiators were prepared by addition of sodium hydride to monomer under nitrogen atmosphere. The initiator and activator (1.5 mol% and 1.2 mol%, respectively) were then added to the CNC-containing monomer dispersion and the mixture was allowed to polymerize at 150°C for 30 minutes in a disk shaped mold under vacuum. The conversion of the monomer into polymer was determined by extracting the unreacted monomer in a Soxhlet apparatus using boiling water as the extracting liquid for 9 hours. The nomenclature used here for the test nanocomposite samples is x% CNC where 'x' denotes the CNC content in weight percentage in the composite sample. The prepared composite plates were cut and granulated into small pieces that were used to prepare standard test samples for the various measurements as described in the following sections. Thermal analysis via thermogravimetric analysis (TA Instruments Q500 TGA) were performed to analyze the thermal stability of the cellulose nanocrystals at polymerization temperature of 150°C and no thermal degradation of CNCs were detected.

2.2.2 Test Sample Preparation

Samples for dynamic mechanical analysis (DMA) tests were prepared from the granulated composite samples obtained from the polymerization mold by compression molding. Rectangular bars with dimensions of $3.2 \times 12.6 \times 20$ mm^3 were compression molded in MTP-24 Tetrahedron$^®$ laminating press at 235°C under 5 tons (or 49 kN) of force. The composite granules were dried overnight in a vacuum oven at 80°C after monomer extraction prior to compression molding. The obtained rectangular bars were dried overnight at 80°C prior to DMA tests that were performed under constant flow of dry nitrogen in order to prevent the interference of moisture absorption of samples in the test data acquisition and analysis. For creep tests, rectangular bars with $1.08 \times 14.90 \times 20$ mm^3 dimensions were injection molded using a Daca$^®$ micro-injector bench-top injection molding machine using a barrel temperature of 235°C and a mold temperature of 120°C followed by ambient cooling of the mold after the injection molding. The injection molded bars were dried overnight in a vacuum oven at 80°C and stored in the desiccator until required for testing.

2.2.3 Atmoic Force and Scanning Electron Microscopy

Atomic force microscopy (AFM) Images of the cellulose nanocrystals (CNCs) were captured using a Multimode scanning probe microscope (Veeco$^®$ instruments). A silicon probe with 125μm silicon cantilever with a nominal force constant of 40 N/m was used in tapping mode surface topography in this study. The AFM test specimens were prepared by drop-casting of CNC dispersion from ethanol on Mica surface by spin-coating (3000 rpm) followed by nitrogen blow-drying. The microstructure of the nanocomposite samples was studied by a Sigma field-emission scanning electron

microscope (ZEISS®, USA) using a 5 kV accelerating voltage. The imaging was performed on cryo-fractured surfaces of the nanocomposite samples sputter-coated with silver for enhanced conductivity.

2.2.4 Dynamic Mechanical and Creep Tests

Dynamic mechanical tests were performed using a Perkin Elmer Diamond® DMA using a dual cantilever mode to study the bulk viscoelastic properties of the samples as functions of temperature and frequency. Dynamic viscoelastic properties were measured in the range of -20 to 200°C at a constant frequency of 1 Hz; and the frequency sweep tests were performed at 30°C in the frequency range of 0.05-100 Hz following standard methods.

A Q800 TA® Instruments DMA was used in three point-bend geometry for the creep tests and analysis. The creep tests were performed at 25°, 50°, 75°, 90° and 105°C under a constant stress of 4 MPa that was previously determined to be in the linear viscoelastic region. For each test, a new sample was used and the strain was measured as a function of time. The samples were pre-equilibrated at the desired temperature for 5 minutes prior to the application of the stress for 60 minutes followed by 60 minutes of recovery after removal of the applied stress.

2.2.5 Melt Rheological Characterization

Melt rheological measurements were performed both in the strain-controlled and stress-controlled modes. Dynamic frequency sweep experiments were carried out on an ARES® rheometer using 25 mm parallel plate geometry, a gap of 1mm and a linear strain of 1.25% that was predetermined from a strain sweep test. For the time sweep test, a frequency of 5 rad/s was used. Stress-controlled experiments were done using a DHR2®

TA-instruments rheometer and 25 mm diameter parallel plate geometry with a gap of 0.8mm while for the steady shear flow curve experiments, a cone-and-plate geometry was used in order to maintain a constant shear rate throughout the sample. All the tests were performed under nitrogen atmosphere and the temperature was kept constant at 226°C to ensure a fully molten system and negligible degradation of the samples that was monitored as a less than 6% reduction in G' under the test conditions used. A thermal soak time of 40 s was found to be sufficient to eliminate the residual stress in the samples from the polymerization process, yielding reproducible results that typically replicated to within about 10% from sample to sample. In order to study the structure break-up and recovery in the samples, the samples were pre-sheared at desired shear rates (i.e., 0.1, 1 and 10 s^{-1}) and subsequently subjected to a dynamic time sweep test with a frequency of 5 rad/s and a linear strain of 1.25% and the evolution of viscoelastic properties (G' and G") over time were obtained.

2.3 Results and Discussion

2.3.1 Cellulose Nanocrystal Preparation and Polymerization Reaction

An AFM image of the prepared cellulose nanocrystals (CNCs) is shown in Figure 2.1. Typically in the acid hydrolysis process, the non-crystalline regions (mostly amorphous) of the lignocellulosic fiber are removed by dissolution in the acid medium. This amorphous region is mainly composed of the para-crystalline regions of hemicellulose and the lignin-based portion of the cellulosic fiber. The cellulose starting material, concentration of sulfuric acid, and temperature of hydrolysis determines the final aspect ratio of the CNCs. As evident in Figure 2.1, the obtained CNCs had an aspect ratio of 14–20.

The conversion of the caprolactam monomer in the different composite samples is shown in Figure 2.2(a). As can be seen in this figure, the monomer conversion ranged from 98.5% (PA6) to 95.8% (nanocomposite with 2% CNC). Increasing the CNC content is seen in Figure 2.2(b) to be associated with the evolution of brown color in the composite samples most likely due to the polymerization reaction inhibition effect of CNC particles. It has already been shown that preparation of PA6 based composites by *in situ* ring-opening polymerization in presence of different types of reinforcing fillers such as organoclay [33], TiO_2 [38], metal nanoparticles[39] and glass fibers [29] results in lower conversions of monomer due to the deactivation of growing anionic chain by proton donating species. In the case of cellulose nanocrystals, the deactivation of growing anions is ascribed to a number of different mechanisms including the cellulose peeling reaction, protonation by the bound water molecules on the hydroxyl rich surface of cellulose which can act as an effective proton donating species during the anionic polymerization reaction in addition to the proton abstraction from surface hydroxyl groups. Although the CNCs were thoroughly dried overnight in a vacuum oven and immediately kept under dry nitrogen atmosphere until required for use, the remaining bound-water on the surface may be difficult to completely remove and may therefore lower the polymerization yield.

The surface hydroxyl groups of the CNC may act as proton donating species and consequently deactivate the anionic centers on the growing polymer chains thereby lowering the final conversion. It is worthy to note that upon sulfuric acid hydrolysis and neutralization process, the most active hydrogen donating species (i.e., the methylol groups on the CNC surface) are converted to sodium sulfonate groups which in turn eliminates the proton donating ability of the methylol groups. Therefore, the proton

donation from these methylol groups is less likely to be the primary reason for lower conversion of the polymerization reaction. It should also be noted that the other hydroxyl groups on the cellulose surface are less accessible to the growing PA6 chain anion due to the significant steric hindrance imposed by cellulose backbone structure. These potential inhibition mechanisms are depicted in reaction schemes of Figure 2.2(c).

2.3.2 Morphological and Dynamic Mechanical Analysis

The microstructures of the samples were studied by SEM imaging of the cryo-fractured surfaces. As shown in Figure 2.3, it is clearly evident that a good dispersion of the CNC in PA6 matrix was obtained using the *in-situ* ROP technique. In fact, a dual structural feature of the CNC particles in the matrix can be seen where the dispersed individual whiskers tend to form a more clustered network-like structure with increasing CNC content. Clearly, the cellulose nanocrystals show a strong tendency to interact with each other and form larger "bundles" and fibrillar structures (see Figure 2.3). As the content of CNC is increased from 0.6 to 2 wt%, initially, the whiskers (i.e., single rod-like crystals in the form of filaments with no dislocations) of CNCs tend to form small clusters promoted by the edge-edge effect rather than side-ways aggregation. This is primarily due to the less number of negatively charged sulfonate groups on the CNC surface at the edges that promotes this type of flocculation. In the sample with 2% of CNC, it is clearly seen that the whiskers are in fact, forming a 3D structure by interconnected bundles. These bundles are larger than the length scale of individual whiskers and are clearly formed by clustering of individual whiskers. The effect of this interconnected network of fibrillar structures will be described later in the sections on structural and melt rheological properties of the nanocomposites.

The dynamic mechanical characterization was performed on the neat PA6 and nanocomposite samples to evaluate the effect of addition of CNCs on the thermomechanical properties of the PA6 matrix. The temperature dependency of storage modulus of the PA6 matrix upon addition of the cellulose nanocrystals is shown in Figure 2.4(a). The storage moduli of the samples at representative temperatures of 30°C and 80°C that are respectively below and above the glass transition temperature of the neat PA6 are shown in Table 2.1 (values are averages of 3 replicates). Clearly, addition of very little amount of cellulose nanocrystals increased the storage modulus of the neat PA6 matrix. For example, with the addition of 2 wt% of the CNCs, the modulus increased from 1.95 to 2.6 and from 0.52 to 0.74 GPa at 30° and 80°C, respectively (see Table 2.1). Cellulose nanocrystals are known to be highly stiff particles with a longitudinal modulus of 150 GPa and shear modulus of 5 GPa [40-41]. Therefore, the obtained increase in modulus is ascribed to the presence of the rigid elastic CNCs even at low concentrations (≤ 2 wt% CNC) that enhanced the rigidity of the matrix by making the molecular motion of polymer chains more difficult. It should be mentioned here that our DSC data (not shown) indicate that upon incorporation of CNCs into PA6 matrix, the overall crystallinity of the system reduces from around 45.9% in pure PA6 to 38%, 37% and 30.9% in nanocomposites with 0.6,1 and 2 wt% of CNC, respectively.

It is worthy to note that the melting peak of the α-type crystals (occurring at around 220.5 ± 0.5°C) of the PA6 does not seem to be significantly affected by the presence of the CNCs. However, a clear evolution of the melting peak corresponding to γ-type crystals at 216 ± 1°C is evident as the CNC content is increased, implying a development of the less ordered crystal structure of polyamide chains on the CNC

surface. A more detailed thermal analysis and crystallization kinetics of PA6/CNC

nanocomposites is the subject of a future publication that will be published elsewhere.

However, it should be noted that based on the thermal analysis study just mentioned, the

observed reduction in overall crystallinity is not consistent with the stiffening of the PA6

as seen in DMA results, suggesting that the CNC particles and their reinforcing effect is

responsible for the observed enhancement of properties.

The variation of the loss tangent (*tan δ*) with respect to temperature is shown in

Figure 2.4(b). The glass transition temperature can be determined from the temperature

corresponding to the maximum peak of *tan δ* because it is the temperature at which the

molecular motion of the polymer main chain segments is maximized. Note that

polyamide 6 has three well-known α-, β− and γ- relaxation processes. However, in this

study, the β− and γ- relaxations are out of the temperature range studied. Typically, the α-

relaxation peak temperature is associated with the glass transition temperature [42].

Therefore, it is evident from Figure 2.4(b) that addition of the cellulose nanocrystals to

PA6 only slightly increased the glass transition temperature. It is worthy to note that

addition of various nano-fillers such as organoclay aluminosilicates [9, 43-44], carbon

nanotubes [45] and silica nanoparticles [46] to PA6 has been reported in the literature to either

increase or decrease the glass transition temperature of PA6 to an extent that depends on

the interfacial interaction and compatibility between the nano-filler and the PA6 matrix.

There are a number of distinctive features in the temperature dependency of *tan δ*

in Figure 2.4(b). The slight increase in the *α*-peak temperature for the highest CNC

content composite shows that addition of a small fraction of CNCs imposes restriction on

chain mobility and therefore results in the slight increase in the *Tg*. Considering the fact

that PA6 is a semi-crystalline polymer; this chain movement restriction originates mainly in the amorphous regions of the polymer structure. CNCs possess hydroxyl group-rich surfaces that are available to form strong hydrogen bonds with the PA6 matrix. This suggests that during the course of polymerization, the simultaneous crystallization of polymer chains in the solid state may disrupt the crystalline structure of the polymer in the areas where the particles are located in the composite. This point is consistent with the reported observation by Kiziltas *et al.* [26] that addition of cellulose reduces the overall crystallinity of PA6-based composite materials. As a consequence, the amorphous regions in the polymer structure can interact tightly with CNC surface through H-bonding to form a rigid fraction in the vicinity of the particles. This "stiffening" of polymer chains results in the hindered molecular relaxation and motion resulting in the observed slight increase in the *Tg* already mentioned. It can also be seen in Figure 2.4(b) that as the concentration of cellulose nanocrystals increases in the matrix, the height of the *tan δ* peak is reduced. This observed decrease in the height of the *tan δ* peak is attributed to the reduction in damping characteristic of the polymer chains which is typically caused by incorporation of highly stiff and elastic particles that resist the dissipation of energy under load and improve the elastic nature of the composite.

The frequency dependency of *tan δ* at 30°C is shown in Figure 2.4(c) showing that the obtained *tan δ* values decreased as the CNC content was increased throughout the whole frequency range studied. As can be seen in this figure, the reduction in *tan δ* is more pronounced in the low frequency domain, and as the CNC content is increased, the nanocomposites showed relatively lower dependency on the frequency. We propose a number of possible reasons for this observation. The loss tangent of the nanocomposite

70

which is a measure of the viscoelastic energy damping characteristics of the constituents is expected to be reduced by the presence of the rigid CNC whiskers dispersed in the matrix. In addition, the strong interaction between the polyamide 6 and CNC surface will significantly reduce the chain mobility at the interface and reduce the conversion of mechanical energy to heat at polymer-particle interface as the polymer and particle slide past one another resulting in dissipation of energy. This last point is consistent with the relative increase in T_g of the nanocomposites with increasing CNC content. Further, the morphological observations showed the development of a more homogenous network of interconnected CNC whiskers that is capable of reducing the heat dissipation by stress variation due to non-homogeneity of viscoelastic constituents (i.e., the matrix and CNC with different elasticities).

2.3.3 Creep and Recovery Behavior

Figure 2.5 shows the creep deformation and recovery process of neat PA6 together with the nanocomposite samples containing 0.6, 1 and 2 wt% of cellulose nanocrystals at three different temperatures. An applied stress of 4 MPa was chosen for the creep measurements to ensure the linear viscoelastic deformation region. The overall creep process is made up of the instantaneous deformation (known as the initial creep), the primary creep, and the secondary rupture creep. The experimental conditions were set so that the "rupture" did not take place for the purpose of theoretical modelling of the data.

Expectedly, as Figure 2.5 illustrates, for all the neat matrix and nanocomposite samples, the creep strain increases with increasing temperature. For example, in the case of the neat PA6 matrix, the final deformation after 1 hour of creep increased by 467%

when the temperature was increased from 25 to 105°C. It also clearly evident in Figure 2.5 that throughout the temperature range studied, the total creep strain is much lower for the nanocomposite samples compared to that of the matrix. By increasing the CNC content in the composite, the creep resistance improved and the final creep strain decreased. It is worthy to note that the temperature is comparatively less effective on the nanocomposite samples in terms of the effect on the creep strain compared to that of the neat matrix. In other words, the nanocomposite samples (especially the 2wt% CNC sample showed less dependence of creep strain on the temperature. The fact that the creep resistance of the samples was improved by addition of CNCs is due to the elasticity and rigidity of the nanocomposite samples. Note that in the presence of stiff cellulose nanocrystals, the polymer molecules show less tendency toward the deformation and chain slippage and can resist the applied load more effectively. From the evolution of the creep curves depicted in Figure 2.5 it can be seen that in the second stage of creep which corresponds to the viscoelastic motion of the material, the sample deformation is significantly reduced with increasing CNC content. For example, by addition of 2wt% of CNC, the creep strain of the PA6 matrix shows a reduction of 48% at 25°C while at the 105°C, this reduction in creep strain is more than 61%. This finding points to the fact that at higher temperatures where molecular motion is facilitated by thermal energy of polymer chains, the presence of rigid stiff CNCs significantly improves the creep resistance of the PA6 thermoplastic matrix. Similar effects were observed in the work of Gong et al [12] and Spoljaric and co-workers [13] where the incorporation of cellulosic nanofiber in poly (vinyl acetate) and micro-crystalline cellulose in polypropylene matrix resulted in significant improvements in the creep resistance of the polymer matrix.

For the creep recovery process in Figure 2.5, the following three distinctive features are clearly evident in the recovery strain. A fast step-wise recovery which corresponds to the elastic recovery of the polymer chains when the load is removed from the sample. This is then followed by a viscoelastic recovery over time which then ends with a certain irrecoverable strain at the end of the experiment. This last stage is related to the pure viscous movement of the polymer chains which is not recoverable after removal of the load and often referred to as the permanent deformation. As expected, in the permanent deformation stage, increasing the temperature for all the samples increased the permanent deformation and reduced the ability of the material to recover the deformation elastically. This observation is due to relatively easier viscous flow and plastic deformation that is exacerbated at higher temperatures. The addition of the CNC particles to the matrix enhanced the nanocomposite's capability to recover the strain and reduced the permanent deformation, clearly showing the elasticity contribution of the cellulose nanocrystals to the physical structure of the composite.

It is instructive to distinguish the instantaneous creep deformation upon application of the stress from the creep deformation that takes place over time. In this context, the time-dependent creep compliance (which excludes the instantaneous elastic deformation in the beginning of creep process) is an important variable through which the information about the effect of particles on viscous behavior and chain slippage of the samples can be directly gleaned. Here, the obtained creep compliance values were reduced by the initial compliance, J_o (which is due to the instantaneous elastic deformation) at each specific time and then normalized by the initial compliance value. The obtained results are presented in Figure 2.6. This figure shows that the overall time-

dependent creep compliance of the samples is reduced as the CNC content within the nanocomposite is increased.

The variation of strain rate with time is shown in Figure 2.6. By comparing the strain rates of the samples, it can be clearly seen that addition of CNC into PA6 matrix reduced the strain rate during the creep period studied. In other words, for the sample with higher CNC content, the rate of deformation at an identical time interval is lower compared to that of the samples with zero or little CNC content. This observed result is closely associated with less dependence of the viscoelastic creep behavior with addition of the cellulose crystals which is ascribed to the result of enhanced stiffness and elasticity caused by incorporation of the rigid CNCs. The preceding results indicate that an increase in the CNC content in the nanocomposite reduced both the instantaneous elastic deformation and the time-dependent creep characteristic of the samples due to higher modulus of the samples. In other words, the presence of CNC particles imposed a physical constraint on the matrix chains that prevented the molecular motion and chain slippage which is responsible for the irrecoverable creep deformation. This chain motion restriction just mentioned is caused by the high stiffness of the CNC particles and strong interfacial interactions through hydrogen bonding. This observation and explanation are consistent with the reported work of Seltzer and co-workers [9] that showed that organoclay aluminosilicate particles reduced the time-dependent creep compliance and enhanced elasticity and rigidity of a polyamide 6 matrix. The fact that these rigid cellulose nanocrystals can beneficially reduce the time-dependent creep compliance, which is associated with the retardation of polymer chains under static load, encouraged

us to further study these systems through appropriate theoretical models to quantify the viscoelastic parameters of these samples.

2.3.4 Theoretical Modelling of the Creep and Recovery Process

A number of theoretical models in the literature have been used to interpret the polymer creep process and to predict the long-term creep behavior under experimental conditions that are inaccessible in the laboratory. One of the successful models used for this purpose is the so-called four element model known as the Burger's model [47-48]. As depicted in Figure 2.7 [49], this viscoelastic model (i.e., Burger's model) is composed of a Maxwell and Kelvin-Voight elements connected in a series arrangement. The total strain in the Burger's model is a sum of three separate parts; an elastic deformation (ε_E), a viscoelastic time-dependent strain (ε_V) and an irrecoverable permanent deformation due to viscoplastic flow of the polymer chains (ε_P). This total strain is formulated as follows (Figure 2.7(a), 2.7(b)) [Jia *et al*. (2011)]:

$$\varepsilon_{Total}(t) = \varepsilon_E + \varepsilon_V(t) + \varepsilon_P(t) \tag{2.1}$$

$$\varepsilon(t) = \frac{\sigma_0}{E_M} + \frac{\sigma_0}{E_M}\left(1 - \exp\left(\frac{-t.E_K}{\eta_K}\right)\right) + \frac{\sigma_0}{\eta_M}.t \tag{2.2}$$

In this equation (2.2), the t is the time, E_M and η_M are respectively the spring modulus and dashpot viscosity of the Maxwell element, the E_K and η_K are the respective spring modulus and viscosity of the dashpot in KV element. The retardation time (i.e. $\tau_d = \eta_K/E_K$) corresponds to the time required to reach 63.2% of the total equilibrium deformation in the KV unit.

In the current study, the obtained experimental data from the creep experiment at 25°C were fitted to the Burger's model using the non-linear regression analysis curve

fitting function of OriginPro 9.1® software and the calculated fitting parameters are shown in Table 2.2 with a correlation coefficient (R^2 value) greater than 0.99. The fitting curve is shown in Figure 2.8(a) which shows a good agreement between the model and the experimental data. Table 2.2 shows that the values of all parameters show an increasing trend with increasing CNC content in the matrix. The E_K parameter corresponds to the instantaneous elastic deformation and is associated with elastic modulus of the Maxwell spring that increased from 2.1GPa to 3.4 GPa by addition of 2wt% of CNC particles. The elasticity of the KV element (E_{KV}) shows improvement by addition of the CNCs. This parameter has been reported to be associated with the amorphous fraction of a semi-crystalline polymer matrix [47]. Now by considering the values of η_K and the retardation time (τ_d) it can be seen that both parameters increased by addition of the CNC. The obtained increase in the retardation time suggests that the viscoelastic relaxation of chains is significantly delayed upon incorporation of CNC particles. The viscosity of the dashpot in the Maxwell element (η_M) has been shown [49] to be associated with the permanent deformation due to the irrecoverable. The higher value of η_M indicates a higher resistance of the composite against the viscoplastic flow (permanent deformation) with increasing the CNC content. Similar observations have been reported for polyurethane (PU)/CNC [47] shape memory systems where addition of small fractions of CNC to PU matrix reduced both the plastic deformation and overall creep strain. Other stiff and rigid nano-additives such as carbon nanotubes have also been reported in the literature to effectively reduce the plastic deformation of thermoplastic [47] and thermoset polymers [49].

The recovery process after the creep deformation is typically characterized by three stages. First an instantaneous recovery due to the elastic portion followed by a viscoelastic time dependent recovery, and a final permanent strain or irrecoverable deformation. In order to interpret and quantify this process, the Weibull distribution function [50] was used here to fit the experimental data based on the following equation (see Figure 2.8):

$$\varepsilon(t) = \varepsilon_V [\exp(-(\frac{t-t_0}{\eta_r})^{\beta_r})] + \varepsilon_P \tag{2.3}$$

In this equation, the ε_V is the time dependent viscoelastic recovery strain, the η_r is the characteristic life, the β_r is the shape factor, t is time, t_0 is the time when the stress is removed and the ε_P is the permanent deformation. Clearly, the viscoelastic strain and the permanent deformation is reduced by addition of CNCs which signifies the fact that the recovery process is enhanced and the nanocomposites show higher tendency towards recovery after deformation. A good fitting of the model to the experimental data ($R^2 > 0.99$) was obtained (Figure 2.8(b)) and the obtained fit parameters are shown in Table 2.2. As can be seen in this Table, the increase in shape factor and characteristic life shows that the nanocomposite tends to reach the equilibrium final strain value more quickly (i.e., shorter time-dependent recovery stage). This enhancement in the ability of the nanocomposites to recover the deformation after the load removal is associated with improved dimensional stability in load bearing applications which is a result of the incorporation of a small amount of CNC in the PA6 matrix.

Note that by comparing the final permanent deformation in experimental results to that predicted by the Weibull distribution model, a very good agreement can be seen and also we can see that 60 minutes of recovery time is not sufficient for the samples to reach the final equilibrium permanent deformation which is suggested by the model. It is interesting to see that the final values of experimental results are closer to the values predicted by the model for samples with higher CNC content. This shows that the CNCs contribute towards the faster and more efficient recovery of the strain in polyamide 6-based nanocomposite samples. In other words, the equilibrium final permanent deformation is reached faster as the CNC content is increased in the matrix.

2.3.5 Time-Temperature Superpositioning of Creep Data

Time-temperature superposition (TTS) principle [51] has been successfully and widely used to predict the viscoelastic behavior of polymeric materials at long times or elevated temperatures that are experimentally inaccessible [47, 52-53]. In the current research, the creep experiments were performed on all samples at five different temperatures namely 25°, 50°, 75°, 90° and 105°C which covers a temperature range (T) below and above the glass transition ($T_g \sim 65°C$) (i.e., $T = T_g \pm 40°C$)..

In the case of semi-crystalline polymers or filled polymer systems, typically the conventional equations (such as WLF equation) do not provide accurate predictions due to the thermo-rheological complexity of the materials near T_g [54-56]. In order to optimize the superposition process, usually a vertical shift factor is applied in conjunction with a horizontal shift factor to compensate for the drastic change in the initial instantaneous change of the studied viscoelastic property caused by the temperature change.

Since α_T cannot be predicted accurately based on the above explanation, the shifting can be carried out in an objective manner like the one reported by Honerkamp and Weese [57]. In the current study, the TTS option of Thermal Advantage software provided by TA Instruments® was used for shifting purposes. The horizontal shift factor can be studied in the form of an Arrhenius equation as follows:

$$\log(a_T) = \frac{\Delta E}{2.303R}\left(\frac{1}{T} - \frac{1}{T_0}\right)$$ (2.4)

where the ΔE is the activation energy, R is the gas constant, T is the temperature and T_0 is the references temperature (chosen here to be 25°C).

The obtained shifted curves are shown in Figure 2.9. As can be seen in this figure, an acceptable superposition is obtained. The creep strain of PA6 matrix and nanocomposites are predicted to an extended time of 10^{13} seconds. By increasing the CNC content in the matrix, it is seen that at extended times the creep resistance is improved and the total strain is reduced. It is interesting to note that at a high level of expected time scale (more than 10^9 s) the significance in the creep strain difference between the matrix and nanocomposite of 0.6wt% becomes more detectable which is basically due to the fact that the matrix enters the viscoelastic state and the reinforcing effect of cellulose nanocrystals even at very low content plays a significant role in improving the creep resistance.

The effect of molecular relaxation and chain slippage in presence of CNCs can be studied through the comparison of activation energies obtained from the linear regression of Arrhenius equation in Figure 2.9 that shows the variation of shift factor with respect to temperature. The activation energies increased from 161.3 kJ/mol in the neat PA6 matrix

79

to 243.9 kJ/mol in the 2wt% CNC composite. For the nanocomposite samples of 0.6 and

1wt% of CNC, the activation energies are respectively 176.5 and 202.7 kJ/mol. It is

interesting to note that in a number of reported studies in the literature such as that of Yao

et al. [49] on polyurethane/CNT systems and of Wu and co-workers on poly (butylene

terephthalate/montmorillonite) nanocomposites [58], the authors found that the addition of

nano-fillers into the polymer matrix did not result in significant changes in activation

energies They attributed this observation to the fact that the poor interfacial interaction

between the filler and matrix does not contribute to the creep resistance improvement but

rather, the particles themselves form a network that resist the deformation. However, the

results of the current study shows that the CNC particles are, in fact, inhibiting the chain

relaxation and molecular motion through strong interfacial adhesion arising from

hydrogen bond formation between the hydroxyl rich surface of cellulose nanocrystals and

amide groups on the polyamide 6 backbone structure that is facilitated by the ROP

processing method used. Therefore, it can be argued that both the presence of relatively

tiny amounts of stiff and rigid CNC particles, as well as, the molecular motion retardation

effect through interfacial interaction, improves the creep resistance of PA6/CNC

nanocomposite materials.

2.3.6 Melt Rheological Studies

Because the melt rheological experiments were performed at 226°C, it was

necessary to investigate plausible thermal degradation of the CNC particles in the

samples during the measurements. For this purpose, a dynamic time sweep test was

carried out to analyze the changes in storage and loss modulus of the sample with 2%

CNCs over time (Figure 2.10). The storage modulus was found to decrease by average of

6% after 10 minutes and 17% after 30 minutes Therefore, all the melt rheological experiments were limited to around a total time duration of 10 minutes so that effects of thermal degradation can be minimized.

Small amplitude oscillatory shear experiments were carried out in order to probe the effect of the CNCs on the melt flow properties of the PA6 matrix and the obtained results are shown in Figure 2.11(a)–(c). As can be seen in this figure, increasing the CNC content increased the elastic modulus of the PA6 matrix, being more pronounced in the low frequency region. Note that it is well known that in filled polymer systems, a non-terminal rheological behavior of the sample at low frequency is indicative of formation of a particle-induced structure to an extent that depends of the polymer/particle interactions [59]. Clearly, in the whole frequency range examined, the sample with 2% CNC showed higher elastic modulus, indicating significant elastic contribution of the CNCs in the melt. The non-terminal nature of the rheological behavior can be studied through the slope of the G' vs ω at the low frequency region which can in turn be effectively used to interpret the structure development [60]. For this purpose, a linear regression of an exponential function of modulus and frequency ($G \propto \omega^n : \ln(G) = n \ln(\omega)$) was performed in the frequency region of $0.1 - 1$ rad/s and the obtained results are shown in Table 2.3. This table shows that the terminal slope changed from 1.46 in the pure PA6 matrix to 0.72 in the sample with 2% CNC. A similar trend was observed for the G'' curve where the terminal region slope changed from 0.87 in the pure matrix to 0.54 in the sample with 2% CNC. This observed decreasing trend in slope with increasing CNC content can be explained by microstructural changes in the samples. With increasing content of CNCs and consequent strong polymer-particles and inter-particles interactions, a structural

81

network is developed that shows a pseudo-solid-like behavior, especially in low

frequency regions, due to the significant restriction imposed on polymer chains[61-62].

Similar to the discussion on the solid-state *tan δ* variations at low frequency region

already discussed, the polymer chains can relax under the dynamic load due to a

relatively large response time. However, the influence of elastic contributions in the melt

resulting from the 3D network of stiff CNCs is evident in the low frequency regime of the

dynamic frequency test results shown in Figure 2.11.

It is interesting to note that in the high frequency region, the values of elastic

modulus of the nanocomposite melts are slightly higher than that of the neat PA6.

However, the nanocomposite samples showed quite similar values of elastic modulus.

The experimental results just mentioned can be ascribed to the fact that the high

frequency region is predominantly governed by short-range dynamics of polymer chains

and the rheological behavior of the system is dominated by the matrix properties [63]. In

contrast, in the low frequency region, the behavior of the materials is governed by

relatively long-range interactions and the formation of CNC network, instead of the

relaxation of matrix polymer molecules as the CNC network resists the structural

relaxation which is responsible for the observed enhanced melt elasticity as already

discussed. The variation in complex viscosity of samples versus frequency is shown in

Figure 2.11(c). As expected, it can be seen from this figure that the nanocomposite

samples showed higher complex viscosities compared to that of the neat PA6 especially

at low frequencies.

At low frequency regions, the viscous flow dominates as the polymer chains are

in their relaxed state, resulting in a terminal flow characteristic. This regime is governed

by the power-law relationships of $G' \sim \omega^2$ and $G'' \sim \omega$ for homo polymers. However, as the CNC is added to the melt and the content is increased, a non-terminality of the flow at these low frequency regions develops and the storage and loss moduli become less dependent on the frequency. As already mentioned, this experimental fact just mentioned is primarily due to the development of an interconnected network of the CNC whiskers and associated pseudo-solid like flow behavior. This behavior is consistent with the lower slopes of G' and G'' and higher slope of complex viscosity at lower frequencies.

A similar type of behavior has been reported in the literature for polypropylene/CNC nanocomposites and PA6/carbon nanotube composites[59-60]. Interestingly, in a comparative study reported by Tung and coworkers [36], PA6/nanoclay samples prepared by melt blending and *in-situ* polymerization were compared for their melt rheological properties.

To better understand the structure of the nanocomposite samples of the current study and its interrelation with rheological properties, a number of steady shear experiments and coupled steady and dynamic experiments were performed. The obtained variation of viscosity versus steady shear rate is shown in Figure 2.12. As can be seen in this figure, the nanocomposite samples showed higher absolute values of viscosity compared to that of neat PA6 matrix. Here, zero-shear viscosity values were approximated by the value at $0.001s^{-1}$ and are tabulated in Table 2.3 for easy comparison. This table shows that this zero-shear viscosity value changed from 118.9 Pa.s for the neat polymer to 283.2 Pa.s for the nanocomposite with 2% of CNC particles.

At the relatively higher shear rates, the filled polymer systems showed onset of shear-thinning behavior at low shear rates compared to that of the neat polymer. Clearly,

not only the onset of shear thinning behavior occurred at low shear rates for the filled

polymer systems, but also the slope of the shear-thinning region is significantly higher for

the nanocomposite samples, especially for the nanocomposite samples with 2% of CNC.

In order to further elaborate on this point, the slope of the shear-thinning region was

calculated for the neat polymer and the nanocomposite with 2% of CNC. The data points

in the shear-thinning region were fitted using a power law function and the power law

index was found using a linear regression of equation (2.5).

$$\tau = k\dot{\gamma}^{n} \rightarrow \eta = k\dot{\gamma}^{n-1} : \ln(\eta) = A + (n-1)\ln\dot{\gamma} \qquad (2.5)$$

For the neat polymer the power law index (n) was found to be 0.37 while this

value for the 2% CNC nanocomposite sample was 0.64. Therefore, the more shear-

thinning characteristic of the CNC filled PA6 composites can be quantified using this

power law index.

The empirical Cox-Merz rule has been shown to be an effective tool in studying

the structure and flow properties of filled and unfilled polymer systems and have been

widely used to correlate oscillatory dynamic experiments with steady shear experiments

[64-66] and it has also been used in Polyamide 6 systems [67]. According to this rule, the

absolute values of the viscosities in an oscillatory dynamic experiment should

superimpose the value of steady shear experiment at identical frequencies and shear rates

particularly at infinitely low angular frequencies (or shear rates) as shown below.

$$\left|\eta^{*}(\omega)_{\omega\to 0}\right| \approx \left|\eta(\dot{\gamma})_{\dot{\gamma}\to 0}\right| \qquad (2.6)$$

Here, the viscosity values at 0.1s^{-1} (0.1 rad/s) were considered for neat PA6 and PA6/2% CNC samples. For the neat polymer, the viscosity values are 61.6 and 79 in oscillatory and steady shear experiments, respectively, indicating a slight difference between these values due to the fact that there are strong interactions between the chains of polyamide 6 through hydrogen bonding. However, for the sample containing 2% CNC particles, the obtained viscosity value of 239.9 Pa.s in oscillatory shear does not correlate to the value of 151.2 Pa.s obtained in the steady shear experiment, indicating the failure of Cox-Merz rule. Like other researchers have reported in the literature, the Cox-Merz rule does not hold when there are specific elastic contributions in the melt. It is proposed here that the elastic contribution of CNC particles network is responsible for the failure of the Cox-Merz approximation. In the current study, it can be concluded that the presence of rigid CNC network and strong interaction of polyamide chains with the surface of the CNC particles results in significant elastic contribution to the melt properties (from the particles) which in turn results in deviation of the rheological behavior from that of neat matrix.

In order to investigate the structure formation of CNC particles in the polyamide 6 matrix, a series of real-time stress development experiments of pre-sheared samples were carried out in order to further look into the break-up and reformation of CNC network in the matrix. In Figure 2.13 the development of elastic modulus (G') over time after a pre-shearing stage of 30 seconds (at 3 different shear rates) is shown. As can be seen, for the neat polymer sample, there is a minimal elastic recovery observed at all different pre-shear rates as the pre-shearing stage solely disrupts the chain entanglements and orient the chains in the flow direction; this again confirms that the pure PA6 sample shows a

dominating viscous behavior with minimum elastic character. However for the filled

systems a completely different behavior is observed.

In addition, all samples showed no changes in structure upon the application of

$0.1s^{-1}$ pre-shear because the melt elastic modulus of the samples remained almost

constant throughout the 600s experiment time. However, as the pre-shear rate was

increased to 1 and $10s^{-1}$ the initial modulus of the filled polymer samples dropped to

lower values (as the shear rate increased). This shows that the application of shear results

in break-up of the existing rigid structure in the sample and also orients the entangled

polymer chains at the interface of cellulose nanocrystals, and consequently the elasticity

(a measure of stiffness) of the melt is decreased. When the time sweep test starts, these

disrupted structures find a second opportunity (in absence of intense shearing force) to

aggregate and form new structures. As the CNC content of the melt increases, there is a

significant reduction in the initial elastic modulus, and the change in elastic modulus

covers a wide range over the experimental timescale investigated. In brief, as the CNC

concentration increases, the elastic modulus of the sample drops more significantly after

the pre-shear stage (indicated by lower start-up modulus in the subsequent time sweep

test). In addition, there is a greater tendency in the sample with higher CNC content to

recover the "elasticity" due to the structure formation of CNC particles in the melt once

the shear is stopped.

The graphs shown in Figure 2.13 clearly indicate that as the CNC content

increases, the stiffness or elastic properties of nanocomposite melts becomes more

dependent on the shear history of the samples. The more cellulose particles in the melt,

the more structural clusters tend to form, which as a consequence, results in more

dependency on the shear, only if the applied shear rate is high enough to break up the network. It can also be concluded from this behavior that the particle-particle affinity of the CNCs in the PA6 melt is more favorable than particle-polymer interactions, as the evolution of the elastic properties is due to the formation of agglomerates and clusters of the CNC particles (which is absent in the neat PA6 sample). Another important aspect of Figure 2.13 that can be considered is the terminal regions of the structure recovery curves. As the Figure shows, increasing the shear rate increased the slope of the terminal region of curves (i.e., at $10s^{-1}$). The same trend was observed when the content of CNC particles was increased in the melt. In contrast, by lowering the shear rate and decreasing the CNC content, the curves appeared to reach their plateau modulus more quickly after which there is no increase in elastic modulus. To quantify this property of the studied materials, the terminal region slope (i.e., in the range of 500-600s) of the curves pre-sheared at $10 \, s^{-1}$ is shown in Table 2.3. This slope shows the rate of evolution of G' in the terminal zone of the experiment. It is shown that as the CNC content in the melt increases, the structure recovery from the disrupted state to the steady state conditions requires longer time intervals. This implies that relatively long experimental times are required to reach the final plateau, but due to thermal degradation effects, the current experiments were limited to 600s as already mentioned.

2.4 Conclusions

This study demonstrates feasibility of preparing novel polyamide 6 (PA6)/cellulose nanocrystal (CNC) nanocomposites via *in-situ* anionic ring-opening polymerization reaction with improved creep resistance and enhanced dynamic mechanical properties, indicating the effective reinforcing ability of the CNCs as novel

"green" reinforcement additives for engineering thermoplastic polymers such as PA6. The obtained results showed that the storage modulus of the PA6 matrix, which is a measure of stiffness of the nanocomposites, can be improved with addition of a relatively small amount of CNC particles ($\leq$ 2 wt% CNC). The creep resistance of the nanocomposites was improved by addition of the CNCs over a wide temperature range relative to Tg, as evidenced by the reduction in final creep strain, lower permanent deformation, and lower creep compliance compared with that of the neat PA6 matrix. Therefore, these novel thermoplastic nanocomposite materials may find uses in load-bearing applications where superior dimensional stability under constant load, light weighting, and favorable melt rheology (or processability) is crucial performance requirements.

A number of extant theoretical models in the literature were used to quantify the creep process and to interpret the changes caused by incorporation of the CNC reinforcement. The results of the theoretical modeling confirmed our expectation of enhanced elasticity due to the presence of a tiny amount of CNC particles in the thermoplastic matrix, which as a consequence, lowered the time-dependent viscoplastic flow and promoted the elastic recovery after the load removal. Time-temperature superpositioning was successfully applied to the creep data to predict the long-term creep behavior and it was found that the incorporation of the relatively rigid and stiff cellulose nanocrystals increased the activation energy of the molecular motion.

The melt rheological tests revealed enhanced melt viscoelastic material functions (i.e., melt viscosity, storage (elastic), loss modulus and complex viscosity). Significant stiffening of the polymer melt was exhibited by the 2% PA6/CNC nanocomposite,

suggesting the onset of formation of percolated network structures and associated high shear thinning characteristics. Structure recovery tests showed that, provided a sufficiently high shear rate is applied, this network of CNC bundles can be broken apart followed by re-formation of the structure once the shear is removed. The observed increase in elastic properties of the PA6 melt containing CNCs increased over time is consistent with significant particle-particle affinity and bundle formation as evidenced by SEM images.

The cost-effectiveness, lightweight, renewability and environmental sustainability of the nanocomposites of this study compared to that of traditional glass or carbon fiber-reinforced (micro) composites may spur a better understanding of the current nanocomposites for a number of engineering applications where traditional carbon or glass fiber-reinforced polymer (micro) composites are not useable.

Commission for jointly funding his Fulbright-Tocqueville Distinguished Chair award in Engineering at the University of Lyon 1; and IMP CNRS 5223 colleagues for their hospitality during his temporary residence in Lyon.

2.5 References

1.   Page, I., *Polyamides as engineering thermoplastic materials*. iSmithers Rapra Publishing: 2000.

2.   Vlasveld, D. P. N.; Bersee, H. E. N.; Picken, S. J., Creep and physical aging behaviour of PA6 nanocomposites. *Polymer* **2005,** *46* (26), 12539-12545.

3.   Yang, J.-L.; Zhang, Z.; Schlarb, A. K.; Friedrich, K., On the characterization of tensile creep resistance of polyamide 66 nanocomposites. Part I. Experimental results and general discussions. *Polymer* **2006,** *47* (8), 2791-2801.

4.   Yang, J.-L.; Zhang, Z.; Schlarb, A. K.; Friedrich, K., On the characterization of tensile creep resistance of polyamide 66 nanocomposites. Part II: Modeling and prediction of long-term performance. *Polymer* **2006,** *47* (19), 6745-6758.

5.   Hasan, M. M.; Zhou, Y.; Mahfuz, H.; Jeelani, S., Effect of SiO 2 nanoparticle on thermal and tensile behavior of nylon-6. *Materials Science and Engineering: A* **2006,** *429* (1), 181-188.

6.   Varlot, K.; Reynaud, E.; Kloppfer, M.; Vigier, G.; Varlet, J., Clay-reinforced polyamide: Preferential orientation of the montmorillonite sheets and the polyamide crystalline lamellae. *Journal of Polymer Science Part B: Polymer Physics* **2001,** *39* (12), 1360-1370.

7.   Xu, Z.; Gao, C., In situ polymerization approach to graphene-reinforced nylon-6 composites. *Macromolecules* **2010,** *43* (16), 6716-6723.

8.   Liu, T.; Phang, I. Y.; Shen, L.; Chow, S. Y.; Zhang, W.-D., Morphology and mechanical properties of multiwalled carbon nanotubes reinforced nylon-6 composites. *Macromolecules* **2004,** *37* (19), 7214-7222.

9.   Seltzer, R.; Mai, Y.-W.; Frontini, P. M., Creep behaviour of injection moulded polyamide 6/organoclay nanocomposites by nanoindentation and cantilever-bending. *Composites Part B: Engineering* **2012,** *43* (1), 83-89.

10.   Wei, H.; Rodriguez, K.; Renneckar, S.; Vikesland, P. J., Environmental science and engineering applications of nanocellulose-based nanocomposites. *Environmental Science: Nano* **2014,** *1* (4), 302-316.

11.   Kim, J.-H.; Shim, B.; Kim, H.; Lee, Y.-J.; Min, S.-K.; Jang, D.; Abas, Z.; Kim, J., Review of nanocellulose for sustainable future materials. *International Journal of Precision Engineering and Manufacturing-Green Technology* **2015,** *2* (2), 197-213.

12.   Gong, G.; Pyo, J.; Mathew, A. P.; Oksman, K., Tensile behavior, morphology and viscoelastic analysis of cellulose nanofiber-reinforced (CNF) polyvinyl acetate (PVAc). *Composites Part A: Applied Science and Manufacturing* **2011,** *42* (9), 1275-1282.

13.   Spoljaric, S.; Genovese, A.; Shanks, R. A., Polypropylene–microcrystalline cellulose composites with enhanced compatibility and properties. *Composites Part A: Applied Science and Manufacturing* **2009,** *40* (6), 791-799.

14.   Moon, R. J.; Martini, A.; Nairn, J.; Simonsen, J.; Youngblood, J., Cellulose nanomaterials review: structure, properties and nanocomposites. *Chemical Society Reviews* **2011,** *40* (7), 3941-3994.

15.   Pranger, L.; Tannenbaum, R., Biobased Nanocomposites Prepared by In Situ Polymerization of Furfuryl Alcohol with Cellulose Whiskers or Montmorillonite Clay. *Macromolecules* **2008,** *41* (22), 8682-8687.

16.   Pei, A.; Malho, J.-M.; Ruokolainen, J.; Zhou, Q.; Berglund, L. A., Strong nanocomposite reinforcement effects in polyurethane elastomer with low volume fraction of cellulose nanocrystals. *Macromolecules* **2011,** *44* (11), 4422-4427.

17.   Wang, T.; Drzal, L. T., Cellulose-nanofiber-reinforced poly (lactic acid) composites prepared by a water-based approach. *ACS applied materials & interfaces* **2012,** *4* (10), 5079-5085.

18.   Rusli, R.; Shanmuganathan, K.; Rowan, S. J.; Weder, C.; Eichhorn, S. J., Stress Transfer in Cellulose Nanowhisker Composites・ Influence of Whisker Aspect Ratio and Surface Charge. *Biomacromolecules* **2011,** *12* (4), 1363-1369.

19.   Kaboorani, A.; Riedl, B.; Blanchet, P.; Fellin, M.; Hosseinaei, O.; Wang, S., Nanocrystalline cellulose (NCC): A renewable nano-material for polyvinyl acetate (PVA) adhesive. *European Polymer Journal* **2012,** *48* (11), 1829-1837.

20.   Auad, M. L.; Contos, V. S.; Nutt, S.; Aranguren, M. I.; Marcovich, N. E., Characterization of nanocellulose-reinforced shape memory polyurethanes. *Polymer International* **2008,** *57* (4), 651-659.

21.   Iyer, K. A.; Schueneman, G. T.; Torkelson, J. M., Cellulose nanocrystal/polyolefin biocomposites prepared by solid-state shear pulverization:

Superior dispersion leading to synergistic property enhancements. *Polymer* **2015,** *56*, 464-475.

22.   Habibi, Y.; Lucia, L. A.; Rojas, O. J., Cellulose nanocrystals: chemistry, self-assembly, and applications. *Chemical reviews* **2010,** *110* (6), 3479-3500.

23.   Dufresne, A., Processing of polymer nanocomposites reinforced with polysaccharide nanocrystals. *Molecules* **2010,** *15* (6), 4111-4128.

24.   Oksman, K.; Mathew, A.; Sain, M., Novel bionanocomposites: processing, properties and potential applications. *Plastics, Rubber and Composites* **2009,** *38* (9-10), 396-405.

25.   Kiziltas, A.; Nazari, B.; Gardner, D. J.; Bousfield, D. W., Polyamide 6–cellulose composites: Effect of cellulose composition on melt rheology and crystallization behavior. *Polymer Engineering & Science* **2014,** *54* (4), 739-746.

26.   Kiziltas, A.; Gardner, D. J.; Han, Y.; Yang, H.-S., Dynamic mechanical behavior and thermal properties of microcrystalline cellulose (MCC)-filled nylon 6 composites. *Thermochimica Acta* **2011,** *519* (1), 38-43.

27.   Corrêa, A. C.; de Morais Teixeira, E.; Carmona, V. B.; Teodoro, K. B. R.; Ribeiro, C.; Mattoso, L. H. C.; Marconcini, J. M., Obtaining nanocomposites of polyamide 6 and cellulose whiskers via extrusion and injection molding. *Cellulose* **2014,** *21* (1), 311-322.

28.   Otaigbe, J. U.; Harland, W. G., Studies in the properties of nylon 6–glass fiber composites. *Journal of Applied Polymer Science* **1988,** *36* (1), 165-175.

29.   Van Rijswijk, K.; Teuwen, J.; Bersee, H.; Beukers, A., Textile fiber-reinforced anionic polyamide-6 composites. Part I: The vacuum infusion process. *Composites Part A: Applied Science and Manufacturing* **2009,** *40* (1), 1-10.

30.   Van Rijswijk, K.; Van Geenen, A.; Bersee, H., Textile fiber-reinforced anionic polyamide-6 composites. Part II: Investigation on interfacial bond formation by short beam shear test. *Composites Part A: Applied Science and Manufacturing* **2009,** *40* (8), 1033-1043.

31.   Van Rijswijk, K.; Bersee, H.; Beukers, A.; Picken, S.; Van Geenen, A., Optimisation of anionic polyamide-6 for vacuum infusion of thermoplastic composites: Influence of polymerisation temperature on matrix properties. *Polymer testing* **2006,** *25* (3), 392-404.

32.   Van Rijswijk, K.; Bersee, H.; Jager, W.; Picken, S., Optimisation of anionic polyamide-6 for vacuum infusion of thermoplastic composites: choice of activator and initiator. *Composites Part A: Applied Science and Manufacturing* **2006,** *37* (6), 949-956.

33.   Liu, A.; Xie, T.; Yang, G., Synthesis of Exfoliated Monomer Casting Polyamide 6/Na+-Montmorillonite Nanocomposites by Anionic Ring Opening Polymerization. *Macromolecular Chemistry and Physics* **2006,** *207* (7), 701-707.

34.   Rusu, G.; Rusu, E., Anionic nylon 6/zinc composite materials: Evaluation of thermal and mechanical behavior. *International Journal of Polymer Analysis and Characterization* **2010,** *15* (8), 509-523.

35.   Yang, M.; Gao, Y.; Li, H.; Adronov, A., Functionalization of multiwalled carbon nanotubes with polyamide 6 by anionic ring-opening polymerization. *Carbon* **2007,** *45* (12), 2327-2333.

36.   Tung, J.; Gupta, R. K.; Simon, G. P.; Edward, G. H.; Bhattacharya, S. N., Rheological and mechanical comparative study of in situ polymerized and melt-blended nylon 6 nanocomposites. *Polymer* **2005,** *46* (23), 10405-10418.

37.   Capadona, J. R.; Van Den Berg, O.; Capadona, L. A.; Schroeter, M.; Rowan, S. J.; Tyler, D. J.; Weder, C., A versatile approach for the processing of polymer nanocomposites with self-assembled nanofibre templates. *Nat Nano* **2007,** *2* (12), 765-769.

38.   Rusu, G.; Rusu, E., Nylon 6/TiO2 Composites by in situ Anionic Ring-Opening Polymerization of ϵ-Caprolactam: Synthesis, Characterization, and Properties. *International Journal of Polymer Analysis and Characterization* **2011,** *16* (8), 561-583.

39.   Rusu, G.; Rusu, E., Nylon 6/copper composites by in situ polymerization. *Journal of optoelectronics and advanced materials* **2009,** *11* (5), 673-680.

40.   Liu, H.; Laborie, M.-P. G., Bio-based nanocomposites by in situ cure of phenolic prepolymers with cellulose whiskers. *Cellulose* **2011,** *18* (3), 619-630.

41.   Helbert, W.; Cavaille, J.; Dufresne, A., Thermoplastic nanocomposites filled with wheat straw cellulose whiskers. Part I: processing and mechanical behavior. *Polymer composites* **1996,** *17* (4), 604-611.

42.   Woodward, A.; Sauer, J.; Deeley, C.; Kline, D., The dynamic mechanical behavior of some nylons. *Journal of Colloid Science* **1957,** *12* (4), 363-377.

43.   Pramoda, K.; Liu, T., Effect of moisture on the dynamic mechanical relaxation of polyamide-6/clay nanocomposites. *Journal of Polymer Science Part B: Polymer Physics* **2004,** *42* (10), 1823-1830.

44.   Zulfiqar, S.; Ishaq, M.; Sarwar, M. I., Effect of surface modification of montmorillonite on the properties of aromatic polyamide/clay nanocomposites. *Surface and Interface Analysis* **2008,** *40* (8), 1195-1201.

45.   Zhao, C.; Hu, G.; Justice, R.; Schaefer, D. W.; Zhang, S.; Yang, M.; Han, C. C., Synthesis and characterization of multi-walled carbon nanotubes reinforced polyamide 6 via in situ polymerization. *Polymer* **2005,** *46* (14), 5125-5132.

46.   Shen, L.; Du, Q.; Wang, H.; Zhong, W.; Yang, Y., In situ polymerization and characterization of polyamide-6/silica nanocomposites derived from water glass. *Polymer International* **2004,** *53* (8), 1153-1160.

47.   Jia, Y.; Peng, K.; Gong, X.-l.; Zhang, Z., Creep and recovery of polypropylene/carbon nanotube composites. *International Journal of Plasticity* **2011,** *27* (8), 1239-1251.

48.   Ward, I. M.; Sweeney, J., *Mechanical properties of solid polymers*. John Wiley & Sons: 2012.

49.   Yao, Z.; Wu, D.; Chen, C.; Zhang, M., Creep behavior of polyurethane nanocomposites with carbon nanotubes. *Composites Part A: Applied Science and Manufacturing* **2013,** *50*, 65-72.

50.   Fancey, K. S., A mechanical model for creep, recovery and stress relaxation in polymeric materials. *Journal of materials science* **2005,** *40* (18), 4827-4831.

51.   Ferry, J. D., *Viscoelastic properties of polymers*. 3rd ed.; John Wiley & Sons: New York, 1980.

52.   Ding, H.-Z.; Wang, Z., Time–temperature superposition method for predicting the permanence of paper by extrapolating accelerated ageing data to ambient conditions. *Cellulose* **2007,** *14* (3), 171-181.

53.   Osman, E. A.; Mutasher, S. A., Viscoelastic properties of kenaf reinforced unsaturated polyester composites. *International Journal of Computational Materials Science and Engineering* **2014,** *3* (01), 1450004.

54.   Likhtman, A. E., Viscoelasticity and molecular rheology. Elsevier BV: Amsterdam: 2012; Vol. 1.

55.   Tajvidi, M.; Falk, R. H.; Hermanson, J. C., Time–temperature superposition principle applied to a kenaf-fiber/high-density polyethylene composite. *Journal of Applied Polymer Science* **2005,** *97* (5), 1995-2004.

56.   Dealy, J.; Plazek, D., Time-temperature superposition—a users guide. *Rheol. Bull* **2009,** *78* (2), 16-31.

57.   Honerkamp, J.; Weese, J., A note on estimating mastercurves. *Rheologica acta* **1993,** *32* (1), 57-64.

58.   Wu, D.; Zhou, C.; Hong, Z.; Mao, D.; Bian, Z., Study on rheological behaviour of poly (butylene terephthalate)/montmorillonite nanocomposites. *European Polymer Journal* **2005,** *41* (9), 2199-2207.

59.   Khoshkava, V.; Kamal, M. R., Effect of Cellulose Nanocrystals (CNC) Particle Morphology on Dispersion and Rheological and Mechanical Properties of

Polypropylene/CNC Nanocomposites. *ACS applied materials & interfaces* **2014,** *6* (11), 8146-8157.

60.   Wang, M.; Wang, W.; Liu, T.; Zhang, W.-D., Melt rheological properties of nylon 6/multi-walled carbon nanotube composites. *Composites Science and Technology* **2008,** *68* (12), 2498-2502.

61.   Mitchell, C. A.; Bahr, J. L.; Arepalli, S.; Tour, J. M.; Krishnamoorti, R., Dispersion of Functionalized Carbon Nanotubes in Polystyrene. *Macromolecules* **2002,** *35* (23), 8825-8830.

62.   Sung, Y. T.; Han, M. S.; Song, K. H.; Jung, J. W.; Lee, H. S.; Kum, C. K.; Joo, J.; Kim, W. N., Rheological and electrical properties of polycarbonate/multi-walled carbon nanotube composites. *Polymer* **2006,** *47* (12), 4434-4439.

63.   Fornes, T. D.; Yoon, P. J.; Keskkula, H.; Paul, D. R., Nylon 6 nanocomposites: the effect of matrix molecular weight. *Polymer* **2001,** *42* (25), 09929-09940.

64.   Cox, W.; Merz, E., Correlation of dynamic and steady flow viscosities. *Journal of Polymer Science* **1958,** *28* (118), 619-622.

65.   Dealy, J. M.; Larson, R. G., Structure and rheology of molten polymers. *Hanser, Munich* **2006**.

66.   Mead, D. W., Analytic derivation of the Cox–Merz rule using the MLD "toy" model for polydisperse linear polymers. *Rheologica acta* **2011,** *50* (9-10), 837-866.

67.   Guštin, A.; Zupančič, A.; Mitsoulis, E., Pressure drop estimation for polyamide 6 flow through spinnerets and filters. *Journal of Applied Polymer Science* **2006,** *100* (2), 1577-1587.
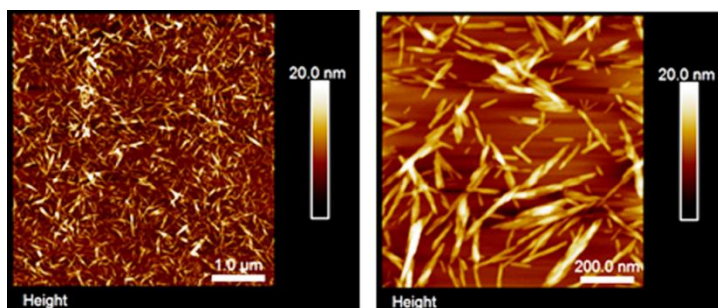
Figure 2.1 AFM images of cellulose nanocrystals prepared by acid hydrolysis
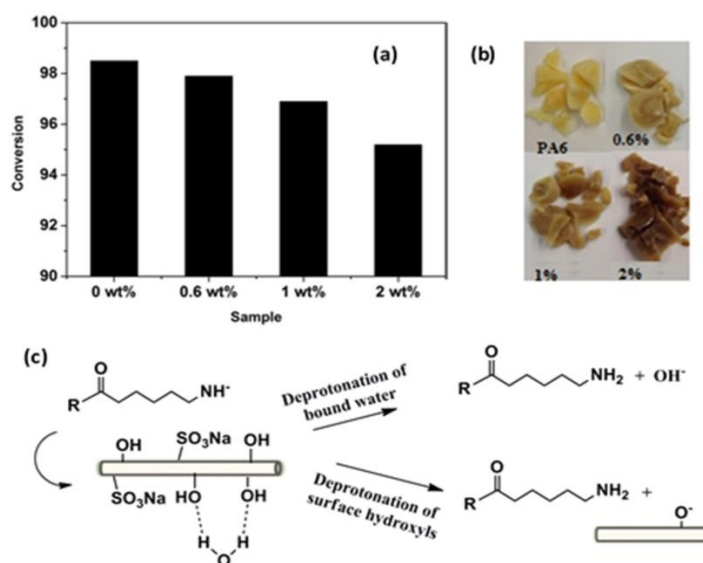
Figure 2.2 (a) Monomer conversion in the composite samples and (b) change in color of the composites with addition of varying CNC contents. (c) Proposed mechanism of termination of propagating anionic centers by proton abstraction
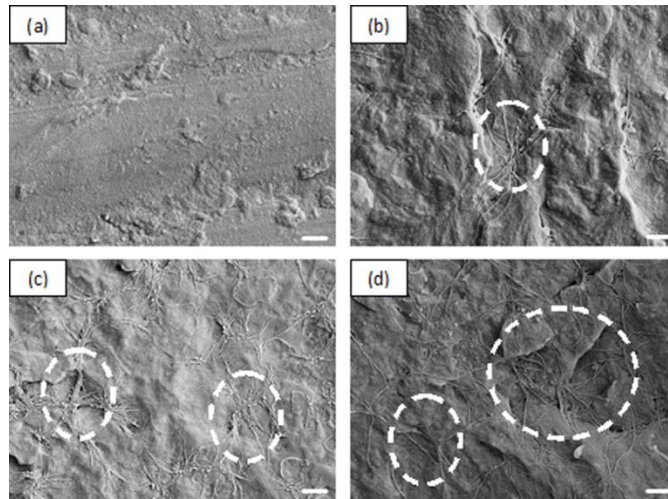
Figure 2.3 Scanning Electron Micrographs of cry-fractured surfaces of (a) PA6, (b) 0.6%CNC, (c) 1%CNC and (d) 2%CNC nanocomposites. (The scale bar shown is 1μm).
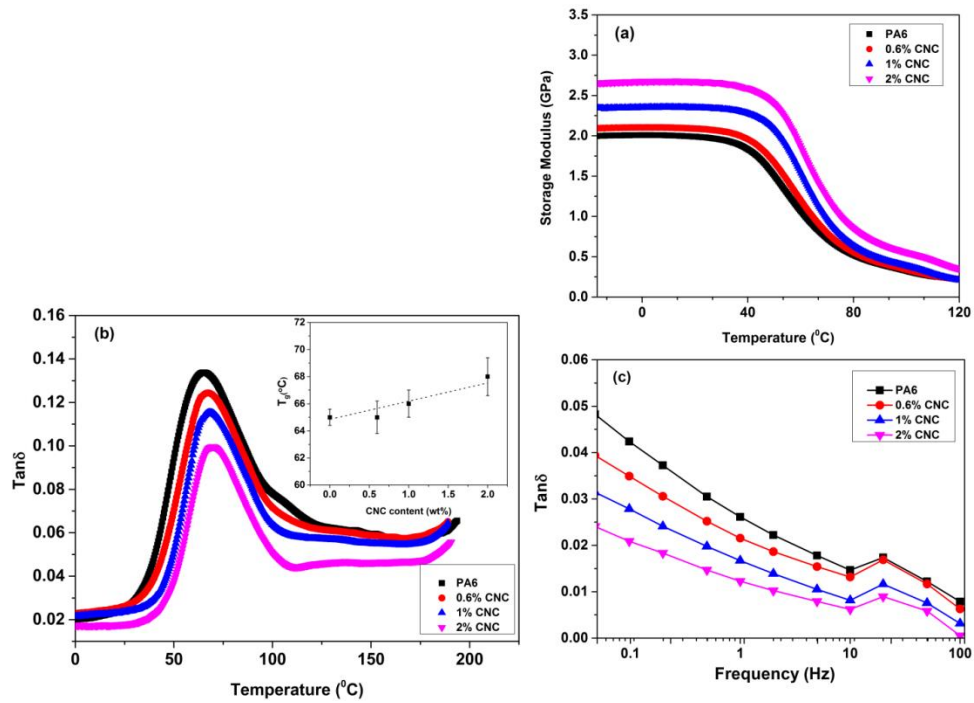
Figure 2.4 Variation of (a) storage modulus with temperature, (b) *tan δ* with frequency and (c) *tan δ* with temperature. Change in glass transition temperature with CNC content (dotted lines) is shown in Figure 4c inserted figure.
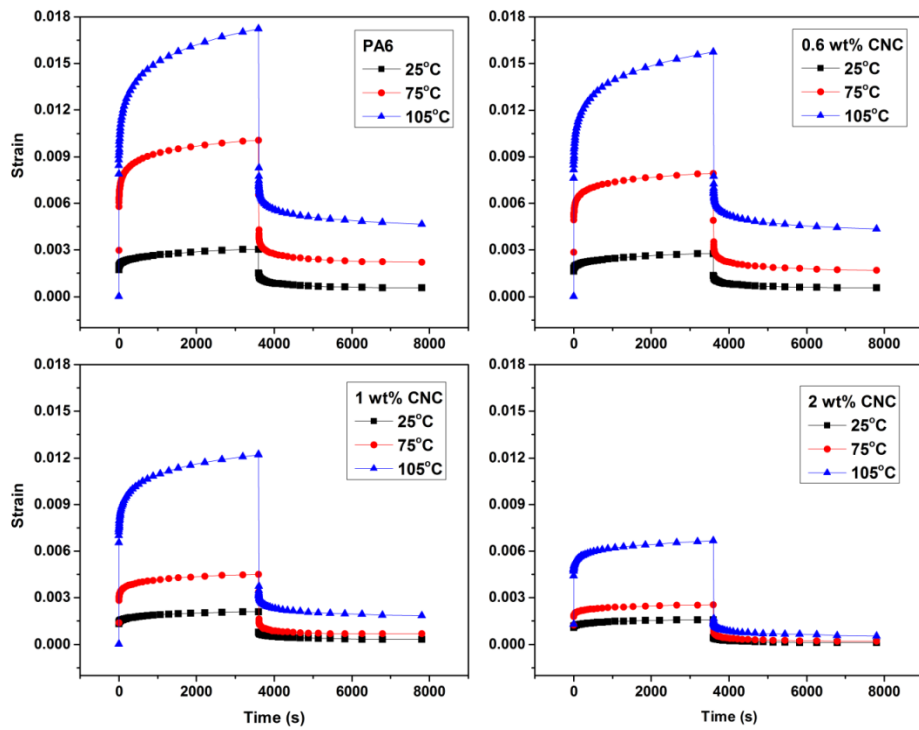
Figure 2.5 Variation of creep strain versus temperature for (a) PA6, (b) 0.6%CNC, (c) 1%CNC and (d) 2%CNC
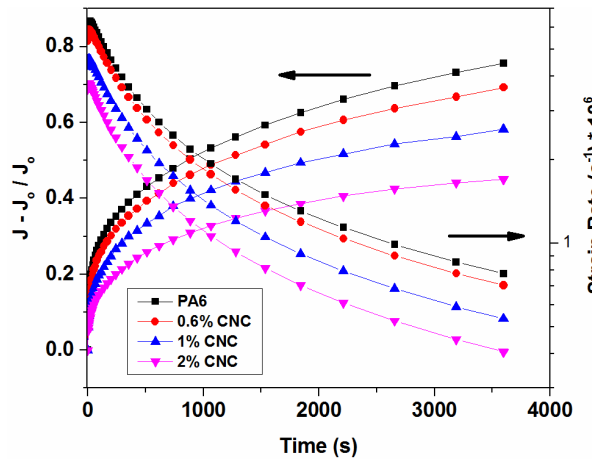
Figure 2.6 Normalized time dependent creep compliance and strain rate for PA6 matrix and PA6/CNC nanocomposites

101
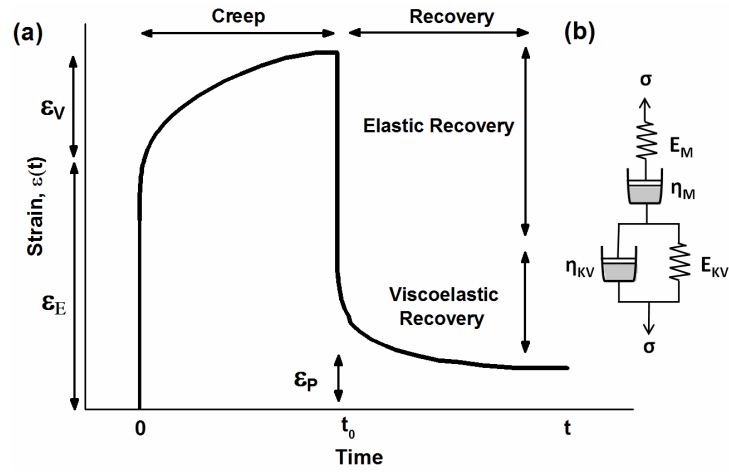
Figure 2.7 A typical creep diagram with three different strain regions and (b) Four-element (Burger's) spring-dashpot viscoelastic model
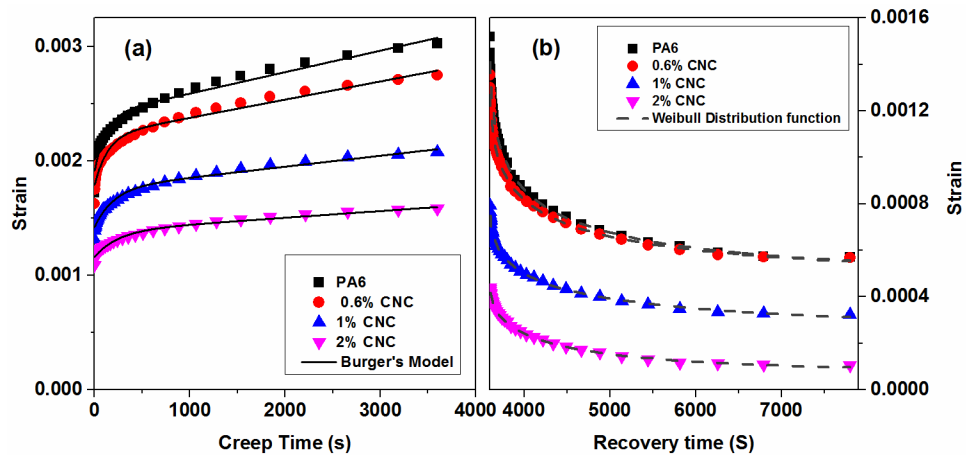
Figure 2.8 (a) Burger's model and (b) Weibull distribution function fit on experimental creep and recovery data
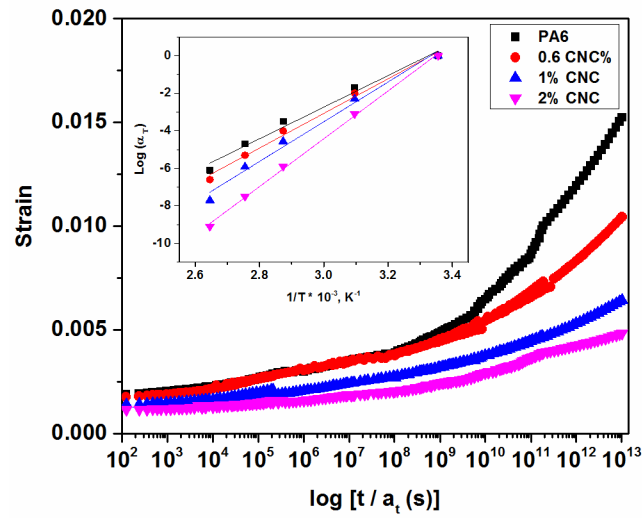
Figure 2.9 Master curves showing the creep strain as a function of time and the horizontal shift factors with the linear Arrhenius equation fit
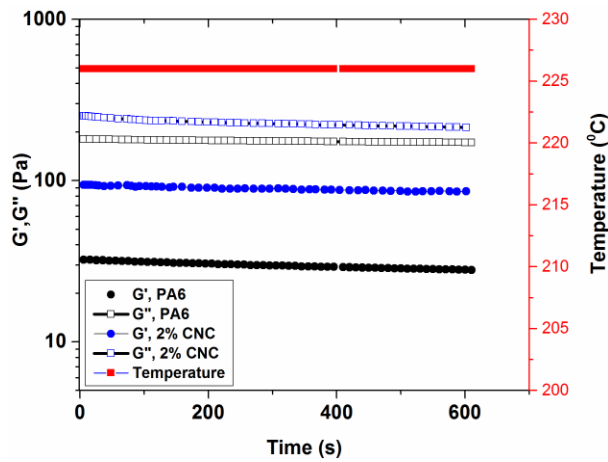
Figure 2.10 Dynamic time sweep experiment showing the variation of viscoelastic properties as a function time at the experimental temperature
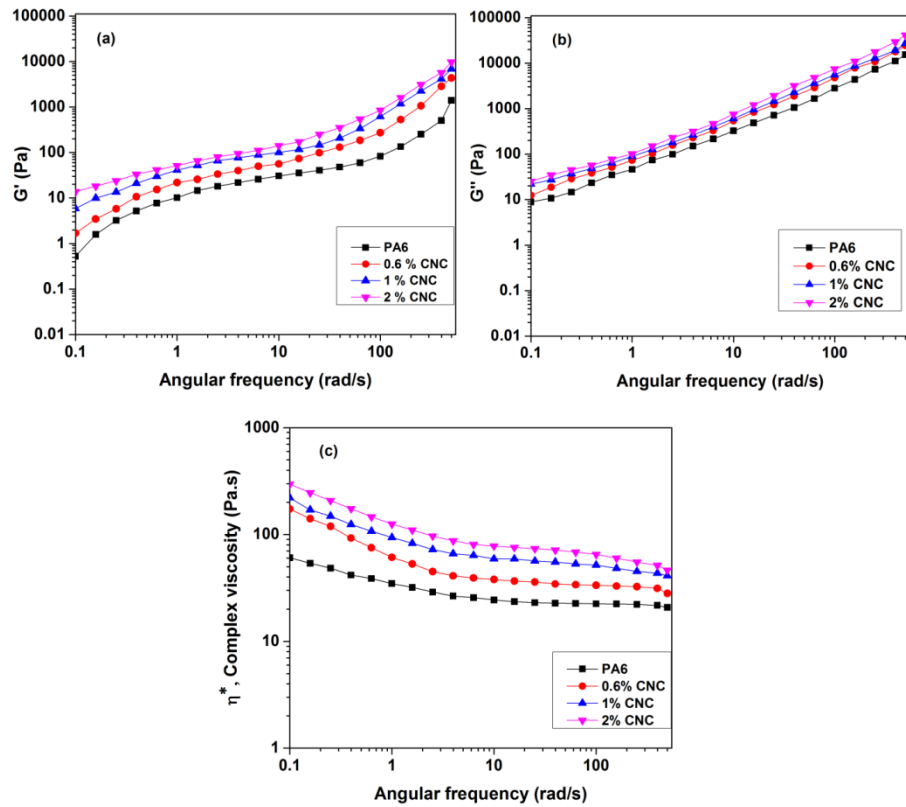
Figure 2.11 Variation of (a)Storage modulus, (b) loss modulus and (c) complex viscosity versus angular frequency for PA6/CNC nanocomposites
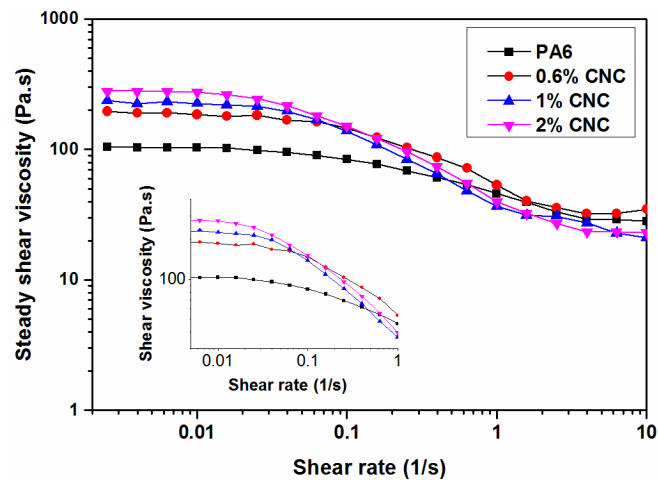
Figure 2.12 Variation of shear viscosity versus shear rate for PA6/CNC nanocomposites

104
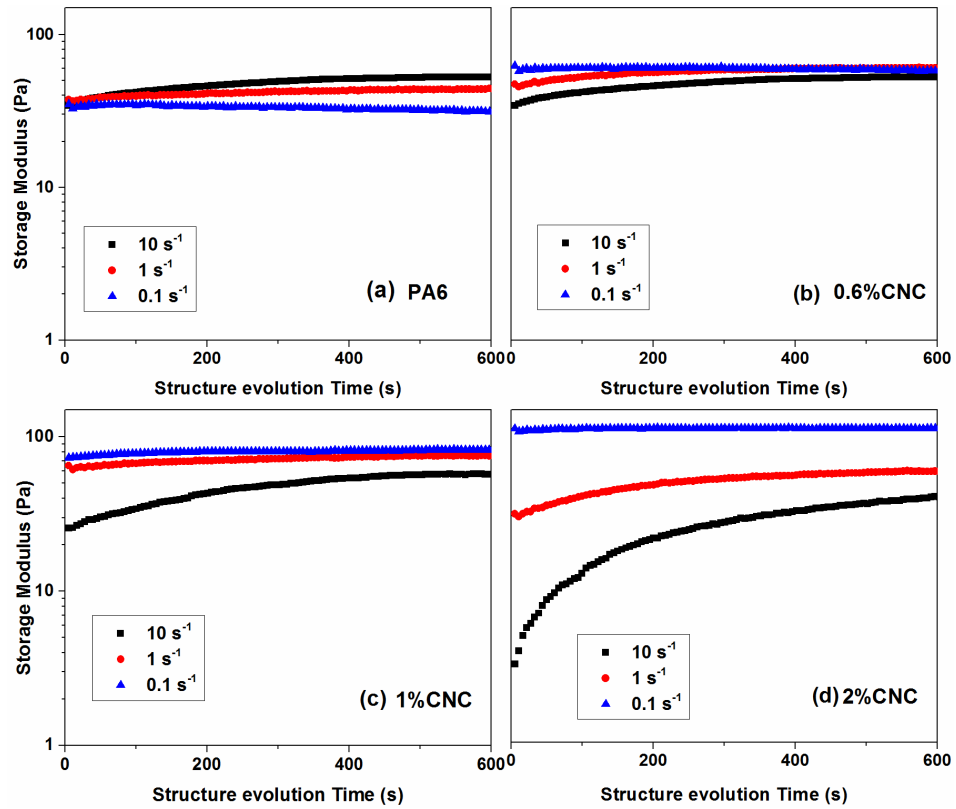
Figure 2.13 Structure recovery after a pre-shearing stage for (a) PA6, (b) 0.6%CNC, (c) 1%CNC and (d) 2%CNC.

Table 2.1

Storage modulus of the nanocomposite samples at 30°C and 80°C as well as the values of the peak temperature and height of the damping factor

Sample/ property	G′ at 30°C (GPa)	G′ at 80°C (GPa)	*tan* δ peak temp (°C)	*tan* δ maximum height
PA6	1.95	0.52	65	0.134
0.6%CNC	1.98	0.45	65	0.124
1%CNC	2.3	0.54	66	0.115
2%CNC	2.6	0.74	68	0.099

Table 2.2

Parameters of Burger's model fit (on creep data) and Weibull distribution function fit (on recovery process)

CNC content (wt%)		0	0.6	1	2
Burger's model (Creep)	E_M **(GPa)**	2.09	2.23	2.81	3.45
	E_{KV} **(GPa)**	8.21	9.34	11.89	14.65
	η_{KV} **(MPa.s)*10⁻⁵**	9.9	12.9	24.2	43.8
	η_M **(MPa.s)*10⁻⁷**	2.1	2.5	4.2	6.8
	τ_d **(s)**	121	137.8	203.1	302.6
Weibull Distribution function (Recovery)	$\mathcal{E}_V$ **(%)**	0.12	0.096	0.058	0.037
	η_r	339.4	390.6	702.7	645.5
	β_r	0.37	0.37	0.41	0.53
	Perm. Def. by model (%)	0.047	0.047	0.024	0.007
	Experimental perm. Def. (%)	0.061	0.057	0.032	0.011

Table 2.3

Terminal slop of storage and loss moduli, zero shear viscosities and terminal slope of structure recovery curves

CNC content (wt%)	Slope of terminal G'	Slope of terminal G"	Zero Shear Viscosity (Pa.s)	$T\infty *10^2$
0	1.46	0.87	118.9	0
0.6	1.26	0.73	176.7	0.02
1	0.95	0.67	226.7	0.9
2	0.72	0.54	283.2	3.8

CHAPTER III – THE ROLE OF PARTICLE SURFACE FUNCTIONALITY AND MICROSTRUCTURE DEVELOPMENT IN ISOTHERMAL AND NON-ISOTHERMAL CRYSTALLIZATION BEHAVIOR OF POLYAMIDE 6/CELLULOSE NANOCRYSTALS NANOCOMPOSITES

Abstract

Polyamide 6 (PA6)/cellulose nanocrystal (CNC) and aminopropyl triethoxy silane (APS) - modified CNC nanocomposites were prepared by *in situ* anionic ring opening polymerization and subsequent melt extrusion. The morphological observation of these hybrid systems revealed that the non-modified nanocrystals developed a network-like fibrillar structure while the APS-modified CNCs were finely dispersed mostly as individual whiskers. The isothermal and non-isothermal crystallization kinetics was extensively studied with emphasis on the effects of CNC surface functionality and the subsequent microstructure development on crystallization behavior of these novel nanocomposite systems. The non-modified CNC particles with corresponding fibrillar microstructure were found significantly hinder the crystallization process and spherultic growth of polyamide 6 chains under both isothermal and non-isothermal conditions. On other hand, the surface modified cellulose nanocrystals with improved sub-micron dispersion enhance crystal nucleation in early stages of crystallization while imposing

opposite effect in later stages of crystallization resulting in development of relatively smaller defective spherulitic structures.

3.1 Introduction

Polyamide 6 (PA6) is one of the most important semi-crystalline engineering thermoplastic materials that has been of great interest both in academic studies and industrial applications due to its superior mechanical strength, chemical resistance towards wide range of solvents and hydrocarbons [1-2] and high stiffness. It is well known that there are two crystalline structures in PA6, the α-type and γ-type polymorphs [3-5]. The α-form is the most thermodynamically stable crystalline form of PA6 consisting of anti-parallel chains connected with the adjacent chains through hydrogen bonds in a planar zig-zag conformation while the γ-form is thermodynamically less stable consisting of pleated sheets of hydrogen bonded parallel chains [6-7].

In the past decade, application of nanomaterials in development of polymer nanocomposites has received much attention in the literature as an effective approach towards controlling the physical and structural properties of the host polymers like their crystallization behavior and properties. These nanomaterial inclusions include layered silicates [8-9], carbon nanotubes [10-11], graphene [12] and silica nanoparticles [13].

Wu et al [14] studied the effect of montmorillonite and saponite nanoparticles on the crystallization behavior of PA6. Their results indicated that the addition of these clay nanoparticles acted as effective heterogeneous nucleating agents in the PA6 matrix at lower clay contents indicated by lower crystallization activation energy. In a reported study by Paul *et al* [15], it was shown that organically modified clay (O-MMT) significantly

reduced the crystallization half time ($t_{1/2}$) of PA6 matrix during non-isothermal crystallization followed by a complicated crystallization mechanism.

Guo and co-workers [16] studied the effect of halloysite nanotubes on non-isothermal crystallization behavior of PA6. Their results revealed that the nanotubes acted as nucleating agents in the PA6 melt while severely restricting the polymer chain mobility. It was also observed that development of γ-phase crystals were significantly promoted in the presence of halloysite nanotubes.

In a series of studies by Li and co-workers [17-18], the effect of carbon nanotubes on isothermal and non-isothermal crystallization behavior of PA6 was investigated. It was found that the CNTs accelerated the nucleation phase as indicated by a shift of onset crystallization temperature towards higher temperatures as well as increased the crystallization half-time. However, it is worthy to note that during the isothermal crystallization, the authors reported a shortened crystallization half-time that points to fast crystallization rate, suggesting special effects of the nanomaterials in the crystallization process under the various conditions studied.

In addition, cellulose based nanomaterials in the form of nanofibers and nanocrystals, as in the current study described in this article, have also been the subject of intense study over the past years for application in polymer composites and nanocomposites due to a number of special advantages of the cellulosic nanomaterials over traditional synthetic fibers and fillers. These advantages include such as having lower density, exceptional mechanical properties, bio-renewability, low cost, and potential environmentally-friendly alternative to conventional fillers [19-20]. In a study [21] on polylactic acid (PLA) composites reinforced with up to 10wt% cellulose whiskers, it was

found that the crystallization of PLA is significantly hindered and the overall

crystallization of the matrix decreased. Han and co-workers [22] studied the role of

cellulose whiskers (CWs) in polyurethane matrix during isothermal crystallization by

using Avrami model and found that the CWs act as nucleating agents during isothermal

crystallization. This effect was validated by lower activation energies of crystallization as

well as shorter half-times of the nanocomposite samples compared to that of the neat

polyurethane matrix. Siqueira et al [23], in a comprehensive reported study of the effect of

the shape of the cellulose nanoparticles in the form of micro-fibrillated cellulose (MFC)

and CWs on the crystallization behavior of poly (ε-caprolactone), showed that both

MFCs and CWs can accelerate the crystallization kinetics by acting as nucleating agents

under isothermal crystallization condition. In addition, the lamellar growth rate analysis

showed that the MFC, and to a lesser extent, the CWs restricted the chain mobility and

the lateral growth rate of the spherulites. On the other hand, other authors reported

increase in relative crystallinity with addition of nanocellulose. For example, recent

reported studies on polyvinyl alcohol reinforced with MFCs either cast from solution [24]

or in the form of spun fibers [25] showed an increase in the degree of crystallinity in the

composite samples compared to that of the neat matrix.

By contrast, studies on the properties of high melting point engineering

thermoplastics such as polyamide 6 reinforced with nanocellulose has been limited due to

the thermal degradation of cellulose at typical temperatures of direct melt mixing process

that reduces the effectiveness and functionality of cellulose in the matrix. A recent study

by Kiziltas et al [26] showed that incorporation of microcrystalline cellulose (MCC) into

polyamide 6 matrix (processed with the aid of lubricant) reduced the overall crystallinity

of the matrix upon addition of 2.5-30 wt% of MCCs. The authors just mentioned also reported that the onset and peak crystallization temperature of the PA6 was shifted towards relatively larger values. However, the analysis of the non-isothermal crystallization of these systems via Avrami and Tobin models, showed no significant changes suggesting a poor nucleation activity of the MCC in the PA6 matrix.

In a previous study, we adopted a novel approach of *in-situ* Ring-Opening polymerization technique to incorporate cellulose nanocrystals (CNCs) in a PA6 matrix that gave PA6/CNC nanocomposites with improved properties such as superior physical and melt property, enhancement obtained even at very low concentration of CNCs reported in our previous publication [27]. This strategy enabled the CNCs to be incorporated in the PA6 matrix prior to processing at temperatures far below the melt processing temperature of the PA6, significantly minimizing the CNC thermal degradation and improving the CNC dispersion in the PA6 in a subsequent melt processing step. The current study described in this article reports a detailed analysis of the crystallization behavior and kinetics under both isothermal and non-isothermal conditions with specific focus on the effects of CNC surface modification and microstructure evolution in the PA6 matrix, and the results interpreted according to reported polymer crystallization models in the literature.

3.2 Experimental

3.2.1 Materials

The caprolactam monomer used in this study is AP-Nylon® caprolactam grade (purchased from Brueggemann Chemical, Pennsylvannia) with low moisture content (< 100 ppm) suitable for anionic ring-opening polymerization. C20, a difunctional

hexamehtylene-1,6- dicarbamoyl caprolactam (the ROP activator), was supplied by

Brueggemann Chemical. Ethylmagnesium bromide (3.0 M in diethyl ether solution) used

as the initiator was purchased from Aldrich. Aminopropyl triethoxy silane (APS) was

purchased from Gelest Inc.

3.2.2 Samples Preparation

The cellulose nanocrystals were prepared by sulfuric acid hydrolysis of bleached

cellulose paper (obtained from Weyerhaeuser) following the method reported by

Capadona *et al* [28] with some modifications. The cellulose paper was cut into small pieces

and blended with de-ionized water (20 g/L) to achieve a "lumpy" cellulose pulp followed

by placement in a glass reactor in an ice bath. Concentrated sulfuric acid (98%) was

slowly added to the cold suspension at 35 v/v% of acid in the total suspension. The

mixture was then heated to 50ºC and stirred for 3.5 hr. The obtained suspension was

subsequently quenched with a 10-fold excess of de-ionized (DI) water and filtered over

fine fritted glass filter and washed slowly with DI water until the running water showed a

pH of ~5-6. The resulting mixture was decanted to remove the unhydrolyzed fibers and

then centrifuged (5 cycles) at 3000 rpm for 10 minutes to concentrate the CNCs. The

nanocrystals were recovered by freeze-drying of the suspension and were neutralized

with 2mM NaOH solution to convert the surface sulfonic acid groups to sodium salt

(indicated by pH neutrality of the CNC dispersions). The obtained neutralized CNCs

were dried overnight to constant weight in a vacuum oven at 90°C prior to preparation of

the nanocomposite samples.

Surface modification of CNCs was carried out using amino propyl triethoxy

silane (or APS). Briefly, a suspension of CNC was prepared in DI water with first mixing

the CNC followed by sonication for 20 minutes. In a separate flask, the APS was added (7 wt% of the CNC) to DI water and mixed for 10 minutes in order to hydrolyze the ethoxy groups into hydroxyls. These separate mixtures were mixed and the final dispersion was allowed to mix for 3 hours under continuous agitation. The dispersion was then frozen in liquid nitrogen and freeze dried for at least 60 hours to recover the CNC powder with APS adsorbed on the surface. Finally, the polycondensation of APS with the CNC surface hydroxyl groups was carried out in vacuum oven at 120°C under vacuum for 1 hour.

The PA6/CNC nanocomposites were prepared by *in situ* ring-opening polymerization of caprolactam monomer in the presence of CNCs. For this purpose, pristine and surface modified CNCs were dispersed in the monomer at 1, 2 and 3 wt% CNC concentrations by high-speed agitation and sonication for 25 minutes at 90°C. This mixture was blended with another master-batch of the activated monomer containing the initiator and activator and the resulting dispersion was infused and polymerized at 150°C for 30 minutes in a disk shaped mold under vacuum. The nanocomposites are named here as x% CNC where 'x' denotes the CNC content in weight percent. The prepared PA6/CNC nanocomposite plates were cut and granulated into small pieces that were dried in a vacuum oven. Subsequently, the nanocomposite granules were melt processed in a second stage at 230°C in a Thermo Haake® minilab micro-compounder (co-rotating conical screws) in the recycle mode for 200 seconds at 120 rpm under inert atmosphere to minimize the thermo-oxidative degradation of CNC.

3.2.3 Microscopy

Scanning Electron Microscopy images were acquired using a Sigma field-emission scanning electron microscope (ZEISS®, USA) using a 5 kV accelerating voltage. Images were taken from the smooth surface of the cry-fractured samples coated with silver for enhanced conductivity.

Polarized optical micrographs were taken using a Nikon Optihot2® optical microscope equipped with a Metler Toledo® hot stage. The cooling rate used for observation of isothermal crystallization from the melt phase was the maximum rate (i.e., 60°C/min) accessible by the instrument used. A blue filter was used for enhanced optical clarity. For POM images taken at nucleation phase, microtomed samples were used while for observation of the fully grown crystals, thin films of about 70-80 μm was prepared by compression molding. Samples were heated to 250°C to clear the thermal history, cooled to crystallization temperature of 200°C followed by isothermal for 45 minutes and cooling to room temperature with the same cooling rate.

3.2.4 Thermal Characterization

Crystallization and melting of the obtained PA6/CNC nanocomposites were studied using a Perkin Elmer Pyris Diamond DSC under inert nitrogen atmosphere. All the samples used were 7.5±0.2 mg (pre-dried overnight to constant weight in vacuum oven prior to measurements) cut into a disk shape and placed in the aluminum pans to minimize the effect of uneven thermal conduction. Special care was taken to obtain similar geometry and thickness for all the tested samples. In order to measure the melting point and crystallinity, the samples were heated at 10°C/min up to 240°C followed by cooling to 25°C and re-heated at 10°C/min to 230°C so that the first and second heat runs

could be obtained. In the isothermal crystallization studies, the samples were first heated up to 240°C at 10°C/min and held for 4 minutes at this temperature in order to erase all previous thermal history followed by rapid quenching at 150°C/min to crystallization temperatures of 194°, 197° and 200°C, respectively. Note that the samples were respectively held at these temperatures until no change in heat flow was recorded over time. The kinetics of isothermal crystallization was studied based on the evolved exothermic enthalpy recorded in this isothermal step.

In the non-isothermal crystallization studies, samples were first heated up to 240°C at 20°C/min and held for 4 minutes followed by cooling at four different cooling rates of 5°, 10°, 15° and 20°C/min. The kinetic study is based on exothermic enthalpy evolved during cooling. All the DSC experiments of this study were performed under inert dry nitrogen atmosphere to prevent thermo-oxidative degradation of the experimental samples. Thermal stability of the samples was verified by thermogravimetric analyses runs prior to DSC experiments.

3.2.5 Solid State ^{13}C NMR analysis

^{13}C NMR spectra were obtained using a Bruker AVANCE I 400 (9.6 T) NMR instrument using a 4 mm broadband MAS Probe. Samples were packed in 4 mm rotors. All spectra were obtained at room temperature and spinning at 6 kHz for ^{13}C. The CPMAS T1 filter NMR spectra were obtained using a 5s recycle delay, a CP contact time of 2 ms, and T1 delay of 5s to emphasize rigid crystalline regions with longer relaxation times (tens of seconds) and to filter out amorphous mobile regions with short relaxation times (< one second). The delay times were chosen as optimal and found to give

117

reproducible results. The ^{13}C chemical shift was referenced to the carbonyl resonance (δ = 176 ppm) of the secondary standard glycine with respect to TMS δ = 0.0 ppm.

3.3 Results and Discussion

3.3.1 Morphology and Microstructure

The observed changes in the morphology and microstructure of the samples as a function of the CNC surface functionalization are discussed to understand the influence of the latter on the observed crystallization behavior of the nanocomposites. Figure 3.1 shows the SEM images of the cryo-fractured surfaces of the neat PA6 and the nanocomposites containing 3% of CNC and APS-CNC.

Clearly, this figure shows that the neat PA6 matrix shows a featureless surface morphology depicted in Figure 3.1(a). In the case of 3%CNC sample, it is evident that the whisker-like cellulose nanocrystals (CNCs) form a microfibrillar-type structure where the bundles of the CNC comprising of interconnected whiskers through edge-to-edge interaction are dispersed in the matrix with a 3D network structure. In a previously reported study on these PA6/CNC nanocomposites systems [27], we observed the network structure development in these systems using melt rheological techniques. Here, it is seen that in the case of the APS-surface modified CNC (or APS-CNC), the dominant morphology is a dispersion of the individual whiskers homogeneously dispersed at the nano-scale within the matrix (see Fig. 3.1(c)). The observed superior dispersion of the APS-CNC in the PA6 is ascribed to excellent interfacial compatibility with the PA6 matrix due to the presence of amino groups on the APS-CNC surface. The interfacial bond formation is expected to proceed through transamidation reaction between the amide bond on the PA6 chain and the surface amino group of APS layer at the elevated

118

processing temperatures used for sample preparation [29-30]. A similar type of morphology was observed for the samples containing 1 and 2 % of both CNC and APS-CNC (not shown). The relationship between these observed micro-structural features and the observed crystallization behavior is discussed in detail in the current article.

3.3.2 Thermal Properties

The melting behavior of the melt processed samples was studied via similar simulated thermal history in the DSC in both the first and second heat runs (the heating and cooling rates were both 10°C/min) in order to obtain the crystallinity data of the processed samples. The obtained data from both heating runs are shown in Figure 3.2.

From these figures, the melting points and degree of crystallinity were extracted from an average of at least 3 replicates and the obtained results are summarized in Table 3.1. It is known that pure PA6 has two major crystalline forms, namely the α- and the γ-crystalline forms where the more thermodynamically stable α-form is comprised of monoclinic cell with a relatively more ordered structure and higher melting point compared to that of the less ordered γ-form with relatively lower melting point. It can be seen in Table 3.1 that in the first heating runs, the predominant crystal structure of PA6 samples and that of 1 and 2% of CNC are α-type crystals while a portion of γ-type crystals are observed to develop in the samples with 3%CNC and 3% APS-CNC.

Interestingly, in the second heat runs all the samples including the neat PA6 reveal a certain amount of γ-type crystals with a relatively very large portion of this γ-crystalline structure that appears to be the dominant crystal form in the case of APS-CNC nanocomposite samples. Note that the α-type crystal is evident as a shoulder peak in the low melting point range of the γ-type crystal melting point. In other to further verify this

observed change in the characteristics of the crystalline structure, we performed solid

state 13C NMR analysis on the samples and the results obtained are presented in Figure

3.3. From the structure of the repeating unit of the PA6 polymer, the peak at 43.5 ppm

corresponds to the C1 carbon atom (i.e., nitrogen neighbor) and the peak at around 30

ppm is attributed to the C2 and C3 carbon atoms, while the peaks at 26.5 and 37 ppm are

respectively ascribed to C4 and C5 carbon atoms. The C1 and C5 carbons appear at 43.5

and 37 in α-polymorph while the corresponding peaks of these carbons in γ-polymorph

appear at around 40 and 34 ppm 31. The NMR spectra of these two samples depicted in

Figure 3.3 clearly shows that in the case of 3%CNC sample, the major crystalline peaks

of C1 and C5 carbon atoms are appeared at the typical positions of α-type crystal. By

contrast, in the sample with 3%APS-CNC, two smaller peaks observed at 34 and 40 ppm

that are exactly located at the positions of C1 and C5 of γ-type crystalline regions.

Therefore, it can be concluded that the solid state NMR results conformed well to the

observed evolution of γ-type crystals when the CNC particles are surface modified with

APS and found to be consistent with DSC thermograms already discussed.

The obtained DSC data in Table 3.1 show that the major melting point

corresponding to α-type (T_{m1} corresponds to α-type and T_{m2} corresponds to γ-type

crystals) of the first heating process decreased as the CNC content was increased, This

observation combined with the observed reduction in the overall absolute degree of

crystallinity ($\chi_c = 100*\Delta H_m/(1-m)\Delta H_0$ where 'm' is the mass fraction of CNC) in the

nanocomposite samples suggests that the presence of CNC whisker particles hinders the

crystallization of the PA6 matrix chains thereby reducing the overall crystallinity. Note

that the major melting points of the crystals are observed to decrease as the CNC content

is increased (see Table 3.1). This observed behavior is consistent with that reported in the literature for high aspect ratio and high performance nano-additives in PA6 samples such as silicates [32] and graphite sheets [33]. A similar trend to the one just described was observed in the case of APS-modified CNC particles with a slight increase in both the T_{m1} and degree of crystallinity.

The DSC data obtained from the second heating runs of the samples reveal similar crystallization trend where the observed shoulder peak on the APS-CNC samples (corresponding to the α-type crystal) shows a relatively higher melting point compared to that of the non-modified CNC samples (see Table 3.1). In addition, there is a slight increase in the overall degree of crystallinity in the APS-CNC compared to that of the pristine CNC/PA6 nanocomposite samples. For example, the 3%APS-CNC composite sample shows 24.4% of crystallinity compared to a value of 23.1% for the 3%CNC sample. Therefore, it is conjectured that the slight enhancement of crystallinity compared to that of the non-modified CNC is due to the competition between the promotion of crystallinity that is caused by the surface functionality of APS-CNC and the counteracting inhibitive effect on the crystal growth. These results indicate that the APS surface modification of the CNC and the associated improved dispersion of the APS-CNC strongly influence crystallization of the nanocomposites of this study and can, therefore, be used as in the current study to control the crystallization with enhanced benefits. The observed crystallization process in both the isothermal and non-isothermal modes are analyzed in details in the following sections to better understand the role of the effects just mentioned.

3.3.3 Theoretical Analysis of Isothermal Crystallization

In order to study the isothermal crystallization kinetics, the heat release during the process was monitored. A typical thermogram showing the isothermal crystallization exotherm at 194°C is shown in Figure 3.4(a). Clearly, this figure shows that addition of pristine CNC particles tends to move the exotherm towards longer crystallization times. However, an opposite effect is observed in the case of APS modified CNC particles where the crystallization process occurs relatively faster than that of the PA6 sample, suggesting as expected that the surface functionality of the CNC particles greatly changes the isothermal crystallization behavior of PA6/CNC nanocomposites.

The kinetics of isothermal crystallization process can be studied by monitoring the variation of the relative degree of crystalline conversion at a constant crystallization temperature over time. The values of the relative degrees of crystallinity, X_c (t), can be obtained from the area under the exothermic peak of isothermal crystallization in the DSC thermogram at time t divided by the total area under the exotherm as shown in equation (3.1)

$$X_c(t) = \frac{\Delta H_t}{\Delta H_\infty} = \frac{\int_0^t \left(\frac{dH}{dt}\right) dt}{\int_0^\infty \left(\frac{dH}{dt}\right) dt} \tag{3.1}$$

The X(t) values can then be converted into the volumetric fractional crystallinity using the following equation [34]:

$$V_c = \frac{X_c}{X_c + \left(\frac{\rho_c}{\rho_a}\right)(1-X_c)} \tag{3.2}$$

The variation of the volumetric fractional crystallinity is plotted against time (at three different crystallization temperatures) in the Figures 3.4(b)-(d). These figures show that as the temperature of crystallization increases, the curves are shifted towards higher

crystallization times, indicating that the rate of crystallization decreases as the temperature is increased from 194°C to 200°C. It is also evident in Figure 3.4 that the curves follow a sigmoidal "S" shape pattern. Initially, the slope of the curve increases and as the time of crystallization progresses, the slope decreases at the later stages of crystallinity indicating a secondary crystallization process followed by the plateau region corresponding to the crystal impingement.

The Johnson-Mel-Avrami-Kolmogorov (or *JMAK)*(or simply Avrami) model has been successfully used in order to describe the kinetics of solid state phase transformations [35]. In the context of isothermal crystallization process, this theory describes the time dependence of fractional crystallinity using the following equation (3.3) [36]:

$$1 - V_c(t) = exp(-kt^n) \tag{3.3}$$

where the $V_c(t)$ is the volumetric fractional crystallinity at time t. K is the Avrami rate constant containing the contribution of both nucleation and growth, and n is the Avrami index which is related to the geometrical features of the spherulitic crystal development and is usually a value between 1 to 4. Equation 3.4 is a form of the Avrami equation written in the double logarithmic format as follows:

$$\log[-\ln(1 - V_c(t))] = logK + n\log t \tag{3.4}$$

If the Avrami model is applicable to the data, fitting of this model to the data should yield a straight line from which the Avrami exponent and rate constant can be respectively obtained from the slope and intercept of the line. The Avrami fit to the obtained data from PA6, 3%CNC and 3%APS-CNC samples are shown in Figure 3.5 (for all samples, $R^2 \geq 0.99$). It can be seen from the curves of the Avrami plots that three

sections with different slopes can be distinguished; an initial stage from the beginning of the crystallinity until 10-20% crystallinity followed by a secondary phase with a higher slope that extends to near 75% crystallinity. This last stage is then followed by a final phase of crystallization with significantly lower slope due to the secondary crystallization and crystal impingement. Interestingly, the shape of the curves is observed to be different in the case of the nanocomposites samples especially those containing the 3%CNC and 3%APS-CNC.

Unlike the PA6 sample, the nanocomposites show negligible secondary crystallization indicated by the absence of the distinctive roll-off behavior at the end of the fitted line (later stages of crystallinity). This observed behavior is ascribed to the strong steric hindrance due to the physical presence of the solid CNCs and the strong interaction and interfacial chemical bond (in the case of APS-CNC sample) that restricts the PA6 macromolecular chain movement into crystalline regions.

The Avrami parameters are obtained from the fits to the experimental data and are shown in Table 3.2. As previously reported by Zhou and coworkers [37] the Avrami exponent "n" is composed of two terms:

$$n = n_n + n_d \tag{3.5}$$

where n_n represents the contribution of the nucleation process in the Avrami constant. The value of n_n is either 1 (in the case of homogenous nucleation) or 0 (in the case of heterogeneous nucleation). However, since in most cases, the nucleation process involves both the homogenous and heterogeneous nucleation, the value is usually between 0 and 1 which explains the common non-integer Avrami exponent seen in many systems. The n_d is related to the morphology and dimension of the crystal growth; and in

124

the case of polymers it usually takes the integers 1, 2 or 3. The number 3 denotes a 3D

spherulitic growth while a reduction of the integer to 2 and 1 signal the epitaxial growth

of two dimensional lamellar structures or defected spherulites. In addition, the Avrami

exponent predicts the dependence of nucleation on time which in turn depends on the

heterogeneity of the nucleation.

Because the nucleation process in filled polymer systems is a relatively

complicated process with a combination of both homogenous and heterogeneous

nucleation types, the overall Avrami exponent, takes non-integer values as depicted in

Table 3.2. The obtained Avrami exponents are found to vary between 3 and 4 for the neat

PA6 and the sample with 3%CNC, indicating a spherulitic morphology of the crystals.

However, the n exponent decreases in the case of samples filled with pristine CNC

particles compared to that of the PA6 sample. This shows the evolution of imperfect

spherulites that tend towards epitaxial growth (i.e., reduction of n value toward values

less than 3).

A similar effect is evident when the CNC concentration is increased from 1 to

3wt%, showing that at higher concentration of CNC whiskers, the crystal growth

mechanism is confronted with less free volume due to the presence of CNCs and

restricted molecular motion. In the case of CNC whiskers with APS surface functionality,

the Avrami exponent decreased even further and eventually to values less than 3 in the

case of 3%APS-CNC sample. In a similar analogy, the formation of interfacial bond

during the course of polymerization/melt extrusion is conjectured to further restrict the

PA6 macromolecular chain motion especially in the interfacial area. In addition, the

nanoscale dispersion of individual whiskers as seen in the SEM images of this sample

already described, suggests that the increased overall interfacial area between the matrix and the surface of the CNC particles have significant effects on the dimensionality of the crystals leading to the formation of 2D structures with less crystal perfection as already mentioned.

Another important parameter in the Avrami equation is the Avrami crystallization parameter or K which is related to both the nucleation and growth rate [14, 38]. The current study shows that with increasing temperature of crystallization this parameter decreases, implying a relatively slower overall nucleation and growth rate at typical elevated temperatures. However, with addition of the CNC whiskers, opposite effects are observed in samples containing pristine CNC and APS-CNC samples. Specifically, the pristine CNC particles tend to decrease the K values, indicating a slower nucleation and growth rate while the APS modified CNCs increase the K value (see Table 3.2). This observed experimental fact that the APS modified CNC particles increase the nucleation and crystal growth rate is thought to be related to the occurrence of heterogeneous nucleation where, in fact, in these samples the solid CNC whiskers act as effective nucleating agents. Because there is a competing effect of both the nucleation process and crystal growth rate retardation, it is evident that in the case of the samples containing pristine CNC particles, the crystal growth rate retardation is the dominating effect especially considering the fibrillar network-like microstructure in these samples as shown in the SEM images already described. For example, at lower temperature when the nucleation is faster than crystal growth, the K value shows a slight increase as the CNC content increases from 1 to 3wt% while it remains smaller than that of the neat PA6. In a previously reported study on the non-surface modified CNC/PA6 nanocomposite systems

[27] we showed that the viscosity of the PA6 matrix can be significantly increased with a very small volume fraction of CNC whiskers. Therefore, the increased viscosity can clearly slow down the transfer of new chains into the growing crystals. On the other hand, in the case of APS-modified samples, the crystal nucleation effect is more pronounced as indicated by an increase in the K value while the lower Avrami exponent (crystal growth dimensionality) shows significant restrictions on crystal growth. Consequently, it can be argued that while the APS-CNC particles tend to promote nucleation of crystals, they also can impose a crystal growth hindrance at the same time. These overall competing effects are deconvoluted and explained further later in more detail in the theoretical analysis of the non-isothermal crystallization data.

Another parameter shown in Table 3.2 is the crystallization half-time or $t_{1/2}$ which is the experimental time required to reach 50% relative crystallinity. The data presented in this table shows that the crystallization half-time increase with increasing temperature, indicating relatively slower crystallization rates at elevated temperatures. With the addition of the pristine CNC, the crystallization half-time increased compared to that of the neat PA6, and decreased further as the CNC concentration was increased. This observation shows that the overall nucleation and growth phenomena are taking place at relatively lower rates when the non-modified CNC whiskers are incorporated into the matrix. By contrast, the samples containing the APS-CNC particles show a decrease in the crystallization half-time that again confirms the significant heterogeneous nucleating effect of these particles that outweighs the crystal growth retardation effect of particles especially at earlier stages of crystallinity as already described.

The data obtained from the isothermal crystallization experiments can be evaluated in the context of Lauritzen-Hoffman (LH) crystal growth theory [39-40] to obtain comparative kinetic parameters of crystal nucleation and growth process for the neat PA6 with that of nanocomposites with 3wt% of pristine CNC and APS-CNC. According to this LH secondary nucleation theory there are two major processes that govern the crystal growth. These processes are the secondary nuclei deposition followed by polymer chain transport and lateral growth along the face where the secondary nuclei were established. Depending on the relative rates of secondary nuclei formation (i) and lateral growth rate (g), three different regimes exist where $i<<g$ (regime I), $i\sim g$ (regime II), and $i>>g$ (regime III).

The growth rate of the crystal can be approximated with the reciprocal crystallization half-time as $G=(t_{1/2})^{1/2}$ where the half-time was calculated from the isothermal crystallization exotherms as already discussed in the previous section. Subsequently, the energetics of the process can be described using the Hoffman equation as follows:

$$G = G_0 \exp\left[-\frac{U^*}{R(T_C-T_\infty)}\right] \exp\left[-\frac{K_g}{T_C \Delta T f}\right] \qquad (3.6)$$

where the G_0 is the pre-exponential term, U^* is the diffusional activation energy for the transport of the crystallizable segments at the melt-crystal interface with a universal value of 1500 cal/mol, T_C is the crystallization temperature, T_∞ is the temperature below which the viscous flow of the polymer ceases which is commonly taken as (T_g - 30° K), f is correction factor to account for the change in the enthalpy of fusion of perfect crystal with the temperature which is taken as $2T_C/(T_m^0+T_C)$ where the T_m^0 is the equilibrium melting point, ΔT is defined by $T_m^0-T_C$, K_g is the nucleation

128

parameter that is related to the necessary free energy to form critical sized nucleus, and R is the gas constant. In this study, the Hoffman-Weeks approach [41] was adopted to find the equilibrium melting point of the neat PA6 and the 3% nanocomposite samples containing pristine CNC and APS-modified CNC that were crystallized at four different temperatures of 194°, 197°, 200° and 203°C, and subsequently heated above the corresponding melting point. The obtained Hoffman-Weeks plot is shown in Figure 3.6(a). The mathematical relationship between the crystallization temperature, melting temperature and the equilibrium melting temperature is described according to the following equation (3.7) [14]:

$$T_m = T_m^0 \left(1 - \frac{1}{\gamma}\right) + \frac{T_C}{\gamma} \tag{3.7}$$

where the γ is a parameter related to the final lamellar thickness. In this plot, a straight line is fitted on the T_m versus T_C data and the intersection with the $T_m = T_C$ line gives the equilibrium melting point as shown in the insert data of Figure 3.6(b).

The obtained equilibrium melting points for the PA6, 3%CNC and the 3% APS-CNC are 231.9°, 229.6° and 227.6°C as indicated in the Figure 3.6(b). It should be noted that for the APS-CNC system, the second melting point corresponding to the α-type crystals are considered. The obtained values for the equilibrium melting points are in good agreement with those previously reported for PA6-based systems [14, 33, 42].

Now using the obtained T_m^0 values obtained, the Hoffman equation can be re-arranged in the following format:

$$\ln G + \frac{U^*}{R(T_C - T_\infty)} = \ln G_0 - \frac{K_g}{T_C(\Delta T)f} \tag{3.8}$$

This equation is plotted for the neat PA6, 3%CNC and 3%APS-CNC samples in Figure 3.6(a) that shows a good linear fit to the experimental data; and from the slope of the lines the nucleation parameter (or K_g) can be obtained. This K_g parameter contains contributions from the folded and lateral surface energies according to the following equation (3.9) [23]:

$$K_g = \frac{mb\sigma\sigma_e T_m^0}{\Delta H_f^0 . k_B} \tag{3.9}$$

where b is the distance between the two adjacent fold planes which in our case corresponds to the α-type crystal with a monoclinic cell structure with lattice parameters of (0.956nm x 0.801nm x 1.72nm) [16], σ and σ_e are respectively the lateral and folded surface energies, ΔH_f^0 is the enthalpy of fusion of a perfect crystal of PA6 equal to 190 J/g [43], k_B is the Boltzman constant and the m is an integer with a value of 2 in the case of regime II and 4 in the case of regimes I and III. Here, a value of $m = 2$ is used as will be shown later that the obtained data correspond to the regime II of crystallization using a Z-test. However, it should be noted that the unit cell values are assumed to be similar because the content of CNC is low in the PA6 matrix like other researchers have reported in the literature in a number of previous studies [14, 43]. From the values of σ and σ_e, the work of chain folding denoting the energetics of the crystallizing chain to fold back into the lamella is obtained using the following expression:

$$q = 2ab\sigma_e \tag{3.10}$$

The results and values of this analysis are tabulated in the Table 3.3. As can be seen from this table, the value of the nucleation constant slightly increases in the case of 3%CNC samples which correlates with the longer half times obtained in the Avrami

analysis already described while for the 3%APS-CNC the K_g values is significantly

decreased. The slight increase in the case of 3%CNC is somewhat contradictory to what

one would expect from a secondary nucleation role of a solid surface as a number of

previous studies have shown that clay [8] and carbon nanotubes [38] nanoparticles can act as

effective nucleating agents in PA6 matrix thereby promoting secondary nuclei formation.

It has also been reported in the literature that CNC whiskers can effectively

promote the nucleation of crystals in poly(caprolactone) [23] and PLA [44]. On the other

hand, in a recent study by Guo et al [16] the Lauritzen-Hoffman analysis on a PA6 system

reinforced with halloysite® nanotubes showed an increase in the K_g parameter with

addition of the nanoparticles which was interpreted to be related to the inhibitive effect of

strong interactions between the nanotube surface and PA6 chains. In the current

PA6/CNC nanocomposite system, it is conjectured that the strong hydrogen bonding

interaction between the PA6 and the hydroxyl-rich surface of cellulose whiskers and the

microfibrillar microstructure that was developed in the case of non-treated CNC imposes

a significant restriction on the molecular motion of the PA6 chains that results in the

slow-down in the crystallization process. This explanation is consistent with a previously

reported study on these systems [27] that shows that the viscous flow of the PA6 chains

both in solid-state and melt-state is significantly reduced in the presence of the CNC

whiskers, thus justifying the increase in K_g parameter.

In contrast to the pristine CNC, the APS-CNC particles used in this study showed

a much finer phase distribution within the PA6 matrix, resulting in much higher available

surface area. Additionally, the interfacial bond formation with the amine groups on the

APS-CNC surface results in enhanced surface activity for crystal nucleation process as

indicated by the lower K_g value. By considering the σ_e values, it is seen that in the case of 3%CNC, the value is increased from 7.46 mJ/m^2 to 7.84 mJ/m^2 suggesting a less energetically favorable folded surface in the lamella. On the other hand, the folded surface energy is reduced to 5.91 mJ/m^2 in the case of the 3%APS-CNC sample, suggesting a lower energy barrier of crystallization process that is facilitated by the modified surface chemistry and more homogenous dispersion of whiskers in the matrix. As already described in the Avrami analysis, even the APS-CNC samples showed a significant crystal growth restriction on the crystals which was verified by the reduction in the obtained Avrami constants to values lower than 3. This observed effect in the current analysis can be discussed using the work of chain folding (q) parameter given in Table 3.3 that shows that the q value is increased from $2.4*10^{-20}$J to $2.6*10^{-20}$J in the case of 3%CNC. This finding suggests a relatively more difficult chain folding process in the presence of CNC whiskers compared to that of the APS-CNC that showed a decrease in q value to $1.9*10^{-20}$J in the 3%APS-CNC sample (see Table 3.3). Although this last result may be interpreted as less work required for the chains to fold back into the lamella, it is believed that the reason for this reduction is due to the fact that the crystals in 3%APS-CNC sample are smaller and less perfect in shape (i.e., distorted crystal structure) that makes it "easier" for the chains to fold back into the crystal.

In summary of the important points of the foregoing discussion, the results show that in the case of pristine CNC whiskers the crystallization rate is reduced due to the significant restriction imposed on the molecular motion of PA6 chains. Considering the competition between the heterogeneous nucleation activity and the restriction of crystal growth, the obtained results indicate that effect of the latter outweighs that of the former.

In the case of APS-modified CNC particles, the nucleation activity is more significant and the reduction in crystal growth is balanced out by the fact that the crystals are less perfect, making the energetics of crystal growth relatively more favorable as will be further verified in the next section using the optical micrograph images. Interestingly, in the reported study by Siqueira and co-workers [23], it was shown that microfibrillated cellulose (MFC) imposed more restriction on PCL crystal growth and limited the crystal dimensions, in contrast to the cellulose whiskers that acted as effective nucleating agents with less crystal growth hindrance effect due to the absence of entangled cellulose structures as in the case of MFC which is consistent with the findings of this current study.

Now in order to verify that the crystallization process is indeed in the regime II of Hoffman-Lauritzen analysis, a Z-test was carried out using the following equation [45]:

$$Z \approx 10^3 . (\frac{L}{2a_0})^2 . \exp\left(-\frac{X}{T_c \Delta T}\right) \tag{3.11}$$

where L is the effective lamellar width, a_0 is the width of the molecular chain in crystal. If the regimes I or III are applicable, the replacement of X with Kg should yield Z ≤ 0.01. Conversely, if the regime II is applicable, the replacement of X with $2K$g should yield $Z \geq 1.0$. This Z-test used the values of K_g already described in equation (3.9) and an estimated L value to check whether or not the latter value is realistic. By using a chain width (a_0) value of 0.37nm for the PA6 chain with the thickness of a monomolecular layer (b_0) of 0.44nm [14], in the first scenario, the equation (3.11) yields $L \leq 0.12$nm which is clearly not realistic. Using the second regime approximation, the equation yields $L \geq$ 6.6nm which is a realistic value for the PA6, therefore, confirming the assumption of the second regime of the crystallization in the Hoffman analysis already discussed

133

To confirm the validity of the hypothetical crystal geometry used in the above Hoffman analysis, cross-polarized optical microscopic images (or POM images) were collected during the isothermal crystallization process. For this purpose, the POM images taken at early stage of crystallization or the nucleation phase and in the state of fully gown crystals after completion of the isothermal crystallization and cooling to room temperature are shown in Figure 3.7. For the early stage of crystallization, the time required to reach less than 15-20% crystallinity was chosen from the obtained DSC data. Unlike a previous study by Katoh *et al* [46] where POM images of PA6 based nanocomposite samples were taken at similar time intervals for all samples, we took the POM images at similar "crystalline content" among the samples to have a better observation of the individual samples and their crystalline morphology. As can be seen in the POM images, for the neat PA6 sample a full Maltese cross and a spherulitic morphology with positive birefringence can be observed. In the case of 3%CNC sample, a remarkably similar type of morphology with a relatively more diffuse Maltese cross patterns is observed, indicating formation of defected spherulites and major linear-shaped crystalline regions that shows the hindrance imposed by CNCs on spherulite development. By contrast, in the case of 3%APS-CNC sample, it is clearly seen that a greater number of nuclei formed at early stage of crystallization which indicates crystal nucleation property of the CNC whiskers as already mentioned. However, the size of the crystals and spheres are observed to be relatively much smaller compared to that of the PA6 spherulites even for the sample containing the highest CNC concentration (i.e., 3%CNC) studied. These results strongly indicate that the surface modified CNC particles exhibit significant heterogeneous nucleating effect while largely restricting the spherulite

134

growth in 3 dimensions. In fact, enhanced dispersion of APS-CNC in the matrix together with the higher surface activity is resulting in formation of relatively large number of nuclei with larger number of smaller spheres and underdeveloped morphology.

3.3.4 Theoretical Analysis of Non-isothermal Crystallization

In order to better understand and interpret the effects of microstructure and surface functionality on the crystallization behavior of the PA6/CNC nanocomposite systems, a series of non-isothermal crystallization experiments were conducted on PA6, PA6/3%CNC and PA6/3%APS-CNC samples. The samples were cooled at controlled cooling rates of 5°, 10°, 15° and 20°C from the melt and the exotherms of the crystallization were monitored. The obtained exothermic peaks of crystallization at different rates are shown in Figure 3.8 with corresponding peak crystallization temperatures reported in Table 3.4. Clearly, Figure 3.8 and Table 3.4 show that increasing the cooling rate results in a decrease in the peak crystallization temperatures for all samples, and in addition, the onset of crystallization temperature occurs at lower temperatures and the crystallization exotherms become broader. In fact, as the cooling rate increases, the available response time of the polymer chains in order to overcome the nucleation energy barrier becomes shorter. Therefore, the crystallization occurs at preferably lower temperature since at lower temperatures, the nucleation rate is enhanced.

Due to the observed lower temperatures of crystallization and associated restriction of the macromolecular motion, the packing of the polymer chains into crystalline regions occurs in a relatively larger time span that results in the obtained crystallization exotherms becoming broader [47]. Comparing the data obtained from PA6 sample with that of 3%CNC and 3%APS-CNC, it is evident in Table 3.4 that the peak

crystallization temperature is slightly decreased in the case of 3%CNC sample, while it

shifts to higher temperatures for the APS modified CNC samples. This clearly shows that

the surface modified CNCs cause the PA6 crystallization to occur at higher temperatures.

A number of theoretical approaches are used here to extract the crystallization

kinetics parameters and to interpret the experimental results as follows: A constant

cooling rate and similar thermal history applied to all the samples in the DSC furnace in

all the experiments and the following equation (3.12) can be used in order to convert the

crystallization temperature span to crystallization time for the purpose of explaining the

observed crystallization kinetics of the samples:

$$t = \left| \frac{T_o - T}{\varphi} \right| \tag{3.12}$$

In equation (3.12), T_o is the onset of crystallization temperature, T is the

temperature at crystallization time of t and φ is the cooling rate. The typical variation of

relative crystallinity versus temperature and time (obtained from the conversion just

mentioned) for PA6 sample are shown in Figure 3.9. As can be seen in this figure, the

variation of relative crystallinity versus both temperature and time follow a sigmoidal

type behavior as expected. It is evident in Figure 3.9 that initially the crystallinity

increases with a sharper curvature corresponding to the primary crystallization stage and,

at higher degrees of relative crystallinity, the curve somewhat levels off with a very small

curvature. Similar data trend was observed for 3%CNC and 3%APS-CNC samples (plots

not shown).

In the case of the PA6 sample, the curvature is relatively sharper which is

indicative of a secondary crystallization. From the variation of relative crystallinity

versus time it is evident that as the cooling rate increases, the time span of the

crystallization decreases and the whole crystallization process takes place over a shorter

period of time, indicating a faster crystallization rate (see Fig. 3.9).

3.3.4.1 Analysis of Non-isothermal Crystallization by Avrami's Model

In order to adapt the Avrami model for analyzing non-isothermal crystallization

process, a correction factor was used by Jeziorny [48] to modify the non-isothermal growth

rate constant (Z_C) using the value derived directly from the Avrami equation (Z_t)

according to the following equations (3.13)–(3.15):

$$1 - X_c = \exp(-Z_t t^n) \tag{3.13}$$

$$\log[-\ln(1 - X_c)] = n \log t + \log Z_t \tag{3.14}$$

$$\log Z_C = \frac{\log Z_t}{\varphi} \tag{3.15}$$

The obtained modified Avrami plots of these three samples are shown in Figure

3.10 and the values of Avrami indices "n", the crystallization half times and the Z_t and Z_C

are given in Table 3.4.

Clearly, Figure 3.10 and Table 3.4 show that the Avrami index for PA6 varies

from 3.9 at lowest cooling rate (indicative of formation of relatively complex 3D shaped

crystals) to 3 at highest cooling rate. This result shows that increasing the cooling rate

from the melt results in development of less perfect PA6 crystals. In addition, both the

nanocomposite samples with 3%CNC and 3%APS-CNC, show lower values of n

compared to that of the neat PA6, with the sample containing APS-CNC having lowest

Avrami indices at all cooling rates. This shows that the surface modified CNC changed

the crystal morphology to less perfect 3D crystals compared to that of the 3%CNC

sample. Another explanation for the reduction of n as the cooling rate increases is the fact

that higher cooling rates increase the crystallization rate, leading to possibility of

spherulite impingement and truncation. This effect will be more important when the heterogeneous nuclei are dispersed non-uniformly (as in the case of the CNC particles) in addition to the increased surface area of the whiskers that are known to reduce the available volume for spherulite growth and therefore, a reduction of the obtained n values. The obtained $t_{1/2}$ values show a decrease with increasing cooling rate for all samples which indicates enhanced crystallization rate (i.e., lower crystallization time) at higher cooling rates.

Comparing the 3%CNC with the PA6 sample reveal that, at each cooling rate, the crystallization half-time is slightly increased. This shows that the pristine CNC whiskers prolong the crystallization process of PA6 chains. By contrast, the 3%APS-CNC sample shows a relatively lower crystallization $t_{1/2}$ compared to that of the 3%CNC sample, suggesting a partial compensation of the crystal growth delay by a plausible increased nucleation rate caused by enhanced surface activity.

Table 3.4 also shows the variation of Z_t and Z_C values which clearly show that increasing the cooling rate results in increasing crystallization rate constants which is consistent with the changes in crystallization half-time already discussed. By comparing the data obtained from the neat PA6 and the nanocomposite samples, it is evident that both 3% CNC and APS-CNC samples show relatively lower overall crystallization rates compared to that of the neat PA6; while the values for APS modified CNC sample are found to be lower than that of the neat PA6 but higher than that of the 3%CNC sample. The variation of Avrami rate constants show that the surface modified CNCs with better dispersion improve the crystallization rate compared to that of the nanocomposite samples containing the pristine CNC with fibrillar morphology. These findings combined

138

with the fact that 3%APS-CNC sample shifted the crystallization temperature to higher values (i.e., acceleration effect) suggest a complicated crystallization behavior that looks contradictory at first sight. However, these results can be explained as follows. The overall rate of crystallization is governed by the combination of rates of nucleation and crystal growth. The presence of solid surfaces of foreign particles in the polymer melt can act as heterogeneous nuclei while at the same time, these solid particles can decelerate the crystal growth due to the imposed restriction on macromolecular PA6 chain motion. The latter effect becomes significantly important and dominating if there are strong interactions between the host polymer and the surface of the particle.

In the current PA6/CNC nanocomposite systems, the CNC whiskers show similar behavior where the strong hydroxyl rich surface of cellulose and amide groups of PA6 chains strongly interact through hydrogen bonding. In addition, the observed morphology of interconnected fibrillar network of whiskers result in severe restriction on molecular motion of PA6 that consequently results in lower overall crystallization rate, longer halt-time, and reduced Avrami exponent due to development of less perfect crystals. Similar effects have been observed with graphite oxide nano-sheets [49] and foliated graphite particles [33] in polyamide 6 matrix as reported in the literature. Further, in the case of APS modified CNC whiskers, because of the observed better dispersion of the particles throughout the matrix, the effect of particles on crystal growth hindrance is more prominent as already described. Here, we speculate that the higher interfacial area between the matrix and the whiskers and the interfacial bonds between the matrix and whiskers support the hypothesis of the CNC surface acting as heterogeneous secondary nuclei as observed in the isothermal crystallization and POM images already described.

In fact, this same explanation is consistent with the observation of the onset and peak crystallization temperatures shifting towards higher temperatures in the case of 3% APS-CNC sample.

3.3.4.2 Analysis of Non-isothermal Crystallization by Ozawa's model

According to the theory reported by Ozawa [50-51], non-isothermal crystallization process was assumed to be a combination of many infinitesimal isothermal crystallization processes over the duration of crystallization process where the cooling rate is constant. In this theory the relative crystallinity X(T) at each temperature T can be written as equation (3.16) [52]:

$$X(T) = 1 - \exp\left[\frac{-K(T)}{\varphi^m}\right] \tag{3.16}$$

where m is the Ozawa exponent and K(T) is the crystallization rate constant. This equation can be re-written in the linear form as:

$$\log\left[-\ln\left(1 - X(T)\right)\right] = \log K(T) - m\log(\varphi) \tag{3.17}$$

If this model is applicable to the non-isothermal crystallization of the current systems, a linear fit to the experimental data should accurately describe the data points and the graphical representation should generate a straight line. The results of the Ozawa analysis of our experimental data obtained at various crystallization temperatures (and corresponding X (T) at each cooling rate) are shown in Figure 3.11.

As can be seen from this figure, no obvious straight line could be fitted to the experimental data points, especially for PA6 and 3%APS-CNC samples. Therefore, this model does not provide a satisfactory description of the obtained data. However, Figure 3.11 shows that the fit on the 3%CNC data gives a relatively linear trend compared to that of the other samples. This finding might be related to the very slow crystallization

rate of this particular sample and the specific network-like microstructure of the CNCs within the PA6 matrix, making the crystallization to occur near the diffusion limit regime. This observation is a typical behavior of systems where there is a significant molecular motion restriction imposed on the polymer chains [49]. Although the Ozawa model has been successfully fitted to data obtained on a number of polymeric and hybrid systems [49, 53], there are a number of cases reported in the literature where this model failed to fit non-isothermal crystallization data [33, 52]. This may be ascribed to the fact that the non-isothermal crystallization process is a dynamic process where the crystallization rate constantly changes with both the time and temperature, making the assumptions of the quasi-isothermal nature of non-isothermal crystallization inadequate to describe this process especially at high heating rates like those used in this study.

In addition, the Ozawa model ignores the secondary crystallization process [51] which is not true in the case of PA6 nanocomposites as it was earlier shown that the variation of relative crystallinity follows a sigmoidal dependence on the time and temperature with the upper curvature indicative of secondary crystallization process. Note that this last point may be less significant in the nanocomposite samples compared to the pure PA6 matrix due to steric factors and impingement of crystals with the solid surface of CNCs. In addition, in the case of 3%APS-CNC sample, the experimental evidence suggests that the crystallization rate process is largely dependent on the extent of relative crystallinity which further complicates the process as will be discussed in the next section.

3.3.4.3 Analysis of Non-isothermal Crystallization by Mo's approach

As already discussed so far, both the Avrami and Ozawa's analysis methods did not provide accurate and clear description of the observed non-isothermal crystallization process. Therefore, as a further approach to address this limitation, Mo and coworkers [54] have proposed a model based on combination of Ozawa and Avrami models according to the following equations (3.18)-(3.19):

$$\ln K(T) - m \ln \varphi = \ln Z_t + n \ln t \tag{3.18}$$

$$\ln \varphi = \ln F(T) - \alpha \ln t \tag{3.19}$$

where the $F(T)$ is defined as $[K(T)/Z_t]^{1/m}$ and the α is the ratio of Avrami exponent over Ozawa exponent ($\alpha = n/m$). The physical meaning of the $F(T)$ parameter is the required cooling rate value in order to achieve a certain relative degree of crystallinity at unit crystallization time. If the left hand side of equation (3.19) is plotted against the $\ln t$ at a fixed degree of crystallinity, a straight line should be obtained with a slope of α and intercept of $\ln F(T)$. The significance of this model is the fact that the crystallization process can be discretized into various relative degrees of crystallinity and the kinetics can be studied at desired "stage" of crystallization.

The linear relationship between the $\ln \varphi$ and the $\ln t$ is demonstrated in Figure 3.12 where linear fits of equation (3.19) to experimental data obtained for PA6, 3%CNC and 3%APS-CNC samples at various relative degrees of crystallinity from 10% to 85% are plotted and the resulting fitting parameters of $F(T)$ and α are given in Table 3.5. The $F(T)$ parameter correlates with the crystallization rate at each relative degree of crystallization in such a way that the higher the $F(T)$ value, the lower the crystallization rate. This is because a high value of $F(T)$ means a higher cooling rate is required to reach

the same degree of crystallinity which means that the crystallization is indeed occurring at lower rates [55]. Table 3.5 shows that the $F(T)$ values of 3%CNC are higher compared to that of the PA6 and 3%APS-CNC samples at all relative degrees of crystallinity considered, supporting the earlier findings that the 3%CNC sample had relatively slower crystallization rate as already described. The most interesting part of this analysis, however, is the obtained $F(T)$ values for the 3%APS-CNC sample which clearly shows that the $F(T)$ values ranged from 2.63 to 4.84 as a function of relative crystallinity ranging from 0.1 to 0.4 which corresponds to the early stages of crystallization or "nucleation phase" which is interestingly found to be lower than that of PA6 and 3%CNC sample. This fact confirms our hypothesis that the APS modification actually enhances the nucleation activity of the CNC surfaces in the PA6 melt through interfacial bond formation with the polyamide 6 chains that facilitates development of the interphase layer that provides a path towards arrangement of macromolecular chains on the surface which in turn leads to enhanced heterogeneous nucleation. However, as the degree of crystallinity increases above 40%, the $F(T)$ values increase rapidly to a level surpassing the $F(T)$ values of PA6 matrix.

This last observation is consistent with the prior analysis showing the overall crystallization rate of this sample to be lower than that of neat PA6 (but still higher than 3%CNC) at these later stages of crystallization due to the growth of the crystals becoming significantly retarded in the presence of well dispersed CNC whiskers and associated strong adhesion at the whisker/polymer interface that restricts the viscous motion of chain segments as already described. The variations in the slope of the fitted lines of equations (3.18) & (3.19) to the experimental data show that addition of both

CNC and APS-CNC nanoparticles increased the α value as shown in the Table 3.5. This means that the presence of CNC whiskers affects the Avrami exponent more significantly compared to the Ozawa exponent. The increase in the values of α with the relative degree of crystallinity show an increasing trend which can be attributed to the fact that at higher degrees of crystallinity, the variation of the crystallinity follows a relatively sharper dependence on the cooling rate which clearly is due to the restricted crystal growth at the later stages of the spherulitic development.

3.3.5 Activation Energy of Non-isothermal Crystallization

The activation energy of the crystallization process is an important kinetic parameter to understanding and interpreting the interrelation of microstructure and crystallization process. There are a number of methods used to obtain the activation energy of typical non-isothermal crystallization process. One of the most commonly used methods is the Kissinger equation [56]. According to this method, a single value of activation energy can be obtained from the slope of the plot of $\ln(\varphi/T_P^2)$ versus $1/T_P$ (T_p is the peak crystallization temperature). However, the Kissinger and other Kissinger-type equations have some important disadvantages especially with respect to the nanocomposites systems of this current study, the most important of which, is that it provides a single activation energy value for the whole crystallization process. As already demonstrated, the non-isothermal crystallization process is a complicated sequence of nucleation and growth, and the crystallization rate is a function of relative degree of crystallinity. As an alternative approach to this method, a number of isoconversional methods have been developed to evaluate the activation energy discretized over relative crystallinity degree [51]. The representative methods include the differential isoconversion

method of Friedman [57] and the Vyazovkin's advanced integral isoconversion approach. In the current study, we adopted the Friedman's differential isoconversion approach that is based on the numerical differentiation of conversion over crystallization time and on using the following equation:

$$\ln\left(\frac{dX}{dt}\right)_{X,i} = constant - \frac{\Delta E_X}{RT_{X,i}} \qquad (3.20)$$

In this equation (3.20), dX/dt is the instantaneous rate of crystallization at a given conversion. In order to apply this method, the values of relative degrees of crystallinity are numerically differentiated with respect to time to obtain the dX/dt values. This process is carried out on a series of conversion points and the left hand side of the equation is correlated with the temperature of crystallization at that specific conversion point so that the discretized activation energy can be obtained from the slope. A typical plot of equation (3.20) is shown in Figure 3.13(a) for neat PA6 sample. A similar type of plot is constructed for 3%CNC and 3%APS-CNC samples and the variation of the obtained activation energies versus relative degree of crystallization is plotted in Figure 3.13(b).

As can be seen from Figure 3.13, the activation energy for all samples increases monotonically as the relative degree of crystallization is increased. This shows that as the fraction of crystalline material increases in the sample, it becomes harder for the macromolecular PA6 chains to further expand the growing spherulite, making this process relatively more energetically difficult. By comparing the data obtained for the nanocomposite samples with that of the PA6, it is clearly evident that the 3%CNC sample shows higher activation energies at all stages of crystallization from 10% to 90%. On the other hand, it is very interesting to note that the 3%APS-CNC sample showed a low

initial activation energy from 10 to 40% of relative crystallinity. However, the obtained activation energy values surpass that of the PA6 sample for higher crystallization degrees above 40%. This clearly shows that in the early stages of crystallization which corresponds to the nucleation phase, the crystal development is more kinetically favorable in the presence of surface modified CNC particles. In addition, as the crystallization fraction increases, this process becomes relatively more difficult as already described.

The schematic shown in Figure 3.14 is proposed for development of the γ-type crystalline structure on the surface of APS-CNC particles as shown in this study. As previously mentioned, the α-type crystals are formed through the hydrogen bonding of the amide linkages on chains in antiparallel arrangement in fully extended chain configuration therefore forming the H-bonded sheets of antiparallel chains. On other hand, the γ-type crystals are formed between the parallel sheets where the amide linkages are twisted 60° out of the plane of the methyl groups. In our system, although the hydroxyl-rich surface of the CNC strongly interacts with PA6 chains, the arrangement of the antiparallel chains could be achieved as depicted in Figure 3.14; however, In the case of the APS-modified cellulose whiskers, the grafted chains of PA6 are chemically locked (tethered) on the surface which forces the nylon chains out of the ordered H-bonded sheets of the α-structure. As a result, a greater number of γ-type crystals where less order is attained are formed. In addition, the SEM images showed a significantly improved dispersion of CNC within the matrix therefore, much higher surface area on the CNC is available for this effect which consequently, results in enhanced γ-nucleation effect.

3.4 Conclusions

This study showed that the crystallization kinetics and morphology of the

nanocomposites of PA6 with cellulose nanocrystals (CNCs) and APS-modified CNCs

prepared by *in-situ* ring opening polymerization and subsequent melt extrusion can be

interpreted by analytic crystallization model equations with improved insights on the

effects of the micro-structure development and surface properties of the nanocellulose

needed to control the crystallization process of polyamide 6. The SEM images showed a

network-like fibrillar microstructure development in the case of non-modified PA6/CNC

while in the case of PA6/APS-CNC system, a finer and more homogenous distribution of

cellulose whiskers at sub-micron level was observed. For analysis of the crystallization

kinetics, the Avrami model was successful in describing the isothermal crystallization

process. The addition of CNCs resulted in longer crystallization half-times and reduction

in Avrami rate constant, indicating a hindrance effect of the cellulose nanocrystals on the

crystallization process. This effect correlated well with the network-like fibrillar structure

of the CNC in the PA6 matrix which imposes significant restriction on molecular motion

and crystal development of PA6 macromolecular chains. However, the APS-modified

CNC particles enhanced the observed nucleation activity and increased the Avrami (K)

constant. The effect of nucleation activity of the surface modified CNCs was confirmed

by the Hoffman theory and polarized optical micrographs. In the non-isothermal

crystallization, it was observed that the APS-modified CNCs shifted the crystallization

peak and its onset temperature towards higher temperatures while an opposite effect was

observed for the non-modified CNCs. The effective heterogeneous nucleation activity of

the APS-CNCs was theoretically demonstrated below the 40% relative crystallinity range

showing an excellent agreement with the experimental observation. The analysis of non-isothermal activation energy revealed that during the nucleation phase, the activation energy of the APS-modified CNC nanocomposite was lower than that of the PA6 and non-modified CNC system while this value surpassed that of the neat PA6 in later stages of non-isothermal crystallization. This study demonstrated how surface modification of cellulose nanocrystals and the associated microstructure development can effectively be used to control the crystallization behavior of polyamide 6 through balancing the competition between PA6 macromolecular motion chain restriction and heterogeneous nucleation activity.

3.5 References

1.   Matthies, P.; Seydl, W. F., History and Development of Nylon 6. In High Performance Polymers: Their Origin and Development: Proceedings of the Symposium on the History of High Performance Polymers at the American Chemical Society Meeting held in New York, April 15–18, 1986, Seymour, R. B.; Kirshenbaum, G. S., Eds. Springer Netherlands: Dordrecht, 1986; pp 39-53.

2.   Page, I., Polyamides as engineering thermoplastic materials. iSmithers Rapra Publishing: 2000; Vol. 121.

3.   Miyasaka, K.; Ishikawa, K., Effects of temperature and water on the γ → α crystalline transition of nylon 6 caused by stretching in the chain direction. Journal of Polymer Science Part A-2: *Polymer Physics* **1968,** 6 (7), 1317-1329.

4.   Miyasaka, K.; Isomoto, T.; Koganeya, H.; Uehara, K.; Ishikawa, K.; Ogata, N., Nylon-6 α-phase crystal: Chain repeat distance and modulus in the chain direction at low temperature. *Journal of Polymer Science: Polymer Physics* Edition **1980,** 18 (5), 1047-1052.

5.   Murthy, N. S., Hydrogen bonding, mobility, and structural transitions in aliphatic polyamides. *Journal of Polymer Science Part B: Polymer Physics* **2006,** 44 (13), 1763-1782.

6.   Murthy, N. S.; Minor, H.; Latif, R. A., Effect of annealing on the structure and morphology of nylon 6 fibers. *Journal of Macromolecular Science*, Part B **1987,** 26 (4), 427-446.

7.   Arimoto, H.; Ishibashi, M.; Hirai, M.; Chatani, Y., Crystal structure of the γ-form of nylon 6. *Journal of Polymer Science Part A*: General Papers **1965,** 3 (1), 317-326.

8.   Liu, X.; Wu, Q., Non-isothermal crystallization behaviors of polyamide 6/clay nanocomposites. *European Polymer Journal* **2002,** 38 (7), 1383-1389.

9.   Tjong, S. C.; Bao, S. P., Preparation and nonisothermal crystallization behavior of polyamide 6/montmorillonite nanocomposites. *Journal of Polymer Science Part B: Polymer Physics* **2004,** 42 (15), 2878-2891.

10.   Kodgire, P. V.; Bhattacharyya, A. R.; Bose, S.; Gupta, N.; Kulkarni, A. R.; Misra, A., Control of multiwall carbon nanotubes dispersion in polyamide6 matrix:

An assessment through electrical conductivity. *Chemical Physics Letters* **2006,** 432 (4–6), 480-485.

11.   Liu; Phang, I. Y.; Shen, L.; Chow, S. Y.; Zhang, W.-D., Morphology and Mechanical Properties of Multiwalled Carbon Nanotubes Reinforced Nylon-6 Composites. *Macromolecules* **2004,** 37 (19), 7214-7222.

12.   Zhang, F.; Peng, X.; Yan, W.; Peng, Z.; Shen, Y., Nonisothermal crystallization kinetics of in situ nylon 6/graphene composites by differential scanning calorimetry. *Journal of Polymer Science Part B: Polymer Physics* **2011,** 49 (19), 1381-1388.

13.   Yang, F.; Ou, Y.; Yu, Z., Polyamide 6/silica nanocomposites prepared by in situ polymerization. *Journal of Applied Polymer Science* **1998,** 69 (2), 355-361.

14.   Wu, T.-M.; Lien, Y.-H.; Hsu, S.-F., Isothermal crystallization kinetics and melting behavior of nylon/saponite and nylon/montmorillonite nanocomposites. *Journal of Applied Polymer Science* **2004,** 94 (5), 2196-2204.

15.   Fornes, T. D.; Paul, D. R., Crystallization behavior of nylon 6 nanocomposites. *Polymer* **2003,** 44 (14), 3945-3961.

16.   Guo, B.; Zou, Q.; Lei, Y.; Du, M.; Liu, M.; Jia, D., Crystallization behavior of polyamide 6/halloysite nanotubes nanocomposites. *Thermochimica Acta* **2009,** 484 (1–2), 48-56.

17.   Li, J.; Fang, Z.; Tong, L.; Gu, A.; Liu, F., Effect of multi-walled carbon nanotubes on non-isothermal crystallization kinetics of polyamide 6. *European Polymer Journal* **2006,** 42 (12), 3230-3235.

18.   Li, J.; Fang, Z.; Zhu, Y.; Tong, L.; Gu, A.; Liu, F., Isothermal crystallization kinetics and melting behavior of multiwalled carbon nanotubes/polyamide-6 composites. *Journal of Applied Polymer Science* **2007,** 105 (6), 3531-3542.

19.   Moon, R. J.; Martini, A.; Nairn, J.; Simonsen, J.; Youngblood, J., Cellulose nanomaterials review: structure, properties and nanocomposites. *Chemical Society Reviews* **2011,** 40 (7), 3941-3994.

20.   Postek, M. T.; Moon, R. J.; Rudie, A. W.; Bilodeau, M. A., Production and applications of cellulose nanomaterials. Technical Association of Pulp and Paper Industry, TAPPI, Peachtree Corners, GA **2013**.

21.   Pandey, J. K.; Lee, C. S.; Ahn, S.-H., Preparation and properties of bio-nanoreinforced composites from biodegradable polymer matrix and cellulose whiskers. *Journal of Applied Polymer Science* **2010,** 115 (4), 2493-2501.

22.   Han, J.; Zhu, Y.; Hu, J.; Luo, H.; Yeung, L.-Y.; Li, W.; Meng, Q.; Ye, G.; Zhang, S.; Fan, Y., Morphology, reversible phase crystallization, and thermal sensitive shape memory effect of cellulose whisker/SMPU nano-composites. *Journal of Applied Polymer Science* **2012,** 123 (2), 749-762.

23.   Siqueira, G.; Fraschini, C.; Bras, J.; Dufresne, A.; Prud'homme, R.; Laborie, M.-P., Impact of the nature and shape of cellulosic nanoparticles on the isothermal crystallization kinetics of poly(ε-caprolactone). *European Polymer Journal* **2011,** 47 (12), 2216-2227.

24.   Lu, J.; Wang, T.; Drzal, L. T., Preparation and properties of microfibrillated cellulose polyvinyl alcohol composite materials. *Composites Part A: Applied Science and Manufacturing* **2008,** 39 (5), 738-746.

151

25.   Jalal Uddin, A.; Araki, J.; Gotoh, Y., Extremely oriented tunicin whiskers in poly(vinyl alcohol) nanocomposites. *Polymer International* **2011,** 60 (8), 1230-1239.

26.   Kiziltas, A.; Nazari, B.; Gardner, D. J.; Bousfield, D. W., Polyamide 6– Cellulose Composites: Effect of Cellulose Composition on Melt Rheology and Crystallization Behavior. *Polymer Engineering & Science* **2014,** 54 (4), 739-746.

27.   Kashani Rahimi, S.; Otaigbe, J. U., Polyamide 6 nanocomposites incorporating cellulose nanocrystals prepared by In-situ ring opening polymerization: Viscoelasticity, creep behavior, and melt rheological properties. *Polymer Engineering & Science* **2016**, 56 (9), 1045-1060 .

28.   Capadona, J. R.; Van Den Berg, O.; Capadona, L. A.; Schroeter, M.; Rowan, S. J.; Tyler, D. J.; Weder, C., A versatile approach for the processing of polymer nanocomposites with self-assembled nanofibre templates. *Nature Nano* **2007,** 2 (12), 765-769.

29.   Mateva, R.; Petrov, P.; Rousseva, S.; Dimitrov, R.; Zolova, G., On the structure of poly-ε-caprolactams, obtained with bifunctional N-carbamyl derivatives of lactams. *European Polymer Journal* **2000,** 36 (4), 813-821.

30.   Udipi, K.; Davé, R. S.; Kruse, R. L.; Stebbins, L. R., Polyamides from lactams via anionic ring-opening polymerization: 1. Chemistry and some recent findings. *Polymer* **1997,** 38 (4), 927-938.

31.   Weeding, T.; Veeman, W.; Gaur, H. A.; Huysmans, W., Structural investigation of polyamide-6 and polyamide-6 composites using carbon-13 cross polarization/magic angle spinning NMR. *Macromolecules* **1988,** 21 (7), 2028-2032.

32.   Liu, L.; Qi, Z.; Zhu, X., Studies on nylon 6/clay nanocomposites by melt-intercalation process. *Journal of Applied Polymer Science* **1999,** 71 (7), 1133-1138.

33.   Weng, W.; Chen, G.; Wu, D., Crystallization kinetics and melting behaviors of nylon 6/foliated graphite nanocomposites. *Polymer* **2003,** 44 (26), 8119-8132.

34.   Lorenzo, A. T.; Arnal, M. L.; Albuerne, J.; Müller, A. J., DSC isothermal polymer crystallization kinetics measurements and the use of the Avrami equation to fit the data: Guidelines to avoid common problems. *Polymer Testing* **2007,** 26 (2), 222-231.

35.   Fanfoni, M.; Tomellini, M., The Johnson-Mehl- Avrami-Kohnogorov model: A brief review. Il *Nuovo Cimento* D **1998,** 20 (7), 1171-1182.

36.   Málek, J., Calorimetry and Thermal AnalysisThe applicability of Johnson-Mehl-Avrami model in the thermal analysis of the crystallization kinetics of glasses. *Thermochimica Acta* **1995,** 267, 61-73.

37.   Zhou, W. Y.; Duan, B.; Wang, M.; Cheung, W. L., Isothermal and Non-isothermal Crystallization Kinetics of Poly (L-Lactide)/Carbonated Hydroxyapatite Nanocomposite Microspheres. *Advances in diverse industrial applications of nanocomposites*. ISBN **2011**, 978-953.

38.   Chen, E.-C.; Wu, T.-M., Isothermal and nonisothermal crystallization kinetics of nylon 6/functionalized multi-walled carbon nanotube composites. *Journal of Polymer Science Part B: Polymer Physics* **2008,** 46 (2), 158-169.

39.   Hoffman, J. D.; Davis, G. T.; Lauritzen, J. I., The Rate of Crystallization of Linear Polymers with Chain Folding. In Treatise on Solid State Chemistry: Volume 3

Crystalline and Noncrystalline Solids, Hannay, N. B., Ed. Springer US: Boston, MA, 1976; pp 497-614.

40.   Sperling, L. H., Introduction to physical polymer science. John Wiley & Sons: 2005.

41.   Hoffman, J. D.; Weeks, J. J., Melting process and the equilibrium melting temperature of polychlorotrifluoroethylene. *Journal of Research of National Bureau of Standards A* **1962,** 66 (1), 13-28.

42.   Ho, J.-C.; Wei, K.-H., Induced γ → α Crystal Transformation in Blends of Polyamide 6 and Liquid Crystalline Copolyester. *Macromolecules* **2000,** 33 (14), 5181-5186.

43.   Barhoumi, N.; Maazouz, A.; Jaziri, M.; Abdelhedi, R., Polyamide from lactams by reactive rotational molding via anionic ring-opening polymerization: Optimization of processing parameters. *Express Polymer Letters* **2013,** 7 (1), 76-87.

44.   Lizundia, E.; Vilas, J.; León, L., Crystallization, structural relaxation and thermal degradation in Poly (l-lactide)/cellulose nanocrystal renewable nanocomposites. *Carbohydrate polymers* **2015,** 123, 256-265.

45.   Chu, M.-J.; Wu, T.-M., Isothermal crystallization kinetics of poly (lactic acid)/montmorillonite nanocomposites. In *Experimental Analysis of Nano and Engineering Materials and Structures*, Springer: 2007; pp 827-828.

46.   Katoh, Y.; Okamoto, M., Crystallization controlled by layered silicates in nylon 6–clay nano-composite. *Polymer* **2009,** 50 (19), 4718-4726.

47. Wu, D.; Zhou, C.; Fan, X.; Mao, D.; Bian, Z., Nonisothermal crystallization kinetics of poly(butylene terephthalate)/montmorillonite nanocomposites. *Journal of Applied Polymer Science* **2006,** 99 (6), 3257-3265.

48. Jeziorny, A., Parameters characterizing the kinetics of the non-isothermal crystallization of poly (ethylene terephthalate) determined by DSC. *Polymer* **1978,** 19 (10), 1142-1144.

49. Liu, Y.; Yang, G., Non-isothermal crystallization kinetics of polyamide-6/graphite oxide nanocomposites. *Thermochimica Acta* **2010,** 500 (1–2), 13-20.

50. Ozawa, T., Kinetics of non-isothermal crystallization. *Polymer* **1971,** 12 (3), 150-158.

51. Papageorgiou, G. Z.; Achilias, D. S.; Bikiaris, D. N.; Karayannidis, G. P., Crystallization kinetics and nucleation activity of filler in polypropylene/surface-treated SiO2 nanocomposites. *Thermochimica Acta* **2005,** 427 (1–2), 117-128.

52. Kuo, M.; Huang, J.; Chen, M., Non-isothermal crystallization kinetic behavior of alumina nanoparticle filled poly (ether ether ketone). *Materials Chemistry and Physics* **2006,** 99 (2), 258-268.

53. Supaphol, P.; Dangseeyun, N.; Srimoaon, P.; Nithitanakul, M., Nonisothermal melt-crystallization kinetics for three linear aromatic polyesters. *Thermochimica Acta* **2003,** 406 (1), 207-220.

54. Liu, T.; Mo, Z.; Zhang, H., Nonisothermal crystallization behavior of a novel poly (aryl ether ketone): *Journal of Applied Polymer Science* **1998,** 67 (5), 815-821.

55. Huang, H.; Gu, L.; Ozaki, Y., Non-isothermal crystallization and thermal transitions of a biodegradable, partially hydrolyzed poly (vinyl alcohol). *Polymer* **2006,** 47 (11), 3935-3945.

56. Kissinger, H. E., Variation of peak temperature with heating rate in differential thermal analysis. *Journal of research of the National Bureau of Standards* **1956,** 57 (4), 217-221.

57. Friedman, H. L. In Kinetics of thermal degradation of char-forming plastics from thermogravimetry. Application to a phenolic plastic, *Journal of Polymer Science Part C: Polymer Symposia*, Wiley Online Library: 1964; pp 183-195.
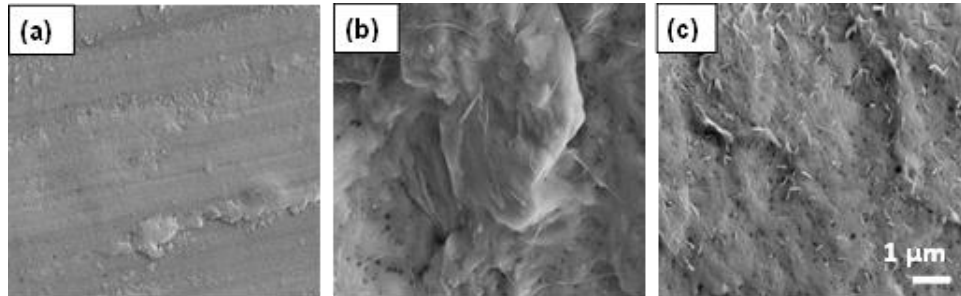
Figure 3.1 SEM images of the cryo-fractured surfaces of (a) PA6, (b) 3%CNC and (c) 3%APS-CNC nanocomposites samples.
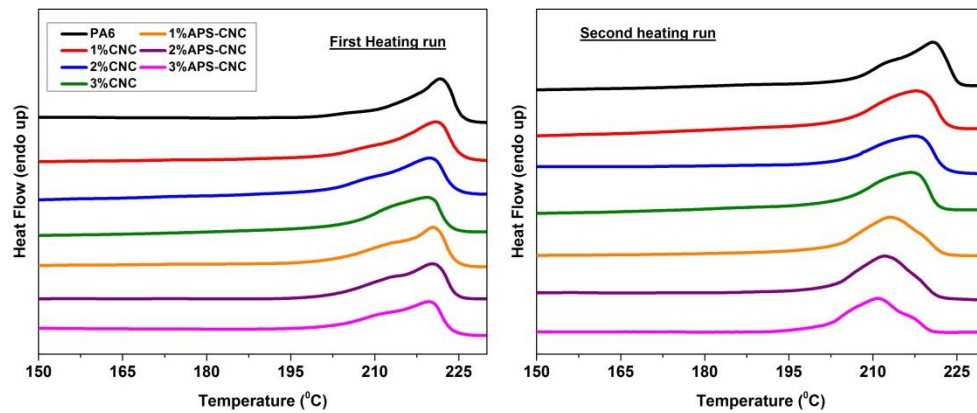
Figure 3.2 First and second DSC heating thermograms of PA6 and its nanocomposite samples.
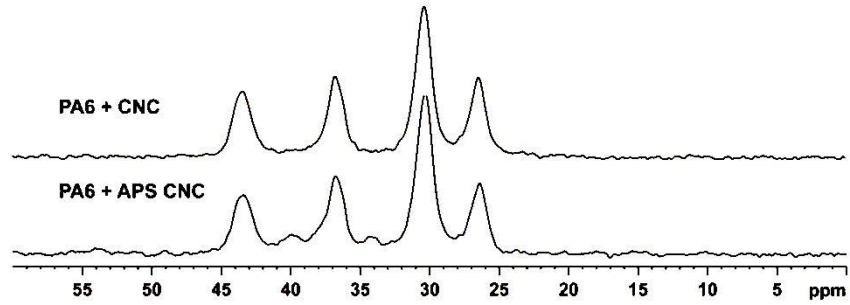
Figure 3.3 Solid state ^{13}C CPMAS NMR spectra for PA6/3%CNC and PA6/3%APS-CNC samples.
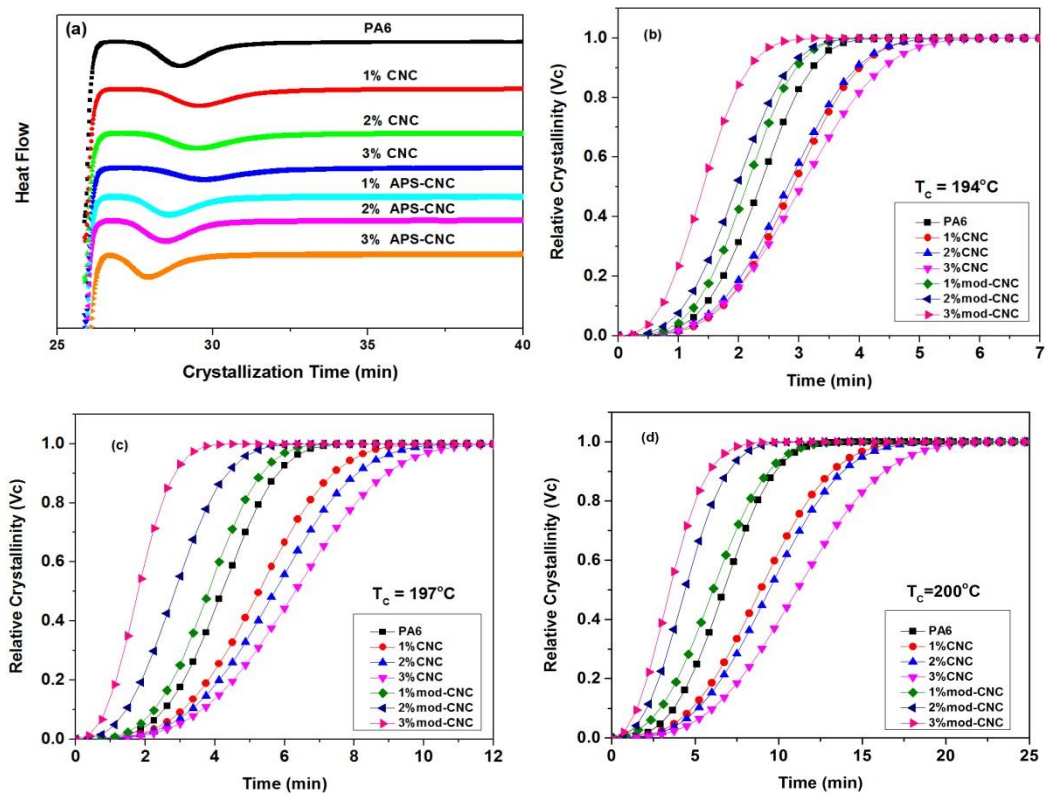
Figure 3.4 (a) Isothermal crystallization exotherms at 194°C, variation of relative degree of crystallinity versus time at crystallization temperatures of (b) 194°C, (c) 197°C and (d) 200°C.
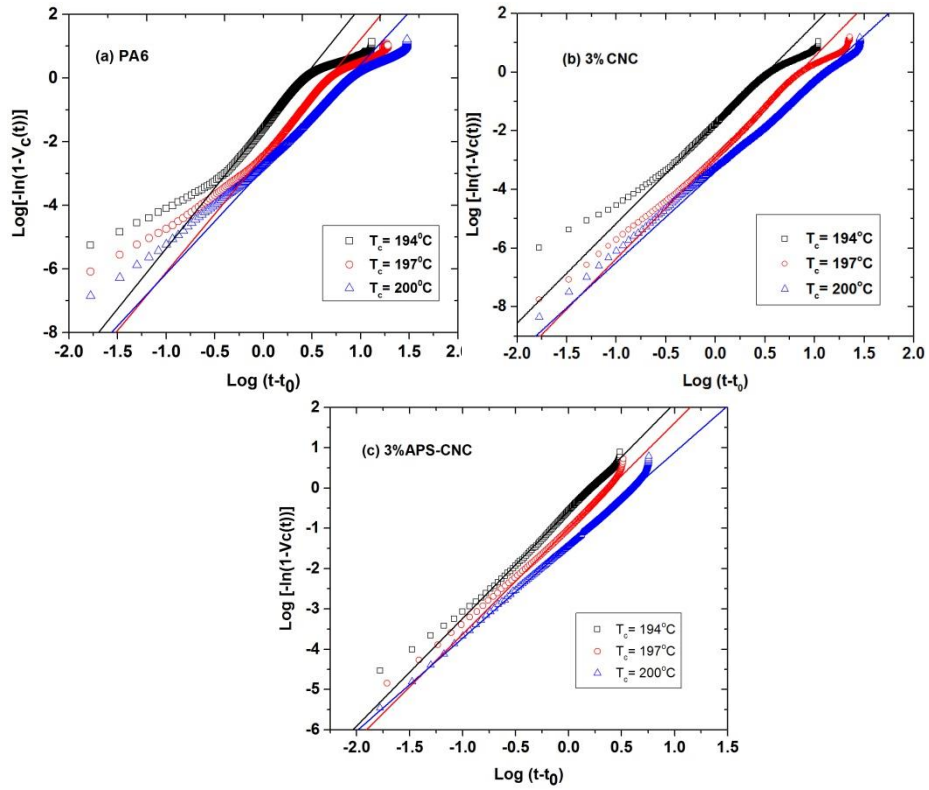
Figure 3.5 Avrami plots of log[-ln(1-V_c(t))] vs log (t-t_0) for isothermal crystallization of (a)PA6, (b)3%CNC and (c)3%APS-CNC nanocomposites.
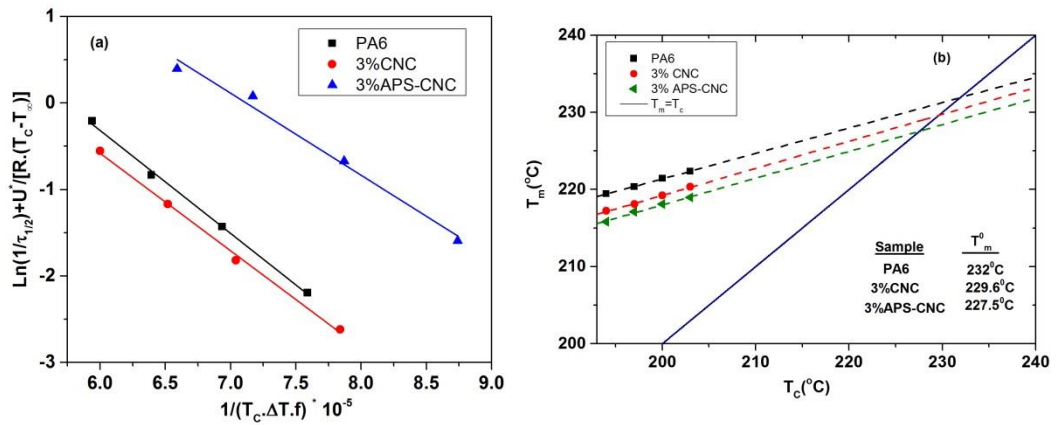
Figure 3.6 (a) Lauritzen-Hoffman plot and (b) Hoffman-Weeks plot for PA6, 3%CNC and 3%APS-CNC nanocomposites.
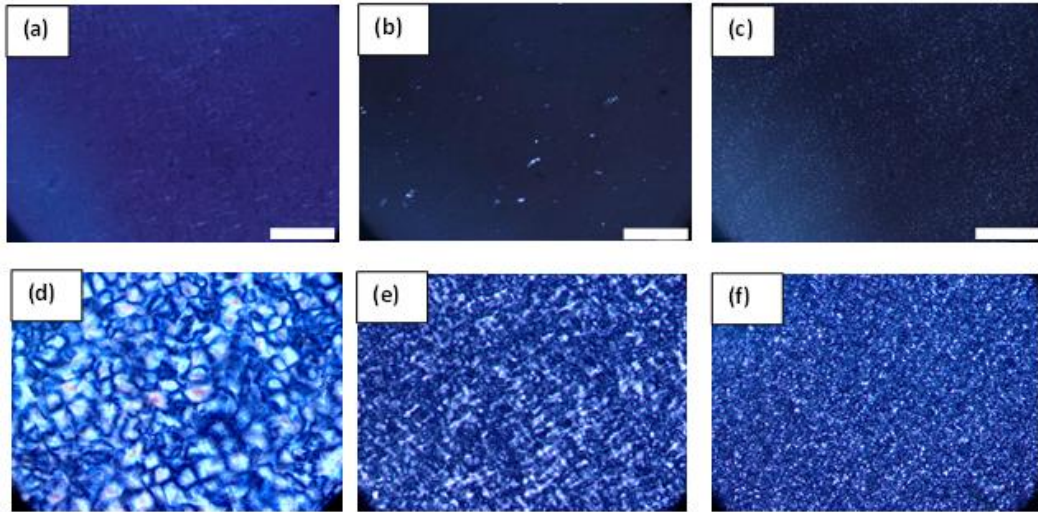
Figure 3.7 POM images during the early stages of crystallization (nucleation) of (a) PA6, (b) 3%CNC and (c)3%APS-CNC and the final morphology of the developed crystals after isothermal crystallization and cooling to room temperature for (d) PA6, (e) 3%CNC and (f)3%APS-CNC samples.(scale bar is 50µm).
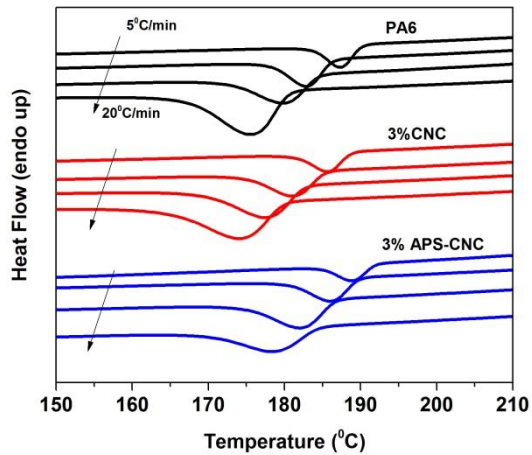
Figure 3.8 Non-isothermal crystallization exotherms of PA6, 3%CNC and 3%APS-CNC samples at four different cooling rates of 5°, 10°, 15° and 20°C/min (The arrow shows the sequence of cooling rate increasing from 5° to 20°C/min).

160
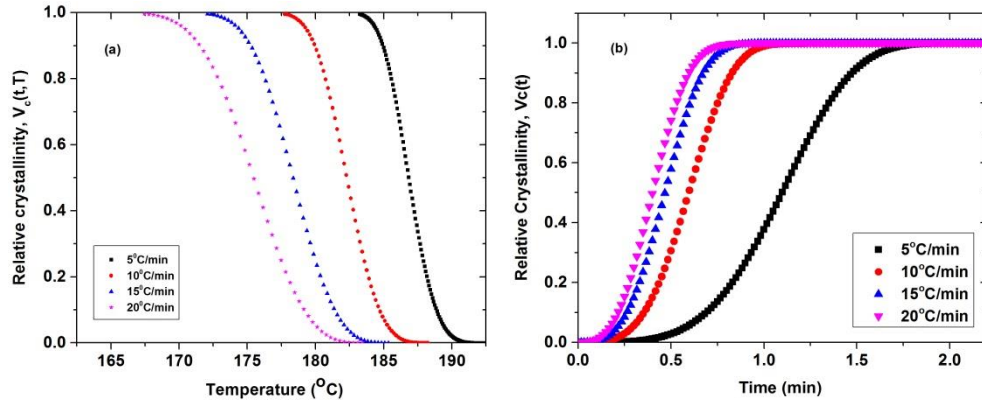
Figure 3.9 Variation of relative degree of crystallinity versus (a) temperature and (b) versus time for neat PA6 sample.
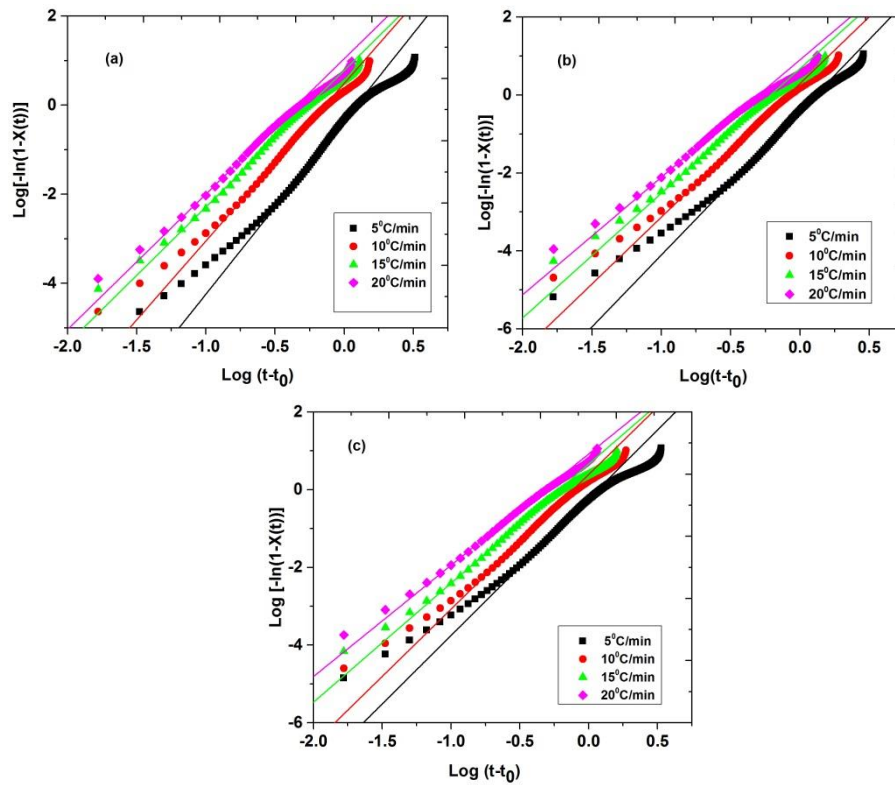
Figure 3.10 Avrami plots of non-isothermal crystallization of (a) PA6, (b) 3%CNC and (c)3%APS-CNC.
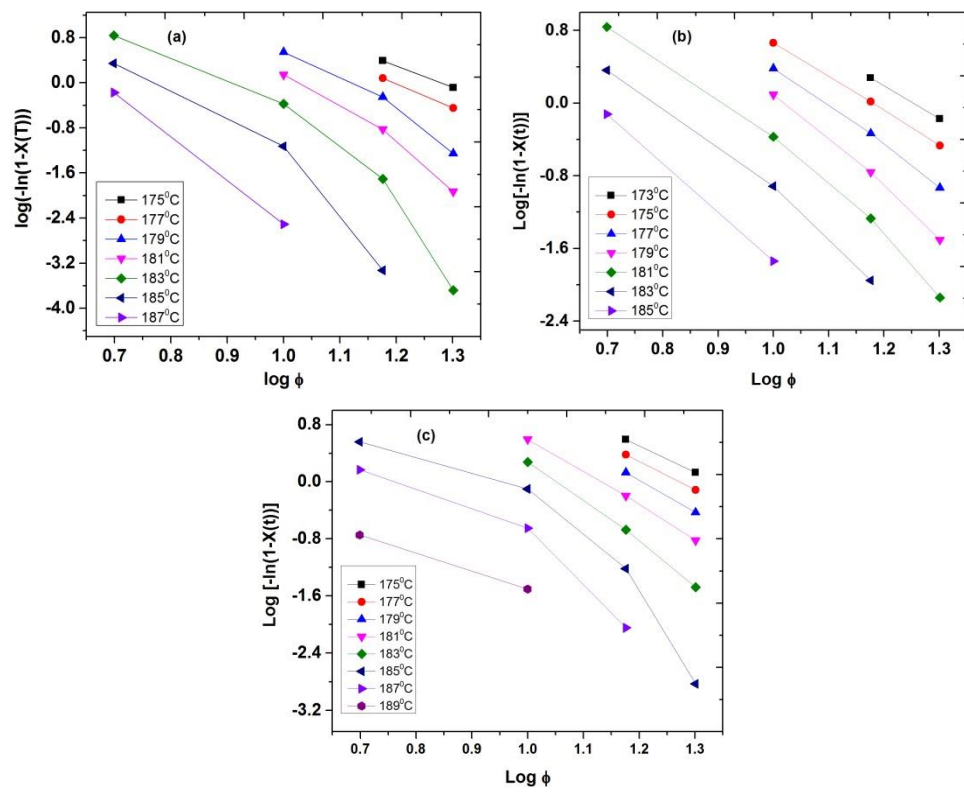
Figure 3.11 Ozawa plots of (a) PA6, (b) 3%CNC and (c) 3%APS-CNC
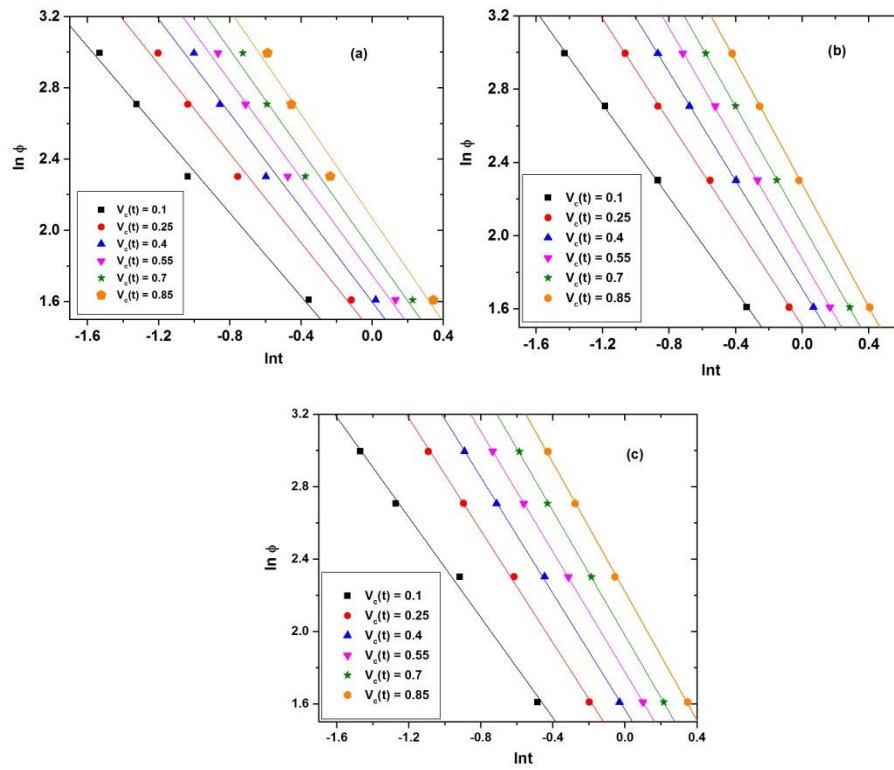
Figure 3.12 Lnφ vs. Lnt from the Mo's equation for (a) PA6, (b) 3%CNC and (c) 3%APS-CNC nanocomposites.
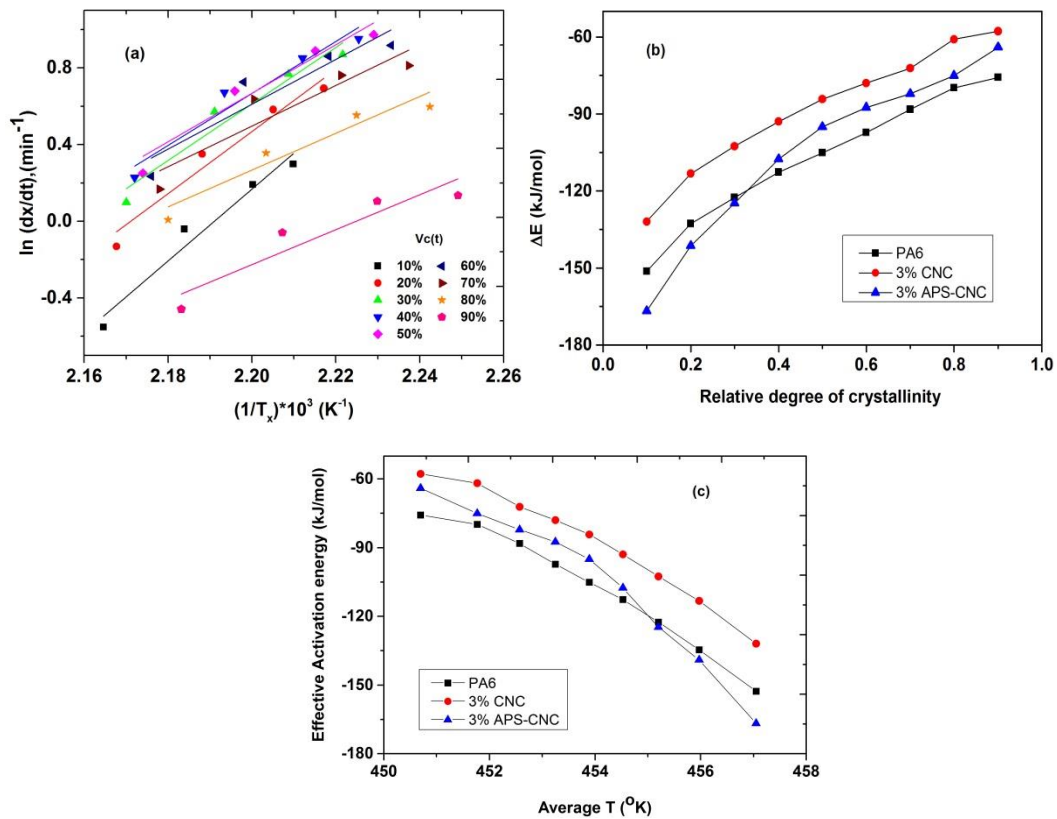
Figure 3.13 (a) Friedman plots of ln (d*X*/d*t*) vs. 1/T_X for the PA6 at different relative degrees of crystallinity, (b) Dependence of the effective energy barrier on the relative degree of crystallinity and (c) dependence of the effective energy barrier on average temperature of PA6, 3%CNC and 3%APS-CNC nanocomposites.
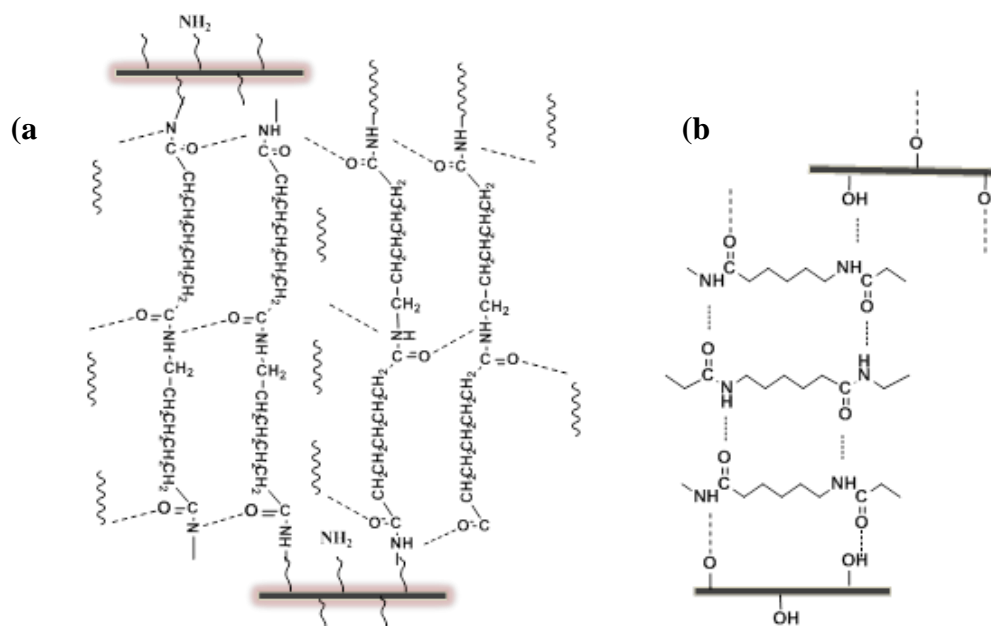
Figure 3.14 Schematic representation of (a) the γ-crystal structure formed at the interfacial area of the APS-modified CNC particles and (b) α-crystal formation in absence of the grafted chains.

Table 3.1

Thermal properties of PA6, PA6/CNC and PA6/APS-CNC nanocomposites.

Sample	First heat run				Second heat run after cooling at 10°C/min			
	T_{m1} (°C)	T_{m2} (°C)	ΔH_m (J/g)	χ_c (%)	T_{m1} (°C)	T_{m2} (°C)	ΔH_m (J/g)	χ_c (%)
PA6	222.4(0.4)	-	55.1(1.5)	29.0	218.6(0.2)	-	52.6(0.4)	27.7
1%CNC	221.1(0.3)	-	53.4(0.9)	28.1	218.1(0.2)	-	48.4(1.2)	25.7
2%CNC	219.8(0.1)	-	48.8(0.4)	25.7	218.1(0.3)	-	45.1(1.1)	24.2
3%CNC	219.2(0.4)	-	44.5(0.2)	23.4	217.3(0.5)	-	42.6(0.6)	23.1
1%APS-CNC	221.2(0.2)	-	53.6(0.4)	28.2	219.1(0.3)	213.3(0.4)	50.8(0.7)	27.0
2%APS-CNC	220.8(0.3)	-	50.8(0.6)	26.8	219.2(0.8)	212.2(0.2)	48.3(0.2)	25.9
3%APS-CNC	220.1(0.5)	-	48.2(0.4)	25.3	217.3(0.5)	211.1(0.1)	45.1(0.4)	24.5

Tm1 and Tm2 respectively denote melting temperatures of α- and γ-type crystals. Values in parenthesis are standard deviation.

Table 3.2

Kinetic parameters obtained from Avrami analysis of isothermal crystallization of PA6, PA6/CNC and PA6/APS-CNC nanocomposites.

Sample	T_c (°C)	n	$K \times 10^4$ (min^{-1})	$t_{1/2}$ (min)
PA6	194	3.81	275.5	2.38
	197	3.66	36.3	4.25
	200	3.28	13.8	6.77
1%CNC	194	3.71	135.1	2.93
	197	3.53	19.7	5.31
	200	3.12	8.4	9.02
2%CNC	194	3.54	187.4	2.87
	197	3.49	15.7	5.75
	200	3.15	5.8	9.51
3%CNC	194	3.39	187.7	3.13
	197	3.44	12.3	6.39
	200	3.09	4.1	11.18
1%APS-CNC	194	3.66	438.1	2.15
	197	3.48	55.5	3.86
	200	2.98	23.6	6.73
2%APS-CNC	194	3.22	794.7	1.98
	197	2.93	356.2	2.87
	200	2.68	147.7	4.43
3%APS-CNC	194	2.67	2754.2	1.42
	197	2.62	1000.3	1.78
	200	2.30	380.2	3.45

The reported crystallization half-times (t1/2) are experimental values.

Table 3.3

Parameters of Hoffman-Lauritzen analysis of isothermal crystallization of PA6, PA6/CNC and PA6/APS-CNC nanocomposites.

	PA6	3%CNC	3%APS-CNC
$K_g * 10^{-5}$ (K^2)	1.17	1.25	0.95
σ (mJ/m^2)	30	30	30
σ_e(mJ/m^2)	7.46	7.87	5.91
q (J)*10^{20}	2.46	2.62	1.91

Table 3.4

Kinetic parameters for non-isothermal crystallization of PA6 and PA6 nanocomposites with 3% of CNC and APS-CNC.

Samples	φ (^{0}C/min)	T_P (^{0}C)	$t_{1/2}$ (min)	n	Z_t	Z_C
PA6	5	187.3	1.12	3.9	0.47	0.86
	10	182.9	0.62	3.6	3.11	1.11
	15	179.4	0.48	3.2	5.92	1.12
	20	176.8	0.42	3.0	11.65	1.13
3%CNC	5	185.6	1.18	3.7	0.38	0.82
	10	181.1	0.75	3.4	1.95	1.06
	15	177.6	0.58	3.2	4.52	1.10
	20	174.4	0.48	3.0	7.94	1.11
3%APS-CNC	5	188.9	1.05	3.5	0.61	0.90
	10	186.1	0.71	3.4	2.63	1.10
	15	182.1	0.57	3.0	4.81	1.11
	20	178.4	0.46	2.8	8.34	1.11

Table 3.5

Results of Mo's analysis kinetic parameters at various degrees of relative crystallinity.

Relative degree of crystallinity	PA6		3%CNC		3%APS-CNC	
	α	F(T)	α	F(T)	α	F(T)
0.1	1.16	3.20	1.27	3.29	1.38	2.63
0.25	1.25	4.18	1.40	4.52	1.55	3.72
0.4	1.32	4.94	1.48	5.53	1.60	4.84
0.55	1.36	5.74	1.58	6.51	1.66	5.91
0.7	1.41	6.46	1.60	7.87	1.72	7.23
0.85	1.45	7.88	1.69	9.78	1.77	9.21

CHAPTER IV – THE EFFECTS OF THE INTERFACE ON MICROSTRUCTURE AND RHEO-MECHANICAL PROPERTIES OF POLYAMIDE 6/ CELLULOSE NANOCRYSTAL NANOCOMPOSITES PREPARED BY *IN-SITU* RING-OPENING POLYMERIZATION AND SUBSEQUENT MELT EXTRSUION

Manuscript submitted to *Macromolecules*

Abstract

Polyamide 6 (PA6) nanocomposites containing cellulose nanocrystals (CNCs) were prepared via a multi-step process consisting of in-situ anionic ring opening polymerization and subsequent melt extrusion. The effect of surface modification of the CNCs with aminopropyl triethoxysilane (APS) was studied in detail using microscopic, mechanical and rheological techniques and compared with those of the neat CNC nanocomposites. Solid state NMR analysis was used to confirm the interfacial bond formation between the PA6 matrix and surface modified CNCs. SEM images showed that upon surface modification, the morphology of CNCs within the matrix transformed from a fribrillar structure towards more individually dispersed nanocrystals with enhanced dispersion and higher interfacial area. The matrix-particle interfacial region was further investigated using quantitative nanomechanical mapping (QNM) to study the role of interfacial modification on thickness of interphase and gradient of modulus across the interface. The quality of dispersion and development of the rigid interfacial layer in modified system resulted in significant improvement in solid state mechanical properties of the nanocomposites. In addition, melt rheological studies suggested a significant improvement of melt elasticity and strength in shear and elongational flows as well as prolonged relaxation behavior in the hybrid systems.

4.1 Introduction

Cellulose nanocrystals (CNCs) have received significant attention in academia and industry in recent years as reinforcement nanofillers in polymer nanocomposites due to their exceptional mechanical properties like a Young's modulus values in the range of 100-170 GPa (depending on the source), high surface area of several hundred m^2/g providing a significant interfacial area to interact with the host polymer, inherent bio-renewability and natural abundance, as well as, their lower density compared to that of other nano-reinforcements such as clay [1-8].

The intrinsic abundance of surface hydroxyl groups on cellulose nanocrystals provides a wide window of opportunity for design flexibility of surface chemistry and potential strong interactions with polymers. However, CNCs have some practical use limitations in terms of achieving a good dispersion in a polymer matrix [9-11]. A typical route for extraction of CNCs from various natural resource materials involves treatment in acidic solutions followed by lyophilization that leaves the nanocrystals in highly aggregated state due to strong hydrogen bonding, making their dispersion in polymers a challenging task [12-14]. As a consequence, most of the applications of CNCs have been limited to either aqueous processing medium such as polymer latex or solution casting of water soluble polymers in order to achieve a desirable state of dispersion due to the colloidal stability of charged CNC surface [2, 15]. In a pioneering work done by Favier et al [16-17], cellulose whiskers were used as reinforcement fillers for poly(styrene-co-butyl acrylate) latex through solvent casting method where a two orders of magnitude improvement of the rubbery storage modulus was observed with the addition of 6 wt% whiskers. This enhancement of mechanical properties was ascribed to formation of a

percolated whisker network within the polymer matrix. Other water soluble polymer nanocomposite systems such as poly (vinyl alcohol) [18] and poly(ethylene oxide) [19] have also been prepared using solution casting from aqueous medium.

In addition to water, a number of organic polar aprotic solvents such as dimethylformamide (DMF), dimethyl sulfoxide (DMSO), N-methylpyrrolidone (NMP), m-Cresol and formic acid have been shown [20] to be capable of dispersing CNC whiskers depending on the surface charge of the CNC surface. For example, stable suspension of CNC in DMF was used in preparation of polyurethane [21] and PMMA [22] nanocomposite films via solution casting method.

In contrast, utilization of conventional melt processing methods widely used for thermoplastic materials such as extrusion has been challenging due to the difficulty of effective dispersion of CNC in the matrix, as well as, thermal degradation of the CNC at typical elevated processing temperatures [9, 23]. A large number of studies have been focused on preparation of CNC based nanocomposites using extrusion process with various polymer matrices including polyethylene [23-24], polypropylene [25-26], polystyrene [27], polylactic acid (PLA) [10, 28], polyvinyl chloride [29] and poly(3-hydroxybutyrate-co-3-hydroxyvalerate) (PHBV) [30] ,poly(ε-caprolactone) [31] and thermoplastic starch [32]. Different strategies have been developed in order to improve the dispersion of CNC and enhance its compatibility with the polymer melt (for e.g., wrapping polymer layer such as poly(vinyl alcohol) [33] in a PLA matrix or PEO layer in a polyethylene matrix [23]). In other approaches, use of anionic surfactant [28] was found to improve the dispersion of CNCs in the PLA matrix during extrusion with improved mechanical properties up to a 5% threshold of surfactant used. In another approach, Goffin *et al* [34] grafted PLA chains on

the CNC surface via surface initiated ring opening polymerization and melt extruded the modified CNC particles with PLA matrix. Their results showed enhanced compatibility between the PLA-*g*-CNC and PLA matrix indicated by improvement of mechanical properties and promotion of crystallization nucleation in the matrix. Using a similar strategy, other researchers grafted poly(ε-caprolactone) (PCL) on the CNC surface by ring-opening polymerization and reported that the dispersion was significantly improved as the result of PCL graft layer due to enhanced interfacial compatibility [35].

Surface modification of CNC particles has also been used in order to improve the CNC dispersion quality and thus the structural properties of the final nanocomposite material. These approaches are mostly based on surface silylation [36] by organo-silane coupling agents and acetylation [37] to convert the surface hydroxyls to alkyl esters. For example, Grunert *et al* [38] trimehtylsilylated the CNC surface in formamide in order to reduce the surface hydrophilicity and make the CNCs compatible with cellulose butyrate acetate matrix. Yu *et al* [39] used 3-isocyanatepropyltriethoxysilane by the reaction of isocyanate groups of the silane coupling agents with CNC surface hydroxyls and incorporated the modified CNCs in silicone elastomer which resulted in significant improvement of CNC dispersion and mechanical properties of the reinforced elastomer.

To our knowledge, the number of research efforts on incorporation of CNCs in engineering thermoplastics with high melting points (above 200°C) has been very limited. Kiziltas and co-workers [40-42] melt processed microcrystalline cellulose (MCC) with polyamide 6 matrix in a Barbender® mixer to yield polyamide 6/MCC composites. The rheological characterization of the composites by the authors just mentioned showed that the melt elasticity and viscosity at high MCC content was increased due to molecular

motion inhibition in crystal formation in presence of MCC. Correra et al [43] used a combination of casting and melt processing method to fabricate nano-cellulose reinforced PA6 composites and their obtained results showed promising reinforcing capability even at very low CNC content of 1 wt% compared to that obtained via direct melt mixing due to better dispersion of CNCs in the matrix.

The current study described in this article is part of a long-range research program aimed at developing a novel technique to process polyamide6/CNC nanocomposites using *in-situ* anionic ring-opening polymerization (ROP) with enhanced and tunable structure and properties that complements our previous study reported elsewhere[44-45]. Here, we specifically describe an approach based on *in-situ* ROP and subsequent melt extrusion of PA6/CNC systems and the role of microstructure development with regard to the effect of surface modification of CNCs on rheological and mechanical properties with special focus on the role of the interfacial characteristics. In addition, the obtained PA6/CNC systems will be compared with that prepared via conventional direct melt processing for their mechanical properties. It is hoped that the current study will provide a better understanding of the relationship amongst processing, structure, and properties of polyamide 6/CNC nanocomposite materials.

4.2 Experimental

4.2.1 Materials and Sample Preparation

The AP-Nylon® caprolactam grade (purchased from Brueggemann Chemical, Pennsylvannia) with low moisture content (< 100 ppm) suitable for anionic ring-opening polymerization was used as the monomer. C20, a difunctional hexamehtylene-1,6-dicarbamoyl caprolactam (activator), was supplied by Brueggemann Chemical.

173

Analytical reagent grade ethyl magnesium bromide (initiator) was purchased from Aldrich. Aminopropyltriethoxysilane (APS) was purchased from Gelest Inc.

The cellulose nanocrystals were prepared by sulfuric acid hydrolysis of bleached cellulose pulp (obtained from Weyerhaeuser) following the method reported by Capadona *et al* [46] with slight modifications as described in our previous publication [45].

Surface modification of CNCs was carried out using aminopropyltriethoxysilane (or APS). Briefly, a dispersion of CNC in distilled water (DI) water was sonicated for 20 minutes. In a separate flask, the APS was added (7 wt% of the CNC) to DI water and mixed for 10 minutes in order to hydrolyze the ethoxy groups into hydroxyls. These separate mixtures were mixed and the final dispersion was allowed to mix for 3 hours under continuous agitation. The dispersion was then frozen in liquid nitrogen and freeze dried to recover the CNC powder with APS adsorbed on the surface. The excess APS was washed with acetone. Finally, the polycondensation of APS with the CNC surface hydroxyl groups was carried out in a vacuum oven at 120°C under vacuum for 1 hour.

The PA6/CNC nanocomposites were prepared by *in situ* ring-opening polymerization of caprolactam monomer in the presence of CNCs and subsequent melt extrusion of the granulated master-batch nanocomposite following the method reported in our previous work [45]. The nanocomposites are named here as x% CNC where 'x' denotes the CNC content in weight percent. The direct melt mixed (control) samples were prepared by granulating a PA6 sample prepared by ROP (with no CNC) followed by direct extrusion at the same screw speed with the desired amount of dried CNC.

174

4.2.2 Microscopy

SEM images were acquired using a Sigma field-emission scanning electron microscope (ZEISS®, USA) using a 5 kV accelerating voltage. Images were taken from the smooth cryo-fractured surfaces as well as fractured surfaces of tensile test samples. The surfaces of the samples were sputter-coated with silver for enhanced conductivity.

TEM images were acquired from CNC dispersions and nanocomposite samples using a ZEISS EM10® transmission electron microscope at accelerating voltage of 50 kV. For the CNC particle imaging, an aqueous dispersion of CNC (unmodified and APS-modified) in the concentration range of 0.1-0.3wt% was prepared and a small drop was placed on a TEM copper grid prior to TEM imaging. For the nanocomposite samples, a thin slice of the sample was microtomed from the tensile dumbbell specimens in perpendicular direction to gauge cross-section (i.e., parallel to injection molding direction) taken from the middle of the sample (not surface layer) using a Leica ultramicrotoming device equipped with a diamond knife. The samples were stained with phosphotungstic acid ($H_3PW_{12}O_{40}$) when needed in order to enhance the contrast.

4.2.3 Thermal Analysis

Thermogravimetric analysis (TGA) was performed on the pristine and APS-modified CNC as well as the nanocomposite samples using a Q500 TA® Instruments TGA with a heating rate of $10°C.min^{-1}$ under a nitrogen atmosphere with a gas flow rate of $40mL.min^{-1}$.

4.2.4 ATR-IR Spectroscopy

ATR-IR spectra were obtained from samples using a Nicolet 6700 FT-IR spectrometer in the range of 4000-400 cm^{-1} with a total number of 1028 scans with the

resolution of 4 cm^{-1}. The samples used were thin films of pristine and APS-modified cellulose nanocrystals.

4.2.5 Solid State NMR

Solid-state ^{13}C NMR spectroscopy was performed on a Varian Unity Inova® 400 NMR spectrometer equipped with a standard Chemagnetics 7.5 mm CP/MAS probe. Samples were loaded into zirconia rotor sleeves, sealed with Kel-F™ caps, and spun at rate of 4.5 kHz. Spectra were obtained via cross-polarization (CP) technique. Cross-polarization spectra were acquired using a 10 ms contact time with the carbon power varied from 41.3 to 50.5 kHz. Other relevant parameters used include a ^{1}H 90 pulsewidth of 5.5 μs, a recycle delay of 3 s, and an acquisition time of 45 ms. The number of co-added scans was 7488. A ^{1}H decoupling field of 53 kHz was implemented during the data acquisition time in order to remove ^{1}H-^{13}C dipolar coupling. Gaussian line broadening of 50 Hz and zero-filling of 128k was applied to the data prior to Fourier transformation. Baselines were corrected using a 3rd order Bernstein polynomial as implemented in the MestReNova® software.

Solid-state ^{29}Si NMR data was obtained using the Varian Unity Inova 400 NMR spectrometer. The cross-polarization technique was used. Data acquisition parameters were as follows: The ^{1}H 90 pulse width was 5.0 μs, the recycle delay was 3 s, and the acquisition time was 45 ms. The contact time was 3 ms, with an amplitude of the ^{29}Si channel varied linearly from 42 - 57 kHz. A ^{1}H decoupling field of 51.0 kHz was implemented to remove ^{1}H-^{29}Si dipolar coupling. Samples were spun at 3.0 kHz, and the number of co-added scans was 106,816. Gaussian line broadening of 100 Hz and zero-filling of 256k was applied to the data prior to Fourier transformation. Baselines were

176

corrected using a 3rd order Bernstein polynomial as implemented in the MestReNova®

software package.

4.2.6 Melt Rheological Characterization

Frequency and strain sweeps, melt relaxation and squeeze flow rheological

characterizations were performed using an Anton Paar® MCR501 rheometer. The

frequency sweep test was performed using a linear strain value of 2% previously found in

strain sweep experiments to be in the linear viscoelastic region of all samples at a

temperature of 229°C in a parallel plate geometry with a gap of 1mm. The melt relaxation

experiment was done using the same experimental conditions with an initial step

deformation of 5% (in the linear region) and data was collected in the 0.07-1000s time

frame. The data point cut-off value of storage modulus of 10 Pa was chosen because the

data was noisy (i.e., data scatter) below this value (due to sensitivity of the instrument)

which could negatively interfere with the data fitting process. Prior to the relaxation

experiments, a time sweep experiment was performed to reach constant viscoelastic

material functions in order to ensure the removal of any residual stress in the melt during

the relaxation experiment. The squeeze flow (SF) tests were performed using an initial

gap value of 0.9mm under a constant force of 1.5N and the variation of gap was

monitored over time. Prior to the test, the samples were relaxed in the initial gap phase

for a thermal soak time of at least 4 minutes. All specimens used for the SF tests were

disk-shaped samples with constant surface area. A squeeze time of 900s (previously

found as a reasonable timeframe to ensure sample thermal stability) and the variation of

gap versus time was recorded.

Extensional rheological properties were investigated using a rotating drum extensional viscosity fixture (EVF) mounted on an ARES® rheometer. Rectangular samples with $18 \times 10 \times 0.75$ mm^3 dimensions were compression molded at 235°C and slowly cooled to room temperature under pressure to relax any residual stress in the sample. The extensional rheological tests were performed at 226°C (slightly lower than that of the shear rheological tests in order to prevent excessive creep and sagging of the samples at higher temperatures). The samples were equilibrated in the oven at the desired temperature for 4 minutes and pre-stretched with a rate of 0.001 s^{-1} for 30 seconds to compensate for any minimal sagging during the thermal equilibration followed by elongation at 0.01, 0.1 and 1 s^{-1} strain rates. It should be noted that all rheological experiments were conducted under dry nitrogen atmosphere. Prior to all rheological experiments, the samples were fully dried to constant weight in a vacuum oven at 80°C for at least 36 hours under a dry nitrogen atmosphere and immediately transferring the samples to vacuum desiccator for 24 hours prior to the tests.

4.2.7 Mechanical and Nanomechanical Tests

Tensile tests were performed on an Instron® 5582 tensile tester with a crosshead speed of 10mm/min at room temperature. At least 5 injection molded dogbone shaped specimens with a span length of 28mm were tested for each composition.

Quantitvative nanomechanical (QNM) properties of the nanocomposites were studied using a peak force (PF) QNM mode of a Bruker Dimension Icon 3000® atomic force microscope in tapping mode at room temperature with a standard Veeco RTESP® silicon probe (cantilever length, 125 mm; nominal force constant, 40 N/m; and resonance frequency, 350 kHz). The image size ranged from 507.8×507.8 nm^2 to 2×2 μm^2. At

least 4 different spots on 2 different thin film samples prepared by compression molding (same thermal and processing history) were analyzed to obtain the reported average modulus values. All image processing techniques were performed on the Nanoscope version 5.30 r2® image analysis software.

4.3 Results and Discussion

4.3.1 Surface Modification of CNCs, Nanocomposite Processing and Structure Development

Surface silylation of cellulose nanocrystals are typically carried out in two major ways. One method is the use of alkyl-chlorosilanes [36] where the surface condensation results in release of hydrochloric acid and a second method where modification reaction proceeds through condensation between hydroxylated organosilane with the surface hydroxyls of CNC in aqueous medium [47]. We adopted the second method because the aqueous medium provides a significantly more efficient dispersion of CNC and possibility of achieving a more uniform surface modification in addition to the more eco-friendliness of the method. The IR spectra of the unmodified and modified CNC particles are shown in Figure 4.1(a). The modification of cellulose with organosilane coupling agents has extensively been reported in the literature using IR spectroscopy [48-49]. In the present study, the evolution of the peak at 1090 cm^{-1} corresponding to –Si-O-Si- and –Si-O-C- band (broad peak at 1220 cm^{-1} corresponding to –Si-O-C- band) the peak around 1520-1530 cm^{-1} corresponding to NH_2 deformation, and also the evolution of peaks at 2850-2900 cm^{-1} corresponding to aliphatic CH_2 stretching vibration and the peaks in the range of 3500-3600 corresponding to NH_2 stretch vibration confirmed the formation of the APS layer on the CNC surface.

179

In order to further investigate the surface modification, as shown in Figure 4.1(c) and (d), the TEM images of the unmodified and APS-modified CNC showed that the modified CNC carries a layer of a graft thin film on the surface. The APS surface modification does not seem to have noticeable effect on the dimensions and thus the aspect ratio of the whiskers. The unmodified and modified CNC were also dispersed in aqueous medium to assess the dispersibility of the particles in water. As seen in the insertion image in Figure 4.1(a), while the unmodified particles are fully dispersed in water at colloidal level forming a rather clear dispersion, the modified particles seem to form less dispersed clusters increasing the dispersion opacity. This shows that the dispersibility of the APS-CNC in water is reduced due to the masking of surface hydroxyl groups by polysiloxane layer, making it less hydrophilic in aqueous medium.

The amount of the grafted polysiloxane layer on the CNC surface was estimated using TGA shown in Figure 4.1(b), the decomposition of the polysiloxane layer is shown to occur in the range of 250-500°C [50] . As evident in Figure in Figure 4.1(b), the difference in mass loss in the unmodified and modified CNC in the temperature range of 250° - 500°C corresponds to an average value of 3.1 wt% which is the average content of the grafted siloxane layer with respect to the CNC weight.

The effect of the presence of the CNC particles on the anionic ROP reaction of ε-caprolactam and the effect of the surface modification of the particles is shown in the insertion plot of Figure 4.1(b). As can be seen in this figure, with increasing CNC content from 1 to 3 wt% of the final PA6, the conversion of the monomer was reduced from 98.9% in the PA6 sample to 95.1% in the samples containing 3%CNC. In a previous publication [44], we reported a similar reduction of conversion with increasing CNC

concentration in a PA6 sample initiated with sodium hydride. This reduction in conversion is ascribed to both the presence of surface hydroxyl groups which could act as a potential protonating agent that deactivates the growing anionic centers, as well as, the reported so-called "peeling" effect of cellulose in strong alkali medium which has been shown to be more prominent in the case of strong alkali [51]. Because a weaker initiator was used in the system in the current study, this effect was minimized. In addition, the conversion of the monomer in the case of APS modified CNC particle showed slight increase across all CNC content which again confirms the role of exposed surface hydroxyls (i.e., methylol) as a deactivation path of anionic polymerization which is expected to be less viable with a polysiloxane layer masking the hydroxyl groups. A more thorough study on the effect of initiator and ROP deactivation in the presence of cellulose is in progress and will be reported in a future paper.

The formation of interfacial bond between the APS-CNC and the matrix was investigated through solid state ^{29}Si NMR analysis. It has been shown that the ^{29}Si NMR spectroscopy is a powerful tool in determining the structure of the polysiloxane oligomeric species [52]. According to the nomenclature used by Glasser *et al* [53] the T structures correspond to the R-Si- moieties with one organic moiety side group and three siloxane bridges. In this context, the T^0 structure corresponds to the silicon moieties without any siloxane bridge, the T^1 structure is the dimer composed of two alkoxy-silanes bonded through a siloxane bridge, the T^2 structure is the linear form of polysiloxane oligomers while the T^3 structure is related to the 3-dimensional polysiloxane network with the silicon atom of interest having three bonded siloxane bridges. The ^{29}Si NMR spectrum of the APS-CNC particles is shown in Figure 4.2(a). It is seen from this figure

that a major peak appears at -68 ppm which correspond to the majority of T^3 structure, showing that the polysiloxane layer formed on the CNC surface is mainly in the form of 3D crosslinked network. In addition, the minor peak at around -59 ppm is related to a minority of linear T^2 structure. In order to investigate the interfacial bond formation, solid state ^{29}Si NMR spectra of the nanocomposite sample (3% APS-CNC) after the *in-situ* ROP reaction and melt extrusion were acquired in order to analyze the differences. It is seen from Figures 4.2(b) that a shoulder in the downfield region of the main peak at -66.1 ppm is appeared which is associated with the change in the polarity of the amine group on the aminopropyl alkyl group where the polarity of N-H bond in primary amine reduces when converted to amide bond. The upfield shift of the main peak could be attributed to the formation of tertiary amine through chain branching of the APS layer with the matrix. Thus, the solid state NMR result is an evidence of the interfacial bond formation.

It is worthy to note that the formation of interfacial bond proceeds via two major routes as depicted in the Figure 4.2(d). The first path is through transamidation reaction that occurs at elevated temperatures by nucleophilic attack of the primary amine group of the aminosilane on the amide bond of the formed PA6 chains in the bulk (i.e., grafting onto CNC) which is a commonly accepted mechanism of the interfacial bond formation in polyamide systems both in anionic polymerization and melt processing [54-55]. The second plausible pathway for interfacial bond formation is through the de-blocking of the isocyanate capped activator (C20) which could consequently result in the reaction of the free isocyanate group with the amino group (i.e., urea bond formation) on the APS thereby chemically tethering the caprolactam monomer (initiating site) on the polysiloxane surface layer resulting in further surface-initiated ROP reaction (grafting

from CNC). This second path is rather less significant because the ROP reaction was carried out at 150°C which is lower than the typical de-blocking temperature of C20 (which is around 162°C). However, the possibility of this second pathway cannot be ruled out due to local elevated temperatures caused by reaction exotherm.

In addition, after the melt extrusion, the relative intensity of the shifted peak (from -68.0 to -70.2 ppm) becomes greater compared to the shoulder (the deconvoluted peaks) that was present at -67.3 ppm (Figure 4.2). This shoulder was indeed located at -65.3 ppm in the APS-CNC particle samples which could be related to a fraction of the linear polysiloxane structure which is also undergoing the upfield shift due to the interfacial reaction with the matrix. These results suggest that the subsequent melt extrusion after *in-situ* ROP enhances the interfacial reaction between the aminosilane and PA6 matrix.

The SEM images of the morphology of the nanocomposite samples are depicted in Figure 4.3 where the microstructure and dispersion of the CNC (both neat CNC and APS-CNC) in the nanocomposite are shown. Clearly, this figure shows that the cellulose whiskers tend to form web-like fibrillar 3-dimensional network structure after *in-situ* ROP reaction which is caused by the edge-edge effect of the CNCs resulting in development of the fibrillar morphology. In our previous publication [44], we demonstrated the evolution of this 3D network structure of CNC fibrils as the concentration of CNC increases from 1 to 3 wt% within the *in-situ* polymerized PA6/CNC samples. Initially, at lower concentrations, smaller CNC clusters are developed that subsequently grow into network-like structures as the CNC content increases.

183

In contrast, it was observed that the melt extrusion step breaks up the fibrils into relatively smaller individually dispersed whiskers. The APS-modified samples show that, after the ROP reaction, the whiskers tend to form smaller bundles instead of large web-like structures which, like the unmodified particles, tend to break up into smaller domains due to the shear force field of the extrusion process. It is clear from these images that the modification of the CNC surface with APS gave significantly improved dispersion of CNC into more individual whiskers within the PA6 matrix, leading to increasing polymer-particle interfacial area and associated enhanced structural properties as described in the following sections.

In order to further investigate the dispersion of the CNC and APS-CNC in the PA6 matrix, solid state CP/MAS ^{13}C NMR studies were conducted on the composite samples and the changes in the NMR peaks were correlated with the observed structural changes. The CP/MAS ^{13}C NMR of the neat CNC, APS-CNC, as well as, that of the 3%CNC and 3%APS-CNC nanocomposite samples are shown in Figure 4.4. Considering the structure of the anhydroglucose units, the peaks at 62-65 ppm correspond to C6 methylol carbon atom where the strong peak at 65.2 ppm correspond to the crystalline core region, the carbons of C2, C3 and C4 overlap in the 70-75 ppm region. In addition, the C4 carbon which corresponds to cellulose I structure appeared at 84 and 89 ppm where the peak at 89 ppm is related to the more ordered structure while the shoulder at 84 ppm correlates with less ordered surface units. The singlet peak at 105.3 ppm corresponds to C1 carbon (allomorph cellulose Iα) [56-57]. These results show that the modification of the CNC with APS does not change the structure of CNC as evidenced by the similar peaks in the NMR data.

The spectra of the nanocomposite samples show that the PA6 peaks appeared in the range of 20-50 ppm where the peaks around 37 and 40 ppm correspond to α- and ω-carbons of polyamide, respectively. The peaks at around 25ppm and 30 ppm correspond to β- and δ/γ-carbons, respectively, and the carbonyl group appeared at 175 ppm. By comparing the spectra of the neat CNC and APS-CNC in the PA6 matrix, it can be seen that the peaks corresponding to crystalline CNC in the 60-90 ppm range merged and formed a broad resonance in this region for the APS-CNC sample while these peaks are nearly unchanged in the case of unmodified CNC in the PA6 sample. This observation indicates that the modified nanocrystals are not in their original form when incorporated into the PA6 melt in contrast to what was observed for the pure CNC and PA6/CNC samples. Note that this observation is in excellent agreement with the morphological images (SEM) showing a relatively finer dispersion of CNC whiskers in the case of APS-CNC within the PA6 matrix compared to that of the neat CNC where larger clusters and fibrillar structure existed in the matrix as already described. In fact, the broadening of the resonance (60-90 ppm) suggests that the highly packed CNC clusters in their pure form (due to strong hydrogen bonding) and in fibrillar form in the composite samples (PA6/CNC) is disrupted in the PA6/APS-CNC sample due to the stronger interfacial adhesion and compatibility and the associated enhanced dispersion within the matrix. It is worthy to note that in a previous study Misra et al [58] used a similar solid state NMR analysis to confirm the improved dispersion of highly crystalline nanoscale polyhedral oligomeric silsesquioxane (or POSS) molecules in polymer matrix by enhancing the particle-polymer compatibility where resonance broadening was observed and attributed to the reported improved nanoparticle dispersion.

The thermal stability of the PA6/CNC nanocomposites was investigated after the

in-situ ROP reaction to investigate the structural stability of these systems during the

subsequent melt extrusion step. The TGA curves of the neat PA6, CNC and that of the

nanocomposite samples with 1-3 wt% of CNC are shown in Figure 4.5. Clearly, this

figure shows that the pure PA6 shows a predominantly single major thermal degradation

peak occurring at around 375°C. The first derivative of TGA graph (DTG) peak of the

CNC appears at 305°. The nanocomposite samples showed a relatively complex

degradation behavior where the 1%CNC sample showed a multi-step degradation process

with the first major DTG peak at 314°C, a second smaller peak at 357°C, and the third

major peak at 392°C. The samples with 2 and 3 wt% CNC showed slight improvement in

the thermal stability with the major degradation peaks occurring at 407°C and 415°C. It is

evident in Figure 4.5 that the initial DTG peak shifted towards higher temperatures and

merge into a shoulder for the samples with higher CNC content. This shows that the

coating of the CNC with PA6 macromolecular chains during the ROP polymerization

increased the thermal stability of the hybrids. In addition, the thermal stability of the

nanocomposite samples (especially the 2 and 3 wt% of CNC samples) showed slight

improvement of 30 and 60% weight loss compared to that of PA6. This observation is

attributed to the synergistic effect and strong interaction of PA6 chains and CNC surface

through hydrogen bonding that delays the degradation of individual components. Similar

observations of the improved thermal stability of cellulose whiskers in presence of

polyamide have been reported by Correa *et al* [43] in a system of solvent cast PA6/cellulose

nanocomposites.

4.3.2 Mechanical Properties and Nanomechanical Analysis of Interface

The mechanical properties of the nanocomposite samples were investigated using mechanical tensile tests. The results are shown in Figure 4.6 and the obtained values are reported in Table 4.1. It is evident in Figure 4.6 and Table 4.1 that the Young's modulus of the neat PA6 (i.e., 2.75 GPa) increased by 16%, 29% and 41% with addition of 1, 2 and 3 wt% of CNC, respectively. It is interesting to note that in the case of APS-modified CNC the modulus values are higher at all CNC concentrations with a nearly 50% increase to 4.1 GPa in the case of the nanocomposite sample with 3 wt% of APS-CNC. Similarly, the tensile strength of samples progressively increased with increasing CNC concentrations up to about 90 and 95 MPa, respectively, compared to a value of 60 MPa in the case of neat PA6 matrix. The variation in the strain at break as a function of the CNC concentration of the samples showed a decreasing trend in nanocomposite samples with both the neat CNC and APS-CNC, indicating a higher elasticity and rigidity of the nanocomposite samples compared to that of the neat PA6 and reduction of the plastic deformation behavior like other researchers have reported in the case of other nano-reinforcement additives such as clay platelets [59] and silica nanoparticles [60]. On the other hand, Figure 4.6 and Table 4.1 show that the strain at break values of the APS-CNC nanocomposite samples are higher than that of the neat CNC.

These results are consistent with the fact that the modification of CNC with reactive APS groups and formation of the interfacial bonds enhanced the elongation at break and toughness of the nanocomposites compared with that of the non-modified CNC particles. To further investigate this effect, the cross section SEM images of the fractured surfaces of the tensile test specimens of the nanocomposites with 3% of CNC and APS-

CNC are shown in Figure 4.7. It is clearly seen from these images that the fractured surface of the 3%CNC sample showed a rather smooth fracture plane with minimal plastic deformation. However, an elongated fibrillar structure is evident on the fractured sample cross-section of the 3%APS-CNC with a lot of ligament-shaped plastically deformed areas.

This observation will be further discussed in the extensional rheological properties section where elongation of the APS-CNC sample resulted in alignment of the nanocrystals in the flow (tension) direction that consequently enhanced the strength of the material in both solid and melt state. In Figure 4.7, the interfacial areas of the matrix that are bonded to the nanocrystals domains are clearly elongated into plastic deformation zones (i.e., stress-whitening regions) which is the reason for the observed enhanced elongation at break for these samples.

In order to study and compare the effect of the processing method used in preparation of the experimental samples of this study, the mechanical properties of the sample with 1-3%CNC prepared by direct twin-screw extrusion process was also tested and the obtained results are shown in Figure 4.6. As can be seen from this figure, the modulus of this sample showed only minimal improvement with increasing CNC concentration up to 2.8 GPa with 3% CNC sample. The tensile strength of the melt processed samples initially dropped to 45 MPa with addition of 1%CNC and eventually increased to a value of around 61 MPa at 2%CNC and showed negligible change with further increase in the CNC concentration to 3%. Note that the strain at break of this sample at all CNC concentrations studied gave lower values compared to that of the multi-step processed samples (i.e., ROP followed by extrusion). The cryo-fractured cross-

section of the melt processed samples is shown in Figure 4.7(c). Clearly, this figure

shows that the cellulose particles formed large agglomerates throughout the matrix due to

the difficulty in achieving good dispersion of the nanocrystals in the polyamide melt

which results in minimal polymer-particle interfacial area and effective aspect ratio of the

filler. This confirms the significant improvement of CNC dispersion in high melting point

thermoplastic matrix through the multi-step process of pre-polymerization and melt-

extrusion already discussed.

The reinforcement of the nanocomposites with cellulose nanocrystals were further

studied using a number of different micro-mechanical models. The Halpin-Tsai semi-

empirical equations are widely used successfully in predicting the elastic properties of

short fiber composites [61]. This model assumes a perfect alignment of short fibers in the

tension direction (i.e., unidirectional) in addition to the existence of a "perfect" matrix-

fiber interface. According to this model the modulus of the composite can be obtained by

the following equations:

$$\frac{E_c}{E_m} = \frac{1 + \xi \eta \emptyset_f}{1 - \eta \emptyset_f} \tag{(4.1)}$$

$$\eta = \frac{\frac{E_f}{E_m} - 1}{\frac{E_f}{E_m} + \xi} \tag{(4.2)}$$

where the E_c, E_m, E_f are respectively the tensile moduli of the composite, matrix

and fiber, φ_f is the volume fraction of the fiber and the ξ parameter is the fiber

geometrical shape parameter which in the case of prediction of tensile modulus for

circular or rectangular fiber cross-sections is considered to be ($\xi=2l/d$) where the (l/d) is

the fiber aspect ratio. The values of the model prediction for various fiber aspect ratios

together with our experimental data points and the results of the fitting on Halpin-Tsai model fit to the experimental data is shown in Figure 4.8(a). Figure 4.8 shows that the experimental values lie in a reasonable range of the aspect ratios of the fiber which was found in our previous study to be around 20 [44]. Here, the fitting parameter in our analysis (i.e., the shape parameter (ξ)) was found to be 12.2 and 17.1 for the unmodified and APS-CNC samples, respectively. These back-calculated values are the "effective" *in-situ* aspect ratios which are reasonably in agreement with the average experimental values (l/d=20).

There are two inter-related key variables to consider in this analysis which are the quality of interface and the aspect ratio of the CNC whiskers. As already discussed, the dispersion of the CNC whiskers was significantly improved upon surface modification with APS which theoretically results in enhanced aspect ratio of the whiskers (due to dispersion of individual particles or smaller clusters). On the other hand, the enhanced interfacial adhesion provided by surface grafting of the matrix on the APS layer provides a higher "quality" interface. However, because the Halpin-Tsai equation assumes existence of a perfect interface, this enhanced interfacial adhesion combined with finer dispersion of the APS-CNCs within the matrix results in the surface modified particles having higher effective *in-situ* aspect ratios as predicted by the model.

In order to investigate the effect of whisker orientation in the tensile specimens on mechanical properties, the Halpin-Kardos model was applied to our experimental data. In this model, the composite specimen is described as short fiber composite laminates of four layers with 0°, 90° and ±45° orientations where the properties of each laminate is described using the Halpin-Tsai equation. The detailed derivation of the equations is

190

presented elsewhere [62]. Briefly, the components of the stiffness matrix (engineering

constants characteristics of each unidirectional ply) are calculated using:

$$Q_{ii} = \frac{E_{ii}}{1 - v_{12}v_{21}} \quad (i = 1,2) \tag{4.3}$$

$$Q_{12} = Q_{11}v_{21} = Q_{22}v_{12} \tag{4.4}$$

$$Q_{66} = G_{12} \tag{4.5}$$

where the in-plane shear modulus can be estimated using the following equation:

$$G_{12} = G_m \cdot \frac{G_m(1-v_f)+G_f(1+v_f)}{G_m(1+v_f)+G_f(1-v_f)} \tag{4.6}$$

In Equation (4.6), the G_m is the shear modulus of the matrix ($G_m = E_m/2(1+v_m)$), v_f

is the fiber volume fraction and v is the Poisson's ratio calculated using the following

equations:

$$v_{12} = v_f \cdot v_f + v_m(1 - v_f) \tag{4.7}$$

$$v_{21} = v_{12} \cdot \frac{E_{22}}{E_{11}} \tag{4.8}$$

Where the E_{11} and E_{22} are ply stiffness parallel and perpendicular to the fiber

direction which can be obtained using the Halpin-Tsai equations:

$$E_{ii} = E_m \cdot \frac{E_{iif}(1+\xi_{ii}v_f)+E_{iif}(1+\xi_{ii}v_f)}{E_m(\xi_{ii}+v_f)+E_{iif}(1-v_f)} \quad (i = 1,2) \tag{4.9}$$

Where the $\xi_{11} = 2l/d$ and $\xi_{22} = 2$. Upon calculation of the above stiffness

parameters, the invariant terms and the modulus of the composite laminate (E_c) can be

obtained using the following sets of equations:

$$U_1 = \frac{1}{8}(3Q_{11} + 3Q_{22} + 2Q_{12} + 2Q_{66}) \qquad (4.10)$$

$$U_2 = \frac{1}{8}(Q_{11} + Q_{22} - 2Q_{12} + 4Q_{66}) \qquad (4.11)$$

$$E_c = \frac{4U_1U_2 - 4U_2^2}{U_1} \qquad (4.12)$$

The values of ν_m, E_{11f}, E_{22f}, G_f and ρ_f used for fitting were resepctively 0.3, 150GPa, 15GPa, 5GPa and 1.5g/cm^3 [63] respectively and the ν_m value used was 0.35. The result of the Halpin-Kardos analysis for various fiber aspect ratios is shown in Figure 4.8(b). This figure shows that, this model clearly underestimates the modulus values of the nanocomposite samples both for non-modified and modified CNC particles. Using this model, the *in-situ* aspect ratio of the whiskers was calculated to be greater than 200 (ξ>400) which is not in agreement with the geometrical characteristics of the CNC whiskers. There are a number of different reasons that could result in the inapplicability of the Halpin-Kardos model for this particular system. First and most important reason is the fiber orientation within the matrix. This model is well suited for fiber composite laminates with multiple orientation directions of fibers in the matrix. However, it was shown in the TEM images (Figures 4.8(c) and 4.8(d)) that the whiskers are highly oriented in the gauge section of the tensile specimens (longitudinal direction) for both the 3%CNC and 3%APS-CNC samples. Considering the anisotropic mechanical properties of the fiber (significant longitudinal strength in the fiber axis direction compared to the transverse direction), this highly-oriented arrangement of fibers results in enhancement of the mechanical properties in the longitudinal direction, therefore, the modulus values predicted by the Halpin-Kardos model are underestimated. In addition, it is known that the Halpin-Kardos model does not take into consideration the large-scale fiber-fiber

192

interactions and the presence of fiber network structures within the matrix which could be the contributing factor in the present system as already described. In the non-modified CNC samples, this effect could originate from the polysiloxane layers acting as bridges with the interfacial rigid molecular layers as will be discussed later with respect to percolation theory. In the non-modified CNC samples, the development of the fibrillar structure of the whiskers is another contributing factor as already discussed.

In order to further study the relationship of the microstructure, mechanical properties and reinforcing mechanism of the nanocomposites, the percolation model which derives from the proposed parallel-series model of Takanayagi [64] and later modified by Ouali [65] is used here. This simulation model takes into account three distinct phases of matrix, percolating filler network and non-percolating filler phase where within the framework of the model, the modulus of the composite laminate can be obtained using the following equations:

$$E_c = \frac{(1-2\psi+\psi\chi_f)E_m E_f + (1-\chi_f)\psi E_f^2}{(\chi_f-\psi)E_m + (1-\chi_f)E_f}$$

(4.13)

where the subscripts m and f refer to filler and polymer phases and ψ is a dependent variable on the volume fraction of the percolating phase (in this case the whiskers) as follows:

$$\psi = 0 \qquad for \ \chi_f < \chi_c$$

(4.14)

$$\psi = \chi_f(\frac{\chi_f-\chi_c}{1-\chi_c})^b \quad for \ \chi_f > \chi_c$$

(4.15)

where $b=0.4$ (critical percolating exponent) for a three dimensional percolating network, X_c is the critical volume fraction at which the percolation begins. According to Favier $et\ al$ [16], this parameter can be estimated using the equation of $Xc = 0.7d/l$ where

193

the *d* and *l* are the diameter and length of the whiskers. X_f is the volume fraction of fiber. The result of the percolation model analysis is shown in Figure 4.9(a).

As can be seen from this figure, the experimental values of the tensile modulus of the composites are higher than those predicted by the percolation model framework. Dufrense [66] and Tang [67] suggested that in presence of strong interfacial interactions between the CNC surface and the polymer matrix, a rigid interfacial "particle-bound" polymer layer around the CNC particles will develop which would effectively increase the "apparent" volume fraction of the rigid phase within the matrix thus resulting in mechanical properties that are higher than that predicted by the model. A number of previous studies [68-69] have also showed that there is an increasing trend in the experimental values of elastic modulus of nanocellulose-based hybrid systems as the polarity of the matrix (and thus the interfacial interaction with the CNC) increases in comparison to simulated values obtained from the model.

In the current system, this explanation is in excellent agreement with the nature of the matrix because polyamides can form strong hydrogen bonding interactions with the CNC surface in the case of non-modified CNC, and for the APS-CNC samples, the polysiloxane chemical bond further enhances the development of the apparent rigid phase. In fact, this is thought to be the main reason for the samples exhibiting larger than expected reinforcement effect even at low volume fractions of CNC.

Encouraged by the results of the micromechanical models and the effect of interface quality on the model predictions, and considering the significant effect of the whisker alignment on the mechanical properties as already discussed, we explored the application of the shear lag theory modified with an interface parameter. The shear lag

194

theory was originally developed by Cox [70] and the extensive derivation of the equations

for different fiber packing arrangements is provided by Piggott[71]. This model assumes a

perfectly elastic and isotropic matrix and fiber reinforcement where the short fibers are

aligned and packed in an orderly manner. In addition, the stress transfer from the matrix

to the fiber occurs through interfacial shear stress where the stress at the end of the fibers

is assumed to be zero. In this theoretical framework, the longitudinal elastic modulus of

the composite can be estimated using the following equation [72]:

$$E_c = E_f \left(1 - \frac{\tanh\left(\frac{\eta L}{2}\right)}{\frac{\eta L}{2}} \right) \varphi_f + E_m \varphi_m \qquad (4.16)$$

The original η function in Cox's shear lag theory depends on the elastic properties

of the matrix and fiber as well as the packing factor of the fiber within the matrix which

is typically taken as a square or hexagonal arrangement. However, Nairn [73] improved the

classical shear lag function (η) based on the equations of elasticity of transversely

isotropic materials using axisymmetric stress condition and further modified the equation

to account for the quality of interface in a generalized case where the shape function

describes the shear stress in the form of the following equation:

$$\eta = \left[\frac{2}{r^2 E_f E_m} \left[\frac{E_f \varphi_f + E_m \varphi_m}{\frac{\varphi_m}{4G_f} + \frac{1}{2G_m}\left[\frac{1}{\varphi_m} \ln\left(\frac{1}{\varphi_f + \chi}\right) - \frac{2 - \varphi_m}{2} \right] + \frac{1}{rD_s}} \right] \right]^{1/} \qquad (4.17)$$

where the χ is a correction factor in order to prevent the natural log term in the

denominator to approach zero in the case of low volume fractions of fiber and it has been

195

shown that the universal value of χ=0.009 results in acceptable agreement of the model

prediction with finite element analysis results for a number of systems [72]. The D_S in

Equation (4.17) is known as "interface parameter" which increases with increasing

interfacial adhesion or interface quality and eventually approaches infinity in the case of

"perfect" interface ($D_S \rightarrow \infty$). The interface parameter accounts for the displacement

discontinuity at the interface which in the simplest form, can be written as [74]:

$$D_s = \frac{\tau_{int}}{[w]} \qquad (4.18)$$

Where the τ_{int} is the interfacial shear stress and [w] is the axial displacement

discontinuity. A zero value of the interface parameter ($D_S \rightarrow 0$) implies a debonded

interface where the interfacial stress will be zero.

The results of the modified shear-lag simulation of the nanocomposite elastic

modulus for various interface parameter values along with the experimental modulus

values are shown in Figure 4.9(b). As suggested by Nairn [74], interfacial stiffening of the

polymer layer at the interface of the polymer-CNC hybrids, results in a "better than

perfect" interface which might even result in the negative values of the interface

parameter [75]. As shown in Figure 4.9(b), the low volume fractions of the nanocomposites

with both CNC and APS-CNC are predicted by the negative value of D_s= -4x10^5

GPa.mm^{-1} while the higher concentrations of the whiskers are predicted by the

significantly large value of $D_s = 10^6$ GPa.mm^{-1}. This result is in agreement with the

results of the percolation model and the expected interface stiffening effect of the PA6

matrix at the polymer-CNC interface. In fact, especially at lower CNC concentrations

where a better dispersion (and thus larger interfacial area) is developed, this effect

196

becomes more prominent. The large values of the D_s that is needed to properly fit the experimental data confirms the formation of the strong interfacial adhesion between the highly polar PA6 matrix and CNC surface that resulted from the hydrogen bonding and the interfacial polysiloxane chemical bonds between the APS layer and matrix in the case of the modified CNC particles.

Further analysis of the interfacial region was performed by using Peak Force QNM® which is a novel experimental tool for analysis of nanomechanical properties of soft materials and polymers. To our knowledge, only a few studies have attempted using this method in analyzing cellulose-polymer interfaces. For example, Nair *et al* [76] used it to study the effect of compatibilization of a PP based wood fiber composite modified with maleic anhydride and their reported modulus mapping results showed the broadening of interface or development of "interphase" upon chemical compatibilization. In a recent study, Pakzad and coworkers [77] studied the nanomechanics of the interface in a poly(vinyl alcohol)-poly(acrylic acid)/CNC nanocomposite systems. Their results showed a dependency of the thickness of interphase (or transitional zone from whisker to surrounding polymer) on the size of the whisker particle where CNCs with larger diameter are surrounded with a thicker interphase. This result is however, contradictory to some previous reports by Brown [78] and Li [79] who showed independency of the interphase thickness on the particle size using molecular dynamic simulations. In the current study, an initial assessment of the interphase properties is presented and more extensive investigation on the effect of the system variables (such as the size of the CNCs) on the interphase thickness is a matter for further investigation that will be reported in a future paper.

In order to study the nanomechanical properties and thickness of the interphase in the nanocomposite systems, bundles of CNC around 30nm or less in diameter were chosen and the average interphase thickness was measured by studying two different batches of each samples with measurements conducted on at least 5 different spots (satisfying the above mentioned requirement) on both sides of the particles. Two representatives QNM images of the 3%CNC and 3%APS-CNC samples together with the modulus profile of the rectangular areas specified on the images are shown in Figure 4.10(a)-(c). It is worth noting that in all samples considered; more isolated areas of the particle dispersion were chosen to minimize the effect of fiber overlapping in these thin film samples.

First of all, in the 3%CNC sample, it can be seen in Figure 4.10 that the modulus of the PA6 matrix regions vary in the range of 5-7 GPa and the modulus of the CNC bundles are in the range of 11-15 GPa as seen in the representative images shown. The modulus values of the CNC are in good agreement with the reported transverse modulus value of 15 GPa [63] and the interfacial thickness in the range of 11-13nm reported in a previous study on poly (vinyl-alcohol)-CNC hybrid systems [77]. In the 3%APS-CNC sample, the modulus of the CNC bundles are higher compared to that of the neat-CNC samples ranging between 22-25 GPa. In addition, the interfacial region extending from the matrix to that of the CNC peaks, show a higher value of modulus compared to the neat CNC samples. This increase in modulus is attributed to the presence of the polysiloxane layer together with the rigid portions of the matrix chemically bonded to the CNC surface.

Another important variable of interest is the interphase thickness which is the

distance from the CNC surface to the nearby matrix region. Here, the modulus profiles

show the CNC diameter and the thickness of interface measured from the AFM (QNM)

images. The average thickness of the interface for the 3%CNC sample was found to be

15.3nm (±4.1nm) which is surprisingly very close to the values reported by Pakzad et al

[77] in a PVA/CNC nanocomposite hybrid system (reported to be 11-13nm). In addition,

the average thickness of the interphase in the 3%APS-CNC system was found to be 118.2

nm (±23.6 nm). From the TEM images of the APS-CNC particles (see Figure 4.1) the

polysiloxane layer on the CNC was found to be in order of 30-50nm thick. Therefore, the

rigid portion of the interfacial matrix layer is roughly around 70-90 nm thick as obtained

from the difference between the polysiloxane thickness and the "overall" thickness of

interphase found by QNM. In addition to the thickness of the interphase, the modulus

gradient along the interphase can be considered. From the two representative graphs in

Figure 4.10, an average of the slope of the modulus profile along the interphase was

calculated. The values obtained are 0.27 (±0.02) for 3%CNC and 0.09 (±0.03) for the

3%APS-CNC sample. This clearly shows that the "broadness" of the interphase is higher

in the surface modified CNC particles indicating a relatively wider and more gradual

stress transfer region between the matrix and the CNC particles. It is conjectured that this

thicker interphase with a higher modulus gradient in the APS-CNC nanocomposite

samples results from the formation of the rigid PA6 layer which is chemically bonded on

the APS surface. In addition, because the ROP polymerization of the PA6 occurs in the

presence of the polysiloxane layer on the particle surface, an interpenetrating polymer

network (IPN)-type structure can develop along the interphase where the polymerized

PA6 chains are in locked position (and chemically bonded) to the siloxane layer on the CNC surface. The findings of the QNM technique are clearly consistent with the results of the micromechanical modeling, confirming the presence of the rigid interfacial matrix layer on the surface modified particles.

4.3.3 Melt Rheological Properties

Small angle oscillatory shear tests (SAOS) were carried out in order to study the rheological behavior of the nanocomposites. The variation of storage, loss modulus, and complex viscosity of the PA6 matrix and PA6/CNC nanocomposites versus frequency are shown in Figure 4.11.

It is evident from this figure that increasing the CNC content in the matrix, increases the storage and loss modulus of the nanocomposites significantly compared to that of the neat PA6 matrix especially at lower frequencies; and it is also evident that the storage modulus values are more sensitive to CNC concertation compared to that of the loss modulus values. A similar data trend has been reported for a number of other systems filled with anisotropic high surface area nano-particulates [80-81]. The low frequency region of the dynamic frequency sweep tests is dominated by large-scale chain motions where polymer chains exhibit terminal behavior in their fully relaxed state. In this region, the slope of the terminal zone of the storage and loss moduli can be described by $G' \sim \omega^2$ and $G'' \sim \omega$ [82]. In the case of the PA6 matrix, $G' \sim \omega^{1.83}$ and $G'' \sim \omega^{0.76}$ are applicable. However, upon addition of increasing CNC concentrations to the matrix, the terminal zone regions are described by $G' \sim \omega^{1.75-0.48}$ and $G'' \sim \omega^{0.76-0.64}$ with 1-3% of CNC. The reduction in the slope of the terminal region (i.e., the development of the non-terminal behavior) in the nanocomposite samples is ascribed to the formation of network-

like structure of particles through the strong interaction of fibrillar CNC with PA6 chains and other fibrils that restricts the viscous motion of polymer chains and enhances the elasticity of the system thereby resulting in the observed pseudo-solid-like behavior which is in agreement with the results of our previous report on *in-situ* polymerized nanocomposite systems [44]. Further evidence for this observation is the dominance of the G' values over G" for the 3%CNC sample throughout the frequency range studied which further supports the pseudo-solid like behavior at higher CNC concentrations. This effect is also observed in the complex viscosity data of the nanocomposites. With addition of the CNC, the zero shear viscosity of the systems increases from 1013 Pa.s for the matrix to 2390, 4620 and 21900 Pa.s in the 1,2 and 3%CNC samples, respectively. The effect of the presence of the whiskers on the shear-thinning characteristic of the PA6 matrix is also clearly evident in Figure 4.11(b). Note that while the neat matrix does not exhibit noticeable shear- thinning behavior in the η^* values (approximately constant throughout the range studied), the addition of the CNCs from 1 to 3 wt% CNC leads to a considerable decrease in viscosity at higher frequency as Figure 4.11(b) shows. This is thought to be related to the orientation of anisotropic particles in polymer melts in the flow direction which, in turn, results in disruption of the chain entanglement of the polymer. With higher CNC particle concentration, this effect is enhanced as more whisker orientation occurs, resulting in relatively higher decrease in viscosity values.

A similar trend in the data was observed in the nanocomposites with 1-3% APS-CNC particles. However, for comparison, the storage modulus and complex viscosities of 3%APS-CNC and 3%CNC are plotted in Figure 4.11(c). First of all, it is seen that both the storage modulus and viscosity values are higher for the sample with the modified

interface especially at the low frequency region. It is also interesting to note that the slope of the terminal zone of storage modulus changes from 0.48 in the 3%CNC to 0.31 in 3%APS-CNC, indicating a relatively higher restriction effect on the short range dynamics. In addition, the absolute value of the shear thinning index changed from 0.36 to 0.51 for 3%CNC to 3%APS-CNC sample respectively, suggesting that the presence of the interfacial bonds significantly enhanced the stress transfer from the matrix to particles, enhanced whisker orientation, and therefore, showed a sharper drop in viscosity. It is also very important to note that in the low frequency region (0.01-0.1 rad/s) there is a sudden sharp increase in the complex viscosity values for the 3%APS-CNC sample. This is known as the nanostructure formation signature (which breaks up at increasing frequency) where essentially an elastic fluid behavior which is a consequence of the strong polymer-particle and inter-particle interactions as already described.

In general, in polymer systems filled with anisotropic nano-scaled particulates, the response of the system in a given force field is governed by two major mechanisms. At low particle loading, the overall rheological behavior is governed by the polymer matrix while the particles affect the behavior to a certain extent through chain motion restriction. However, as the concentration of the particles and the interfacial area increases, nanostructure or network formation due to particle-particle and polymer-particles interaction dominate the observed rheological behavior [83]. The interface also plays a crucial role as the bonded interfacial polymer chains may play a role in particle interconnectivity even in cases where the particles are not overlapping (i.e., physical connection) within the matrix. In addition, the efficient stress transfer from matrix to particles (by the improved interfacial adhesion) could significantly change the rheological

behavior as observed in the current PA6/CNC system. The interfacial area created by the nanoparticles significantly changes the relaxation of the adjacent polymers in the interphase as described in more detail in the following section.

The experimentally determined plots of linear stress relaxation modulus are shown in Figure 4.12 for the nanocomposite systems with unmodified and APS-modified CNC particles. Clearly, this figure shows that in both cases at each fixed time after applying the strain, the modulus increased with increasing CNC content. A similar effect was observed with the surface modified systems. This is thought to be due to the significant chain relaxation restriction that is imposed by the cellulose whiskers which reduces the viscous flow behavior of the polymer and results in extension of the modulus relaxation under constant strain. In addition, incorporation of higher CNC concentration that is highly rigid and elastic, contributes towards the longer delay in the relaxation process. This effect is more pronounced in the APS-CNC systems because a relatively better stress transfer from matrix to CNC is offered through strong interfacial adhesion.

The relaxation process of the polymers can be described by the generalized Maxwell model with the following equation:

$$G(t) = \sum_{i=1}^{N} G_i \exp(-\frac{t}{\tau_i})$$
(4.19)

Where the τ_i and G_i are the i-th relaxation time and modulus. The value of N should be large enough to achieve a proper quantitative fit of the model to the experimental data. The relaxation modulus along with the Maxwell model fits are shown in Figure 4.12 and the spring constants and relaxation times are presented in Table 4.2 of the supporting information. It is observed that compared with the neat PA6, the

203

nanocomposite samples require a relatively large number of Maxwell elements to properly describe their relaxation process. As the CNC concentration is increased in the matrix, a higher number of Maxwell elements are required to fit the data. Similarly, More Maxwell elements are required to properly fit the experimental data obtained from the APS-CNC samples with improved interfacial adhesion compared with that required for the unmodified CNC samples, indicating a delayed relaxation process that is consistent with the observed significant reduction in viscous flow and enhanced melt elasticity. For example, while 3 elements are sufficient to adequately fit the PA6 relaxation data, 5 and 7 elements are needed to fit the samples with 3%CNC and 3%APS-CNC, respectively.

Further, the relaxation time of the elements as well as the corresponding modulus (spring constant) increases with increasing CNC content, and the interfacial adhesion is enhanced. In the neat PA6 matrix, the longest relaxation time is 0.87s, this value increased to 3.1, 7.9 and 9.4s for the 1%, 2%, and 3%CNC, respectively, and further increased to 120.3s for the 3% APS-CNC sample. This last observation is attributed to significant chain motion restriction of the APS modified cellulose whiskers on the polymer chains that is exacerbated by the strong interfacial adhesion in the surface modified samples.

Theoretically, each relaxation element corresponds to a certain mechanism within the material that undergoes this relaxation process. For the nanocomposites samples, we adopted the previously reported approach [84] where three Maxwell elements were used in order to account for the three major relaxation process namely: the polymer chains relaxation (intermediate relaxation time), interfacial relaxation at polymer-filler interface or fiber "pull-out" (longest relaxation time) and fiber-fiber interaction break-up (shortest

relaxation time). The 3-element fit to the data obtained from 3%CNC and 3%APS-CNC

is shown in Figure 4.12(c) of supporting information. This figure does not provide an

adequate fit to the experimental data especially at longer relaxation times. Nevertheless,

the fitting parameters are shown in Table 4.3. It is seen that the 3%APS-CNC sample has

higher interfacial relaxation time (6.7s) compared to that of the 3%CNC (i.e., 2.6s),

indicating a significantly harder fiber pull-out mechanism due to the strong adhesion at

the interface. This effect is further supported by the better dispersion of APS-CNC within

the matrix (as already shown in the microscopic images of Figure 4.3) that depicts

significantly higher surface area for fiber-matrix interactions that hinders the relaxation

processes.

The extensional rheological properties of polymer nanocomposites reinforced

with cellulose nanocrystals have not been a subject of study especially in engineering

thermoplastic matrices. This is an important property of these systems due to the

anisotropic properties and needle-like geometry of these nanoparticles that can

significantly change the material properties due to their orientation. The extensional

viscosity of PA6 and the nanocomposites as a function of time with an extension rate of

$0.1s^{-1}$ are plotted in Figure 4.13 showing that, with increasing the CNC content within the

matrix, the extensional viscosity increased with increasing CNC concentration. For all the

samples studied, it was observed that the extensional viscosity values initially show a

gradual increase with time until it reaches a plateau in the long-time region. As the CNC

content is increased, the viscosity starts to show a sudden further increase at longer times

which is even more prominent in the case of APS-CNC samples. This behavior is known

as "strain hardening" and has been observed previously in the case of layered-silicate

based nanocomposites [85]. For the 2% and 3% APS-CNC samples, no fixed plateau region was observed because the viscosity show an increasing rate until the strain hardening zone. As the CNC content increases, the slope of the strain hardening zone is increased. The elongated samples of 3%CNC and 3%APS-CNC were immediately quenched in liquid nitrogen and the SEM images of the surface of these stretched strings are shown in Figure 4.13(c) and (d).

Clearly, this figure shows that there is a clear orientation of cellulose whiskers in the extension direction. A primary reason for the observed strain hardening at this strain rate (which is not seen in the neat matrix) is ascribed to the orientation of whiskers in the applied force direction. In addition, the images of Figure 4.13(e) show that the thread of 3%APS-CNC sample has not ruptured after the elongation at up to 4 Hencky strain due to its higher "melt strength" compared to that of the neat PA6 matrix which ruptured. This is a beneficial attribute in applications where these nanocomposite systems are to be used in the fiber form and high melt strength of the melt is required.

The effect of various strain rates on elongational viscosity was studied on the PA6 matrix and PA6/APS-CNC nanocomposites (due to their higher melt strength) and the results are shown in Figure 4.14. It is clearly evident from this figure that for the lower strain rates of 0.01 and $0.1s^{-1}$ no strain hardening behavior was observed for the neat matrix and 1%APS-CNC sample. For the 2 and 3%APS-CNC samples, the plateau region slowly disappears as the viscosity shows an increasing trend with time especially for the highest CNC content sample. In addition, the slope of the hardening region increases even at these relatively slower strain rates for the 3%APS-CNC samples. For the highest

strain rate ($1s^{-1}$), all samples show an increase of elongational viscosity to various extents with the highest slope observed for the 3%APS-CNC nanocomposite.

Further, Figure 4.14 clearly shows that as the CNC content increases within the matrix, the response of the samples becomes more sensitive to the applied strain rate in terms of the long-time strain hardening character. This experimental fact is ascribed to the orientation of CNC whiskers in the uniaxial elongational force field which contributes to the strain hardening and enhanced thread strength at larger Hencky strains (long extension times). The favorable interfacial interactions and improvement in melt elasticity due to the presence of high surface area rigid nanoparticles in polymers has been shown to enhance the strain hardening character even at lower strain rates [86].

In order to better understand the role of the CNC structure within the PA6 melt in the rheological analysis results already described, the effect of pre-shearing on the structure break up and subsequent associated effects was studied through squeeze flow experiment. Squeeze flow tests have received considerable attention in investigation of various fiber suspensions, nanoparticle dispersions and gels [87] and an extensive analysis and modelling of the flow with various boundary conditions and viscoelastic behavior of materials are presented elsewhere [88]. The squeeze flow test was carried out in the constant force mode and reduction of gap as a function of time was recorded. In addition, tests were carried out in the constant area mode where the material was squeezed out of the plates as the gap between the top and bottom plates were reduced. Although it has been shown that buildup of material on the periphery of the plates results in an unknown pressure buildup [89], nonetheless, this mode was preferred over the constant mass mode as the area of the sample under squeezing force was known throughout the experiment. In

addition, the boundary condition of the squeeze flow plays a critical role in flow behavior and is closely related to the roughness of the plates [90]. As shown by Shaukat *et al* [89], smooth plates provide the slip boundary condition that results in development of the elongational flow in addition to the shear flow and, therefore, larger deformations and flow driving force. In contrast, rougher plate surface provides a no-slip boundary condition that eliminates the *in-situ* elongational flow. In this study, abrasive papers were used to achieve a surface roughness of above 35μm that has been suggested as a no-slip boundary condition [91]. The reason for this consideration was to eliminate (or minimize) the elongational flow that could contribute to the orientation of whiskers so that the exclusive effect of pre-shear could be studied. The results of the squeeze flow of the PA6 matrix and nanocomposites with 3%CNC and 3%APS-CNC are shown in Figure 4.14(d). This figure shows that, initially, the gap decreases rapidly followed by the reduction of the slope of the curve ultimately reaching a plateau-like zone. The residual finite gap in the plateau region is indicative of a material with yield stress and has been used in a number of previous studies to find the yield stress. It should be noted that a squeeze time of 900s is based on a reasonable timeframe of the material to remain thermally stable. The yield stress of the Herschel-Bulkley model associated with limiting gap under no-slip boundary condition can be found by using the following equation [89]:

$$\tau_y = \frac{3Fd_L}{2\pi R^3} \qquad (4.20)$$

Where the d_L is the limiting gap, F is the applied force and R is the radius of the plate. Using this equation, the yield stress of the 3%CNC and 3%APS-CNC samples before shear were found to be 16.9 and 23.2 Pa, respectively. After the pre-shearing step,

208

the yield stress values were found to be 15.9 and 19.1 Pa for the 3%CNC and 3%APS-CNC. This shows an approximately 18 and 6% drop in the yield stress values after the pre-shearing step. This clearly shows that, firstly, the nanocomposite samples undergo structural changes during the pre-shearing that results in what is believed to be the break-up of the nanostructure and a consequent reduction of the final yield stress.

Secondly, this shows that the nanostructure of 3%APS-CNC sample shows a higher sensitivity to the shear as the stress drop is more significant for this sample due to the more efficient stress transfer from the melt to the whiskers and higher interfacial area that could significantly affect the structural changes during the shear. It should be noted that we have not ruled out the fact that a number of other factors may contribute to the results including the time and scale of the pre-shear, squeeze force and the effect of plate roughness. This is a matter for further investigation in a future proposed study.

4.4 Conclusion

A novel multi-step process based on *in-situ* ring opening polymerization and subsequent melt extrusion was developed to incorporate cellulose nanocrystals (CNCs) into polyamide 6 (PA6) matrix and the effect of surface modification of CNCs with aminopropyltriethoxysilane (APS) on microstructure development, mechanical and rheological properties of the resulting nanocomposites were studied and compared with that of the neat CNC. Solid state NMR studies confirmed the interfacial bond formation and better dispersion of modified CNC in the matrix. Microscopic images showed that in the case of the neat CNC, a relatively significant fibrillar structure developed within the matrix while for the surface modified CNCs a much better dispersion was obtained. Mechanical testing results suggested a significant improvement of tensile properties (at

small CNC concentrations ≤ 3wt%) compared to that of the neat PA6 or nanocomposites prepared by direct melt mixing. This was attributed to the significantly better CNC dispersion within the matrix using the current process. The observed reinforcement effect was found to be higher than that predicted by a number of micromechanical models in the literature, suggesting the development of a rigid interphase around the CNC particles due to the strong interfacial interaction and polysiloxane bond formation.

This hypothesis was tested and confirmed by Peak Force-QNM modulus mapping technique (using AFM) where, especially for surface modified CNCs, a thicker interphase with higher modulus was detected. Small amplitude oscillatory shear rheological tests showed that upon incorporation of CNCs in the PA6 matrix, the magnitude of rheological properties increased even at the relatively low CNC concentrations studied. At higher CNC content, a non-terminal (in the low frequency zone) and an enhanced shear-thinning property were observed which is known to be a nanostructure formation signature. As expected, this effect was found to be pronounced in the case of APS-CNC samples. Melt stress relaxation and extensional viscosity results showed a considerable enhancement of melt elasticity and increases in relaxation time. In addition, orientation of the CNCs (in their axial direction) along the extension direction was found to be significantly improved by the strain hardening and melt strength of the PA6 matrix. Squeeze flow test was used as a novel tool to probe the effect of pre-shearing on the nanostructure of the neat and APS-modified CNC in the matrix. It was found that break-up of the nanostructure caused by the pre-shear was more pronounced in the case of modified particles which, in turn, gave a relatively higher magnitude of reduction in the melt yield stress. Overall, the results of this study point to a better

understanding of the *in situ* tailoring of the interface, nanostructure, and rheo-mechanical properties of polymer nanocomposites containing CNCs with enhanced benefits in applications where conventional micro (nano)composites are not useable.

Acknowledgements

4.5 References

1.   Bondeson, D.; Mathew, A.; Oksman, K., Optimization of the isolation of nanocrystals from microcrystalline cellulose by acid hydrolysis. *Cellulose* **2006,** *13* (2), 171-180.

2.   Habibi, Y.; Lucia, L. A.; Rojas, O. J., Cellulose nanocrystals: chemistry, self-assembly, and applications. *Chemical reviews* **2010,** *110* (6), 3479-3500.

3.   Hubbe, M. A.; Rojas, O. J.; Lucia, L. A.; Sain, M., Cellulosic nanocomposites: a review. *BioResources* **2008,** *3* (3), 929-980.

4.   Kalia, S.; Dufresne, A.; Cherian, B. M.; Kaith, B.; Avérous, L.; Njuguna, J.; Nassiopoulos, E., Cellulose-based bio-and nanocomposites: a review. *International Journal of Polymer Science* **2011,** *2011*.

5.   Lin, N.; Huang, J.; Dufresne, A., Preparation, properties and applications of polysaccharide nanocrystals in advanced functional nanomaterials: a review. *Nanoscale* **2012,** *4* (11), 3274-3294.

6.   Mariano, M.; El Kissi, N.; Dufresne, A., Cellulose nanocrystals and related nanocomposites: review of some properties and challenges. *Journal of Polymer Science Part B: Polymer Physics* **2014,** *52* (12), 791-806.

7.   Siqueira, G.; Bras, J.; Dufresne, A., Luffa cylindrica as a lignocellulosic source of fiber, microfibrillated cellulose and cellulose nanocrystals. *BioResources* **2010,** *5* (2), 727-740.

8.   Tashiro, K.; Kobayashi, M., Theoretical evaluation of three-dimensional elastic constants of native and regenerated celluloses: role of hydrogen bonds. *Polymer* **1991,** *32* (8), 1516-1526.

9.   de Menezes, A. J.; Siqueira, G.; Curvelo, A. A.; Dufresne, A., Extrusion and characterization of functionalized cellulose whiskers reinforced polyethylene nanocomposites. *Polymer* **2009,** *50* (19), 4552-4563.

10.   Oksman, K.; Mathew, A. P.; Bondeson, D.; Kvien, I., Manufacturing process of cellulose whiskers/polylactic acid nanocomposites. *Composites Science and Technology* **2006,** *66* (15), 2776-2784.

11.   Dufresne, A., Processing of polymer nanocomposites reinforced with polysaccharide nanocrystals. *Molecules* **2010,** *15* (6), 4111-4128.

12.   Lu, P.; Hsieh, Y.-L., Preparation and properties of cellulose nanocrystals: rods, spheres, and network. *Carbohydrate Polymers* **2010,** *82* (2), 329-336.

13.   Han, J.; Zhou, C.; Wu, Y.; Liu, F.; Wu, Q., Self-assembling behavior of cellulose nanoparticles during freeze-drying: Effect of suspension concentration, particle size, crystal structure, and surface charge. *Biomacromolecules* **2013,** *14* (5), 1529-1540.

14.   Peng, Y.; Gardner, D. J.; Han, Y., Drying cellulose nanofibrils: in search of a suitable method. *Cellulose* **2012,** *19* (1), 91-102.

15.   Cao, X.; Dong, H.; Li, C. M., New nanocomposite materials reinforced with flax cellulose nanocrystals in waterborne polyurethane. *Biomacromolecules* **2007,** *8* (3), 899-904.

16.   Favier, V.; Canova, G.; Cavaillé, J.; Chanzy, H.; Dufresne, A.; Gauthier, C., Nanocomposite materials from latex and cellulose whiskers. *Polymers for Advanced Technologies* **1995,** *6* (5), 351-355.

17.   Hajji, P.; Cavaille, J.; Favier, V.; Gauthier, C.; Vigier, G., Tensile behavior of nanocomposites from latex and cellulose whiskers. *Polymer Composites* **1996,** *17* (4), 612-619.

18.   Paralikar, S. A.; Simonsen, J.; Lombardi, J., Poly (vinyl alcohol)/cellulose nanocrystal barrier membranes. *Journal of Membrane Science* **2008,** *320* (1), 248-258.

19.   Zhou, C.; Chu, R.; Wu, R.; Wu, Q., Electrospun polyethylene oxide/cellulose nanocrystal composite nanofibrous mats with homogeneous and heterogeneous microstructures. *Biomacromolecules* **2011,** *12* (7), 2617-2625.

20.   van den Berg, O.; Capadona, J. R.; Weder, C., Preparation of Homogeneous Dispersions of Tunicate Cellulose Whiskers in Organic Solvents. *Biomacromolecules* **2007,** *8* (4), 1353-1357.

21.   Auad, M. L.; Contos, V. S.; Nutt, S.; Aranguren, M. I.; Marcovich, N. E., Characterization of nanocellulose-reinforced shape memory polyurethanes. *Polymer International* **2008,** *57* (4), 651-659.

22.   Liu, H.; Liu, D.; Yao, F.; Wu, Q., Fabrication and properties of transparent polymethylmethacrylate/cellulose nanocrystals composites. *Bioresource Technology* **2010,** *101* (14), 5685-5692.

23.   Ben Azouz, K.; Ramires, E. C.; Van den Fonteyne, W.; El Kissi, N.; Dufresne, A., Simple method for the melt extrusion of a cellulose nanocrystal reinforced hydrophobic polymer. *ACS Macro Letters* **2011,** *1* (1), 236-240.

24.   Junior de Menezes, A.; Siqueira, G.; Curvelo, A. A. S.; Dufresne, A., Extrusion and characterization of functionalized cellulose whiskers reinforced polyethylene nanocomposites. *Polymer* **2009,** *50* (19), 4552-4563.

25.   Lee, K.-Y.; Aitomäki, Y.; Berglund, L. A.; Oksman, K.; Bismarck, A., On the use of nanocellulose as reinforcement in polymer matrix composites. *Composites Science and Technology* **2014,** *105*, 15-27.

26.   Pandey, J. K.; Lee, H. T.; Takagi, H.; Ahn, S. H.; Saini, D. R.; Misra, M., Dispersion of Nanocellulose (NC) in Polypropylene (PP) and Polyethylene (PE) Matrix. In *Handbook of Polymer Nanocomposites. Processing, Performance and Application: Volume C: Polymer Nanocomposites of Cellulose Nanoparticles*, Pandey, K. J.; Takagi, H.; Nakagaito, N. A.; Kim, H.-J., Eds. Springer Berlin Heidelberg: Berlin, Heidelberg, 2015; pp 179-189.

27.   Lin, N.; Dufresne, A., Physical and/or chemical compatibilization of extruded cellulose nanocrystal reinforced polystyrene nanocomposites. *Macromolecules* **2013,** *46* (14), 5570-5583.

28.   Bondeson, D.; Oksman, K., Dispersion and characteristics of surfactant modified cellulose whiskers nanocomposites. *Composite Interfaces* **2007,** *14* (7-9), 617-630.

29.   Chazeau, L.; Cavaillé, J. Y.; Terech, P., Mechanical behaviour above Tg of a plasticised PVC reinforced with cellulose whiskers; a SANS structural study. *Polymer* **1999,** *40* (19), 5333-5344.

30.   Jiang, L.; Morelius, E.; Zhang, J.; Wolcott, M.; Holbery, J., Study of the poly (3-hydroxybutyrate-co-3-hydroxyvalerate)/cellulose nanowhisker composites prepared by solution casting and melt processing. *Journal of Composite Materials* **2008,** *42* (24), 2629-2645.

31.   Goffin, A. L.; Raquez, J. M.; Duquesne, E.; Siqueira, G.; Habibi, Y.; Dufresne, A.; Dubois, P., Poly(ε-caprolactone) based nanocomposites reinforced by surface-grafted cellulose nanowhiskers via extrusion processing: Morphology, rheology, and thermo-mechanical properties. *Polymer* **2011,** *52* (7), 1532-1538.

32.   Karimi, S.; Tahir, P. M.; Dufresne, A.; Karimi, A.; Abdulkhani, A., A comparative study on characteristics of nanocellulose reinforced thermoplastic starch biofilms prepared with different techniques. *Nordic Pulp & Paper Research Journal* **2014,** *29* (1).

33.   Bondeson, D.; Oksman, K., Polylactic acid/cellulose whisker nanocomposites modified by polyvinyl alcohol. *Composites Part A: Applied Science and Manufacturing* **2007,** *38* (12), 2486-2492.

34.   Goffin, A.-L.; Raquez, J.-M.; Duquesne, E.; Siqueira, G.; Habibi, Y.; Dufresne, A.; Dubois, P., From Interfacial Ring-Opening Polymerization to Melt Processing of Cellulose Nanowhisker-Filled Polylactide-Based Nanocomposites. *Biomacromolecules* **2011,** *12* (7), 2456-2465.

35.   Habibi, Y.; Goffin, A.-L.; Schiltz, N.; Duquesne, E.; Dubois, P.; Dufresne, A., Bionanocomposites based on poly (ε-caprolactone)-grafted cellulose nanocrystals by ring-opening polymerization. *Journal of Materials Chemistry* **2008,** *18* (41), 5002-5010.

36.   Goussé, C.; Chanzy, H.; Excoffier, G.; Soubeyrand, L.; Fleury, E., Stable suspensions of partially silylated cellulose whiskers dispersed in organic solvents. *Polymer* **2002,** *43* (9), 2645-2651.

37.   Yu, X.; Tong, S.; Ge, M.; Wu, L.; Zuo, J.; Cao, C.; Song, W., Adsorption of heavy metal ions from aqueous solution by carboxylated cellulose nanocrystals. *Journal of Environmental Sciences* **2013,** *25* (5), 933-943.

38.   Grunert, M.; Winter, W. T., Nanocomposites of Cellulose Acetate Butyrate Reinforced with Cellulose Nanocrystals. *Journal of Polymers and the Environment* **2002,** *10* (1), 27-30.

39.   Yu, H.-Y.; Chen, R.; Chen, G.-Y.; Liu, L.; Yang, X.-G.; Yao, J.-M., Silylation of cellulose nanocrystals and their reinforcement of commercial silicone rubber. *Journal of Nanoparticle Research* **2015,** *17* (9), 1-13.

40.   Kiziltas, A.; Gardner, D. J.; Han, Y.; Yang, H.-S., Mechanical properties of microcrystalline cellulose (MCC) filled engineering thermoplastic composites. *Journal of Polymers and the Environment* **2014,** *22* (3), 365-372.

41.   Kiziltas, A.; Gardner, D. J.; Han, Y.; Yang, H.-S., Dynamic mechanical behavior and thermal properties of microcrystalline cellulose (MCC)-filled nylon 6 composites. *Thermochimica Acta* **2011,** *519* (1), 38-43.

42.   Kiziltas, A.; Nazari, B.; Gardner, D. J.; Bousfield, D. W., Polyamide 6–cellulose composites: Effect of cellulose composition on melt rheology and crystallization behavior. *Polymer Engineering & Science* **2014,** *54* (4), 739-746.

43.   Corrêa, A. C.; de Morais Teixeira, E.; Carmona, V. B.; Teodoro, K. B. R.; Ribeiro, C.; Mattoso, L. H. C.; Marconcini, J. M., Obtaining nanocomposites of polyamide 6 and cellulose whiskers via extrusion and injection molding. *Cellulose* **2014,** *21* (1), 311-322.

44.   Kashani Rahimi, S.; Otaigbe, J. U., Polyamide 6 nanocomposites incorporating cellulose nanocrystals prepared by In situ ring-opening polymerization: Viscoelasticity, creep behavior, and melt rheological properties. *Polymer Engineering & Science* **2016,** *56* (9), 1045-1060.

45.   Rahimi, S. K.; Otaigbe, J. U., The role of particle surface functionality and microstructure development in isothermal and non-isothermal crystallization behavior of polyamide 6/cellulose nanocrystals nanocomposites. *Polymer* **2016,** *107*, 316-331.

46.   Capadona, J. R.; Van Den Berg, O.; Capadona, L. A.; Schroeter, M.; Rowan, S. J.; Tyler, D. J.; Weder, C., A versatile approach for the processing of polymer

217

nanocomposites with self-assembled nanofibre templates. *Nat Nano* **2007,** *2* (12), 765-769.

47.   Raquez, J.-M.; Murena, Y.; Goffin, A.-L.; Habibi, Y.; Ruelle, B.; DeBuyl, F.; Dubois, P., Surface-modification of cellulose nanowhiskers and their use as nanoreinforcers into polylactide: a sustainably-integrated approach. *Composites Science and Technology* **2012,** *72* (5), 544-549.

48.   Abdelmouleh, M.; Boufi, S.; ben Salah, A.; Belgacem, M. N.; Gandini, A., Interaction of silane coupling agents with cellulose. *Langmuir* **2002,** *18* (8), 3203-3208.

49.   Mohd, N. H.; Ismail, N. F. H.; Zahari, J. I.; Wan Fathilah, W. F. b.; Kargarzadeh, H.; Ramli, S.; Ahmad, I.; Yarmo, M. A.; Othaman, R., Effect of Aminosilane Modification on Nanocrystalline Cellulose Properties. *Journal of Nanomaterials* **2016,** *2016*, 8.

50.   Reddy, C. R.; Simon, L. C., Surface Modification of Wood Fiber and Preparation of a Wood Fiber–Polypropylene Hybrid by In situ Polymerization. *Macromolecular Materials and Engineering* **2010,** *295* (10), 906-914.

51.   Pavasars, I.; Hagberg, J.; Borén, H.; Allard, B., Alkaline Degradation of Cellulose: Mechanisms and Kinetics. *Journal of Polymers and the Environment* **2003,** *11* (2), 39-47.

52.   Salon, M. C. B.; Gerbaud, G.; Abdelmouleh, M.; Bruzzese, C.; Boufi, S.; Belgacem, M. N., Studies of interactions between silane coupling agents and cellulose fibers with liquid and solid-state NMR. *Magnetic Resonance in Chemistry* **2007,** *45* (6), 473-483.

53.   Glaser, R. H.; Wilkes, G. L., Structure property behavior of polydimethylsiloxane and poly(tetramethylene oxide) modified TEOS based sol-gel materials. *Polymer Bulletin* **1988,** *19* (1), 51-57.

54.   Udipi, K.; Davé, R. S.; Kruse, R. L.; Stebbins, L. R., Polyamides from lactams via anionic ring-opening polymerization: 1. Chemistry and some recent findings. *Polymer* **1997,** *38* (4), 927-938.

55.   Mateva, R.; Petrov, P.; Rousseva, S.; Dimitrov, R.; Zolova, G., On the structure of poly-ε-caprolactams, obtained with bifunctional N-carbamyl derivatives of lactams. *European polymer journal* **2000,** *36* (4), 813-821.

56.   Mariño, M.; Lopes da Silva, L.; Durán, N.; Tasic, L., Enhanced materials from nature: nanocellulose from citrus waste. *Molecules* **2015,** *20* (4), 5908-5923.

57.   Hassan, M. L.; Moorefield, C. M.; Elbatal, H. S.; Newkome, G. R.; Modarelli, D. A.; Romano, N. C., Fluorescent cellulose nanocrystals via supramolecular assembly of terpyridine-modified cellulose nanocrystals and terpyridine-modified perylene. *Materials Science and Engineering: B* **2012,** *177* (4), 350-358.

58.   Misra, R.; Alidedeoglu, A. H.; Jarrett, W. L.; Morgan, S. E., Molecular miscibility and chain dynamics in POSS/polystyrene blends: control of POSS preferential dispersion states. *Polymer* **2009,** *50* (13), 2906-2918.

59.   Liu, T.; Liu, Z.; Ma, K.; Shen, L.; Zeng, K.; He, C., Morphology, thermal and mechanical behavior of polyamide 6/layered-silicate nanocomposites. *Composites science and technology* **2003,** *63* (3), 331-337.

60.   Yang, F.; Ou, Y.; Yu, Z., Polyamide 6/silica nanocomposites prepared by in situ polymerization. *Journal of Applied Polymer Science* **1998,** *69* (2), 355-361.

61.   Affdl, J.; Kardos, J., The Halpin-Tsai equations: a review. *Polymer Engineering & Science* **1976,** *16* (5), 344-352.

62.   Halpin, J.; Kardos, J., Moduli of crystalline polymers employing composite theory. *Journal of Applied Physics* **1972,** *43* (5), 2235-2241.

63.   Helbert, W.; Cavaille, J.; Dufresne, A., Thermoplastic nanocomposites filled with wheat straw cellulose whiskers. Part I: processing and mechanical behavior. *Polymer composites* **1996,** *17* (4), 604-611.

64.   Takayanagi, M.; Uemura, S.; Minami, S. In *Application of equivalent model method to dynamic rheo-optical properties of crystalline polymer*, Journal of Polymer Science Part C: Polymer Symposia, Wiley Online Library: 1964; pp 113-122.

65.   Ouali, N.; Cavaillé, J.; Perez, J., Elastic, viscoelastic and plastic behavior of multiphase polymer blends. *Plastics, Rubber and Composites Processing and Applications(UK)* **1991,** *16* (1), 55-60.

66.   Dubief, D.; Samain, E.; Dufresne, A., Polysaccharide microcrystals reinforced amorphous poly (β-hydroxyoctanoate) nanocomposite materials. *Macromolecules* **1999,** *32* (18), 5765-5771.

67.   Tang, L.; Weder, C., Cellulose whisker/epoxy resin nanocomposites. *ACS Applied Materials & Interfaces* **2010,** *2* (4), 1073-1080.

68.   Capadona, J. R.; Shanmuganathan, K.; Tyler, D. J.; Rowan, S. J.; Weder, C., Stimuli-responsive polymer nanocomposites inspired by the sea cucumber dermis. *Science* **2008,** *319* (5868), 1370-1374.

69.	Shanmuganathan, K.; Capadona, J. R.; Rowan, S. J.; Weder, C., Bio-inspired mechanically-adaptive nanocomposites derived from cotton cellulose whiskers. *Journal of Materials Chemistry* **2010,** *20* (1), 180-186.

70.	Cox, H., The elasticity and strength of paper and other fibrous materials. *British journal of applied physics* **1952,** *3* (3), 72.

71.	Piggott, M., *Load bearing fibre composites*. Pergamon Press: Willowdale, Ontario, Canada, 1980.

72.	Facca, A. G.; Kortschot, M. T.; Yan, N., Predicting the elastic modulus of natural fibre reinforced thermoplastics. *Composites Part A: Applied Science and Manufacturing* **2006,** *37* (10), 1660-1671.

73.	Nairn, J. A., On the use of shear-lag methods for analysis of stress transfer in unidirectional composites. *Mechanics of Materials* **1997,** *26* (2), 63-80.

74.	Moon, R. J.; Martini, A.; Nairn, J.; Simonsen, J.; Youngblood, J., Cellulose nanomaterials review: structure, properties and nanocomposites. *Chemical Society Reviews* **2011,** *40* (7), 3941-3994.

75.	Nairn, J. A., Numerical implementation of imperfect interfaces. *Computational Materials Science* **2007,** *40* (4), 525-536.

76.	Nair, S. S.; Wang, S.; Hurley, D. C., Nanoscale characterization of natural fibers and their composites using contact-resonance force microscopy. *Composites Part A: Applied Science and Manufacturing* **2010,** *41* (5), 624-631.

77.	Pakzad, A.; Simonsen, J.; Yassar, R. S., Gradient of nanomechanical properties in the interphase of cellulose nanocrystal composites. *Composites Science and Technology* **2012,** *72* (2), 314-319.

221

78. Brown, D.; Marcadon, V.; Mele, P.; Alberola, N., Effect of filler particle size on the properties of model nanocomposites. *Macromolecules* **2008,** *41* (4), 1499-1511.

79. Li, Y.; Waas, A. M.; Arruda, E. M., A closed-form, hierarchical, multi-interphase model for composites—Derivation, verification and application to nanocomposites. *Journal of the Mechanics and Physics of Solids* **2011,** *59* (1), 43-63.

80. Khoshkava, V.; Kamal, M. R., Effect of Cellulose Nanocrystals (CNC) Particle Morphology on Dispersion and Rheological and Mechanical Properties of Polypropylene/CNC Nanocomposites. *ACS Applied Materials & Interfaces* **2014,** *6* (11), 8146-8157.

81. Litchfield, D. W.; Baird, D. G., The rheology of high aspect ratio nano-particle filled liquids. *Rheology Reviews* **2006,** *2006*, 1.

82. Wang, M.; Wang, W.; Liu, T.; Zhang, W.-D., Melt rheological properties of nylon 6/multi-walled carbon nanotube composites. *Composites Science and Technology* **2008,** *68* (12), 2498-2502.

83. Galgali, G.; Ramesh, C.; Lele, A., A rheological study on the kinetics of hybrid formation in polypropylene nanocomposites. *Macromolecules* **2001,** *34* (4), 852-858.

84. Maria, H. J.; Lyczko, N.; Nzihou, A.; Joseph, K.; Mathew, C.; Thomas, S., Stress relaxation behavior of organically modified montmorillonite filled natural rubber/nitrile rubber nanocomposites. *Applied Clay Science* **2014,** *87*, 120-128.

85.   Gupta, R. K.; Pasanovic-Zujo, V.; Bhattacharya, S., Shear and extensional rheology of EVA/layered silicate-nanocomposites. *Journal of Non-Newtonian Fluid Mechanics* **2005,** *128* (2), 116-125.

86.   Laske, S.; Kracalik, M.; Gschweitl, M.; Feuchter, M.; Maier, G.; Pinter, G.; Thomann, R.; Friesenbichler, W.; Langecker, G. R., Estimation of reinforcement in compatibilized polypropylene nanocomposites by extensional rheology. *Journal of Applied Polymer Science* **2009,** *111* (5), 2253-2259.

87.   Meeten, G. H., Yield stress of structured fluids measured by squeeze flow. *Rheologica acta* **2000,** *39* (4), 399-408.

88.   Engmann, J.; Servais, C.; Burbidge, A. S., Squeeze flow theory and applications to rheometry: a review. *Journal of non-newtonian fluid mechanics* **2005,** *132* (1), 1-27.

89.   Shaukat, A.; Sharma, A.; Joshi, Y. M., Squeeze flow behavior of (soft glassy) thixotropic material. *Journal of Non-Newtonian Fluid Mechanics* **2012,** *167*, 9-17.

90.   Meeten, G. H., Effects of plate roughness in squeeze-flow rheometry. *Journal of non-newtonian fluid mechanics* **2004,** *124* (1), 51-60.

91.   Meeten, G. H., Squeeze flow of soft solids between rough surfaces. *Rheologica acta* **2004,** *43* (1), 6-16.
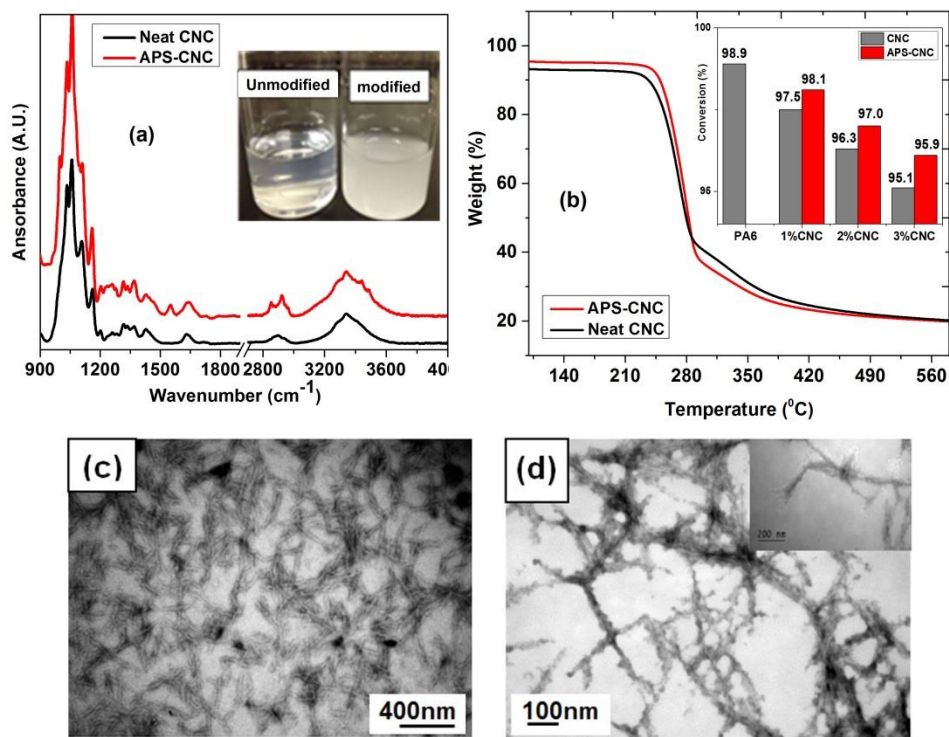
Figure 4.1 (a) FTIR spectrum of neat and APS-CNC, (b) mass loss of neat and APS-CNC and the variation of conversion versus CNC content, (c) TEM image of neat CNC and (d) TEM images of APS-CNC.
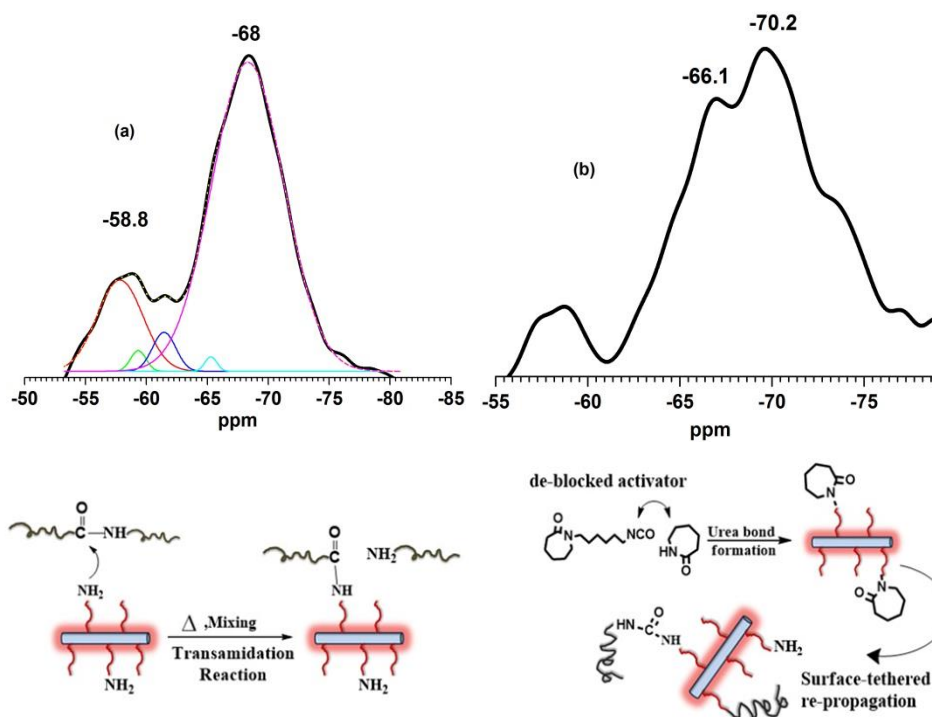
Figure 4.2 Solid-State ^{29}Si NMR spectrum of (a)APS-CNC, (b)in-situ ROPed and melt extruded and (d) interfacial bond formation through transamidation and surface-initiated polymerization.
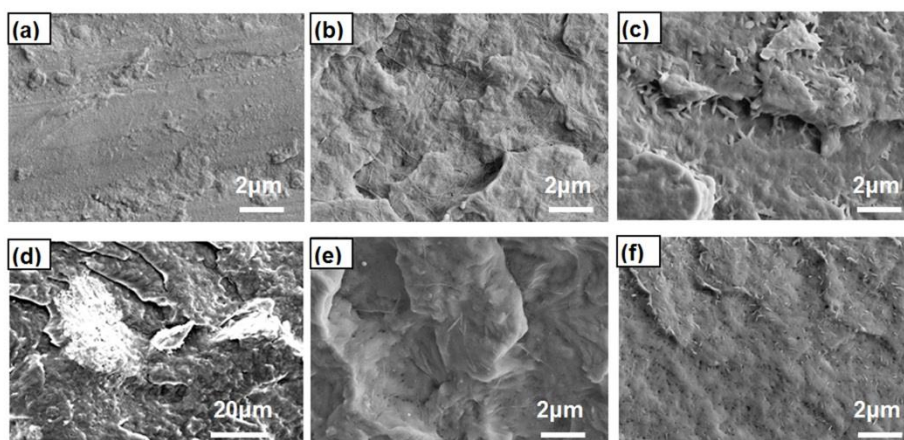
Figure 4.3 SEM images showing the cryo-fractured surface of (a) PA6, (b) 3%CNC after ROP, (c) 3%APS-CNC after ROP, (d) 3%CNC direct melt extruded, (e) 3%CNC after ROP and extrusion and (f) 3%APS-CNC after ROP and extrusion.
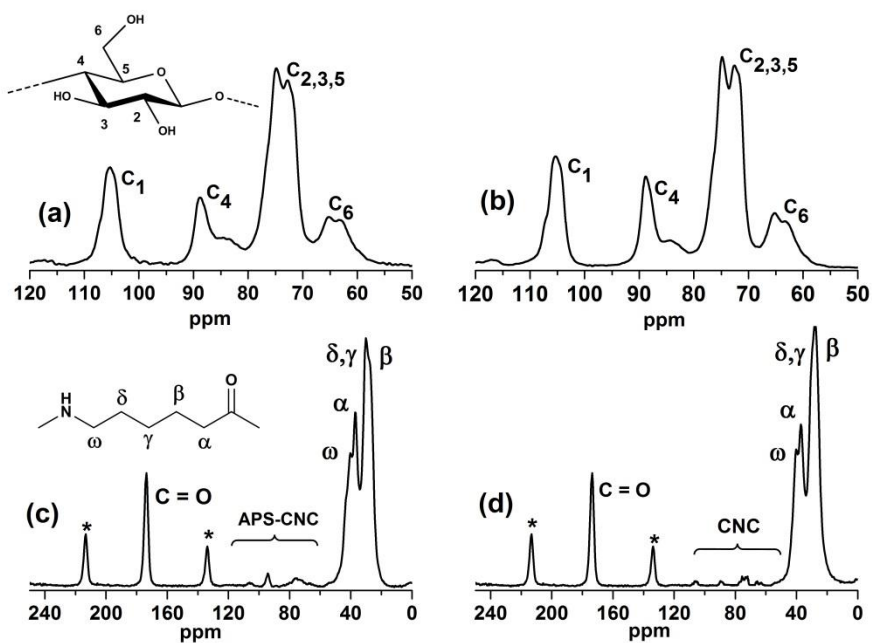
Figure 4.4 Solid state CP/MAS ^{13}C NMR spectra of (a) CNC, (b) APS-CNC, (c) 3% APS-CNC nanocomposite and (d) 3% CNC nanocomposite (spinning sidebands are marked with asterisk).
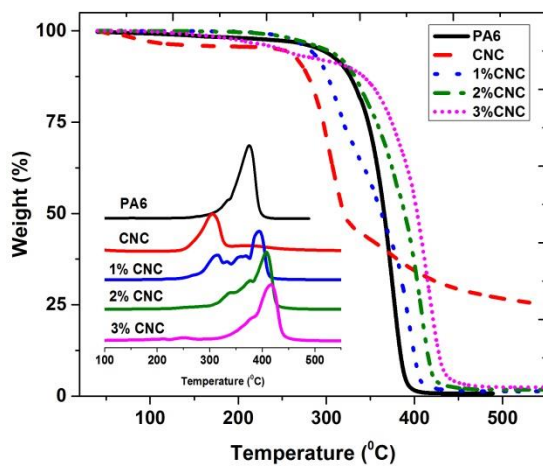
Figure 4.5 TGA and DTG curves of PA6 and PA6/CNC nanocomposites.

226
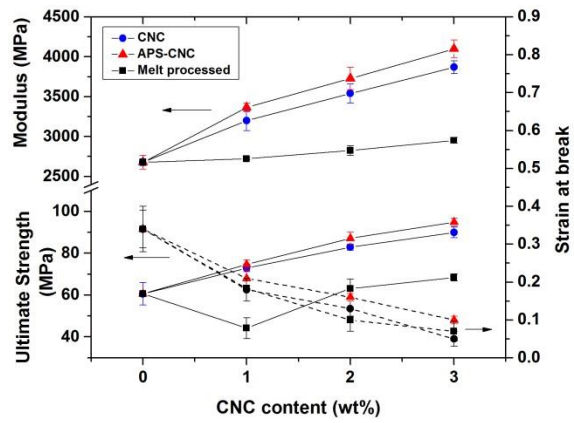
Figure 4.6 (a) Tensile modulus, tensile strength and strain at break of PA6, PA6/CNC and PA6/APS-CNC nanocomposites.
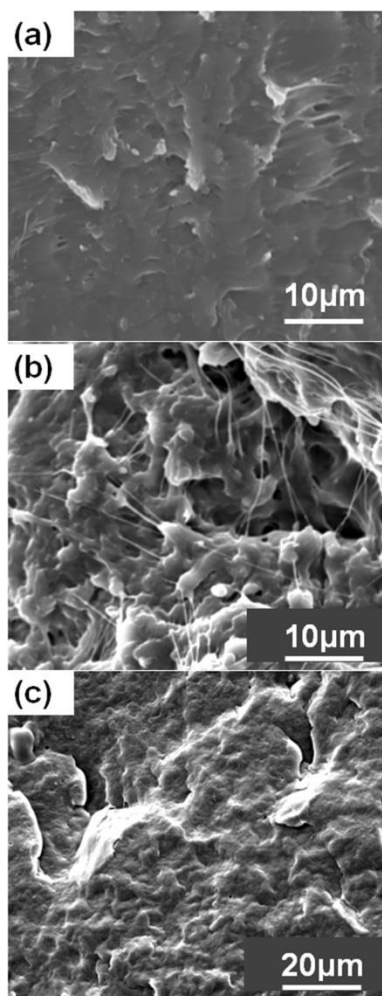
Figure 4.7 Tensile-fractured surfaces of (a) 3%CNC (multi-step processed), (b)3%APS-CNC (multi-step processed) and (c) 3%CNC (direct melt mixed).
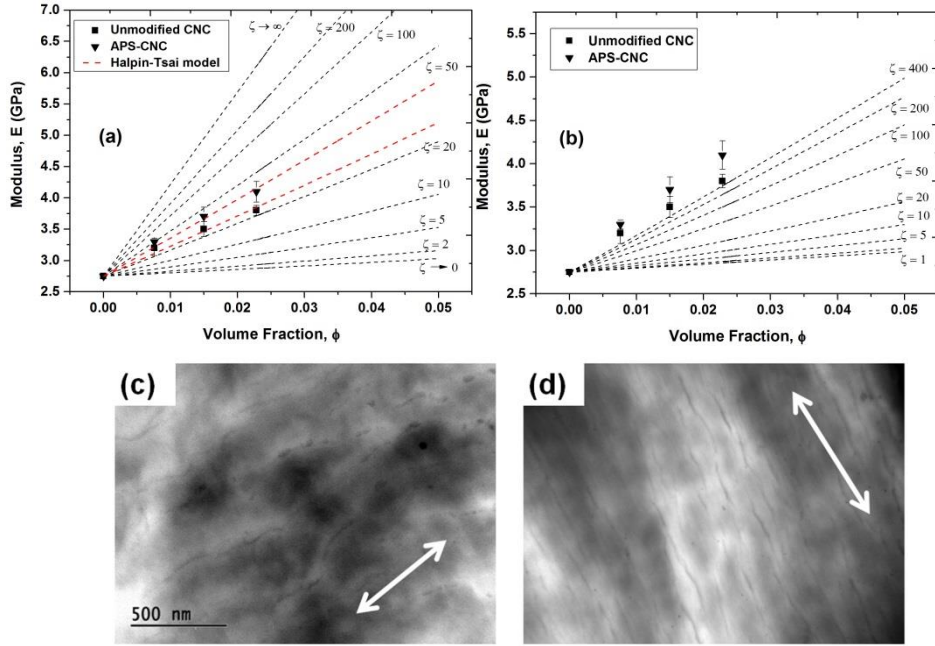
Figure 4.8 (a) Halpin-Tsai model curves for various aspect ratios and model fit on experimental data, (b) Halpin-Kardos model curves for various aspect ratios, (d)TEM image of the 3%CNC and (e) 3%APS-CNC injection molded samples (injection direction shown with arrows). Both TEM figures have similar scale bar.
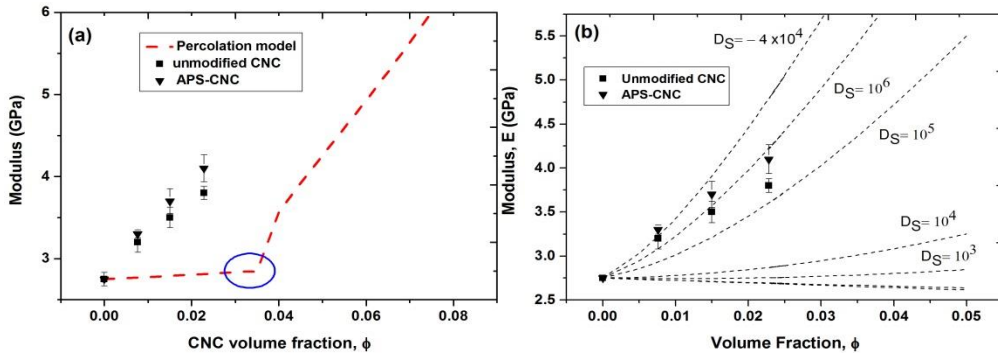
Figure 4.9 (a) Percolation model and (b) modified shear lag model with interface parameter.
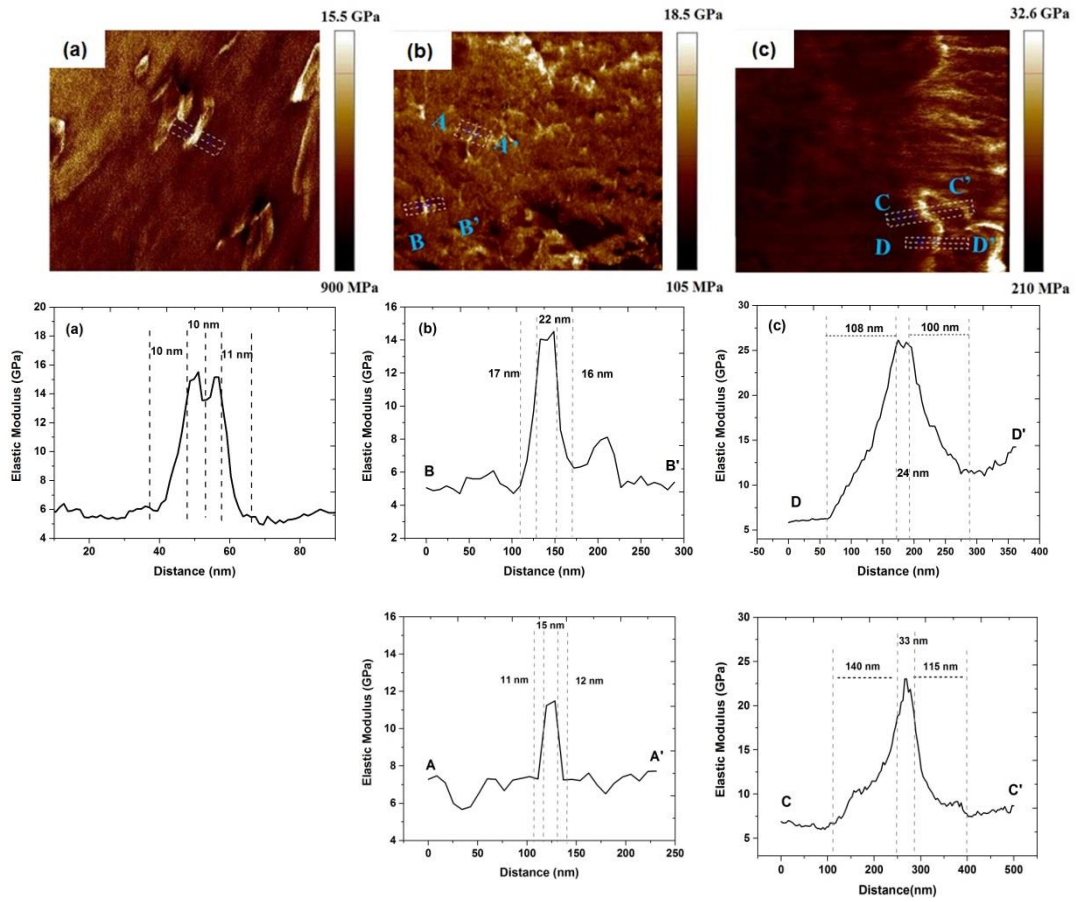
Figure 4.10 Modulus maps and the corresponding modulus gradient profiles of (a)3%CNC with 0.5*0.5μm^2 images size, (b)3%CNC with 2*2 μm^2 and (c)3%APS-CNC with 2*2 μm2 image size.
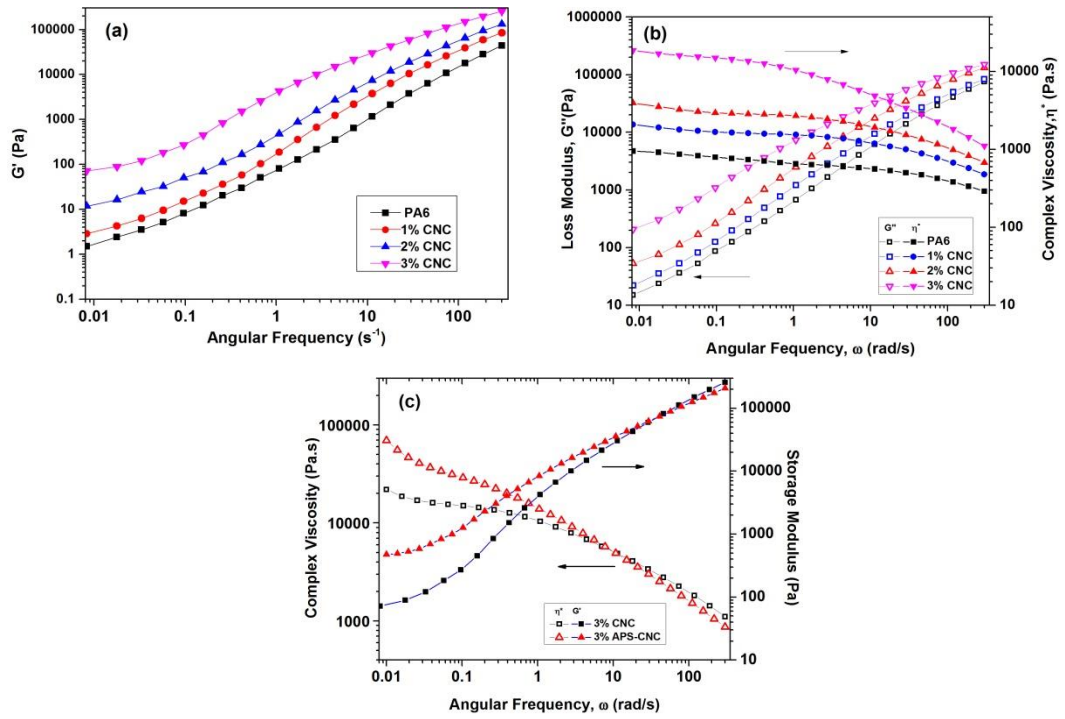
Figure 4.11 Variation of (a) storage modulus, (b) loss modulus and complex viscosity for PA6/CNC nanocomposites and (c) comparison of storage modulus and complex viscosity of 3%CNC and 3%APS-CNC.
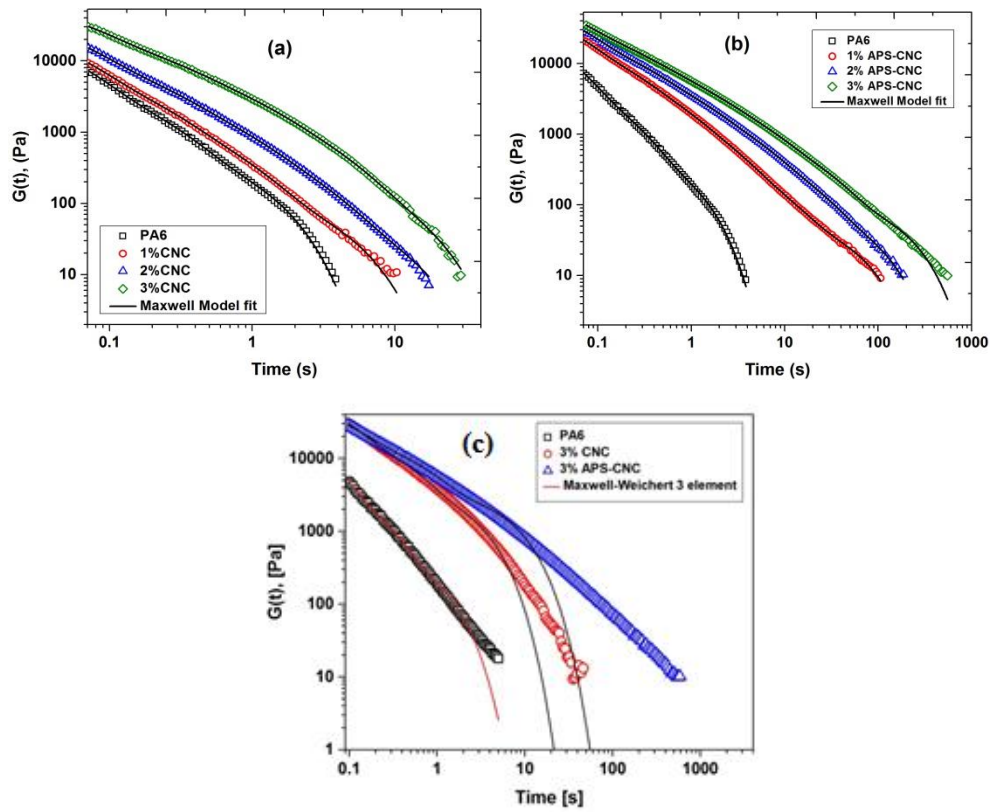
Figure 4.12 Linear stress relaxation experimental data and the Maxwell model fit of (a) unmodified, (b) APS-modified CNC nanocomposites and (c) 3-element Maxwell fit.

232
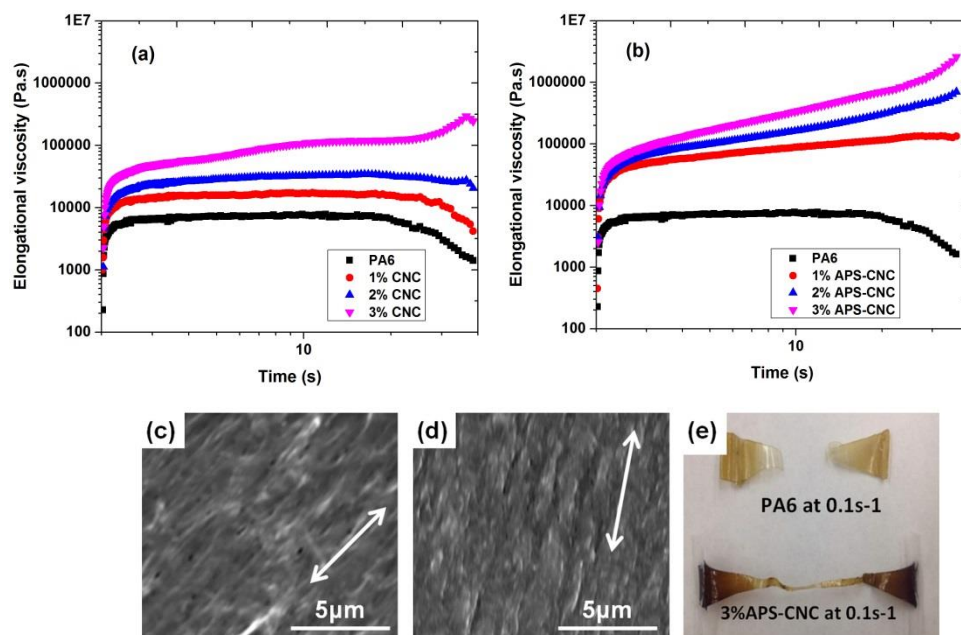
Figure 4.13 Extensional viscosity of (a) PA6/CNC, (b) PA6/APS-CNC nanocomposites, (c)SEM Image of quenched elongated 3%CNC, (d)3%APS samples (extension direction shown by arrows) and (e) graphical representation of the melt strength for PA6 matrix and 3%APS nanocomposites stretched at $0.1s^{-1}$.
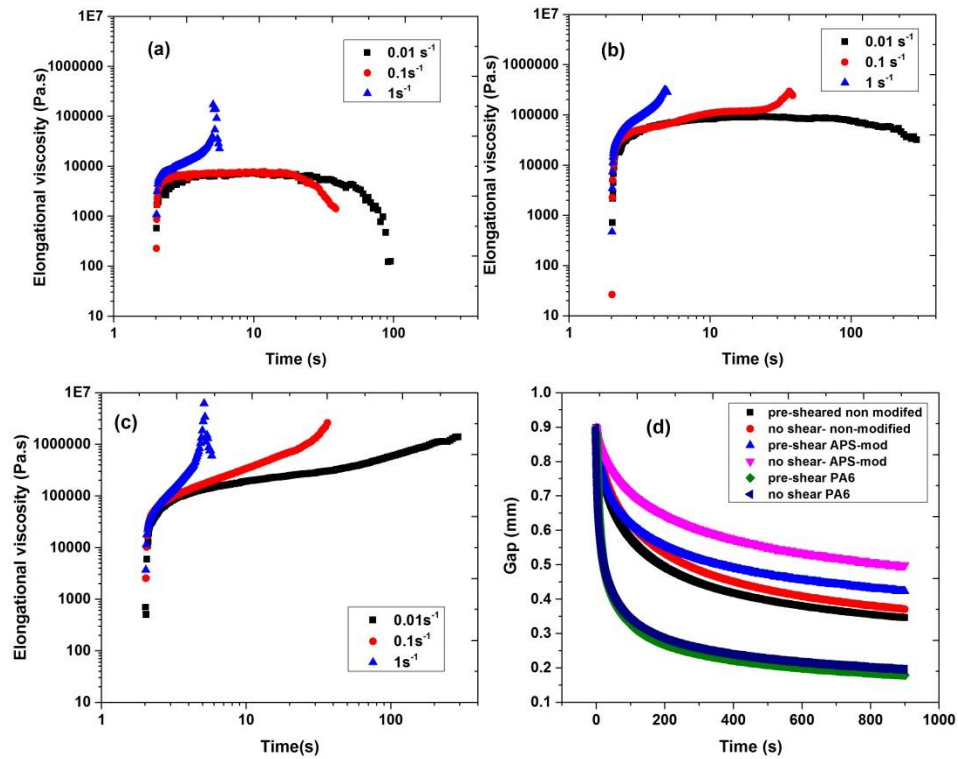
Figure 4.14 The effect of strain rate on extensional viscosity of (a) PA6, (b)3%CNC, (c)3%APS-CNC and (d) variation of gap versus time in squeeze flow test of the nanocomposite samples both with and without pre-shear.

Table 4.1

Mechanical properties of PA6, PA6/CNC and PA6/APS-CNC nanocomposites

Sample	Tensile Modulus (MPa)	Tensile Strength (MPa)	Elongation at break
PA6	2748.7 (85.6)	60.6 (5.4)	0.34 (0.05)
1%CNC	3198.2 (122.9)	72.9 (1.7)	0.18 (0.03)
1% APS-	3364.9 (54.4)	74.6 (2.2)	0.21 (0.02)
2%CNC	3538.85 (121.1)	82.9(1.4)	0.13 (0.02)
2% APS-	3728.7 (150.1)	87.1 (3.0)	0.16 (0.01)
3%CNC	3868.5 (78.6)	89.9 (2.5)	0.05 (0.02)
3% APS-	4100.6 (114.6)	94.8 (1.9)	0.1 (0.01)

Table 4.2

Maxwell model fitting parameters

Parameter/ sample	PA6	1%CNC	2%CNC	3%CNC	1%APS-CNC	2%APS-CNC	3%APS-CNC
T_1 (s)	0.03	0.03	0.04	0.05	0.04	0.05	0.04
T_2 (s)	0.16	0.15	0.16	0.20	0.17	0.24	0.13
T_3 (s)	0.88	0.58	0.55	0.71	0.58	0.26	0.41
T_4 (s)	-	3.11	1.86	2.41	1.19	0.98	1.41
T_5 (s)	-	-	8.1	9.37	7.26	3.98	4.82
T_6 (s)	-	-	-	-	54.05	15.14	21.54
T_7 (s)	-	-	-	-	-	82.98	160.03
G_1(Pa)	27391.2	30018.1	40085.3	56803.1	45196.3	53757.2	61914.6
G_2(Pa)	4322.4	5774.5	8434.6	15540.1	11940.8	7038.7	18359.6
G_3(Pa)	591.2	1379.6	2466.9	5660.9	4216.9	6283.5	9844.4
G_4(Pa)	-	153.8	640.6	1838.3	1426.4	4587.1	4797.6
G_5(Pa)	-	-	79.4	264.8	321.8	1542.1	2162.1
G_6(Pa)	-	-	-	-	59.9	419.2	695.1
G_7(Pa)	-	-	-	-	-	84.3	120.3
R^2	0.999	0.999	0.999	0.999	0.999	0.999	0.999

Table 4.3

Three-element Maxwell model fit parameters

Sample	i^{th} element	τ_i (s)
PA6	1	0.034
	2	0.160
	3	0.926
3% CNC	1	0.068
	2	0.38
	3	2.59
3% APS-CNC	1	0.085
	2	0.58
	3	6.73

CHAPTER V – PREPARATION AND PROPERTIES OF NATURAL FIBER
REINFORCED POLYAMIDE 6 THERMOPLASTIC COMPOSITES BY IN-SITU
ANIONIC RING-OPENING POLYMERIZATION

Manuscript in preparation for submission to *Polymer Composites*

Abstract

Polyamide 6 thermoplastic composites reinforced with flax fiber fabric and karft pulp cellulose mat were prepared via anionic in-situ ring-opening polymerization using vacuum assisted resin infusion process. The effects of the polymerization initiator in combination with the fiber alkali pre-treatment on the polymerization inhibition and conversion were studied. In addition, the effect of the fiber type, polymerization temperature and surface modification of fibers with organosilane coupling agents on the physical and mechanical properties of the composites were investigated in detail. The results showed that a combination of alkali pre-treatment and the use of less reactive magnesium bromide based anionic initiator ensures a successful polymerization while the use of the more reactive sodium salt based initiator results in severe cellulose peeling reaction and consequently the inhibition of polymerization. The analysis of the physical and mechanical properties of the composite panels showed that the highest mechanical properties could be achieved by polymerization temperature of 150°C while polymerization at higher temperatures lowers both flexural and tensile properties due to generation of more internal microvoids as well as decreased crystallinity of the matrix. In addition, it was found that the optimal mechanical properties could be attained with using 2wt% aminopropyltriehtoxysilane (APS) as higher APS negatively impacts the interfacial adhesion resulting in lower mechanical properties.

238

5.1 Introduction

With an increasing demand from materials and energy industrial sectors for sustainable "green" alternatives of the current resources, there has been a myriad of research activities aiming at developing renewable eco-friendly materials and technologies. A long lasting goal for new sustainable materials has been to develop high-performance, polymer composites reinforced by natural fibers [1-4]. If successful, these materials are highly competitive candidates for replacement of glass fiber reinforced plastics (GFRPs) with much greater utilization of renewable materials resources which are more sustainable. Natural fibers compared to glass fibers, are typically more ductile, less abrasive to processing equipment therefore more cost effective in terms of production line, have significantly lower density (cellulose density of 1.5 g/cm^3 compared to that of glass in the range of 2.5-2.8 g/cm^3) that can used to make engineering components that are surprisingly lighter, are recyclable after their service life for energy recovery and are by far more cost effective in terms of raw material cost [5-7]. There are a number of potential applications for high performance natural fiber reinforced composites such as automotive components, construction materials, and transportation materials [5].

Development of thermoset resins reinforced with natural fibers is a straightforward process due to the low viscosity and low processing temperature of most resins such as epoxy [8], unsaturated polyester [9] and vinyl ester [10] which could efficiently impregnate the natural fibers with standard processes based on liquid molding techniques. However, in the case of thermoplastic based composites, the application of cellulosic fibers as reinforcement faces a number of different challenges; the most important being the high melt viscosity of thermoplastic materials (typically in the range of 100-10,000

Pa.s) which makes the fiber impregnation step a difficult process. Therefore, cellulose fibers have been typically used in conventional thermoplastic melt processes such as extrusion [11]. However, this process is limited to commodity polymers such as polyethylene [12], polypropylene [13] and PVC [14] with melting and processing temperatures less than 200°C in order to avoid the thermal degradation of fibers (with the onset of 200°C) during processing. These composites are known as Wood Polymer Composites (WPCs) where due to the incompatible nature of the hydrophobic matrix polymer and hydrophilic cellulosic fillers, the true reinforcement of the cellulose fiber is not achieved. The challenge in path of incorporating natural fibers as "true reinforcements" in engineering thermoplastic polymers lies in the high melting point of those polymers such as Nylons and thermoplastic polyesters (with melting points above 200°C).

Cyclomer technology [15] is a promising technique to overcome these difficulties. In this technique, the engineering thermoplastic plastic composites are made by infusion of the reinforcement fibers with reactive mixture of the precursors of the matrix being a cyclic monomer or cyclic oligomers, which is then converted to the polymer via in-situ ring opening polymerization (ROP) reaction. The significant advantages associated with this process is the extremely lower viscosity of the monomer at the temperature of injection/infusion, rapid reaction rates resulting in de-molding cycle times of only a few minutes and the reaction with no by-product [15-16]. These monomers include ε-caprolactam and lauryllactam for polyamides and cyclic butylene terephthalate for polyester (poly butylene terephthalate) which could be used in liquid composite processes such as resin transfer molding (RTM) or vacuum assisted resin infusion (VARI).

Anionic ring-opening polymerization of ε-caprolactam has been extensively studied in detail [17]. A thorough study on glass fiber reinforced polyamide6 composites using the in-situ ROP reaction by vacuum infusion process have been carried out by Rijswijk and co-workers in [16, 18-20]. The effect of a number of different variables such as the polymerization temperature and time, the catalyst type and the effect of fiber sizing and interfacial bond formation on the properties of the final composite were studied. In terms of choice of polymerization catalysts, they reported that the use of caprolactam magnesium bromide provided a slower reaction rate (thus longer processing window) while the use of sodium caprolactamamte resulted in much shorter reaction times. Pillay and coworkers [21] developed carbon fiber reinforced PA6 composites using in-situ ROP reaction via vacuum assisted resin transfer molding. They achieved a successful impregnation of the carbon fabrics with up to 70 wt% of the fiber content together with a monomer conversion of around 98%. Gong *et al* [22] developed a series of polyamide fiber reinforced PA6 "all polymer" composites via the in-situ ROP of ε-carpolactam in presence of PA6 fibers. Optimum mechanical properties were found to be achieved at polymerization temperature 160°C while the composite panels exhibited low void content (<2.5%) and relatively high conversion of around 93%.

In another study by Yan *et al* [23], a continuous glass fiber reinforced PA6 composite panels were developed using in-situ ROP reaction. The authors reported that while the initiator/catalyst content plays a critical role on the final mechanical properties of the composites, quenching of the panels after reaction significantly reduced the mechanical properties while post-treatment via annealing hardly showed improvement of the properties.

In the current study, a process is developed based on the in-situ ROP reaction of PA6 to fabricate composite panels reinforced with cellulosic fabrics. For this purpose, two types of discontinuous short fiber cellulose pulp as well as continuous woven flax fabric are used. In addition, the effect of fiber pre-treatment and the processing conditions on the mechanical properties and the microstructure of the composite panels are reported.

5.2 Experimental

5.2.1 Materials

The caprolactam monomer was an AP-Nylon® grade (Brueggemann Chemical, Pennsylvania) with low moisture content (< 100 ppm) suitable for anionic ring-opening polymerization. C20, a difunctional hexamehtylene-1,6- dicarbamoyl caprolactam (the ROP activator) was supplied by Brueggemann Chemical. Ethylmagnesium bromide and sodium hydride were purchased from Aldrich. The chemical structure of the monomer, initiators and activator are shown in Figure 5.1. Sodium hydroxide pellets (certified ACS, $\geq 97\%$) purchased from Fischer Scientific. Bleached flax fabric (density of 1.59×10^{-3} g/cm^2, warp/weft yarn: 50×54) was purchased from Dharma Trading Co. Bleached kraft cellulose pulp in the form of fluff was supplied by Weyerhaeuser. The bleached fibers and the bleached flax fabric have the lignin, pectin and other extractives removed during the cooking process. Aminopropyltriethoxysilane (APS) was purchased from Gelest Inc.

5.2.2 Composite Processing and Sample Preparation

The processing setup schematic is shown in Figure 5.2. First, caprolactam monomer was fully dried in vacuum oven at 50°C overnight prior to use for the ROP reaction. The monomer was then added to a 1L glass reactor and melted at 95°C followed by degassing under vacuum for 15 minutes. The reactor was then purged and

242

continuously held under a dry nitrogen atmosphere during the entire process. Initiator (1.5 mol%) was added to the monomer followed by another degassing step for 20 minutes (under vacuum) and a nitrogen purge cycle. Finally, just prior to the injection, the C20 activator (0.9 mol%) was added and mixed for maximum of 30 seconds.

The vacuum assisted resin infusion (VARIM) setup is made up a transfer line from the feed tank to the bag assembly to the resin trap and vacuum pump. The bag assembly consists of a Teflon release films, stack of fiber fabric (or mat), a porous Teflon breathing cloth (peel-ply and breather) to allow the evacuation of excess resin and removal of gases as well as the temperature resistant bagging film. Four different polymerization temperature programs were applied: three isothermal polymerizations at 150°, 162° and 175°C in addition to a ramp program from an initial temperature of 100°C up to the final temperature of 150°C with a rate of 7°C/min.

Cellulose pulp mat was prepared by first forming a slurry of the fibers in water by a two-step homogenization at 700 and 1400 rpm for 15 minutes (each step) using an overhead stirrer. The slurry was then drained using vacuum filtration on a Whatman 1 filter paper. The mat was first dried for 12 hours in room temperature and further dried and compacted for 1 hour at 60°C under a pressure of 1 ton using a Tetrahedron® compression molding machine in order to prevent warpage and deformation upon drying-induced shrinkage.

Alkali pre-treatment of the fibers were carried out at 95°C under nitrogen atmosphere (in order to prevent the oxygen induced cleavage of glycosidic bonds) in 7.5% NaOH solution (1:25 liquor ratio) for 6 hours. After treatment, fibers were

thoroughly washed in multiple steps with hot water (≥80°C) to fully remove the peeling reaction byproducts.

The surface modification of the fibers with aminopropyltriethoxysilane (APS) was carried out using ethanolic solution of APS (water/ethanol: 20/80 v%) in which the desired amount of APS (with respect to the weigh fraction of fibers) was pre-hydrolyzed for 1 hour and sprayed onto the fibers until fiber were fully soaked in the solution. Fibers were then dried in room temperature overnight and washed with acetone to remove the excess silane. Finally, the crosslinking of the APS onto the fiber surface was carried out by curing the fibers (to facilitate the surface polycondensation of adsorbed APS) in vacuum oven at 120°C for 1 hour under vacuum.

5.2.3 ^{13}C NMR analysis

Solution spectra for the polymerization byproducts were acquired using a Bruker Avance 600 spectrometer operating at a proton frequency of 600.13 MHz and equipped with a standard BFO 5mm two channel probe. The probe temperature was 30˚C during data acquisition. Quantitative ^{1}H data was obtained using a relaxation delay of 10.04 s, a 90˚ pulse width of 13.35 μs, and an acquisition time of 4.96 s. The spectral width was 11.0 ppm, with 64 scans accumulated for the spectrum. The number of FID points was 65,536; the FID was zero-filled to 256K points and an exponential broadening of 0.50 Hz applied prior to Fourier Transformation. Carbon spectral acquisition parameters included a 90˚ pulse width of 11.0 μs, a relaxation delay of 2.02 seconds, an acquisition time of 0.98 seconds, and a spectral width of 220.9 ppm. The number of FID data points was 65,536 and were zero-filled to 256K points prior to Fourier Transformation. The number of accumulated transients for the spectrum was 20,368. Spectral baselines were corrected

using the ablative algorithm implemented in the MestReNova® software package. Samples for NMR experiments were prepared as follows: fibers were grinded into fine particles and dried overnight at 80°C. The activated polymerization mixture (with different initiators) was prepared and added to the fiber powder in a test tube which was purged with dry nitrogen (fiber content was about 50wt%). After 45 minutes of reaction time at 150°C the mixture was removed from the tube, grinded and mixed in DI water. The mixture was then centrifuged at 4000 rpm for 15 minutes to settle the fibers. In the case of sodium hydride initiator no polymer was formed while in the case of magnesium bromide initiator the solid polymer formed was removed during the centrifugation step. The polymerization by-products and the residual monomer remain soluble in water. In order to enhance the resolution of the NMR peaks corresponding to the by-product material, first, the solution was cast on a Teflon petri dish and water was completely removed. Then, the residual compound was dried in vacuum oven at 90°C to remove the majority of unreacted monomer (to decrease the NMR signal interference). The remaining residue was then used for NMR analysis.

In order to calculate the conversion of polymerization, solid sample pieces were grinded and subjected to Soxhlet extraction over boiling methanol to remove the residual monomer. The remaining solid fraction was fully dried in vacuum oven and the conversion was found using the ratio of the residue over the initial solid mass (fiber content was deducted from both samples before and after the extraction).

5.2.4 Mechanical Properties

Tensile tests were performed on an INSTRON 5582 MTS tensile tester with a crosshead speed of 5mm/min at room temperature according to the ASTM D-3039

standard. Flexural properties were determined according to the ASTM D790-02 standard using the same instrument. A three point bending jig equipped with 3.2 mm supports and loading nose radius was adjusted to a span of 40mm ensuring a 16:1 of span/thickness ratio. Samples for mechanical testing were rectangular bars cut from the composite panels with dimensions of $60{\times}12.7{\times}2.5$ mm^3 and at least five specimens were tested for each sample. All specimens were dried in vacuum oven for 24 hours at 70°C and then kept in a desiccator until tested.

5.2.5 Thermal Properties

Thermogravimetric data were obtained on a Q500 TA Instruments TGA with a heating rate of 10°C.min^{-1} under nitrogen atmosphere with a gas flow rate of 40mL.min^{-1}. Samples of 10-20mg were heated from room temperature up to 600°C. Degree of crystallinity (X_C), melting enthalpy and melting temperature of the composites was studied using a TA Instruments Q100 DSC with a heating rate of 10°C/min under dry nitrogen atmosphere. X_C was calculated using the following equation:

$$X_C(\%)=100*\frac{\Delta H_m}{\Delta H_{100\%}*(1-x_w)} \tag{5.1}$$

Where ΔH_m and $\Delta H_{100\%}$ are enthalpy of melting of the sample and that of 100% crystalline PA6 taken as 190 J/g [24]. The x_w is the weight fraction of fibers.

5.2.6 Microscopy

SEM images were acquired using a Sigma field-emission scanning electron microscope (ZEISS®, USA) using a 5 kV accelerating voltage. Images were taken from the fractured surfaces of the composites and also surface of fibers with prior sputter-coating with silver for enhanced conductivity.

5.2.7 Void Content Measurement

In order to find the void fraction of the composites, first, the weight fraction was calculated using the following equation:

$$w_f\,(\%)=100 \times \frac{x\rho_s S_c}{m_c}$$
(5.2)

Where the "x" is the number of reinforcement plies in the composite panel, ρ_s is the area density of a single ply of the fiber which is 1.59×10^{-3} and 5×10^{-3} g/cm^2 for flax and kraft pulp mats respectively, S_c is the sample area, and m_c is the sample mass.

Void fraction of the composites was calculated using the following equation:

$$\varphi_V\,(\%) =100 \times \frac{\rho_t - \rho_e}{\rho_t}$$
(5.3)

Where the ρ_t and ρ_e are the theoretical and experimental density values respectively. Void content measurements were conducted on three specimens for each sample and the average values are reported.

5.3 Results and Discussion

5.3.1 Investigation of Fiber Alkali Pre-treatment

Anionic ring-opening (ROP) polymerization of caprolactam monomer is inhibited in presence of cellulosic fibers indicated by discoloration of the fibers and the reactive mixture into dark brownish color. In order to study the inhibition phenomenon and the effect of polymerization initiator and fiber pre-treatment, two different systems consisting of sodium caprolactamate and magnesium bromide caprolactamate were chosen to study the effect of anionic initiator. Kan *et al* [25] reported the inhibition of the anionic PA6 polymerization in presence of ramie fibers to be associated with the well-known peeling reaction of cellulose in strong alkaline and high temperature conditions where the acidic

byproducts of the reaction terminate the active anionic centers of the initiator. While they reported that use of weaker initiator such as magnesium bromide caprolactamate could mitigate the inhibitive effect of the fibers on the PA6 polymerization reaction, we found that in presence of the kraft pulp cellulose fibers, application of both sodium and magnesium bromide caprolactamate resulted in inhibition of polymerization without proper pre-treatment of fibers.

As shown in Figure 5.3, the solution of the inhibited reaction medium in water shows a brownish color which is more predominant in the case of sodium caprolactamate initiator. The mechanism of peeling reaction of cellulose in strong alkaline environment has been extensively studied in literature [26]. The mechanism of peeling reaction is shown in Figure 5.4. Briefly, the open-chain form of the terminal unit of the cellulose is associated with the presence of an aldehyde group on the C1 unit (the anomeric carbon of the terminal glucose unit). Under alkaline condition, first step of the peeling reaction is the aldose-ketose isomerization which is followed by keto-enol isomerization. In the third step, the equilibrium of enediol with ketone is associated with the β-alkoxy elimination which cleaves the glyosidic bond thus removing one sugar unit from the chain end. This removed unit is eventually converted to gluco-(or xylo- when hemicellulose undergoes peeling reaction) isosaccharinic acid which could effectively deactivate the anionic centers.

The peeling reaction however, proceeds until a stabilized end group is formed through the competing "stropping" reaction as shown in Figure 5.4. The stabilized end unit which is a metasaccharinic acid unit does not undergo any further peeling reaction and is not removed from the cellulose chain end. Therefore, a preemptive induced

248

stopping reaction prior to the polymerization could be utilized to prevent (or minimize) the inhibitive effect of the peeling reaction during the polymerization thus making the in-situ ROP reaction successful.

The ^{13}C NMR spectrum of the byproducts of pre-treatment of kraft pulp cellulose fibers with sodium hydroxide solution is presented in Figure 5.5. The peeling reaction of cellulose in presence of strong alkali is usually a complex reaction with wide range of various byproducts depending on the reaction conditions, cellulose species and the type of alkali. Knill et al [26] has tabulated a number of different byproducts of the cellulose peeling reaction. The three major components of the byproduct material are shown in Figure 5.5. The gluco- and xylo-isosaccharinic acids are the primary compounds of the peeling reaction. The diketone moiety during the later stages of the peeling reaction can undergo retro-Aldol reaction to form the 2,3-dihydroxy-2-methylpropanoic acid [27]. In addition it has been shown [28] that the isosaccharinic acid moiety can undergo a number of further reaction through 3-keto intermediate that liberates various acidic compounds such as formic and lactic acid. (Although less likely to occur during the ROP reaction as no water is present in the system). It is observed in the ^{13}C NMR spectrum of NaOH pre-treatment byproduct that a number of different characteristic signals appear in the 20-40 and 60-80 ppm range corresponding to the carbons of the compounds showed in Figure 5. Based on the structures shown, the characteristic signals are at δ= 160-180 (^{1}C, ^{7}C, ^{11}C), 60-80 (^{2}C, ^{3}C, ^{5}C, ^{6}C, ^{8}C, ^{10}C, ^{12}C, ^{13}C, ^{15}C), 38.1 (^{4}C), 30.2 (^{14}C) and 20.3(^{9}C). The signal shown as C* located at 102.2 correspond to the C1 carbon of soluble cellulose (glucose unit) [29]. This observation confirms the presence of the peeling reaction byproducts in the alkali pre-treated fiber medium.

Now in order to study the effect of alkali pre-treatment on the polymerization reaction inhibition, the ^{13}CNMR spectra of the ROP reaction byproducts in the case of sodium and magnesium bromide caprolactamate initiators are presented in Figure 5.5. First of all, it should be mentioned that compared to the NaOH pre-treatment reaction, the signal of the byproducts of the ROP are weaker due to the interference of the signals corresponding to the residual monomer and the initiator in the solution. The characteristic resonance of the caprolactam monomer are at δ= 181.1 (^{a}C), 22.6 (^{c}C), 28.5(^{d}C), 29.8(^{e}C), 35.5(^{b}C) and 42.3(^{f}C). The signals of sodium caprolactamate appear at δ= 182.3($^{a'}$C), 24.6($^{c'}$C), 26.5($^{d'}$C), 29.8($^{e'}$C), 35.5($^{b'}$C), 39.4($^{f'}$C) and for the magnesium bromide caprolactamate the signals are at δ= 183.5($^{a'}$C), 25.2($^{c'}$C), 26.5($^{d'}$C), 29.8($^{e'}$C), 37.2($^{b'}$C), 39.4($^{f'}$C).

In the case of the Na-caprolactamate initiator, we see that a series of signals are appearing in the range of 60-80 and 160-170 ppm that corresponds to the signals of the saccharinic acid moieties from the in-situ ROP byproducts. Looking at the Figure 5.3, it is clearly seen that even after alkali pre-treatment of the fibers, the peeling reaction still occurs in the case of sodium caprolactamate anions however, it is interesting to see that in the case of the magnesium bromide caprolactamate anion, the signals of byproducts are significantly reduced before alkali pre-treatment and after the pre-treatment no characteristic signals corresponding to the peeling reaction byproducts are observed. This is due to the fact the magnesium bromide counter ion has a larger size compared to the sodium therefore; the rate of dissociation in the molten caprolactam is much lower than that of the sodium counter ion. As a result, this decreased ionization potential and less mobility results in lower initiator activity of the magnesium bromide. It has been

previously shown [18] that, compared to sodium caprolactamate, the magnesium bromide caprolactamate initiator induces a significantly larger induction time before the viscosity of the activated system increases (due to the same counter ion effect) which interestingly, makes this choice of initiator suitable for infusion process (in terms of infusion processing timeframe).

In order to study the effects of the alkali pre-treatment on the pulp fibers, microstructure of the fiber before and after the alkali treatment was analyzed by SEM as shown in Figure 5.6(a), (b). It is seen that upon pre-treatment of the fibers with alkali, the surface roughness of the fibers is significantly enhanced. In fact, the appearance of the fibrillary structure of the cellulose fiber shows that the alkali treatment, removes most of the inter-fibrillar material which is mostly the hemicellulosic part as well as the paracrystalline cellulose or amorphous fractions that exist in between the cellulose fibrils. This enhancement of the surface roughness will benefit the mechanical properties by providing more interfacial interlocking between the matrix and the fiber as well as providing more interfacial area for the interaction and adhesion of the fiber-matrix pair. In order further investigate the removal of the interfibrillar material, the thermal stability of the fibers before and after the alkali treatment was studied by TGA and the results are presented in Figure 5.6(c). As can be seen, upon treating the fibers with alkali, the onset of degradation shifts from 339.1°C (±3.5°C) in the untreated fibers to 352.5°C (±2.2°C) in the case of the treated fibers. It has been shown [30-31] that hemicellulose has lower thermal stability compared to the cellulose due to its amorphous structure which is more easily degraded upon heating while the more crystalline and ordered cellulosic domains possess better thermal stability. In addition, hemicellulose leaves a higher amount char

residue compared to cellulose. Looking at the TGA graphs, it is clearly seen that increasing the onset thermal stability and the observed decrease in the final char yield (total of 4.4 wt% difference) could be attributed to the removal of the amorphous and hemicellulosic portion of the fibers upon treatment with NaOH solution.

In order to assess the effect of pre-treatment of the pulp fibers with alkali on the subsequent ROP reaction inhibition, the variation of the mass loss of the fibers versus pre-treatment time, and the corresponding conversion of the monomer during the subsequent ROP reaction were studied and the results are shown in Figure 5.6(d). For this purpose, around 40% of the treated fiber (certain pre-treatment times) were placed in a test tube followed by the ROP reaction in inert atmosphere. It is seen that increasing the pre-treatment time initially results in a higher mass loss in the pulp up to around 4 hours and 10% mass loss. However, the rate of mass loss decreases after this point and the mass loss variation reaches a semi-plateau region where the mass loss rate slowly changes with further increasing the treatment time. Interestingly, the conversion of the subsequent polymerization only reaches the 90% at the same point. With further increasing the time the conversion reaches around 95% at and above 6 hours of pre-treatment time (which is time chosen in this study for alkali pre-treatment). With Further increasing the pre-treatment time, only minimal changes in mass loss and conversion of the subsequent ROP reaction is observed.

5.3.2 Morphology and Mechanical Properties

5.3.2.1 Analysis of Property Variations in the Composite Panel

The composite panels prepared by the VARI process of in-situ ROP reaction were studied for variation of some important physical and structural properties along the flow

direction of the monomer. For this purpose, a typical panel of flax fabric and kraft pulp mat infused with the activated caprolactam monomer and polymerized using two different temperature programs were prepared. The panels were 8 cm across the length and the resin inlet was placed in the middle of one side and properties were taken at 1, 3, 5 and 7 cm from the inlet point towards the outlet that was placed in the sample position but on the opposite side. A schematic of the panel is shown in Figure 5.7(a).

First of all, it is seen in Figure 5.7(b) that the conversion of the polymerization reaction shows a slight change across the length of the panel. Interestingly, the conversion slightly reduces in the case of the flax fabric reinforced PA6 composite as the flow front travels along the panel length. This could be attributed to the consumption/deactivation of a number of active anionic centers as the flow travels within the fabric bed and gets in contact with the cellulosic substrate.

Moreover, for the panels that were infused at 100°C and polymerized with a ramping from 100 to 150°C, the weight fraction of the fibers in the composite is initially smaller in the outlet section and it gradually increases as the flow front travels through the fiber length. It is known that the inlet of infused bag assemblies is a resin-reach zone where the fiber fraction is smaller compared to the middle sections of the panel [21]. It is seen that compared to the flax fabric reinforcement, the use of the kraft pulp mat reinforcement results in relatively lower weight fraction of fiber with the average weight fraction of 38.3 wt% in the case of the flax fabric composite and 34.3 wt% in the case of pulp mat. This observation is attributed to the structure of the pulp mat where the compact fiber bed and high porosity of the mat (due to the short fiber nature of the pulp mat) results in lower permeability of the resin during the infusion process. This lower

permeability results in less available time for the resin within the pulp mat to bleed out through the breather cloth before polymerization kicks off and viscosity increases. Thus, higher relative amount of resin is trapped within the mat (compared to the woven flax fabric with open channels) resulting in decreased fiber fraction.

In addition, the variation of the weight fraction across the panel length is lower for the flax fabric composite compared to that of the pulp mat. This could again be attributed to the more difficult resin bleeding process in the case of the pulp mat fiber bed.

Furthermore, the effect of polymerization temperature on the variation of fiber weight fraction across the panel length is also shown in Figure 5.7(b). While the average weight fraction is 38.3% in the case of the flax fiber composite processed by gradually increasing the temperature from 100°C to 150°C, it reduces to an average of 35.7% for the sample polymerized at 175°C. This is attributed to the fact that at higher temperatures, the viscosity of the resin increases more rapidly due to higher rate of polymerization which restricts the bleeding of excess resin through the fiber weight thus resulting in slightly lower weight fraction. In addition, it is seen that the weight fractions are slightly more uniform in the case of the sample polymerized at 175°C compared to that of the lower temperature. This could be attributed to the lower initial viscosity of the resin when it enters the pre-heated bag assembly at 175°C which would aloe more uniform rein flow in the early stages of the infusion process.

5.3.2.2 Effect of Polymerization Temperature

The effect of polymerization temperature on the mechanical properties of the composite panels reinforced with both the flax fabric and the pulp mat were studied by polymerizing the samples using four different temperature programs: a heating ramp starting with infusion temperature of 100°C and final temperature of 150°C, and three isothermal polymerizations at 150°C, 162°C and 175°C. The results of the tensile and flexural mechanical tests are shown in Figure 5.8. As can be seen, in the case of both fiber types, the flexural modulus initially increases when the polymerization is conducted isothermally at 150°C compared to the heating ramp program from 100°C to 150°C. However, further increasing the polymerization temperature to 162°C and 175°C results in significant reduction in both tensile and flexural moduli as well as the tensile and flexural strength. For example, in the case of the flax fabric reinforced PA6, the tensile modulus initially increases from 4.35 GPa to 4.81 GPa, but further increasing the temperature to 162°C and 175°C reduces the modulus to 4.02 and 3.78 GPa respectively. Similarly, the tensile strength of the flax fabric composite increases from 110.5 MPa to 121.3 MPa by changing the processing temperature from 100°C-150°C to isothermal polymerization temperature of 150°C while it decreases to 105.1 and 91.6 MPa for composite processed at 162°C and 175°C.

A number of different reasons are proposed to be responsible for the observed changes. First, it has been previously shown [25] that the peeling reaction extent and inhibitive property of the cellulose fibers on anionic polymerization of caprolactam increases with increasing the temperature. This is confirmed in our study by looking at the conversion values of the samples polymerized at different temperatures shown in

Table 5.1. As can be seen, increasing the polymerization temperature results in relatively lower average conversion of the monomer in the composite samples. Therefore, samples polymerized at higher temperatures have higher amount of residual monomer within the matrix that could act as a defect during the mechanical testing thus reducing the modulus and strength.

In addition, as shown in Table 5.1, as the temperature of polymerization increases, the void content of the composite panels increases in both flax and pulp mat reinforced PA6 composites. As discussed by Van Rijswijk *et al* [32], several factors could contribute to the void formation during the PA6 polymerization. The fist reason could be attributed to the voids formed by local boiling of caprolactam monomer as the temperature of the bag assembly is increased. Since in our systems, the monomer is infused into the mold by the application of vacuum, this reduced pressure conditions will result in reduced vapor pressure of the caprolctam inside the pre-heated mold thus converting the monomer into caprolactam vapor which upon removal could leave internal microvoids within the matrix. This could also contribute to the observed reduction in final conversion as the local boiling of monomer could results in subsequent precipitation of the trapped vapors in the voids that are created by the dissolved nitrogen gas (from the monomer tank blanket) [32]. This precipitation of caporlcatam "packets" occur once the bag assembly is cooled down that results in reduced conversion and act as local plasticizers reducing the mechanical strength of the composites.

Moreover, the polymerization temperature affects the crystallinity of the matrix. A typical representative DSC diagram of the flax fabric reinforced composite at four different processing temperature programs are shown in Figure 5.9 and the melting point

and degree of crystallinity of the composite is shown in Table 5.2. It is observed that as the processing temperature increases, the overall degree of crystallinity decreases from 44.9% in the sample polymerized non-isothermally from 100°-150°C to 28.5% in the samples polymerized isothermally at 175°C. This reduction is due to the higher rate of polymerization (chain propagation) which limits the macromolecular chain packing into ordered crystalline regions during the polymerization thus reducing the overall crystallinity. In addition, the melting point of the formed crystals are also reduced which indicates the formation of less ordered γ-type crystals (with lower T_m compared to α-type crystals with higher T_m). This change in the crystal structure and the crystal content, results in reduced stiffness of the matrix that adversely affects the mechanical properties of the composite material.

The morphologies of the tensile fractured surface of the kraft pulp composite panels prepared at different temperatures are shown in SEM images of Figure 5.10. Samples that were polymerized by non-isothermal ramping and isothermal at 150°C show predominantly fractures fibers on the surface while for the samples that were prepared at 162°C and 175°C, fiber "pull-out" is the main mechanism of failure as indicated by the presence of cavities and protruding fibers on the surface. The difference in the failure mode of the samples is mainly related to the interfacial adhesion and extent of stress transfer from the matrix to fibers. As mentioned above, for the sample polymerized above 160°C, the formation of low molecular weight oligomeric species (due to the enhanced inhibitive effect of fibers at elevated temperatures) at the interface of the matrix-fiber, could results in less efficient stress transfer process. In addition, as discussed before, formation of internal micro-voids at higher processing temperatures,

257

combined with lower crystallinity of those samples, could result in more defective interfacial area which consequently, adversely impacts the adhesion at the interface and stress transfer process from matrix to fiber. On the contrary, in the samples polymerized below 160°C, higher stiffness of the matrix (due to higher crystallinity) as well as higher conversion and less internal voids, ensures a much more efficient transition of load from matrix to fibers.

5.3.2.3 Effect of Surface Modification

In order to further investigate the effect of interfacial adhesion on the mechanical properties and failure mechanism, the effect of the surface modification of the fibers with aminopropyltriehtoxysilane (APS) in the flax fabric reinforced composites were investigated. In a study by Van Rijswijk and coworkers [33], it was shown the modification of glass fibers with APS could improve the mechanical properties and interlaminar shear strength. This was attributed to the interfacial bond formation between the polyamide 6 matrix and the APS layer on glass surface primarily through transamidation reaction [34-35]. Nonetheless, in the present work, the effect of the APS modification of cellulose fibers with regard to the APS content was investigated.

The results of the mechanical testing of the samples modified with 0, 2, 4 and 6 wt% of APS (with regard to the fiber weight) are shown in Figure 5.11. Interestingly, it is seen that by applying a 2 wt% of the APS, the highest tensile modulus and strength (5.59 GPa and 125.6 MPa respectively) as well as the highest flexural modulus and strength (6.74 GPa and 140.9 MPa respectively) are obtained. Further increasing the APS content results in slight reduction in tensile and flexural strength (for the 4wt% APS, the values are all still higher than that of non-modified fibers). With addition of 6wt% of the APS,

the tensile and flexural strength values drop below that of non-modified fibers. This observation is attributed to the structure of polysiloxane layer on the flax fiber surface. It has been proposed [36] that optimal interfacial adhesion with organosilane surface modifiers could be achieved with few layers of the polysiloxane layers on the surface. Application of excessive amount of APS, results in development of muli-layered polysiloxane network on the surface in the form of aggregates that negatively impacts the interfacial adhesion due to the brittleness of the interfacial network layer which as a consequence, is counterproductive towards the improvement of mechanical properties. The fractured surfaces (in tensile test) of these samples are shown in SEM images of Figure 5.12. As can be seen, with 2 wt% APS, a plastically deformed layer of the matrix wrapping the fibers are observed in the fracture surface, however, with further increasing the APS content, the coating of siloxane on the fiber becomes thicker and the brittleness of this thick coating is observed through the development of microcracks in the interfacial region on the fiber surface.

5.4 Conclusion

Thermoplastic polyamide 6 composites reinforced by continuous woven flax fabric and discontinuous kraft cellulose pulp mat were successfully developed by in-situ anionic ring-opening polymerization (ROP) of caprolactam using a vacuum assisted resin infusion process. It was found that pre-treatment of the fibers with alkali in combination with a less reactive magnesium bromide based anionic initiator is necessary in order to minimize the severe inhibitive effect of cellulosic fibers on the ROP reaction. Analysis of the physical and mechanical properties revealed that optimum mechanical properties are obtained at polymerization temperature of 150°C as increasing the polymerization

259

temperature results in decreased conversion of polymerization due to the enhanced inhibitive effect of the cellulose on polymerization, increased void content and decreased degree of crystallinity. In addition, while application of aminopropyltriethoxysilane (APS) surface modifier enhances the mechanical properties by improving the interfacial adhesion, the optimum APS content was found to be at 2wt% of fibers as further increasing the APS results in multiplayer polysiloxane aggregates on the fiber surface witch has detrimental effect on interfacial properties.

5.5 References

1. Khalil, H. A.; Bhat, A.; Yusra, A. I., Green composites from sustainable cellulose nanofibrils: a review. *Carbohydrate Polymers* **2012,** *87* (2), 963-979.

2. Koronis, G.; Silva, A.; Fontul, M., Green composites: a review of adequate materials for automotive applications. *Composites Part B: Engineering* **2013,** *44* (1), 120-127.

3.	La Mantia, F.; Morreale, M., Green composites: A brief review. *Composites Part A: Applied Science and Manufacturing* **2011,** *42* (6), 579-588.

4.	Tharanathan, R., Biodegradable films and composite coatings: past, present and future. *Trends in Food Science & Technology* **2003,** *14* (3), 71-78.

5.	Holbery, J.; Houston, D., Natural-fiber-reinforced polymer composites in automotive applications. *JOM Journal of the Minerals, Metals and Materials Society* **2006,** *58* (11), 80-86.

6.	Joshi, S. V.; Drzal, L.; Mohanty, A.; Arora, S., Are natural fiber composites environmentally superior to glass fiber reinforced composites? *Composites Part A: Applied science and manufacturing* **2004,** *35* (3), 371-376.

7.	Thakur, V. K.; Thakur, M. K.; Gupta, R. K., Review: raw natural fiber–based polymer composites. *International Journal of Polymer Analysis and Characterization* **2014,** *19* (3), 256-271.

8.	Rong, M. Z.; Zhang, M. Q.; Liu, Y.; Yang, G. C.; Zeng, H. M., The effect of fiber treatment on the mechanical properties of unidirectional sisal-reinforced epoxy composites. *Composites Science and technology* **2001,** *61* (10), 1437-1447.

9.	Dhakal, H.; Zhang, Z.; Richardson, M., Effect of water absorption on the mechanical properties of hemp fibre reinforced unsaturated polyester composites. *Composites Science and Technology* **2007,** *67* (7), 1674-1683.

10.	Chen, H.; Miao, M.; Ding, X., Influence of moisture absorption on the interfacial strength of bamboo/vinyl ester composites. *Composites Part A: Applied Science and Manufacturing* **2009,** *40* (12), 2013-2019.

11.   Clemons, C., Wood-plastic composites in the United States: The interfacing of two industries. *Forest Products Journal* **2002,** *52* (6), 10.

12.   Brahmakumar, M.; Pavithran, C.; Pillai, R., Coconut fibre reinforced polyethylene composites: effect of natural waxy surface layer of the fibre on fibre/matrix interfacial bonding and strength of composites. *Composites Science and technology* **2005,** *65* (3), 563-569.

13.   Zampaloni, M.; Pourboghrat, F.; Yankovich, S.; Rodgers, B.; Moore, J.; Drzal, L.; Mohanty, A.; Misra, M., Kenaf natural fiber reinforced polypropylene composites: a discussion on manufacturing problems and solutions. *Composites Part A: Applied Science and Manufacturing* **2007,** *38* (6), 1569-1580.

14.   Jiang, H.; Kamdem, D. P., Development of poly (vinyl chloride)/wood composites. A literature review. *Journal of Vinyl and Additive Technology* **2004,** *10* (2), 59-69.

15.   Ding, Y.; Hay, A., Cyclomer Technology for High Performance Polymers. In *Cyclic Polymers*, Semlyen, J. A., Ed. Springer Netherlands: 2002; pp 307-345.

16.   van Rijswijk, K.; Bersee, H. E. N., Reactive processing of textile fiber-reinforced thermoplastic composites – An overview. *Composites Part A: Applied Science and Manufacturing* **2007,** *38* (3), 666-681.

17.   Udipi, K.; Davé, R. S.; Kruse, R. L.; Stebbins, L. R., Polyamides from lactams via anionic ring-opening polymerization: 1. Chemistry and some recent findings. *Polymer* **1997,** *38* (4), 927-938.

18.   van Rijswijk, K.; Bersee, H. E. N.; Jager, W. F.; Picken, S. J., Optimisation of anionic polyamide-6 for vacuum infusion of thermoplastic composites:

choice of activator and initiator. *Composites Part A: Applied Science and Manufacturing* **2006,** *37* (6), 949-956.

19.   van Rijswijk, K.; van Geenen, A. A.; Bersee, H. E. N., Textile fiber-reinforced anionic polyamide-6 composites. Part II: Investigation on interfacial bond formation by short beam shear test. *Composites Part A: Applied Science and Manufacturing* **2009,** *40* (8), 1033-1043.

20.   Rijswijk, K. v.; Teuwen, J. J. E.; Bersee, H. E. N.; Beukers, A., Textile fiber-reinforced anionic polyamide-6 composites. Part I: The vacuum infusion process. *Composites Part A: Applied Science and Manufacturing* **2009,** *40* (1), 1-10.

21.   Pillay, S.; Vaidya, U. K.; Janowski, G. M., Liquid molding of carbon fabric-reinforced nylon matrix composite laminates. *Journal of Thermoplastic Composite Materials* **2005,** *18* (6), 509-527.

22.   Gong, Y.; Liu, A.; Yang, G., Polyamide single polymer composites prepared via in situ anionic polymerization of ε-caprolactam. *Composites Part A: Applied Science and Manufacturing* **2010,** *41* (8), 1006-1011.

23.   Yan, C.; Li, H.; Zhang, X.; Zhu, Y.; Fan, X.; Yu, L., Preparation and properties of continuous glass fiber reinforced anionic polyamide-6 thermoplastic composites. *Materials & Design* **2013,** *46*, 688-695.

24.   Barhoumi, N.; Maazouz, A.; Jaziri, M.; Abdelhedi, R., Polyamide from lactams by reactive rotational molding via anionic ring-opening polymerization: Optimization of processing parameters. *Express Polym Lett* **2013,** *7* (1), 76-87.

25.   Kan, Z.; Yang, M.-b.; Yang, W.; Liu, Z.-y.; Xie, B.-h., Investigation on the reactive processing of textile-ramie fiber reinforced anionic polyamide-6 composites. *Composites Science and Technology* **2015,** *110*, 188-195.

26.   Knill, C. J.; Kennedy, J. F., Degradation of cellulose under alkaline conditions. *Carbohydrate Polymers* **2003,** *51* (3), 281-300.

27.   G. Mayr; F. Zeppetzauer; T. Zweckmair; D. Bauer; S. Hild; A. Potthast; T. Rosenau; Röder, T., The Reactions of Cellulose and Hemicellulose Degradation Products in the Viscose Fibre Spin Bath. *Lenzinger Berichte* **2015,** *92*, 53-58.

28.   Paananen, M.; Rovio, S.; Liitiä, T.; Sixta, H., Stabilization, degradation, and dissolution behavior of Scots pine polysaccharides during polysulfide (K-PS) and polysulfide anthraquinone (K-PSAQ) pulping. *Holzforschung* **2015,** *69* (9), 1049-1058.

29.   Bootten, T. J.; Harris, P. J.; Melton, L. D.; Newman, R. H., Solid-state 13C-NMR spectroscopy shows that the xyloglucans in the primary cell walls of mung bean (Vigna radiata L.) occur in different domains: a new model for xyloglucan–cellulose interactions in the cell wall. *Journal of experimental botany* **2004,** *55* (397), 571-583.

30.   Yang, H.; Yan, R.; Chen, H.; Lee, D. H.; Zheng, C., Characteristics of hemicellulose, cellulose and lignin pyrolysis. *Fuel* **2007,** *86* (12), 1781-1788.

31.   Jin, W.; Singh, K.; Zondlo, J., Pyrolysis kinetics of physical components of wood and wood-polymers using isoconversion method. *Agriculture* **2013,** *3* (1), 12-32.

32.   Van Rijswijk, K.; Bersee, H.; Beukers, A.; Picken, S.; Van Geenen, A., Optimisation of anionic polyamide-6 for vacuum infusion of thermoplastic composites: Influence of polymerisation temperature on matrix properties. *Polymer testing* **2006,** *25* (3), 392-404.

33.   Van Rijswijk, K.; Van Geenen, A.; Bersee, H., Textile fiber-reinforced anionic polyamide-6 composites. Part II: Investigation on interfacial bond formation by short beam shear test. *Composites Part A: Applied Science and Manufacturing* **2009,** *40* (8), 1033-1043.

34.   Mateva, R.; Petrov, P.; Rousseva, S.; Dimitrov, R.; Zolova, G., On the structure of poly-ε-caprolactams, obtained with bifunctional N-carbamyl derivatives of lactams. *European polymer journal* **2000,** *36* (4), 813-821.

35.   Ricco, L.; Russo, S.; Orefice, G.; Riva, F., Anionic poly (ε-caprolactam): relationships among conditions of synthesis, chain regularity, reticular order, and polymorphism. *Macromolecules* **1999,** *32* (23), 7726-7731.

36.   Xie, Y.; Hill, C. A.; Xiao, Z.; Militz, H.; Mai, C., Silane coupling agents used for natural fiber/polymer composites: A review. *Composites Part A: Applied Science and Manufacturing* **2010,** *41* (7), 806-819.
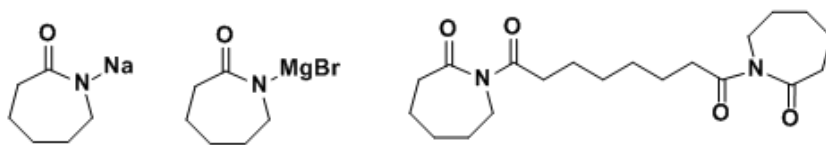
Figure 5.1 Structure of sodium caprolactamate, magnesium bromide caprolactamate and C20 activator (hexamethylene-1,6- dicarbamoyl caprolactam)
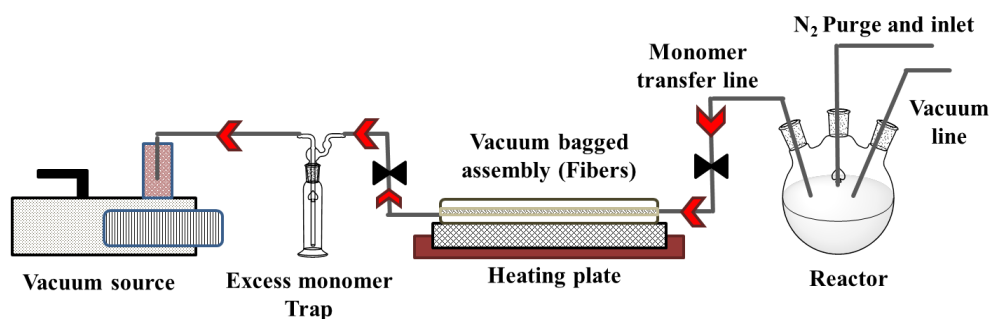
Figure 5.2 Vacuum Assisted Resin Infusion (VARI) set up
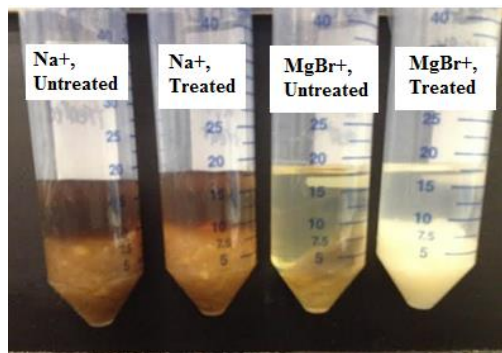
Figure 5.3 Solution of the *in-situ* ROP byproducts using sodium and magnesium bromide caprolactamate initiator in presence of untreated and alkali-treated cellulose pulp
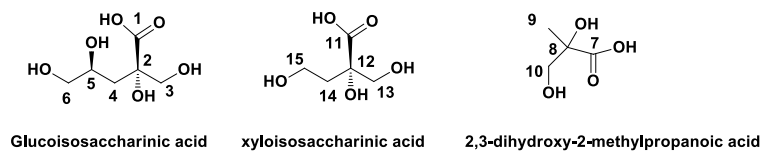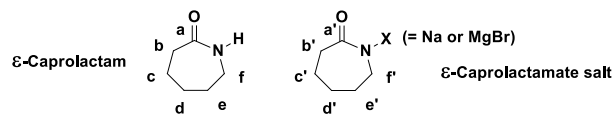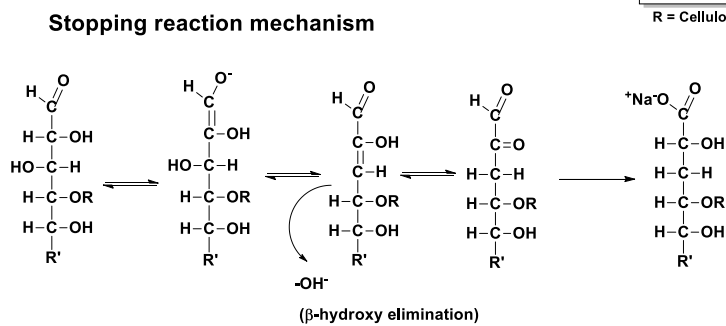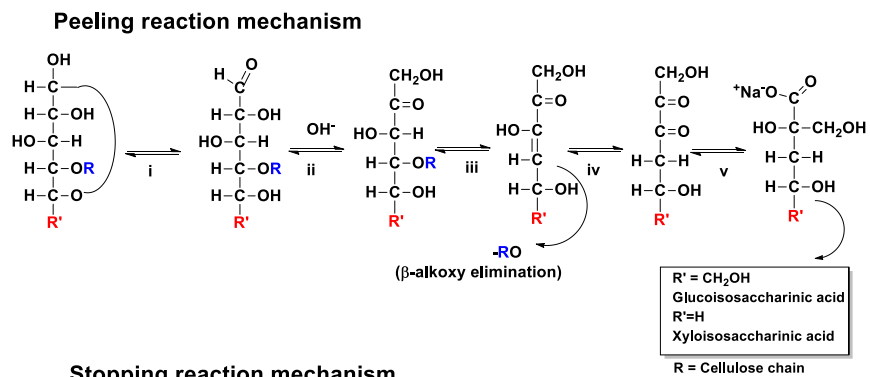
Figure 5.4 Mechanism of peeling and stopping reaction as well as three major peeling byproducts
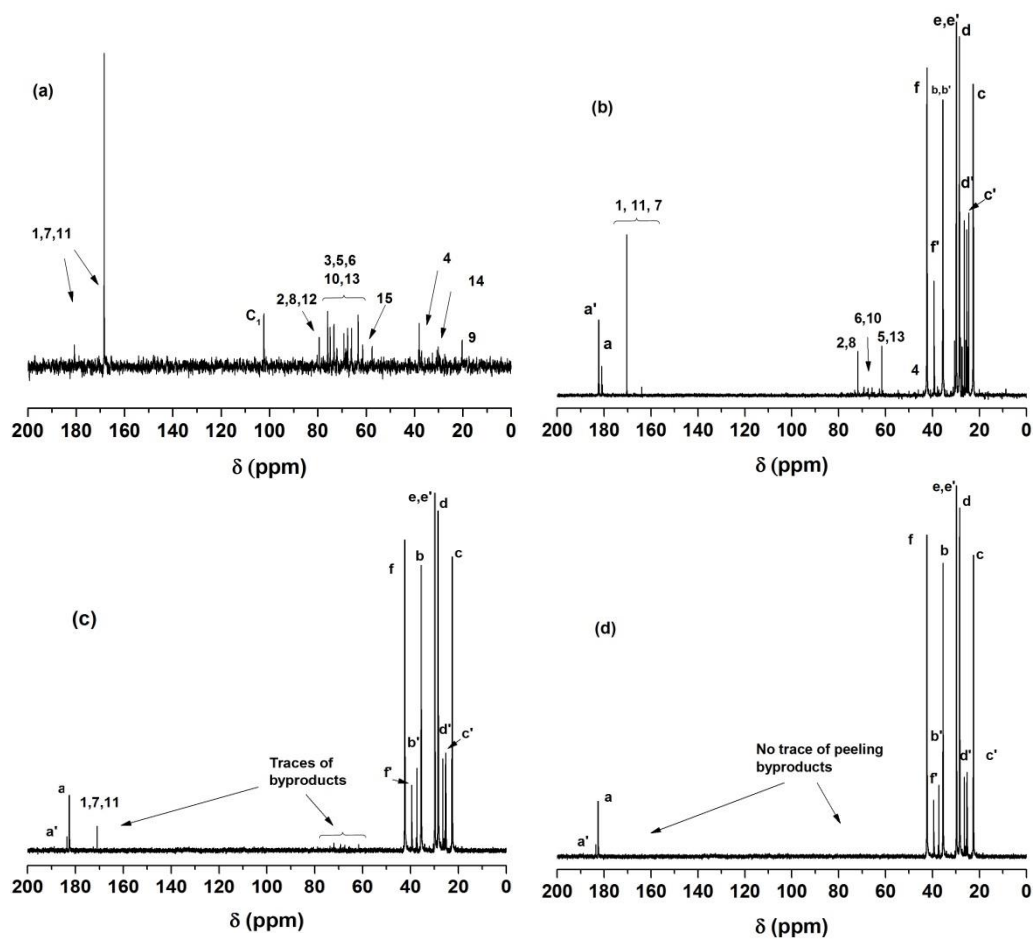
Figure 5.5 ^{13}C NMR spectra of (a) alkali pre-treatment byproducts, (b) sodium caprolactamate initiator byproducts, (c) magnesium bromide caprolactamate initiator byproducts (without alkali pre-treatment) and (d) magnesium bromide caprolactamate initiator byproducts (after alkali pre-treatment)
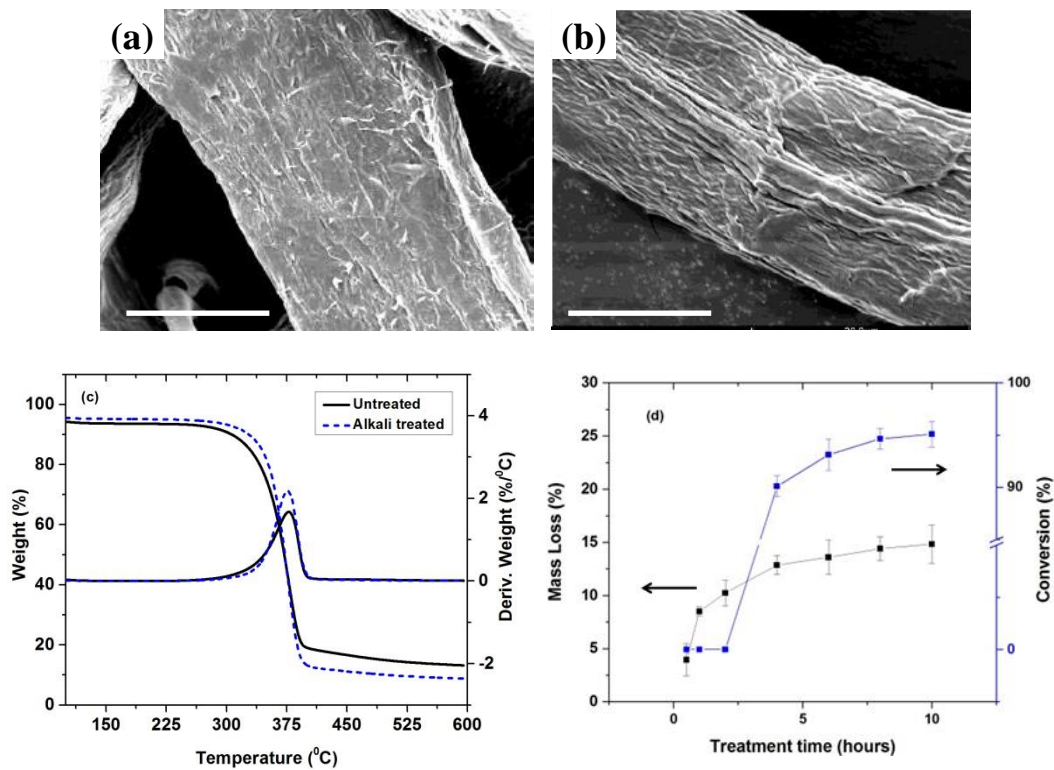
Figure 5.6 SEM image of (a) untreated cellulose pulp fiber, (b) Alkali treated cellulose pulp fiber, (c) TGA and DTG curves of untreated and alkali-treated pulp fiber and (d) variation of mass loss and subsequent ROP conversion as a function of alkali pre-treatment time.

The scale bar of SEM images is 20μm
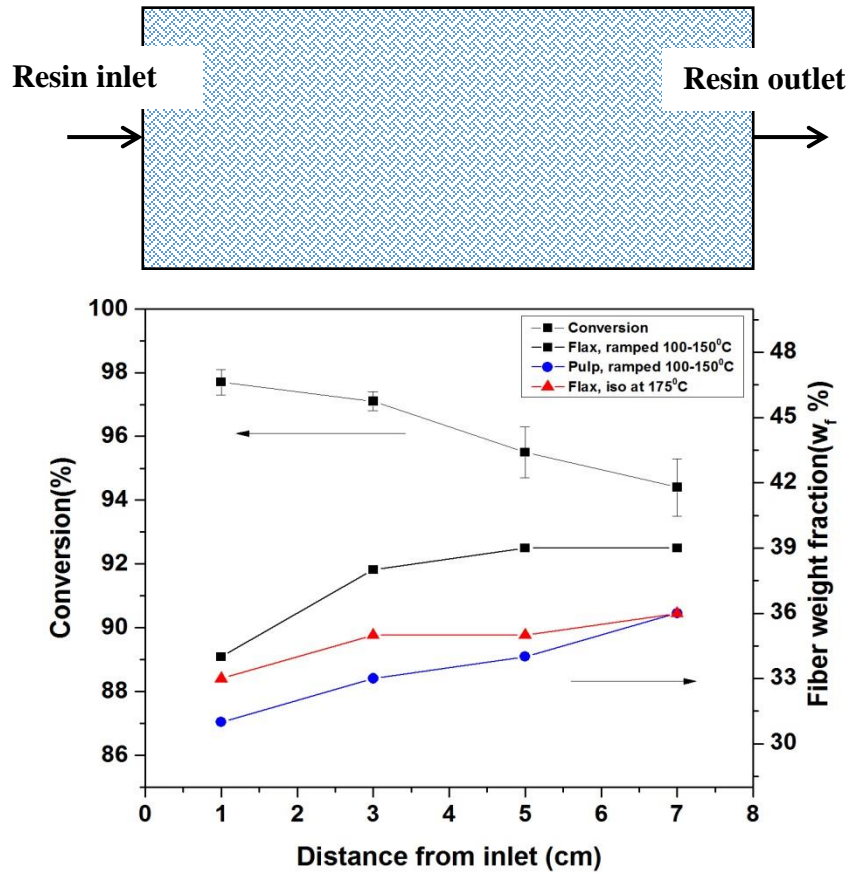
Figure 5.7 Spatial variation of the conversion and fiber weight fraction of flax fiber reinforced polyamide 6 composite panel
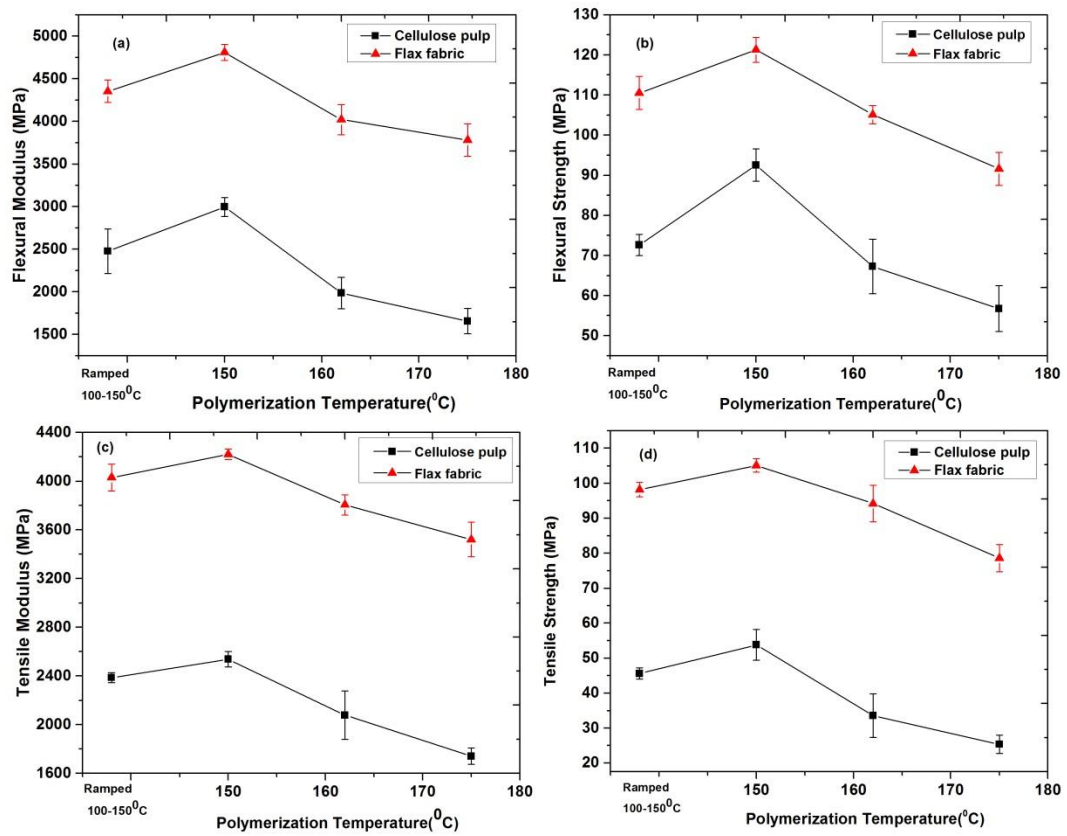
Figure 5.8 Effect of polymerization temperature on tensile and flexural properties of flax fiber and kraft pulp fiber reinforced polyamide 6 composites
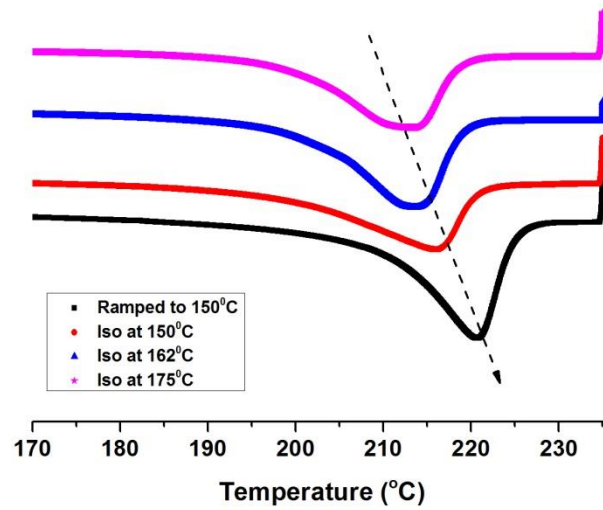
Figure 5.9 DSC thermogram showing the effect of the polymerization temperature on melting point of the flax fiber reinforced PA6 composites
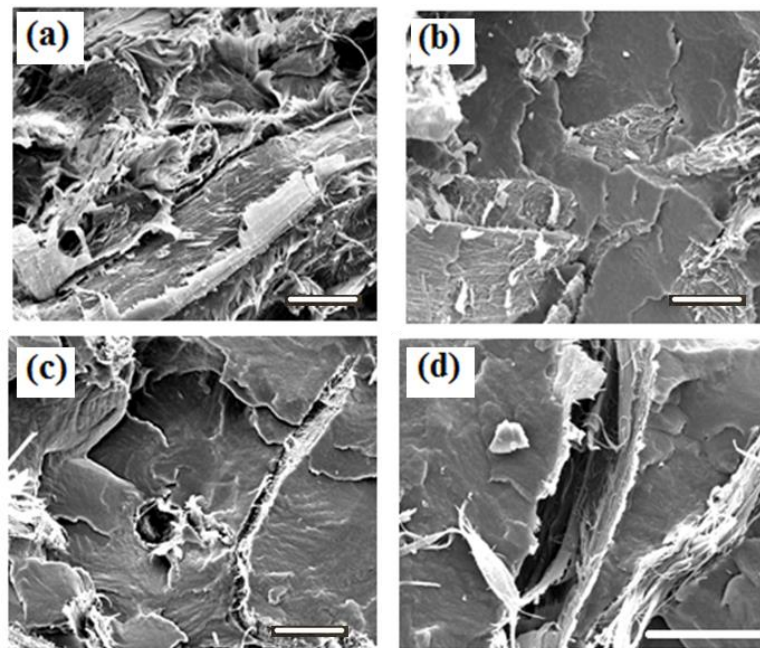
Figure 5.10 SEM images of the fractured surface of kraft pulp composite polymerized at (a) non-isothermal from 100° to 150°C, (b) 150°C, (c) 162°C and (d) 175°C.

The scale bar on the images is 20μm.
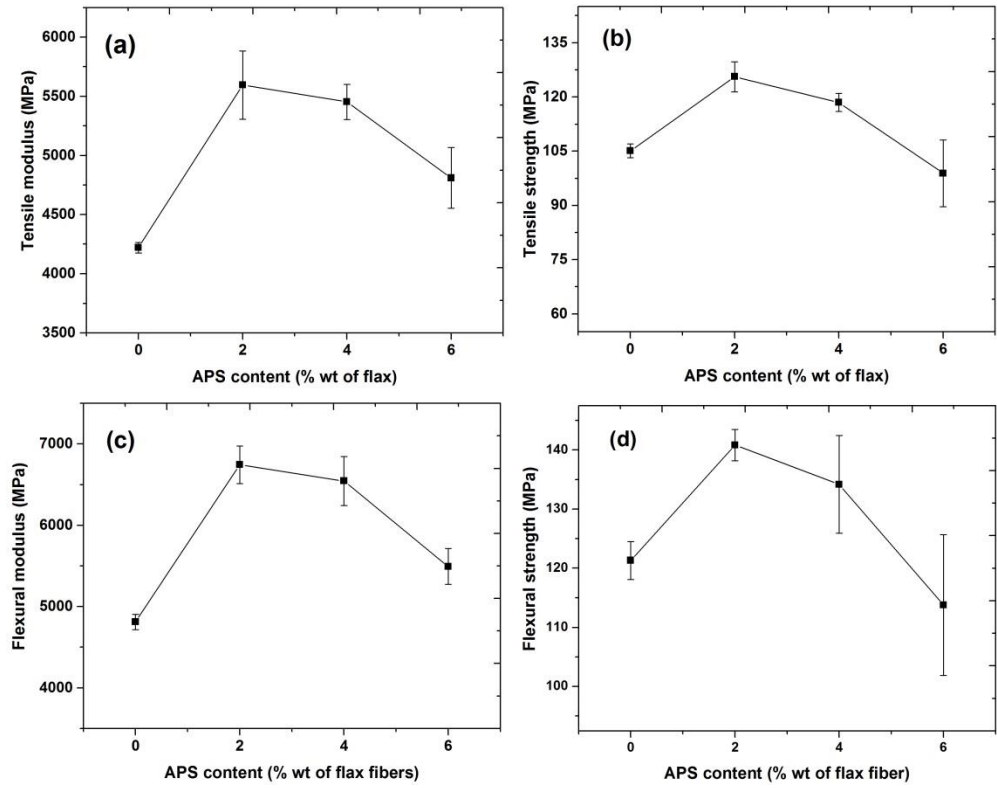
Figure 5.11 The effect of APS concentration on tensile and flexural properties of flax fabric reinforced PA6 composites
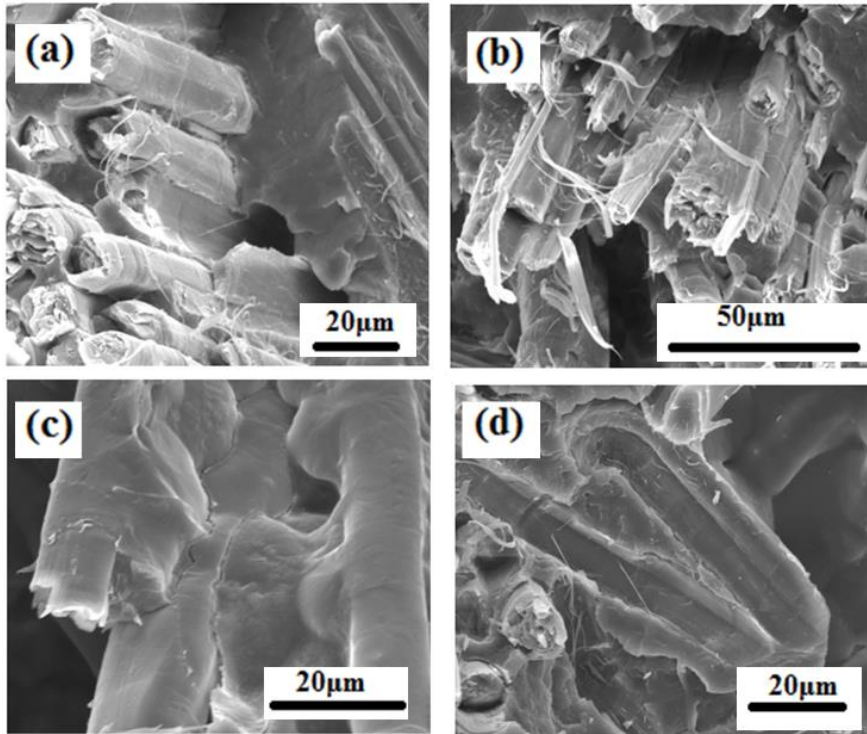
Figure 5.12 SEM images of the fractured surfaces of flax fabric composites with (a) no APS, (b) 2%APS, (c) 4%APS, (d) 6%APS

Table 5.1

Effect of polymerization temperature on void content and conversion of flax fabric and

kraft pulp PA6 composites

Temperature program	Sample	Void content (%)	Conversion
Ramped 100-150°C	Flax	1.9 ± 0.1	93.6
	Pulp	3.2 ± 0.2	93.1
	PA6	-	96.1
Isothermal 150°C	Flax	1.8 ± 0.3	96.5
	Pulp	3.4 ± 0.2	95.2
	PA6	-	98.3
Isothermal 162°C	Flax	2.1 ± 0.1	95.7
	Pulp	4.2 ± 0.1	94.3
	PA6	-	97.4
Isothermal 175°C	Flax	2.3 ± 0.2	93.5
	Pulp	5.3 ± 0.3	92.7
	PA6	-	96.8

Table 5.2

Effect of polymerization temperature on crystallinity of flax fabric reinforced PA6

composite

Processing temperature program	Melting point, T_m (°C)	Degree of crystallinity, X%
Ramped 100°C-150°C	222.1 ± 0.2	44.9
Isothermal 150°C	218.1 ± 0.6	36.8
Isothermal 162°C	216.2 ± 0.5	31.7
Isothermal 170°C	214.5 ± 0.7	28.5

CHAPTER VI –THE STRUCTURE, PROPERTIES AND BIOCOMPATIBILITY OF

BIOABSORBABLE NANOCOMPOSITES OF ALIPHATIC-AROMATIC CO-

POLYESTER AND CELLULOSE NANOCRSYTALS PREPARED BY REACTIVE

EXTRSUION

Manuscript submitted to *Biomacromolecules*

Abstract

Poly(butylene adipate-co-terephthalate) (PBAT) was first chemically modified via

free radical grafting with maleic anhydride (MA) and the MA-g-PBAT graft copolymer

was then used as a matrix material to obtain cellulose nanocrystal (CNC)-reinforced MA-

g-PBAT bio-nanocomposites via reactive extrusion process to accelerate efforts to

develop functional bioabsorbable polymer nanocomposites with improved properties.

The molecular structure of the PBAT after chemical modification with maleic anhydride

was confirmed by 1H NMR and FTIR spectroscopy. The morphological observation of

the nanocomposites revealed that the CNCs were finely dispersed in the matrix. Thermal

analysis of the hybrids showed an improvement of the thermal stability of the

nanocomposites upon increasing the CNC content. In addition, it was found that the CNC

nucleated crystallization of the PBAT in the nanocomposites. Extensive melt rheological

characterization of the nanocomposite samples revealed a significant improvement of the

viscoelastic properties of the matrix due to the strong interfacial adhesion of the CNC

particles to the PBAT. Further, development of the non-terminal characteristics of the

viscoelastic material functions and exhibition of yield stress were correlated with the

evolution of a 3D-netowork nanostructure of CNCs in the matrix. This CNC

nanostructure was interpreted in the framework of scaling theory of fractal elastic gels,

and found to be consistent with the structure of open-porous flocs. Tensile testing of the samples showed considerable improvement in the modulus as well as the ultimate strength of the samples with increasing the CNC content. In addition, a positive shift of the glass transition temperature was found in dynamic mechanical analysis. Finally, in-vitro biocompatibility using Thiazolyl blue tetrazolium bromide (MTT) assay and cell adhesion studies with L929 fibroblast cells revealed no cytotoxic effect of CNCs, confirming the biocompatibility of the nanocomposites and the associated significant improvement of cell adhesion, suggesting a great potential of using these special functional nanocomposites in biomedical and tissue engineering applications.

6.1 Introduction

With the increasing concern regarding the adverse impact of petroleum-based materials on the environment in the past couple of decades, there has been a growing interest and demand in both academia and industry, in developing novel polymeric materials derived from natural and renewable resources with enhanced benefits [1-2]. These research efforts have mostly involved development of novel biodegradable polymers and biocomposite materials containing natural-organic fillers with improved physio-chemical properties and enhanced functionality [3]. For this purpose, cellulose nanocrystals (CNCs) are among the most interesting biobased materials with exceptional structural properties such as high stiffness and axial elastic modulus of up to 150 GPa, lower density compared to silicates, high surface area with optimal benefits like design of various prescribed surface functionalities complete fully biodegradability after their useful service life [4-5]. Consequently, these highly crystalline rod-like nanoparticles (or cellulose "whiskers") are finding a number of uses in a wide array of applications such as

reinforcing fillers in various polymer composites [6], rheology modifiers and colloidal additives [7], antimicrobial additives [8], additives for gas barrier improvement [9], and synthesis platform for designing of functional materials [10].

The processing of the CNC-based nanocomposite materials is normally involves a number of different techniques such as solvent casting which involves the dispersion of CNC in mostly aqueous [11] or organic solvents [12], followed by mixing with the host soluble polymer and subsequent final casting and *in-situ* polymerization [13], and melt extrusion [14]. It is worthy to note that regardless of the process used in the preparation of CNC nanocomposites, the ultimate mechanical and structural properties of the nanocomposites are dictated by the microstructure and extent of dispersion of CNCs within the continuous polymer matrix. Development of a 3D percolated network of whiskers within the matrix polymer has been shown to significantly increase the physical properties of the polymer which normally occurs above the nanofiller percolation threshold [15]. The development of the network structure is facilitated by the strong intra-particle hydrogen bonding of the CNCs, therefore, a highly dispersed physical state promotes the network formation by increasing the surface area of the particles. The formation of this nanofiller percolated network structure has been reported in a number of different matrix polymers such as acrylic latex [16], polyurethane [17], PVA [18] and sodium caseinate [19]. In addition, a strong interfacial adhesion between the polar matrices and CNC surface hydroxyl groups have been reported to promote the development of a constrained rigid interphase that results in significant enchantment of mechanical properties even at very low CNC content compared to the percolation threshold. For example, Tang *et al* [20] studied the reinforcing role of the CNCs within an epoxy matrix

prepared via solvent casting. The significant enhancement of tensile modulus observed in the system was attributed by the authors just mentioned to the formation of a whisker-bound polymer layer that could effectively increase the volume fraction of "rigid" phase, thus, resulting in tensile modulus values that are significantly greater than that predicted by the percolation model. This strong interfacial adhesion and presence of the rigid interfacial polymer layer which was described by Narin [5] as "better than perfect" interface is crucial in achieving the maximum reinforcing effect of CNCs in polymer matrix.

In addition to naturally-derived materials, synthetic bio-polymers have also been the subject of extensive research and development due to a number of advantageous properties compared that of their natural counterparts such as enhanced functionality, better processability and tunable inherent biodegradability [21]. In this context, poly (butylene adipate-co-terephthalate) or PBAT is an aromatic-aliphatic co-polyester having a combination of the biodegradability of aliphatic polyesters and structural properties of aromatic polyesters and at optimal aliphatic-aromatic ratio of 35-55% mol of aromatic units [22]. PBAT is a commercially available semi-crystalline biodegradable thermoplastic used widely in a number of industrial applications such as extrudable plastic films for mulch and greenhouse film and packaging applications [23-24] and, more recently, found a number of uses in biomedical and tissue engineering due to its inherent biocompatibility [25]. In spite of these interesting properties, there are some drawbacks associated with properties of PBAT copolymer such as poor mechanical properties (especially for biomedical applications) and low thermal stability. Therefore, various strategies have been proposed to improve these limitations. One approach is the blending of PBAT with

other biodegradable polyesters with better mechanical properties and, in particular, poly (lactic acid) (or PLA) to take advantage of the high modulus of PLA while retaining higher elongation at break and toughness imparted by PBAT [26]. Another approach is application of nano-additives such as layered silicates [27], carbon nanotubes [28] and graphene [29]. Addition of up to 10wt% neat montmorillonite clay and organically-modified clay to PBAT prepared via melt intercalation [30-31] was shown to improve the mechanical properties of the PBAT while further improvements could be achieved by the use of organically modified clay due to better particle dispersion.

Although use of bio-based high performance reinforcing additives such as cellulose nanocrystals in PBAT matrix is of great interest due to the biodegradable and eco-friendliness of the matrix and the reinforcement phases, its practical application is a challenging task due to the hydrophobic nature of PBAT and highly hydrophilic nature of cellulosic fibers. Development of CNC-reinforced PBAT system has been little studied in detail. Only recently, Zhang *et al* [31] reported the effect of addition of surface acetylated CNC into PBAT matrix. Their results showed that, although some improvement could be achieved by hydrophobization of the CNC through the modification of CNC surface with acetyl group, this improvement in properties was moderate and only small volume fractions of CNC (up to 2%) was used due to the difficulty in achieving effective CNC dispersion at high CNC concentrations. In fact, the modification of the CNC surface, imparts partial compatibility between the acetylated-CNC and PBAT. However, due to the lack of strong interfacial adhesion, the true potential of CNCs as reinforcement could not be achieved.

The current study is part of a long-range research program on development of functional biocompatible and bioabsorbable polymer nanocomposites with prescribed macromolecular structure and biological function in biomedical and tissue engineering applications. Here, we report an alternative approach of modifying the PBAT matrix with reactive maleic anhydride groups (MA-*g*-PBAT) in order to provide an opportunity for optimal chemical bond formation at the interface of CNC and PBAT. The current article describes an extensive investigation of the developed special MA-*g*-PBAT/CNC nanocomposites at higher CNC concentrations with a focus on development of functional CNC microstructure within the PBAT matrix, and the associated effects on mechanical, rheological and thermal properties of the nanocomposites. In addition, the biocompatibility of the obtained fully biodegradable nanocomposites via *in-vitro* tests is reported in order to provide a better understanding of prescribed macromolecular structure and biological function in potential uses in biomedical and tissue engineering.

6.2 Experimental

6.2.1 Materials and Sample Preparation

The PBAT polymer used was an Ecoflex® C1200 grade (purchased from BASF) with melt flow index (MFI) of 2.5-4.5 (at 190°C; 2.16kg), density of 1.26 ± 0.01g/cm^3, melting point of 115 ± 5°C. Maleic anhydride (MA) and benzoyl peroxide (BPO, radical initiator) were purchased from Aldrich and used without further purification. Modification of PBAT with MA was carried out according to the method reported by Nabar *et al* [32] with the following modifications. In a round bottom flask, a masterbatch of PBAT containing the MA were prepared as follows: Desired amount of fully dried PBAT was dissolved in chloroform already purged with dry nitrogen followed by addition of the

MA, and the resulting solution was mixed for 1 hour under inert atmosphere. Finally, the solution was poured in a Teflon® petri dish and kept under reduced pressure (under dry nitrogen) until the solvent was evaporated. Similarly, in a separate flask a masterbatch of the PBAT containing the BPO was prepared. Preparation of MA-*g*-PBAT was carried out by melt processing of PBAT granules and the two masterbatches containing the MA and BPO with a total MA content of 5wt% and BPO content of 0.5wt% in a Thermo Haake® Polydrive internal mixer for 8 minutes at 185°C using a rotor speed of 80 rpm. Subsequently, the MA-*g*-PBAT was taken out and quenched in liquid nitrogen and granulated into small pieces for further analysis and a second melt processing step with CNC.

The extent of MA grafting was measured using titration following the protocol described previously [32]. First, the unreacted MA of the sample was removed by drying the granulated sample in vacuum oven at 90°C overnight to constant weight. Next, a 0.01 g/mL solution of MA-*g*-PBAT in chloroform was prepared followed by 30 minutes of mixing with 1mL of 1M hydrochloric acid in order to hydrolyze the anhydride groups to carboxylic acid. The MA-*g*-PBAT (with hydrolyzed MA groups) was recovered by precipitation in methanol, filtration, and drying at 90°C. Subsequently, a solution of purified MA-*g*-PBAT was titrated with a methanolic solution of potassium hydroxide (KOH) to phenolphthalein end point. The grafted MA content was calculated using the following equation:

$$\% \text{ grafted MA} = \frac{0.5 V_{KOH} N_{KOH}}{W_{sample}} \times 98.06 \times 100 \qquad (6.1)$$

where the *N* and *V* are respectively normality and volume (per liter) of KOH and *W* is the mass of the MA-*g*-PBAT sample in grams. The MA grafted content was found to be 0.92%.

The cellulose nanocrystals were prepared using the sulfuric acid hydrolysis of bleached cellulose pulp as described in our previous publication [33]. The CNC surface sulfate groups were neutralized by NaOH solution to form sodium sulfate groups followed by dialysis in distilled (DI) water to pH neutrality. The dispersion of CNC in DI water was sonicated and sprayed into agitating liquid nitrogen bath to form a slurry. The slurry was then freeze dried to recover the CNCs (i.e., spray freeze-drying technique). This method of recovery results in relatively less CNC particle aggregation compared to that obtained from the conventional bulk freeze drying technique.

The nanocomposite samples were prepared by reactive twin screw extrusion process. The granulated MA-*g*-PBAT was briefly washed with anhydrous acetone (to remove the majority of unreacted MA) and dried in a vacuum oven for at least 24hrs at 90°C to constant weight to remove the moisture and any remaining unreacted MA monomer. The polymer granules and cellulose powder were physically mixed and fed into a Thermo Haake® Minilab® micro-compounder (co-rotating conical screws) in the recycle mode at 140°C for 8 minutes at 120 rpm under a dried nitrogen atmosphere. Nanocomposites with 1, 3, 6 and 9 wt% of CNC were prepared and hereinafter referred to as "*x*%CNC" where "*x*" denotes the content of CNC in the nanocomposite sample.

6.2.2 Characterization of Molecular Structure

^{1}H NMR spectra were obtained using a 300 MHz Varian® Mercury plus NMR (VNMR 6.1C) spectrometer using $CDCl_3$ as the solvent. Standard ^{1}H pulse sequences were used, and all ^{1}H chemical shifts were referenced to TMS (0ppm).

Size Exclusion Chromatography (SEC) measurements were conducted on a GPC consisting of Waters® Alliance 2695 separation module equipped with a multi-angle laser light scattering (MALLS) detector (miniDAWN TREOS, Wyatt Technology Inc) and interferometric refractometer (T-rex, Wyatt Technology Inc.) using a freshly distilled tetrahydrofuran (or THF) as the mobile phase and polystyrene standards for calibration operating at 35°C.

Attenuated total reflectance-infrared (ATR-IR) spectroscopy measurements were carried out on a Nicolet® 6700 FT-IR spectrometer in the range of 4000-400 cm^{-1} with a total number of 1028 scans with the resolution of 4 cm^{-1}. Compression molded thin films of the samples were used for the IR analysis.

6.2.3 Microscopy

SEM images were acquired using a Sigma® field-emission scanning electron microscope (ZEISS®, USA) using a 5 kV accelerating voltage. Images were taken from the smooth cryo-fractured surfaces sputter-coated with silver for enhanced conductivity. TEM image of the cellulose nanocrystals were obtained using a ZEISS® EM10 transmission electron microscope at accelerating voltage of 50 kV. An aqueous dispersion of CNC in the concentration range of 0.1-0.3wt% was prepared and a small drop was placed on a TEM copper grid for image acquisition.

6.2.4 Thermal Analysis

Thermogravimetric analysis (TGA) data were obtained on a Q500 TA$^{®}$ Instruments TGA with a heating rate of $10°C.min^{-1}$ under nitrogen atmosphere with a gas flow rate of $40mL.min^{-1}$. Samples (10-20mg) were heated from room temperature up to 600°C. Crystallization and melting behavior of the materials were studied using a TA$^{®}$ Instruments Q100 DSC with a heating and cooling rate of 10°C/min. A heat-cool-heat cycle in the temperature range of 25-180°C was applied with the first heating run used to remove the thermal history of the samples. The crystallization during the cooling run and the subsequent melting data were acquired via DSC experiments that were conducted under a dry nitrogen atmosphere.

Dynamic mechanical properties of the MA-*g*-PBAT matrix and the nanocomposites were measured using a TA$^{®}$ Instruments Q800 dynamic mechanical analyzer (DMA) in tension mode. Dynamic viscoelastic properties were measured in the range of -50 to 60°C with a rate of 3°C/min at a constant frequency of 1 Hz.

6.2.5 Mechanical and Rheological Properties

Tensile tests were performed on an Instron$^{®}$ 5582 MTS$^{®}$ tensile tester with a crosshead speed of 10mm/min at room temperature. At least 5 injection molded dogbone shaped specimens with a span length of 28mm were tested for each composition. Rheological experiments were conducted using an Anton Paar$^{®}$ MCR501 shear rheometer using 25mm parallel pate geometry at a temperature of 140°C. Frequency sweep tests were performed in the 0.01-100rad/s range with strain amplitude of 1% (which was found to be in the linear viscoelastic region in a prior strain sweep tests).

6.2.6 Cell Culture and Cell Adhesion studies

The proliferation rates of fibroblast (i.e., L929) cells on the bio-nanocomposites were investigated via MTT assay which is a colorimetric assay for measuring the activity of cellular enzymes that reduce the tetrazolium dye, MTT, to its insoluble formazan, giving a purple color. First, a 96-well culture plate was selected for seeding of 1.5×10^4 cells/cm^2 using the culture medium of Dulbecco's modified Eagle's medium, DMEM (Gibco$^®$) + 10% Fetal Bovine Serum (Gibco$^®$) and supplemented with antibiotic-antimycotic solution (100 µg/mL of each, Gibco$^®$). Samples of 1×1 cm^2 size were first sterilized for 45 minutes on each side with ultra-violet (UV) light (CNC was filtered through a 0.22µm PVDF syringe) and then in each well, and incubated at 37 ℃ and 5% CO$_2$ for 1 week. Subsequently, 1ml of the extract medium was added to the culture plates followed by 1, 2 and 3 days of incubation time. At selected times the supernatant was removed from the cells culture medium and the cells were washed three times with phosphate buffered saline (PBS) solution to eliminate nonviable cells. 100 µl of MTT solution (10 mg/ml in Dulbecco's modified Eagle medium) was added to each well. For conversion of MTT to formazan crystals by mitochondrial dehydrogenases of living cells, the plate was incubated at 37 ℃ for 4 hours.

After removing the culture media, 0.5 ml of isopropanol was added to each well followed by 20 minutes of shaking in incubator to allow total color release. The optical density was recorded at a wavelength of 570 nm in a micro-plate ELISA$^®$ reader. The same procedure was performed for cells cultured on empty wells of the polystyrene culture medium as a control sample. The experiments were carried out in triplicate with the average results reported. The relative viability or cell growth (%) normalized by

287

control group was calculated by the equation, $[A]_s/[A]_c \times 100\%$, where $[A]_s$ is the absorbance of the cells with nanocomposites and $[A]_c$ is the absorbance of the control cells.

In order to assess the cell adhesion, the sterilized thin films (1×1 cm^2) of the MA-g-PBAT and 9%CNC samples were placed on a coverglass in a 6-well plate and then pre-equilibrated with the culture medium for 12 hours at 37°C in a 5% CO$_2$ atmosphere. Approximately 15×10^4 cells were added to the medium and left for 4 hours for adhesion. Subsequently, the culture medium was added to each individual well and followed by incubation for 72 hours. After the 3 days incubation period, the supernatant was removed and the cells were washed by PBS and then were fixed by glutaraldehyde for 15 min. Finally, the glutaraldehyde was removed from the cells and the cells were respectively washed three times with phosphate-buffered saline (or PBS) solution and water and dried.

6.3 Results and Discussion

6.3.1 Investigation of Chemical Structure

The free radical grafting of maleic-anhydride on PBAT follows a number of different reaction mechanisms which is depicted in Figure 6.1. The main mechanism of grafting has been suggested by some previous authors [32], to be through the H-abstraction from the α-carbon of the adipate segment due to the free radical stabilization effect of the carbonyl group. This is followed by chemical bond formation with the maleic anhydride group to form a succinic anhydride pendant on the PBAT chain. This free radical graft copolymerization reaction has been shown to undergo β-scission reaction splitting of the chain to yield a succinic anhydride end group. In addition, this anhydride free radical can abstract further hydrogens or couple (i.e., recombine) with other free radical moieties

288

shown as "R" group in structure 2 of Figure 6.1. Another proposed mechanism [34] for maleic anhydride grating onto polyesters is chain-end grafting based on the abstraction of the α-carbon hydrogen followed by β-scission and formation of a vinylidene and macro-radical chain ends. The macro-radical chain ends can react with anhydride group (as shown in Figure 6.1) following a number of different paths to couple with other free radical moieties. It is worth noting that the β-scission is usually favored in melt processing while during the solution free radical reaction, coupling of macro-radicals before scission is the dominating mechanism [35]. In addition, since the grafting reaction was carried out at the extrusion temperature of 185°C, homo-polymerization of MA units are unlikely to occur [36-37].

The ^{1}H NMR spectra of PBAT and MA-g-PBAT are shown in Figure 6.2. The dominating protons of the both materials are depicted on the graphs. The resonance peaks observed at 1.6 ppm and 1.8-1.9 ppm correspond to f, d and d' protons respectively. The c protons appear at 2.3 ppm. The b' protons show up at 4.0-4.1 ppm while the peaks showing at 4.3-4.4 correspond to b'' protons respectively. The (a) protons of phenyl group are those at 8.03 ppm.

In order to further investigate the MA grafting reaction on PBAT by ^{1}H NMR, the resonance range of 2.0-4.0 ppm is considered and shown in the insertion graphs of Figure 6.2. By comparing this with the spectrum of neat PBAT, the resonance at 3.3-3.4 ppm is attributed to the g protons of the structure 1 (see Figure 6.1). The peak at 2.9 ppm corresponds to the J proton of the α-carbon attached to the MA unit. The evolution of this peak in the 3.7-3.8 ppm is attributed to the K type protons of the MA unit attached to the α-carbon of the PBAT chain (structure 2).

In addition, it has been shown [38] that the MA units can abstract a proton from a non-α carbon of the polyolefins. In the case of PBAT, this could be carbons of terephthalate or butylene segments. The evidence of such grafting is in the ^{1}H NMR peaks showing at 2.7 ppm which is attributed to the *M*-type protons (structure 3). The *N*-type proton is merged into the peak appearing at 2.9 ppm. The analysis of the molecular weight of the PBAT before and after MA modification showed a decrease in molecular weight from 88420 g/mol to 61600 g/mol confirming the chain scission of the PBAT.

Further, the ATR-FTIR spectra of neat and MA-modified PBAT are presented in Figure 6.3. The major characteristic peaks of the PBAT are as follows [39-40]: stretching vibration of carbonyl group (C=O) at 1710 cm^{-1} , stretching vibration of ester bond (C-O) at 1105 cm^{-1} and 1274 cm^{-1} , characteristic peaks of the phenylene group with stretching vibration at 1390 cm^{-1}, 1400 cm^{-1}, 1456 cm^{-1} and 1510 cm^{-1}, planar bending vibration at 735 cm^{-1} and 1020 cm^{-1}, and the asymmetric stretching of the aliphatic –CH$_2$- groups at 2955 cm^{-1}.

In the case of the MA-*g*-PBAT sample, in addition to the peak seen in the neat PBAT, there is a distinctive peak appearing at 1855 cm^{-1} in addition to the broadening of the shoulder in the range of 1710-1750 cm^{-1}. These peaks are attributed to asymmetric and symmetric stretching vibration of C=O in the grafted succinic anhydride group, respectively. In addition, the peak at 1660 cm^{-1} corresponds to stretching vibration of C=C which is formed as already discussed above in the chain end grafting mechanism. The vibration of =C-H bond appears in the 3000-3100 cm^{-1}.

In the 9% nanocomposite sample, the evolution of a distinctive peak at 1740 cm^{-1} is clearly evident. This peak has been attributed [41] to the formation of an ester bond

resulting from transesterification reaction which confirms the formation of the interfacial

bond between the anhydride groups and the surface hydroxyl groups of the cellulose. The

broad peak in the range of 3100-3600 cm^{-1} is assigned to the H-bonded stretching

vibration of cellulose hydroxyls.

6.3.2 Thermal Analysis

The thermal stability of the MA-*g*-PBAT/CNC nanocomposites is shown in the

TGA scans depicted in Figure 6.4(a) with the extracted values presented in Table 6.1.

This figure shows that the MA-*g*-PBAT matrix undergoes a two-step degradation

process. The first drop in the weight loss occurs around 320°C and the second major

weight loss occurs at around 400°C. In the DTG curve shown in the insertion plot of

Figure 6.4, this 2-step thermal degradation process is clearly evident as two separate

peaks showing the temperature at which the maximum thermal degradation occurs for

each step. While the major weight loss occurring around 400°C is close to the values

reported in literature for PBAT polymer [31], the lower degradation temperature observed

in the current study is attributed to the chain branches and the broken chain segments

during the melt processing. Figure 6.4 also shows that, with addition of CNC particles,

the first weight loss step gradually decreased and almost disappeared with the highest

CNC concentration as evidenced by the shoulder (first minor weight loss) gradually

moving towards higher temperatures. In fact, as shown in Table 6.1, the onset

degradation temperature for the first step is increased from 320°C for the neat matrix to

395°C for the 9%CNC nanocomposites. This increase is also observed for the second

major weight loss step increasing from 401°C for the neat matrix to 431°C for the

6%CNC. This onset is not clearly detectable in the case of 9%CNC as it increases to

higher temperatures. The onset degradation temperature of maximum degradation rate (i.e., peaks of DTG curve) also undergo major shift towards higher temperatures with increasing CNC concentration. The shoulder peak increases from 356°C for the matrix to 390°C for the 9%CNC nanocomposite while the major DTG peak shows slight increase in the temperature.

The enhanced thermal stability of the hybrid systems is also implied by the temperature of residual weight at 70% and 30% mass. Clearly, with increasing CNC content, the temperature corresponding to 30 and 70% mass loss increases towards higher values. This enhancement of thermal stability could be attributed to the formation of crosslinked segments upon interfacial reaction of MA units of PBAT with the surface hydroxyl groups of CNC. In fact, the cellulose whiskers act as crosslinkers binding the PBAT chains together that enhances the thermal stability of polymer.

The crystallization and melting behavior of the MA-*g*-PBAT/CNC nanocomposites were studied using DSC as already described. A heat-cool-heat program was used to first remove the thermal history of the samples followed by crystallization during cooling and subsequent heat run to study the melting behavior. The exothermic crystallization peaks in the second and third (cool-heat) runs are shown in Figure 6.5(a) and the extracted data are presented in Table 6.2. Clearly, the incorporation of the nanocrystals in the MA-*g*-PBAT matrix showed that the crystallization temperature of the matrix gradually increased towards higher temperatures. *T*c is 81°C and it increases to 87°C with incorporation of CNC particles. This clearly shows that the presence of the cellulose whiskers gave a heterogeneous nucleation effect by increasing the nucleating sites for promotion of crystallization of the PBAT like other researchers have reported for

a silica-reinforced PBAT systems [31] where silicate platelets provided nucleating sites for matrix crystallization. Cellulose whiskers have also been found to promote crystal nucleation in other polyester matrix nanocomposites such as PLA [42].

In the second heating cycle (Figure 6.5(b)), it can be seen that while the pure PBAT showed an endothermic melting peak at 122°C, with increasing content of cellulose nanocrystals, the melting temperatures showed a gradual increase up to the maximum temperature of 126°C in the case of 9%CNC sample. In order to obtain the degree of crystallinity (χ%) of the nanocomposite samples, the heat of fusion of a 100% crystalline PBAT was calculated using the approach of Herrera *et al* [43] that involves the contributions of methylene, *p*-phenylene and ester linkages with values of 4.0 *kJ*/mol, 5.0 k*J*/mol and -2.5 kJ/mol, respectively, resulting a final value of 114 *J/g* as the enthalpy of fusion of 100% crystalline PBAT. The absolute degrees of crystallinities were calculated using the following equation:

$$\chi_c(\%) = 100 * \frac{\Delta H_m}{\Delta H_{100\%} * (1 - x_w)} \qquad (6.2)$$

where the ΔH_m and x_w are respectively the experimental enthalpy of fusion and the weight content of the CNCs.

Based on the values obtained, it can be seen that the enthalpy of fusion initially decreased from 11.2 J/*g* to 9.1 and 8.2 J/*g* for the samples containing 1 and 3 wt% of the CNC particles, respectively. However, upon further increasing the CNC concentration, the ΔH_m values increase d again to 9.5 J/g but still remained lower than that of the neat MA-*g*-PBAT sample. Similarly, the degree of crystallinity decreased from 9.8% of the MA-*g*-PBAT matrix to 7.4% of the 3%CNC nanocomposite while it increased again with

293

6 and 9% of CNC back to 9.2%. Overall, it is believed that the presence of the cellulose nanocrystals inhibited the crystallization process of PBAT chains due to the chain motion restriction and increasing viscosity of the matrix during the cooling process that, in turn, prevents sufficient crystal growth from occurring. On the other hand, with higher CNC concentration (i.e., $\geq$ 6%), the heterogeneous nucleating effect of CNC on PBAT crystallization becomes more prominent therefore, competing with the crystal growth inhibition and therefore, slightly increasing the crystallinity content as observed in the samples. Despite this relative increase compared to the samples with 1 and 3% CNC, the overall degree of crystallization remains lower than that of the MA-*g*-PBAT because of the chain motion restriction effect of CNCs on the interfacial polymer layer around the whiskers in the melt state as well as the physical barrier (due to the presence of CNC) against spherulitic growth. A similar behavior was reported for a system of poly (3-hydroxybutyrate-co-3-hydroxyvalerate) nanocomposite reinforced with CNC [44] where a dual effect of chain confinement together with heterogeneous nucleation due to the presence of cellulose whiskers was proposed.

The dynamic mechanical properties of the MA-*g*-PBAT matrix and the nanocomposites were evaluated using DMA and the obtained results are presented in Table 6.3. The variation of the storage modulus (E') versus temperature is shown in Figure 6.6(a). PBAT has two transition temperatures: the major transition is the glass transition temperature corresponding to linear butylene-adipate segments observed around -20°C while the second minor transition is due to the relaxation of the relatively stiffer terephthalate unit occurring around 35°C. The variation of storage modulus versus temperature showed that upon increasing the CNC concentration, there is a significant

increase in the modulus of the sample before the first transition temperature. For example, at a temperature of -40°C, the storage modulus value increased from 1.64 GPa to 3.45 GPa upon addition of 9% CNC. This strong reinforcing effect of cellulose nanocrystals is due to the strong interfacial adhesion by the chemical bond formation at the polymer-particle interface which facilitates the stress transfer to the stiff and highly elastic cellulose nanocrystals. Above the major glass transition temperature, a similar reinforcing effect is still observed as evidenced by the increase of the modulus value from 52.1 MPa to 121.4 MPa at 9%CNC sample.

The variation of the mechanical damping factor (or $tan\delta$) is shown in Figure 6.6(b). The glass transition (α-transition) point is taken as the temperature of the peak of $tan\delta$ curve. For the MA-g-PBAT sample, the temperature is found to be -24.3°C± 1.1°C. Interestingly, with addition of cellulose nanocrystals, this transition temperature is shifted towards higher temperature where, for the 9%CNC nanocomposite sample, a transition temperature of -17.3°C± 1.2°C was observed. This positive shift of the Tg is a clear indication that the presence of the CNC whiskers significantly restricts the molecular motion of the PBAT chains in the glass-rubber transition region. This effect is indeed, enhanced by the strong interfacial adhesion in the reactive system.

It should also be noted that the second (minor) transition temperature does not show any noticeable change with the addition of nanocrystals suggesting that the impact of the CNC on chain motion restriction is significantly more prominent in the case of more flexible butylene-adipate units are in fact, in comparison to the stiffer phenylene segment. In addition, as seen in the Table 6.3, the height of the $tan\delta$ peak ($tan\delta_{max}$) reduces with increasing the nanocrystal concentration. The height of the $tan\delta$ is

associated with the energy dissipation ability of the material which is inversely related to the material elasticity. As expected, the presence of highly elastic cellulose whiskers as well as the enhanced elasticity of the matrix due to the interaction with the particles reduced the energy dissipation of the system. This reduction in energy dissipation is facilitated by the already described relatively strong polymer-particle interaction, especially at high CNC concentrations.

6.3.3 Morphology and Mechanical Properties

The SEM images of the cryo-fractured surfaces of the neat MA-*g*-PBAT matrix, the nanocomposite samples, as well as, the TEM image of the cellulose nanocrystals used in this study are shown in Figure 6.7. The CNCs have an average aspect ratio (i.e., length/diameter ratio) of approximately 20. The SEM images showed that the cellulose nanocrystals are mostly dispersed in submicron-sized bundles. No significant CNC particle aggregation was observed in the highest CNC concentration. In addition, the whiskers are mostly wrapped by the interfacial polymer layer (instead of being neatly pulled out after cryo-factoring), confirming a strong interfacial adhesion between the particles and matrix. Further, there is a clear increase of surface roughness as the CNC content is increased within the matrix. For the purpose of comparison, the SEM image of a control sample with the unmodified PBAT and 9%CNC is also presented in Figure 6.7(f), showing clearly that the CNCs formed large agglomerates in the hydrophobic matrix similar to the observation of macro-phase separation of the molded samples.

The tensile tests results are shown in Figure 6.8 and Table 6.4. The neat MA-*g*-PBAT matrix shows a tensile modulus and strength at break of 50 and 16 MPa, respectively. With addition of the cellulose nanocrystals, it was observed that not only the

296

Young's modulus of the specimens increased up to 108 MPa showing more than 100%

increases, the stress at break of the samples also showed an increasing trend with

increasing CNC concentration reaching a maximum value of 20 MPa with 9% CNC (i.e.,

nearly 25% increase in the strength).

In contrast, in a study by Zhang and co-workers [45], the surface acetylation of CNC

was also shown to improve the dispersion of particles in the PBAT matrix which

improved the elastic modulus of the samples. However, the ultimate strength of the

nanocomposites showed a decreasing trend with respect to CNC concentration,

suggesting that the particles did not optimally reinforce the samples. In the systems of

this study, the enhancement of the stress at break showed relatively improved reinforcing

ability of cellulose nanocrystals in the PBAT matrix due to the strong interfacial adhesion

that facilitates the efficient stress transfer from the polymer matrix to the CNC particles.

The strain at break of the samples showed a decreasing trend with addition of the

cellulose nanocrystals as Figure 6.8 shows. This is in fact due to the increased elasticity

of the samples which , in turn, reduced the elongation at break. In addition to the

enhanced elasticity of the samples due to the presence of CNCs, formation of crosslinked

structures at the polymer-CNC interface, further limits the chain slippage and drawing

behavior of PBAT matrix thereby reducing the strain at break values.

6.3.4 Melt Rheological Properties

The frequency dependencies of storage and loss moduli of the MA-*g*-PBAT/CNC

nanocomposites at 140°C are shown in Figures 6.9(a) and 6.9(b). It can be seen from this

figure that the addition of cellulose whiskers gave a significant effect on the viscoelastic

properties of the matrix. Both the storage (G') and loss (G'') moduli increased upon

incorporation of cellulose nanocrystal particles. This increase is, however, more noticeable at the lower frequency region. It is well known that the rheological properties of polymer systems at high frequency region is dominated by the short-range chain motion and relaxation process while in the low frequency zone the behavior is dictated by large-scale chain motion. In fact, at low frequencies, polymer chains exhibit the characteristics of fully relaxed chains, showing a terminal behavior that is characterized by the power law relations of $G''{\sim}\omega$ and $G'{\sim}\omega^2$ [46]. However, as shown in Table 6.5, the nanocomposite materials showed completely different behavior in this terminal zone. It was observed that slope of the terminal zone of G' in the matrix is 1.16 which is reduced to 0.96 with addition of 1%CNC, and further significantly reduced to 0.12 in the case of 9%CNC. Similarly, the terminal slope of the G" curves changed from 0.98 in the matrix to 0.55 in the 9%CNC nanocomposite. This reduction of the slope and reduced dependency of storage and loss modulus on the frequency (or development of the "non-terminal" behavior in the nanocomposites systems) are attributed to the development of the network-like interconnected nanostructure of the cellulose whiskers in the matrix. This network structure develops at higher concentrations above the percolation threshold where the particle-particle and polymer-particle interactions dominate the rheological behavior of the sample, resulting in a pseudo-solid like melt behavior.

In addition, it can be seen that for the 3%CNC sample, there is a crossover point between the G' and G'' values in the low frequency region which is attributed to the point where the particles start to interact like others researchers have reported for somewhat similar systems [47-48]. However, for the 6 and 9%CNC samples, the G' values dominate

the G'' values across the entire frequency range studied, showing that these samples are effectively behaving like elastic melts.

In order to further correlate the microstructure of the nanocomposites with the observed rheological behavior, the fractal model of elastic colloidal gels developed by Shih *et al* [49] was applied to interpret the experimental results. According to this theory, a closely packed arrangement of fractal "flocs" is proposed to be connected throughout the matrix material above the gelation (percolation) threshold. Depending on the floc size, weak-link regime and strong-link regime were proposed. Because in the current nanocomposite systems, the threshold of non-linearity in the strain sweep experiments (performed prior to frequency sweep tests) characterized by the critical strain value (γ_c) reduced with increasing floc concentration (or CNC content), a strong-link regime is applicable. Using the polymer solution scaling theory the following correlations were suggested:

$$G'_P \sim \varphi^{(D+x)/(D-d_f)} \tag{6.3}$$
$$\gamma_c \sim \varphi^{-(1+x)/(D-d_f)} \tag{6.4}$$

where the G'_P is the plateau modulus (considered here to be that at $\omega=0.0.1$ rad/s), D is the Euclidean dimension of the system (i.e., $D=3$ for the current system), x is scaling power correlating the number of particles per floc with floc size, and d_f is the fractal dimension (or filler network). In the current system of this study, the flocs are considered to be composed of bundles of cellulose whiskers and the fractal network is formed by elastic linkage of these bundles (or flocs). A linear regression analysis of the data points above the percolation threshold gave a d_f value of 1.65. In a study by Durmus *et al* [50] on polymer/clay nanocomposites, it was found that enhancing the polymer-clay interfacial

adhesion reduced the fractal dimension from 2.32 to 2.17 which resulted in relatively more exfoliated aggregates (better dispersion). In addition, a value of 1.7 was found in a PP/nanocellulose composite with web-like structure [15]. The value of 1.65 found in current system of this study indicates a 3D web-like and porous open fractal structure.

It is worthy to note that the formation of a network-like percolated structure of CNC within the PBAT matrix can be studied by using the Van Gurp-Palmen plot as shown in Figure 6.9(c). In this plot, the variation of the phase angle (δ) is plotted against the complex modulus values obtained from the dynamic frequency sweep experiments. The evolution of the structure within the matrix could be traced by variation of the phase angle as the complex viscoelastic material functions values are decreased. It is seen, for example, that in the case of the MA-g-PBAT and 1%CNC nanocomposite, with decreasing G^* values, the phase angle monotonically increased in the direction of the full 90° phase angle (i.e., viscous behavior). On the other hand, for the 3%CNC sample, it can be seen that a maximum point is reached and, upon further reduction of G^*, the phase angle is also reduced. A relatively more significant deviation from the monotonic change just mentioned is also seen for the 6% and 9% CNC samples. The evolution of the curve maxima has been attributed to the structural changes linked to the development of the elastic percolated structure in the melt as opposed to the behavior of the melt from purely viscous (full chain relaxation) at low frequencies.

Additionally, the variation of $tan\delta$ with angular frequency is shown in Figure 6.9(d). Typically, the transition from liquid-like to solid-like behavior occurs at the crossover of the G' and G'' where $tan\delta=1$. The inverse of the frequency at which this transition point occurs is considered as the relaxation time of the polymer chains. For the

PBAT/CNC systems, it is evident that with decreasing frequency, the *tanδ* values

constantly increased to higher values crossing the *tanδ*=1 point at certain frequencies. By

contrast, for the 1 and 3%CNC samples, this crossover occurred at lower frequencies,

suggesting relatively longer relaxation times. In the case of the 3%CNC samples, upon

further decreasing the frequency, it can be seen that there is a downward shift where the

tanδ reaches a maximum and follows a decreasing trend. This shows that for this sample,

there are some elastic contributions in the low frequency region that reduce the viscous

character of the polymer melt and, thus, decrease the *tanδ* value. This observation is

attributed to the onset of percolated network structure formation. Further increasing the

CNC concentration to 6 and 9%, resulted in *tanδ* values being constantly less that the

tanδ=1 threshold, suggesting that these samples are effectively behaving like an elastic

fluid.

The variation of the complex viscosity (η^*) versus angular frequency is shown in

Figure 6.10(a). Incorporation of the CNC particles to the MA-*g*-PBAT matrix

monotonically increased the viscosity of the samples throughout the studied frequency

range. There is, however, a noticeable upward shift in the viscosity values at low

frequencies as the CNC concentration increased. This effect is more notable in the case of

6 and 9%CNC samples. This upward shift in data is a nanostructure formation signature

and indicates an apparent yield stress in the samples. This effect is also observed in the

Figure 6.10(b) where complex viscosity is plotted against complex modulus. In the case

of the 3%CNC nanocomposite, there is an upward shift in the complex viscosity at low

complex modulus values while this shift is significantly increased for the 6 and 9%CNC

samples. This behavior has been reported for polymer systems that are highly filled with

microparticles [51]. The development of the non-terminal characteristic associated with this observed yield stress is attributed to the network-like structure formation above the 3% concentration of CNCs. In order to further investigate this behavior and to calculate the yield stress values, the modified Cross model [15] that includes a yield stress term can be applied to the experimental data according to the following equation:

$$\eta = \sigma_y . \omega^{-1} + \eta_P (1 + \alpha \omega^m)^{-1} \tag{6.5}$$

where the η_p (Pa.s), α (s) and m are the model fit parameters. The results of the Cross model fitting to the experimental data are shown in Table 6.6. It can be seen from this Table while the neat matrix does not show any yield stress behavior, the nanocomposite samples showed the yield stress values that increased with increasing CNC concentration up to the value of 17 kPa for the 9%CNC concentration. As already discussed, the formation of the interconnected network above the percolation threshold within the sample may be attributed to the formation of flocs which, in the current system, is composed of CNC bundles that are above the percolation threshold that form interconnected structures. The characteristic size of these flocs can be estimated using the obtained yield stress values. Assuming that the 3D network is composed of spheres with a random distribution and N number of CNC particles are encapsulated within the spheres with a volume of V_P [52]. The percolation threshold of the overlapping spheres with random packing arrangement occurs at the volume fraction of 0.32. Thus the volume fraction of CNC within each sphere can be written as:

$$\varphi = \frac{0.32 N V_P}{4 \pi r^3 / 3} \tag{6.6}$$

According to the Rumpf's theory of strength of granular materials and aggregates [53], the strength of an aggregate can be written as:

$$\sigma_T = \frac{1-\varepsilon}{\varepsilon} \frac{A_H}{\frac{3}{2}\pi z_0^2 d} \tag{6.7}$$

where the ε is the porosity of the spherical units ($=1-\varphi/0.32$), A_H is the Hamaker constant, z_0 is the cutoff distance and d is the effective agglomerate diameter. The Hamaker constant is calculated by $A_H = 2\pi z_0^2 \gamma$ where γ is the surface energy of the cellulose nanocrystals taken as 18.6 mJ/m^2 [54]. In the current system, it is assumed that upon yielding, the yield stress overcomes the strength of the aggregates (i.e., $\sigma_T = \sigma_y$). Finally, the effective aggregate diameter can be found by the inverse of the slope of the linear regression of the following equation:

$$\sigma_y = \left(\frac{1-\varepsilon}{\varepsilon}\right)\frac{4}{3\gamma} \times \left(\frac{1}{d}\right) \tag{6.8}$$

For each volume fraction of the CNC, the yield stress is plotted against the $\left(\frac{1-\varepsilon}{\varepsilon}\right)$. The calculated aggregate diameter was found to be 334nm. This value is in a reasonable agreement with the value of 102nm found in a previous study on polypropylene/CNC nanocomposite systems [15].

In summary of this section, it is worth noting that in the current nanocomposite materials, the evolution of the pseudo-solid like behavior above the percolation threshold is the result of the particle-particle interactions. However, the "bridging" effect of the interfacial polymer layers should not be neglected. As already shown in the *tanδ* plot, the relaxation time of the polymer increased with increasing the CNC content. This increase

in relaxation time may in fact be related to the development of the constrained polymer layer in contact with CNC particles due to the strong interfacial adhesion. This "rigid interphase" has been shown in a number of previous studies [20], especially in cases where strong interfacial interaction exists, to effectively increase the volume fraction of the "rigid phase", thus, lowering the effective percolation threshold.

6.3.5 *In-vitro* Biocompatiblity and Cell Adhesion Studies

Cellulose nanocrystals have been shown in a number of previous publications in the literature to be generally biocompatible with no significant cytotoxicity [55]. In a study by Dong *et al* [56], the cytotoxicity of cellulose nanocrystals were studied against a wide range of cell lines including HBMEC, KB, PC-3, C6 and MDA-MB using MTT and LDH assays in the concentration range of 0–50 μg/mL and exposure time of 48 h, and no noticeable cytotoxic effect was observed in any of the systems studied. In addition, a wide range of polymer nanocomposites reinforced with cellulose nanocrystals such as polyurethanes [57] collagen [58] and polylactic acid [59] have been successfully evaluated to show favorable biocompatible properties with improved cell proliferation and adhesion. On the other hand, a number of studies have reported a concentration dependency of cytotoxicity of CNC in selected culture media where no (or little) cytotoxic effect was observed against various cell lines up to a concentration of 250μg/mL[60].

Because a number of PBAT based composite materials have been successfully used for tissue engineering and biomedical applications [27], the current system of PABT reinforced with cellulose nanocrystals shows great potential for such application. Therefore, the cell response and cell adhesion properties of the nanocomposites were studied to assess its viability in the applications just mentioned.

Here, fibroblast L929 cell line was chosen for the MTT assay analysis because it has been recommended by the International Standard Organization (ISO) as the cell line for *in-vitro* MTT assay test [61]. The MTT assay is based on reduction of tetrazolium compound by a functioning mithocondria into a non-soluble purple formazan precipitate that accumulates in the culture medium, and can be assessed calorimetrically to quantify the number of living cells. The quantitative results of MTT assay cell viability tests for PBAT/CNC nanocomposites with 3 and 9%CNC after incubation periods of 24, 48 and 72 hours are presented in Figure 6.11. Additionally, a sample of the CNC in the culture medium was also tested as 'control' sample. The concentration of CNC was chosen as 50 µg/mL to prevent particle aggregation and interference during the MTT assay tests [62].

The obtained results showed that all the samples including the CNC dispersion gave no sign of cytotoxicity against L929 fibroblast cells as evidenced by the experimental fact that they all had cell growth rates of above 30% which is considered to be the threshold for cytotoxicity [63]. For all the samples, the viability of the L929 cells increased monotonically with increasing culture times. It is clear from these results that all the nanocomposite samples are biocompatible and no samples showed observable cytotoxicity. In addition, the cellulose nanocrystals did not show cytotoxic effect at the studied concentrations as evidenced by the cell growth rate over the 72 hours period. Moreover, there is no significant difference in the viability of the samples *albeit* the neat MA-*g*-PBAT showed a slightly higher proliferation compared to that of the nanocomposite samples, especially in the first 2 days of the incubation time. The optical micrograph showing the cell viability of the 9%CNC sample at the beginning and after 72 hours of culture is presented in Figure 6.12. As can be seen in this figure, the cells are

305

significantly populated the sample after 72 hours which is in agreement with the results

of the cell proliferation assay.

The adhesion of the fibroblast cells on the MA-*g*-PBAT and 9%CNC samples

after 72 hours of incubation are shown in Figure 6.13. In both samples the surface of the

specimen is massively colonized by the cells where they proliferated and were adhered

very well, confirming the L929 cell viability of both the matrix and the nanocomposite

sample. More interestingly, the morphology of the cells on the surface of the MA-*g*-

PBAT sample showed a spindle-like shape of the cells while in the case of the

nanocomposite sample, the cells are much more flat with a spread-out web-like structure

on the surface with more clear pseudopods that showed a better intercellular connection.

Note that a number of different surface characteristics can affect the cell adhesion such as

topography, surface charge and specific interaction [64]. An important factor for the current

observation in this study is attributed to the significantly enhanced surface roughness of

the nanocomposites samples due to the presence of CNC bundles (which was evident

from the SEM images of the nanocomposite surface in Figure 6.7 already discussed). It is

worthy to note that enhancement of cell adhesion has been shown to significantly

increase with increased surface roughness of the substrates [65]. In a study by Palin *et al* [64],

it was shown that mimicking the surface roughness of bone with creation of surface

"nano-features" using ceramic nanoparticles significantly enhanced the osteoblast cell

adhesion on the synthetic mold. In another study [66], it was shown that coating the melt-

drawn polylactic acid fibers with cellulose whiskers resulted in significant improvement

of NIH-3T3 cell adhesion on the fibers due to enhanced surface roughness of the fibers.

In current study, as shown in the rheological studies already described, the observed

porous nanostructure of nanocrystals within the matrix enhanced the cell adhesion by mimicking the extracellular matrix topology.

In addition to the surface roughness, it is believed that the enhanced surface hydrophilicity of the nanocomposites compared to that of the matrix due to the presence of the cellulose whiskers with hydroxyl group-rich surfaces played a critical role in improving the cell adhesion and development of intercellular connections. The critical role of the surface functionality and wettability on cell adhesion was shown in the work of Arima and co-workers [67] who reported maximum cell adhesion on artificial surfaces of self-assembled monolayers functionalized with hydroxyl (-OH) and carboxyl (-COOH) groups with low water contact angle (i.e., high wettability). In the current PBAT/CNC nanocomposite system, it is believed that the synergistic effect of both the enhanced surface roughness and higher surface energy of the nanocomposite samples are responsible for the observed cell adhesion and growth on the sample surface.

6.4 Conclusions

In this study, a series of MA-*g*-PBAT/CNC nanocomposites with 1,3,6 and 9wt% of CNC were successfully prepared by first modifying the PBAT polymer with maleic anhydride groups via free radical grafting followed by reactive extrusion processing of the MA-*g*-PBAT with cellulose nanocrystals (CNCs). The molecular characterization results with H NMR and ATR-IR confirmed the successful grafting of the MA onto the PBAT chains, as well as, the possible associated structural changes. Thermal characterization of the nanocomposites showed thermal stability improvement of the materials with increasing the CNC concentrations. In addition, it was found that the CNCs promoted crystallization of the PBAT due to the heterogeneous nucleation effect.

307

The analysis of the mechanical properties of the samples showed a significant improvement in the elastic modulus of the PBAT (up to 114% with 9% of CNC) as well as a 25% increase in the ultimate tensile strength. Dynamic mechanical analysis results showed that upon introducing the CNCs into the modified PBAT matrix, the T_g of the matrix shifted towards higher temperature indicative of the PBAT chain motion restriction effect of CNCs. This effect was further investigated using melt theological studies where it was found that the viscoelastic material functions of the PBAT showed a monotonous increase with increasing CNC content while the observed development of the non-terminal behavior suggested the evolution of the 3D web-like percolated network of CNC within the matrix above 3%CNC. The in-vitro cytotoxicity evaluation of the nanocomposites showed no cytotoxic effect, confirming the excellent biocompatibility of these nanocomposites. In addition, the morphological observation of the cultured surfaces showed an enhanced cell adhesion for the 9%CNC nanocomposite compared to that of the MA-g-PBAT matrix due to alteration of the surface properties which favors the cell differentiation. Overall, the results of this study demonstrated the great potential of these fully biodegradable and biocompatible PBAT/CNC nanocomposites for a wide variety of applications with enhanced benefits, especially in biomedical and tissue engineering fields. In addition, the results of this study point to a better understanding of rational development of functional polymer nanocomposites with prescribed macromolecular structure and functionality for uses in a number of applications where existing materials are not useable.

6.5 References

1.   La Mantia, F.; Morreale, M., Green composites: A brief review. *Composites Part A: Applied Science and Manufacturing* **2011,** *42* (6), 579-588.

2.   Doppalapudi, S.; Jain, A.; Khan, W.; Domb, A. J., Biodegradable polymers—an overview. *Polymers for Advanced Technologies* **2014,** *25* (5), 427-435.

3.   Dicker, M. P.; Duckworth, P. F.; Baker, A. B.; Francois, G.; Hazzard, M. K.; Weaver, P. M., Green composites: A review of material attributes and complementary applications. *Composites part A: applied science and manufacturing* **2014,** *56*, 280-289.

4.   Habibi, Y.; Lucia, L. A.; Rojas, O. J., Cellulose nanocrystals: chemistry, self-assembly, and applications. *Chemical reviews* **2010,** *110* (6), 3479-3500.

5.   Moon, R. J.; Martini, A.; Nairn, J.; Simonsen, J.; Youngblood, J., Cellulose nanomaterials review: structure, properties and nanocomposites. *Chemical Society Reviews* **2011,** *40* (7), 3941-3994.

6.   Mariano, M.; El Kissi, N.; Dufresne, A., Cellulose nanocrystals and related nanocomposites: review of some properties and challenges. *Journal of Polymer Science Part B: Polymer Physics* **2014,** *52* (12), 791-806.

7.   Salas, C.; Nypelö, T.; Rodriguez-Abreu, C.; Carrillo, C.; Rojas, O. J., Nanocellulose properties and applications in colloids and interfaces. *Current Opinion in Colloid & Interface Science* **2014,** *19* (5), 383-396.

8.   Feese, E.; Sadeghifar, H.; Gracz, H. S.; Argyropoulos, D. S.; Ghiladi, R. A., Photobactericidal porphyrin-cellulose nanocrystals: synthesis, characterization, and antimicrobial properties. *Biomacromolecules* **2011,** *12* (10), 3528-3539.

9.   Belbekhouche, S.; Bras, J.; Siqueira, G.; Chappey, C.; Lebrun, L.; Khelifi, B.; Marais, S.; Dufresne, A., Water sorption behavior and gas barrier properties of cellulose whiskers and microfibrils films. *Carbohydrate Polymers* **2011,** *83* (4), 1740-1748.

10.   Tingaut, P.; Zimmermann, T.; Sèbe, G., Cellulose nanocrystals and microfibrillated cellulose as building blocks for the design of hierarchical functional materials. *Journal of Materials Chemistry* **2012,** *22* (38), 20105-20111.

11.   Peresin, M. S.; Habibi, Y.; Zoppe, J. O.; Pawlak, J. J.; Rojas, O. J., Nanofiber composites of polyvinyl alcohol and cellulose nanocrystals: manufacture and characterization. *Biomacromolecules* **2010,** *11* (3), 674-681.

12.   Liu, H.; Liu, D.; Yao, F.; Wu, Q., Fabrication and properties of transparent polymethylmethacrylate/cellulose nanocrystals composites. *Bioresource Technology* **2010,** *101* (14), 5685-5692.

13.   Kashani Rahimi, S.; Otaigbe, J. U., Polyamide 6 nanocomposites incorporating cellulose nanocrystals prepared by In situ ring-opening polymerization: Viscoelasticity, creep behavior, and melt rheological properties. *Polymer Engineering & Science* **2016,** *56* (9), 1045-1060.

14.   Goffin, A.-L.; Raquez, J.-M.; Duquesne, E.; Siqueira, G.; Habibi, Y.; Dufresne, A.; Dubois, P., Poly (ε-caprolactone) based nanocomposites reinforced by surface-grafted cellulose nanowhiskers via extrusion processing: morphology, rheology, and thermo-mechanical properties. *Polymer* **2011,** *52* (7), 1532-1538.

15.   Khoshkava, V.; Kamal, M. R., Effect of cellulose nanocrystals (CNC) particle morphology on dispersion and rheological and mechanical properties of polypropylene/CNC nanocomposites. *ACS applied materials & interfaces* **2014,** *6* (11), 8146-8157.

16.   Favier, V.; Dendievel, R.; Canova, G.; Cavaille, J.; Gilormini, P., Simulation and modeling of three-dimensional percolating structures: case of a latex matrix reinforced by a network of cellulose fibers. *Acta Materialia* **1997,** *45* (4), 1557-1565.

17.   Cao, X.; Dong, H.; Li, C. M., New nanocomposite materials reinforced with flax cellulose nanocrystals in waterborne polyurethane. *Biomacromolecules* **2007,** *8* (3), 899-904.

18.   Roohani, M.; Habibi, Y.; Belgacem, N. M.; Ebrahim, G.; Karimi, A. N.; Dufresne, A., Cellulose whiskers reinforced polyvinyl alcohol copolymers nanocomposites. *European polymer journal* **2008,** *44* (8), 2489-2498.

19.   Pereda, M.; Amica, G.; Rácz, I.; Marcovich, N. E., Structure and properties of nanocomposite films based on sodium caseinate and nanocellulose fibers. *Journal of Food Engineering* **2011,** *103* (1), 76-83.

20.   Tang, L.; Weder, C., Cellulose whisker/epoxy resin nanocomposites. *ACS Applied Materials & Interfaces* **2010,** *2* (4), 1073-1080.

21.   Gupta, A.; Kumar, V., New emerging trends in synthetic biodegradable polymers–Polylactide: A critique. *European polymer journal* **2007,** *43* (10), 4053-4074.

22.   Shi, X.; Ito, H.; Kikutani, T., Characterization on mixed-crystal structure and properties of poly (butylene adipate-co-terephthalate) biodegradable fibers. *Polymer* **2005,** *46* (25), 11442-11450.

23.   Kijchavengkul, T.; Auras, R.; Rubino, M.; Alvarado, E.; Montero, J. R. C.; Rosales, J. M., Atmospheric and soil degradation of aliphatic–aromatic polyester films. *Polymer Degradation and Stability* **2010,** *95* (2), 99-107.

24.   Averous, L.; Le Digabel, F., Properties of biocomposites based on lignocellulosic fillers. *Carbohydrate polymers* **2006,** *66* (4), 480-493.

25.   Fukushima, K.; Rasyida, A.; Yang, M.-C., Biocompatibility of organically modified nanocomposites based on PBAT. *Journal of Polymer Research* **2013,** *20* (11), 302.

26.   Al-Itry, R.; Lamnawar, K.; Maazouz, A., Improvement of thermal stability, rheological and mechanical properties of PLA, PBAT and their blends by reactive extrusion with functionalized epoxy. *Polymer Degradation and Stability* **2012,** *97* (10), 1898-1914.

27.   Fukushima, K.; Wu, M.-H.; Bocchini, S.; Rasyida, A.; Yang, M.-C., PBAT based nanocomposites for medical and industrial applications. *Materials Science and Engineering: C* **2012,** *32* (6), 1331-1351.

28.   Hong, S.; Ko, S.; Choi, H.; Lee, J., Multi-walled carbon nanotube/biodegradable poly (butyleneadipate-co-butyleneterephthalate) nanocomposites

and their physical characteristics. *Journal of Macromolecular Science, Part B* **2012,** *51* (1), 125-133.

29.   Kashi, S.; Gupta, R. K.; Kao, N.; Bhattacharya, S. N., Electrical, thermal, and viscoelastic properties of graphene nanoplatelet/poly (butylene adipate-co-terephthalate) biodegradable nanocomposites. *Journal of Applied Polymer Science* **2016,** *133* (27).

30.   Someya, Y.; Sugahara, Y.; Shibata, M., Nanocomposites based on poly (butylene adipate-co-terephthalate) and montmorillonite. *Journal of applied polymer science* **2005,** *95* (2), 386-392.

31.   Mohanty, S.; Nayak, S. K., Aromatic-aliphatic poly (butylene adipate-co-terephthalate) bionanocomposite: Influence of organic modification on structure and properties. *Polymer Composites* **2010,** *31* (7), 1194-1204.

32.   Nabar, Y.; Raquez, J. M.; Dubois, P.; Narayan, R., Production of starch foams by twin-screw extrusion: Effect of maleated poly (butylene adipate-co-terephthalate) as a compatibilizer. *Biomacromolecules* **2005,** *6* (2), 807-817.

33.   Rahimi, S. K.; Otaigbe, J. U., The role of particle surface functionality and microstructure development in isothermal and non-isothermal crystallization behavior of polyamide 6/cellulose nanocrystals nanocomposites. *Polymer* **2016,** *107*, 316-331.

34.   Mani, R.; Bhattacharya, M.; Tang, J., Functionalization of polyesters with maleic anhydride by reactive extrusion. *Journal of Polymer Science Part A: Polymer Chemistry* **1999,** *37* (11), 1693-1702.

35.   Bratawidjaja, A. S.; Gitopadmoyo, I.; Watanabe, Y.; Hatakeyama, T., Adhesive property of polypropylene modified with maleic anhydride by extrusion molding. *Journal of applied polymer science* **1989,** *37* (4), 1141-1145.

36.   Carlson, D.; Nie, L.; Narayan, R.; Dubois, P., Maleation of polylactide (PLA) by reactive extrusion. *Journal of applied polymer science* **1999,** *72* (4), 477-485.

37.   Carlson, D.; Dubois, P.; Nie, L.; Narayan, R., Free radical branching of polylactide by reactive extrusion. *Polymer Engineering & Science* **1998,** *38* (2), 311-321.

38.   Miyauchi, K.; Saito, K., 1H NMR assignment of oligomeric grafts of maleic anhydride-grafted polyolefin. *Magnetic Resonance in Chemistry* **2012,** *50* (8), 580-583.

39.   Zhao, P.; Liu, W.; Wu, Q.; Ren, J., Preparation, mechanical, and thermal properties of biodegradable polyesters/poly (lactic acid) blends. *Journal of Nanomaterials* **2010,** *2010*, 4.

40.   Weng, Y.-X.; Jin, Y.-J.; Meng, Q.-Y.; Wang, L.; Zhang, M.; Wang, Y.-Z., Biodegradation behavior of poly (butylene adipate-co-terephthalate)(PBAT), poly (lactic acid)(PLA), and their blend under soil conditions. *Polymer Testing* **2013,** *32* (5), 918-926.

41.   Wu, C.-S., Characterization of cellulose acetate-reinforced aliphatic–aromatic copolyester composites. *Carbohydrate polymers* **2012,** *87* (2), 1249-1256.

42.   Kamal, M. R.; Khoshkava, V., Effect of cellulose nanocrystals (CNC) on rheological and mechanical properties and crystallization behavior of PLA/CNC nanocomposites. *Carbohydrate polymers* **2015,** *123*, 105-114.

43.   Herrera, R.; Franco, L.; Rodríguez-Galán, A.; Puiggalí, J., Characterization and degradation behavior of poly (butylene adipate-co-terephthalate) s. *Journal of Polymer Science Part A: Polymer Chemistry* **2002,** *40* (23), 4141-4157.

44.   Ten, E.; Jiang, L.; Wolcott, M. P., Crystallization kinetics of poly (3-hydroxybutyrate-co-3-hydroxyvalerate)/cellulose nanowhiskers composites. *Carbohydrate polymers* **2012,** *90* (1), 541-550.

45.   Zhang, X.; Ma, P.; Zhang, Y., Structure and properties of surface-acetylated cellulose nanocrystal/poly (butylene adipate-co. *Polymer Bulletin* **2016,** *73* (7), 2073-2085.

46.   Krishnamoorti, R.; Vaia, R. A.; Giannelis, E. P., Structure and dynamics of polymer-layered silicate nanocomposites. *Chemistry of Materials* **1996,** *8* (8), 1728-1734.

47.   Litchfield, D. W.; Baird, D. G., The rheology of high aspect ratio nano-particle filled liquids. *Rheology Reviews* **2006,** *2006*, 1.

48.   Chauve, G.; Heux, L.; Arouini, R.; Mazeau, K., Cellulose poly (ethylene-co-vinyl acetate) nanocomposites studied by molecular modeling and mechanical spectroscopy. *Biomacromolecules* **2005,** *6* (4), 2025-2031.

49.   Shih, W.-H.; Shih, W. Y.; Kim, S.-I.; Liu, J.; Aksay, I. A., Scaling behavior of the elastic properties of colloidal gels. *Physical review A* **1990,** *42* (8), 4772.

50.   Durmus, A.; Kasgoz, A.; Macosko, C. W., Linear low density polyethylene (LLDPE)/clay nanocomposites. Part I: Structural characterization and quantifying clay dispersion by melt rheology. *Polymer* **2007,** *48* (15), 4492-4502.

51.   Utracki, L., Flow and flow orientation of composites containing anisometric particles. *Polymer composites* **1986,** *7* (5), 274-282.

52.   Ren, J.; Silva, A. S.; Krishnamoorti, R., Linear viscoelasticity of disordered polystyrene− polyisoprene block copolymer based layered-silicate nanocomposites. *Macromolecules* **2000,** *33* (10), 3739-3746.

53.   Schilde, C., *Structure, mechanics and fracture of nanoparticulate aggregates*. Sierke Verlag: Gottingen 2012; Vol. 10.

54.   Khoshkava, V.; Kamal, M., Effect of surface energy on dispersion and mechanical properties of polymer/nanocrystalline cellulose nanocomposites. *Biomacromolecules* **2013,** *14* (9), 3155-3163.

55.   Lin, N.; Dufresne, A., Nanocellulose in biomedicine: Current status and future prospect. *European Polymer Journal* **2014,** *59*, 302-325.

56.   Dong, S.; Hirani, A. A.; Colacino, K. R.; Lee, Y. W.; Roman, M., Cytotoxicity and cellular uptake of cellulose nanocrystals. *Nano Life* **2012,** *2* (03), 1241006.

57.   Rueda, L.; Saralegi, A.; Fernández-d'Arlas, B.; Zhou, Q.; Alonso-Varona, A.; Berglund, L. A.; Mondragon, I.; Corcuera, M.; Eceiza, A., In situ polymerization and characterization of elastomeric polyurethane-cellulose nanocrystal nanocomposites. Cell response evaluation. *Cellulose* **2013,** *20* (4), 1819-1828.

58.   Li, W.; Guo, R.; Lan, Y.; Zhang, Y.; Xue, W.; Zhang, Y., Preparation and properties of cellulose nanocrystals reinforced collagen composite films. *Journal of Biomedical Materials Research Part A* **2014,** *102* (4), 1131-1139.

59.   Fortunati, E.; Armentano, I.; Zhou, Q.; Iannoni, A.; Saino, E.; Visai, L.; Berglund, L. A.; Kenny, J., Multifunctional bionanocomposite films of poly (lactic acid), cellulose nanocrystals and silver nanoparticles. *Carbohydrate polymers* **2012,** *87* (2), 1596-1605.

60.   Domingues, R. M.; Gomes, M. E.; Reis, R. L., The potential of cellulose nanocrystals in tissue engineering strategies. *Biomacromolecules* **2014,** *15* (7), 2327-2346.

61.   ISO, B., 10993-5: Biological evaluation of medical devices. *Tests for in vitro cytotoxicity* **1999**.

62.   Kroll, A.; Dierker, C.; Rommel, C.; Hahn, D.; Wohlleben, W.; Schulze-Isfort, C.; Göbbert, C.; Voetz, M.; Hardinghaus, F.; Schnekenburger, J., Cytotoxicity screening of 23 engineered nanomaterials using a test matrix of ten cell lines and three different assays. *Particle and fibre toxicology* **2011,** *8* (1), 9.

63.   Jao, W. C.; Lin, C. H.; Hsieh, J. Y.; Yeh, Y. H.; Liu, C. Y.; Yang, M. C., Effect of immobilization of polysaccharides on the biocompatibility of poly (butyleneadipate-co-terephthalate) films. *Polymers for Advanced Technologies* **2010,** *21* (8), 543-553.

64.   Palin, E.; Liu, H.; Webster, T. J., Mimicking the nanofeatures of bone increases bone-forming cell adhesion and proliferation. *Nanotechnology* **2005,** *16* (9), 1828.

65.   Hallab, N. J.; Bundy, K. J.; O'Connor, K.; Moses, R. L.; Jacobs, J. J., Evaluation of metallic and polymeric biomaterial surface energy and surface roughness characteristics for directed cell adhesion. *Tissue engineering* **2001,** *7* (1), 55-71.

66.   Hossain, K. M. Z.; Hasan, M. S.; Boyd, D.; Rudd, C. D.; Ahmed, I.; Thielemans, W., Effect of cellulose nanowhiskers on surface morphology, mechanical properties, and cell adhesion of melt-drawn polylactic acid fibers. *Biomacromolecules* **2014,** *15* (4), 1498-1506.

67.   Arima, Y.; Iwata, H., Effect of wettability and surface functional groups on protein adsorption and cell adhesion using well-defined mixed self-assembled monolayers. *Biomaterials* **2007,** *28* (20), 3074-3082.
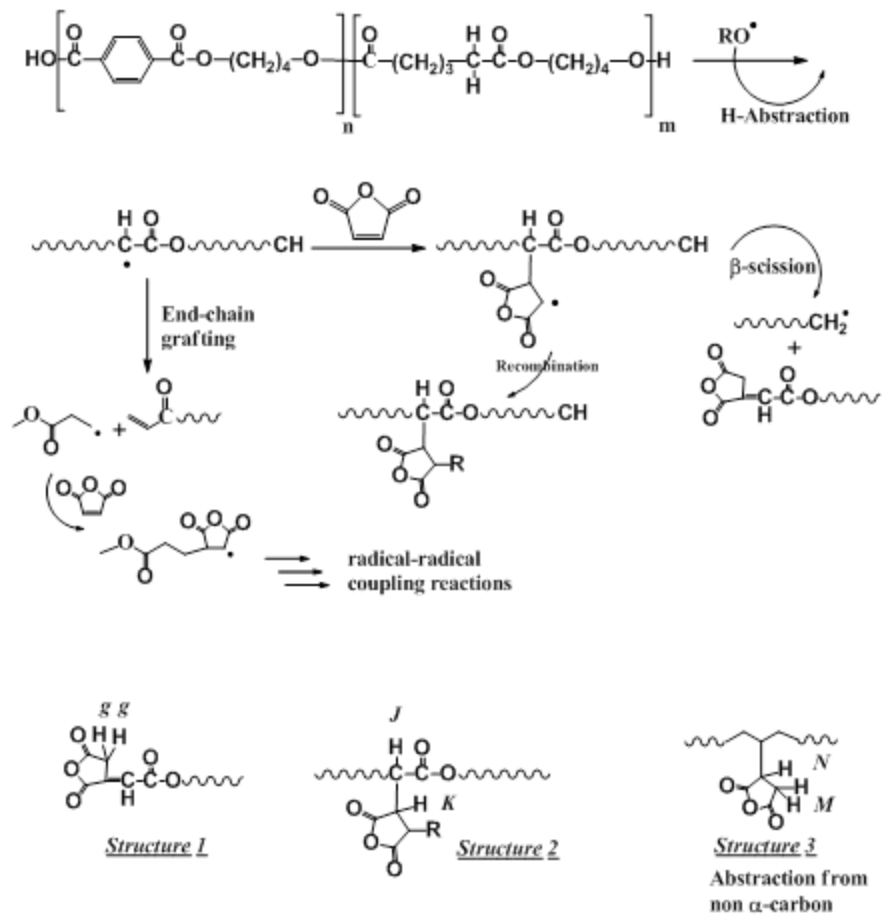
Figure 6.1 Reaction Mechanisms of grafting of MA onto PBAT chains and the subsequent termination pathways
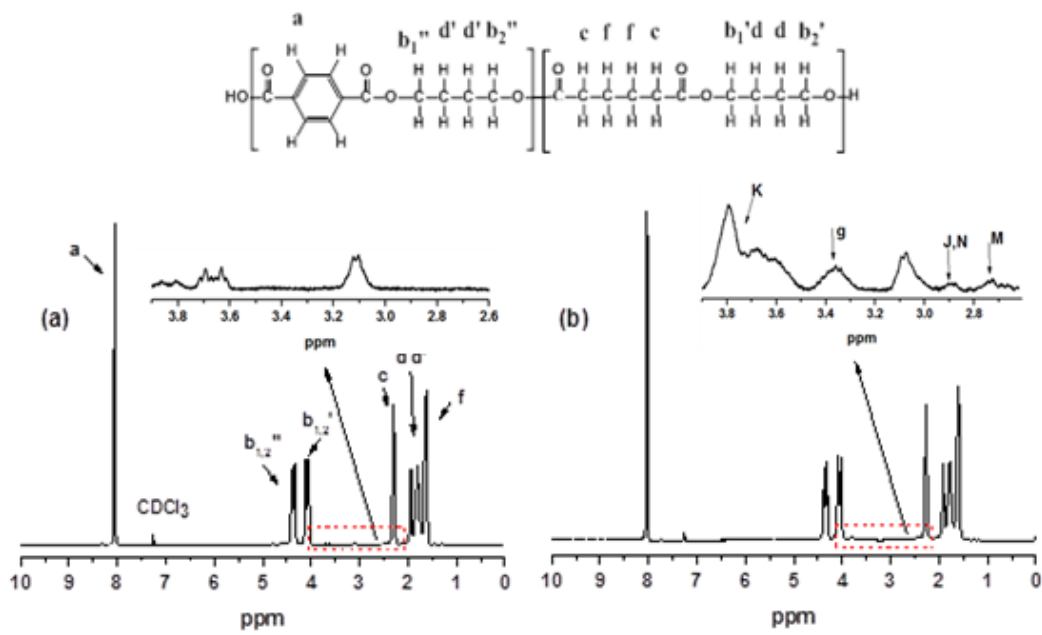
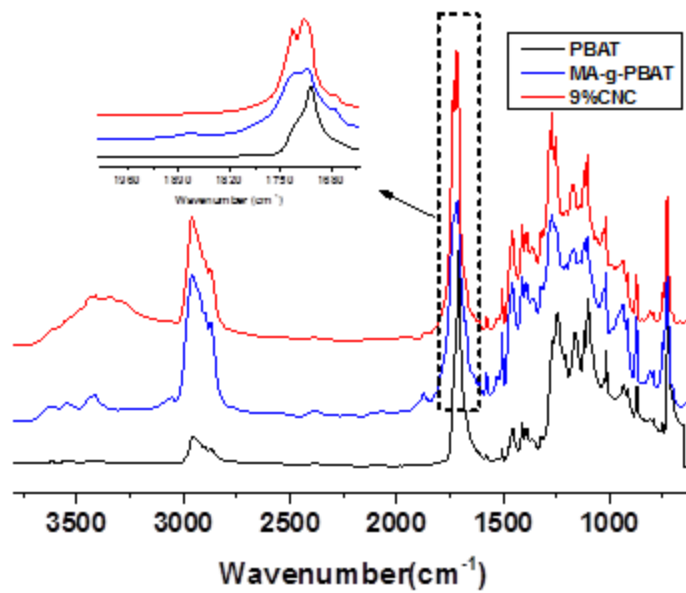Figure 6.2 ^{1}H NMR spectra of PBAT and MA-*g*-PBAT

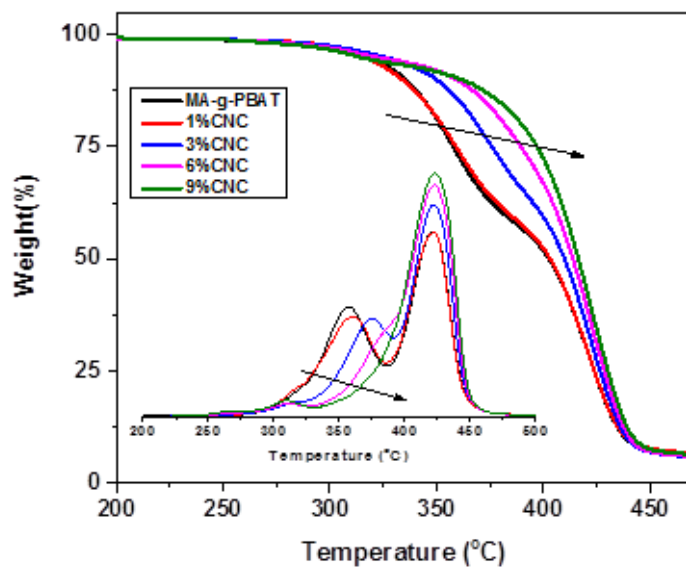Figure 6.3 ATR-IR spectra of PBAT, MA-*g*-PBAT and 9%CNC nanocomposite

Figure 6.4 TGA and DTG curves of MA-*g*-PBAT and MA-*g*-PBAT/CNC nanocomposites
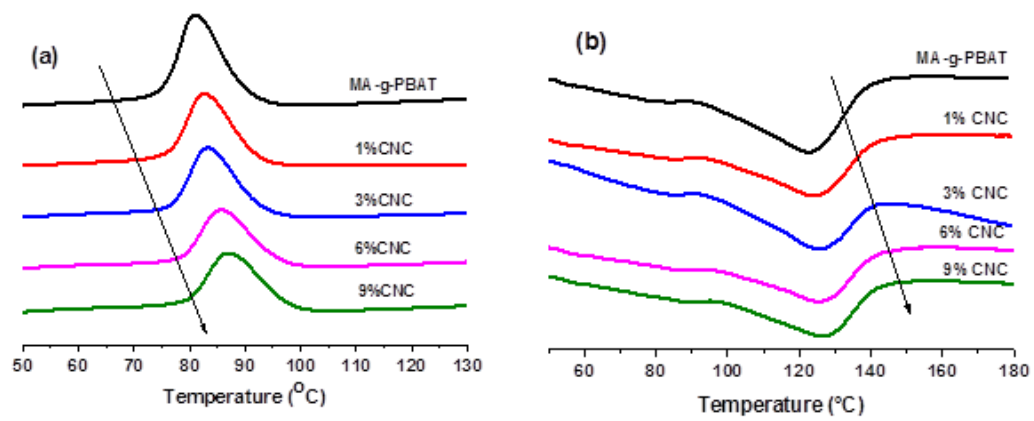
Figure 6.5 (a) Crystallization exotherms and (b) melting endotherms of MA-*g*-PBAT/CNC nanocomposites
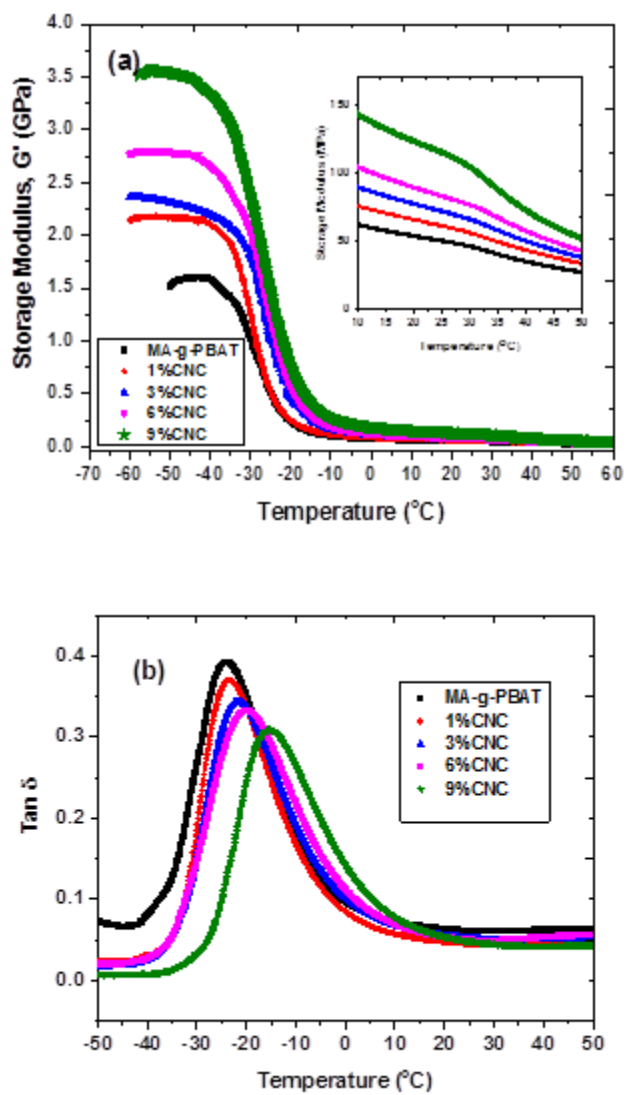
Figure 6.6 (a) Variation of storage modulus versus temperature and (b) variation of damping factor versus temperature of MA-*g*-PBAT/CNC nanocomposites
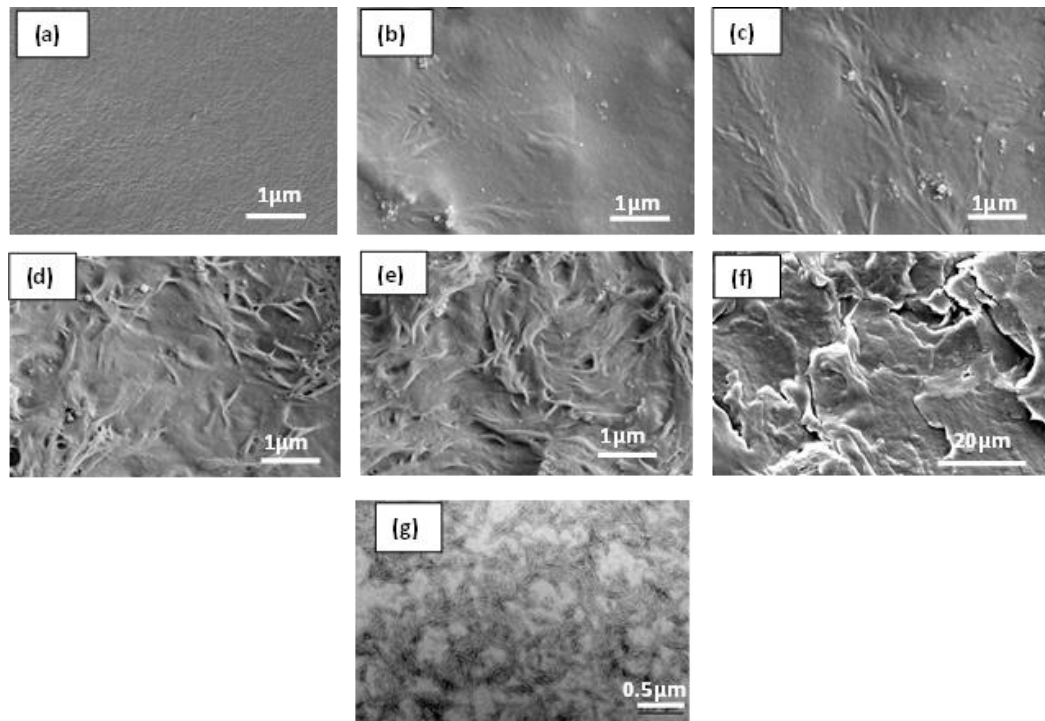
Figure 6.7 SEM images of (a) MA-g-PBAT, (b) 1%CNC, (c) 3%CNC, (d) 6%CNC, (e) 9%CNC, (f) unmodified PBAT/9%CNC and (g) TEM images of cellulose nanocrystals
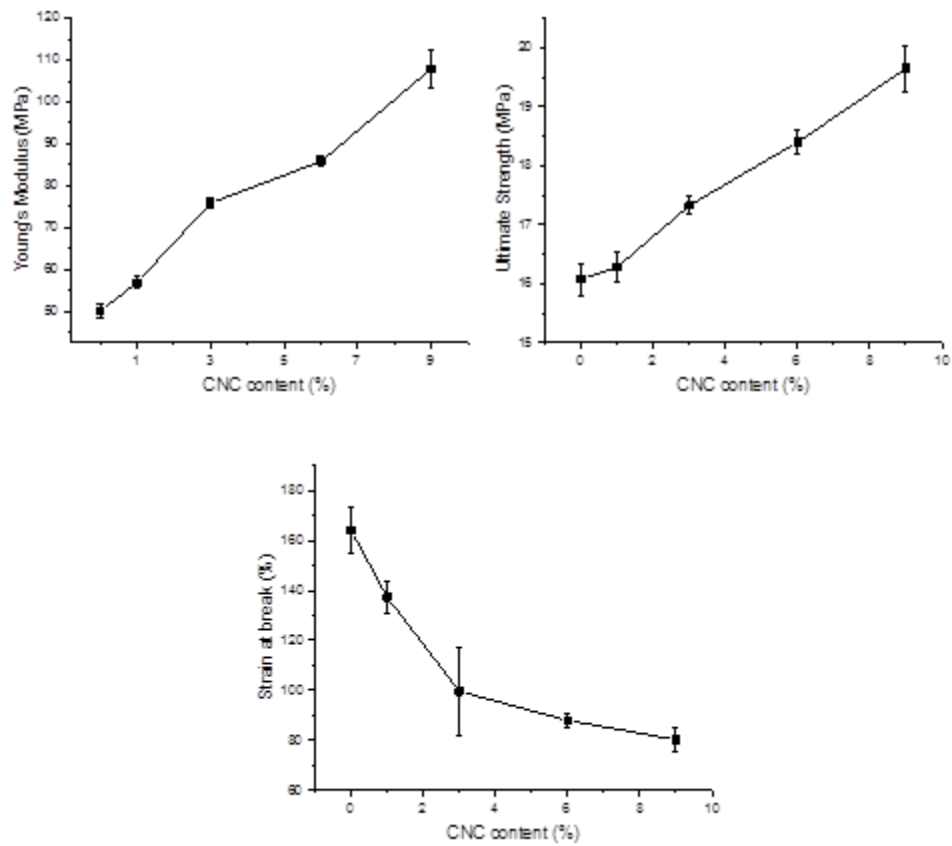
Figure 6.8 Effect of CNC content on modulus, stress and strain at break of MA-*g*-PBAT nanocomposites
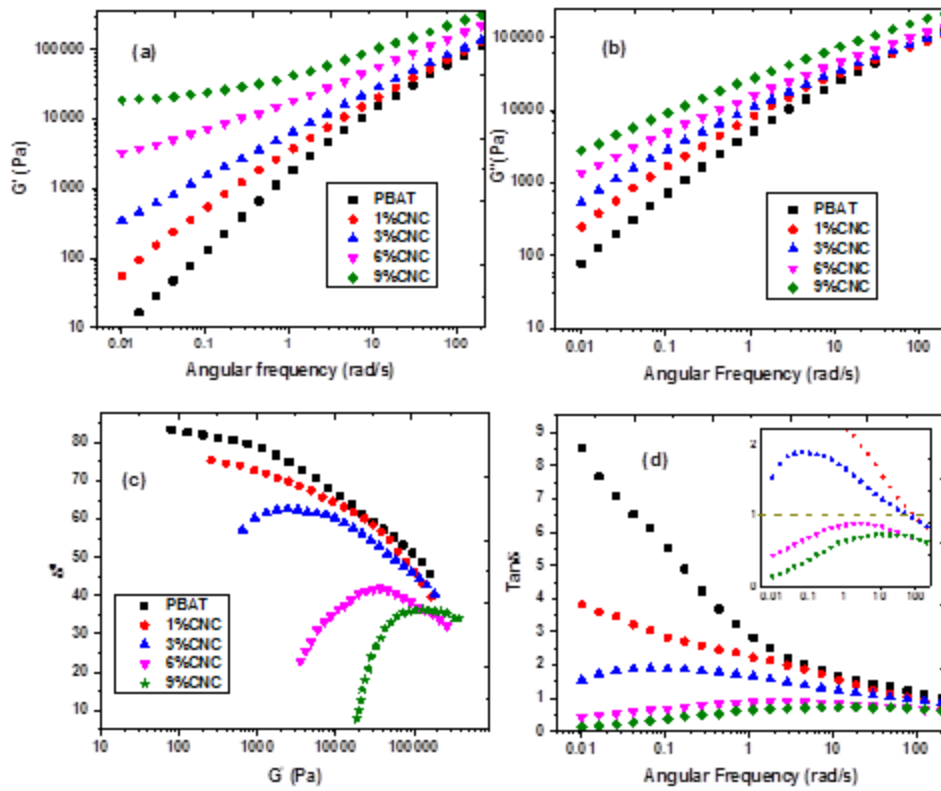
Figure 6.9 (a) Variation of storage modulus versus frequency, (b) variation of loss modulus versus frequency, (c) variation of phase angle versus complex modulus and (d) variation of tanδ versus frequency.
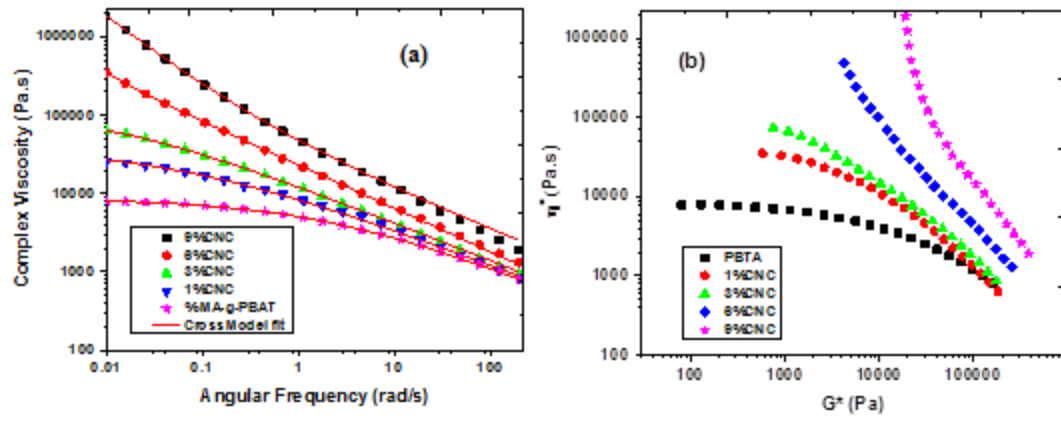
Figure 6.10 (a) Variation of Complex viscosity versus frequency and (b) variation of complex viscosity versus complex modulus.
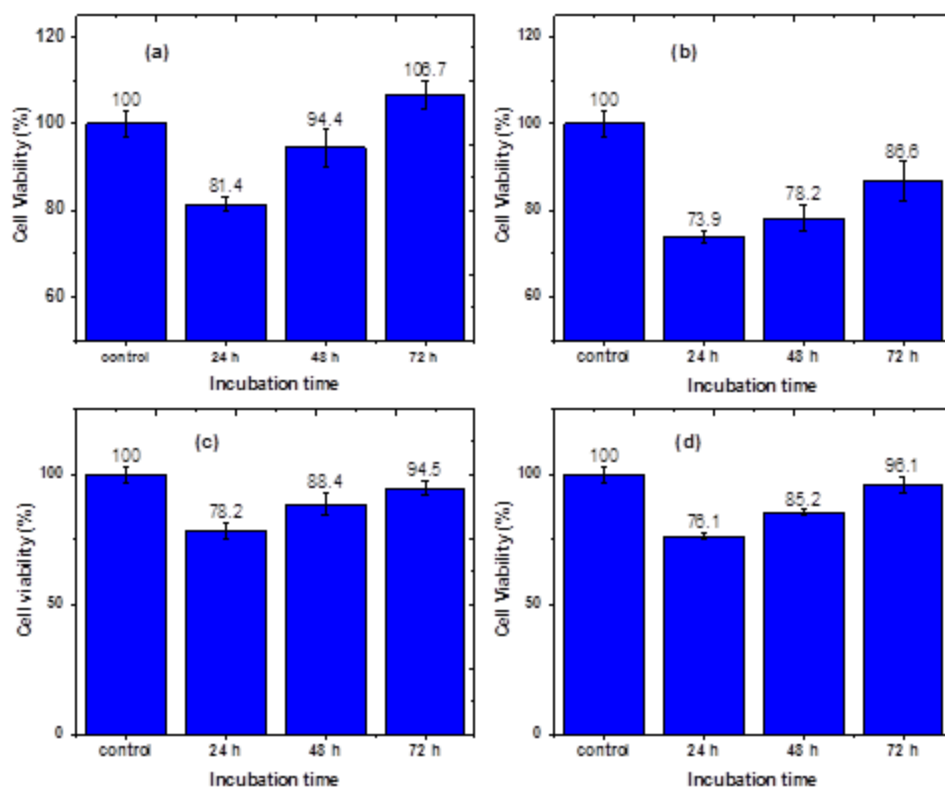
Figure 6.11 MTT assay cell viability of L929 cells for (a) MA-g-PBAT, (b) cellulose nanocrystals, (c) 3%CNC and (d) 9% CNC nanocomposites.

Figure 6.12 L929 cell proliferation on 9%CNC nanocomposite after (a) 0 hours and (b) 48 hours of incubation time.

Images are taken at 10 fold magnification.

Figure 6.13 SEM images showing the L929 cell adhesion and growth on (top) MA-g-PBAT and (bottom) 9%CNC nanocomposite after 72 hours of culture.

Table 6.1

Results of the TGA experiments on the nanocomposites samples
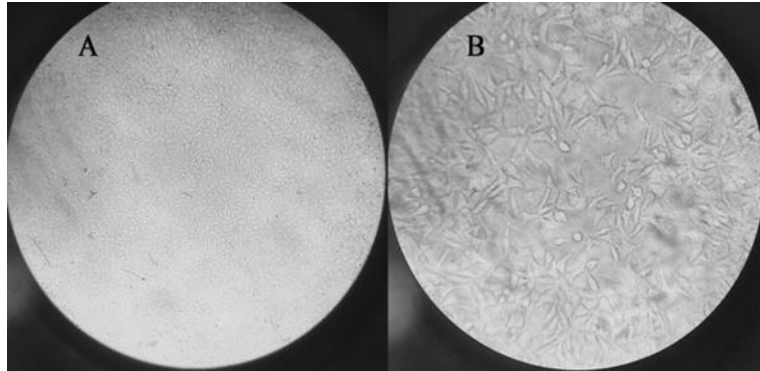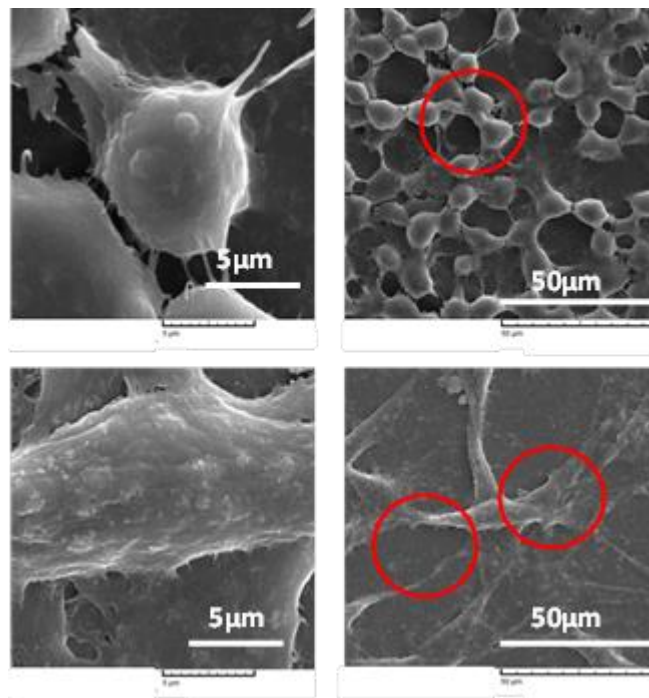
	T_{onset} (°C)		$T_{30\%}$(°C)	$T_{70\%}$(°C)	DTG peak 1 (°C)	DTG peak 2 (°C)
MA-g-PBAT	320.1	401.3	363.9	420.3	356.4	420.9
1%CNC	321.8	403.2	365.8	420.4	358.3	422.1
3%CNC	345.6	421.5	382.9	423.6	372.5	422.5
6%CNC	377.2	430.9	396.3	426.1	381.7	423.7
9%CNC	395.4	-	403.4	427.0	390.1	423.9

Table 6.2

Crystallizaiton and melting temperature, enthalpy of fusion and degree of crystallinity for

MA-*g*-PBAT/CNC nanocomposites

	T_c(°C)	T_m(°C)	ΔH_m(J/g)	χ (%)
MA-g-PBAT	81.1(0.6)	122.8(0.1)	11.2(0.3)	9.8
1%CNC	82.8(0.1)	124.4(0.3)	9.1(0.3)	8.1
3%CNC	83.3(0.2)	125.1(0.4)	8.2(0.4)	7.4
6%CNC	85.7(0.5)	125.7(0.1)	8.6(0.1)	8.0
9%CNC	87.4(0.3)	126.1(0.5)	9.5(0.2)	9.2

Table 6.3

The results of DMA experiments on MA-g-PBAT/CNC nanocomposite samples.

	E'$_{-40°C}$(GPa)	E'$_{20°C}$(MPa)	tanδ_{max}	Peak tanδ_{max}(°C)
MA-g-PBAT	1.64 (0.12)	52.1 (4.1)	0.39	-24.3 (1.1)
1%CNC	2.12 (0.22)	65.5 (5.3)	0.37	-23.1 (0.9)
3%CNC	2.27 (0.18)	81.2 (2.4)	0.34	-21.3 (1.1)
6%CNC	2.75 (0.15)	95.5 (4.6)	0.32	-19.8 (1.2)
9%CNC	3.45 (0.21)	121.4 (4.5)	0.29	-17.3 (1.2)

Table 6.4

Mechanical properties of MA-g-PBAT/CNC nanocomposites

sample	E (Mpa)	Max. Stress (Mpa)	Max. Strain (%)

MA-g-PBAT	50.1 ± 1.7	16.1 ± 0.3	164.1 ± 9.1
1%CNC	56.9 ± 1.5	16.3 ± 0.3	157.3 ± 6.4
3%CNC	76.1 ±	17.4 ±0.1	99.7 ± 17.7
6%CNC	85.8 ± 1.3	18.6 ±0.2	88.1 ± 2.6
9%CNC	107.9± 4.6	19.7 ±0.4	80.3 ± 4.0

Sample	Slope of terminal G'	Slope of terminal G"	G_P (pa)
MA-g-PBAT	1.16	0.98	18787
1% CNC	0.96	0.87	3267
3% CNC	0.64	0.73	348
6% CNC	0.32	0.59	55
9%CNC	0.11	0.55	9

Table 6.5

Terminal slopes of storage and loss modulus as well as the plateau modulus of the MA-g-

PBAT/CNC nanocomposites samples.

Table 6.6

Cross model fit parameters

sample	σ_y (Pa)	η_P (Pa.s)	α (S)	m
MA-g-PBAT	0	8622.6	0.69	0.49
1%CNC	41.3	38800	3.27	0.57
3%CNC	741.7	39425.1	2.2	0.61
6%CNC	2616.4	329255.3	11.8	0.56
9%CNC	17161.8	406697.4	12.9	0.5

CHAPTER VII –CONCLUDING REMARKS AND POTENTIAL FUTURE

RESEARCH DIRECTIONS

The dissertation investigates the complex inter-relationship between the

processing, microstructure and properties of high performance thermoplastic composites

reinforced with cellulosic fibers. The main focus of this study was to explore the

utilization of ring-opening polymerization of caproalctam to develop an in-situ anionic

ring-opening polymerization process to fabricate the hybrid materials. The rationale

behind this approach was that using the cyclomer technology, a good dispersion of

nanoscale cellulose whiskers could be achieved while bypassing the degradative effects

of direct conventional melt mixing methods such as extrusion due to the difficulty in

dispersion of CNC in high viscosity polymer melts as well as the possibility of thermal

degradation of fibers at such high temperatures.

Incorporation of CNCs into PA6 matrix was successfully achieved via the in-situ

ROP process. Analysis of the structural and mechanical properties of the nanocomposites

revealed that even at low CNC concentrations (up to 2w%), a true reinforcing effect

could be exploited. The significant changes in viscoelastic properties in both solid state

and melt state revealed that with increasing the CNC concentration, the melt elasticity

and strength, as well as the creep resistance and recovery upon load removal even at

elevated temperatures could be surprisingly improved. The morphological observation of

the microstructure of the ROPed nanocomposites showed that the CNCs initially form

very fine clusters within he matrix while increasing the CNC loading, changes the

microstructure into more fibrillary-type morphology. The analysis of structure break up

and recovery in the melt state showed that the fibrillary structure could effectively be

disrupted by application of shear flow and subsequently undergo a gradual structure recovery.

A surprising result was the observation of the enhanced thermal stability of the ROPed nanocomposite systems compared to the pure PA6. This was an encouraging finding as it allowed the research to further explore into utilization of a short subsequent melt extrusion step while using the ROPed system as the extrusion masterbatch in order to further improve the dispersion of CNC in the matrix.

Considering the crucial effect of the interfacial adhesion between the CNC particles and the PA6 matrix, the effects of modification of the CNC surface with aminopropyltriethoxysilane (APS) on various properties of the nanocomposites were studied in detail. First of all, the interfacial bond formation between the modified CNC and the PA6 matrix was confirmed by solid state ^{29}Si NMR spectroscopy. It was found that modification of the CNC surface with APS, significantly changes the microstructure of the CNC in the matrix from fibrillary type more towards individually dispersed whiskers. This is was of utmost importance as not only the interfacial adhesion could be significantly improved but also the finer dispersion of APS-CNCs would result in significantly larger interfacial area with the matrix.

Analysis of the crystallization behavior of the nanocomposite samples showed that while the nanocomposite containing the pristine CNC significantly hindered the crystallization process primarily due to the increased viscosity of the PA6 melt as well as acting as a physical barrier against crystals growth of PA6 chains, the surface modified particles promoted the formation of a majority of γ-type crystals in the nucleation phase. Both unmodified and modified samples, severely restricted the crystal growth of the PA6

resulting in formation of much smaller defected spherulites as observed by polarized optical microscope.

Investigation of the mechanical properties of the resulting nanocomposites showed an exceptional reinforcing effect of CNC within the PA6 matrix which was even further enhanced by modification of CNC surface with APS. The analysis of the mechanical behavior using various micromechanical models showed that while the orientation of the whiskers in the samples was important in obtaining high reinforcing effect, formation of the rigid interface or "interphase" plays a key role in controlling the nanocomposite properties. In fact, underestimation of the modulus values by percolation and shear lag theory showed that the rigid interphase could effectively increase the total rigid "fraction" of the nanocomposites and act as a bridging layer between the particles even at volume fractions below the percolation threshold. This was further investigated by quantitative nanomechanical analysis of interface where it was found that surface modified CNC particles generated a thicker and broader interphase with higher local modulus. This interphase is in fact, the major factor in efficient stress transfer from the matrix to particles.

In addition, the analysis of the melt rheological properties of these systems was carried out in shear elongation and squeeze flow regimes. The results of the extensional viscosity measurements showed that the orientation of whiskers within he melt could significantly improve the melt strength of the matrix during elongation flow by strain hardening effect. The results of the shear rheological experiments showed that with increasing the CNC concentration, a non-terminality of viscoelastic properties at low

336

frequencies was developed which was attributed to the formation of CNC nanostructure in the matrix.

This work was further extended to the macro-composites of polyamide 6 reinforced with flax fabric and kraft cellulose pulp mat. A successful vacuum assisted resin infusion set up was developed to infuse the fiber beds with activated caprolactam monomer. Analysis of the effect of initiator type and fiber pre-treatment on the conversion of ROP reaction revealed that a combination of alkali-pretreatment of the fibers with the use of magnesium-bromide caprolactamate initiator could result in successful ROP reaction in presence of the natural fibers. In addition, it was found that the optimal polymerization temperature to achieve the desirable mechanical properties was 150°C as lower polymerization temperatures limit the monomer conversion while higher temperatures result in more polymerization inhibition by the fibers as well as generation of higher void content. In addition, with increasing the polymerization temperature the stiffness of the matrix reduces due to reduction in degree of crystallinity.

This work was further extended to the application of cellulose nanocrystals as reinforcement in poly(butylene adipate-co-terephthalate) thermoplastic material. A reactive extrusion process was utilized to first modify the PBAT with reactive maleic anhydride groups and then subsequent processing with CNCs resulted in superior dispersion of particles in the matrix. The importance of such system was the fact that both the polymer and reinforcement were biodegradable and could potentially be used for biomedical applications. This was studied through L929 cell culture on the nanocomposite samples where it was found that the nanocomposites containing up to 9wt% CNC are fully biocompatible. In addition, the enhanced roughness of the samples

337

caused by cellulose nanocrystals, improved the cell adhesion and growth compared to the neat polymer.

There are several pathways to further extend this project and conduct more experimental studies to better understand these systems. First, the nanocomposite samples could be studied using dielectric spectroscopy to gain a better understanding of the relaxation process of the polymer in the vicinity of the cellulose nanocrystals especially with various surface functionalities. In addition, another important aspect of these PA6/CNC systems that need to be investigated is the effect of moisture on structural and interfacial properties. Since both the matrix and the CNC are highly hydrophilic, controlled exposure of the samples to various humidity conditions could help us to get a better understanding of the effect of moisture ingress on the properties of the nanocomposites.

Another pathway for further investigation is the modification of CNC surface via surface-initiated ring opening polymerization of caprolactam with pre-attached initiating sites on the surface. This approach could significantly improve the interfacial adhesion with the PA6 matrix as the surface polyamide groups are fully compatible with the similar matrix in addition to the possibility of bond formation through transamidation reaction.

Finally, the macro-composite research could be extended to hybridizing the natural fibers with glass fibers towards the ultimate goal of replacing the glass fibers with cellulosics. In fact, incorporation of cellulose fabric together with the glass fiber reinforcement could improve the fracture toughness and potentially the impact strength of the composites that could be a topic of future investigation.

338